Search of the Standard Model Higgs boson decaying into two lepton taus with the Run2 data of ATLAS detector in LHC

Mohamad Kassem Ayoub

université PARIS-SACLAY

UNIVERSITÉ PARIS SUD
Comprendre le monde, construire l'avenir

NNT : 2016SACLS420

THESE DE DOCTORAT
DE
L'UNIVERSITE PARIS-SACLAY
PREPAREE A
L'UNIVERSITE PARIS-SUD

Laboratoire de l'Accélérateur Linéaire

ECOLE DOCTORALE N° 576
PHENIICS

Spécialité : Physique des particules

Par

M. Mohamad Kassem Ayoub

Recherche du boson de Higgs se désintégrant en deux leptons taus dans le canal $\tau_{lep}\tau_{had}$ dans l'expérience ATLAS avec les données à 13 TeV du LHC

Thèse présentée et soutenue au LAL (Bures-sur-yvette), le 23 novembre 2016 :

Composition du Jury :

M. Achille Stocchi	Directeur (LAL)	Président
M. Gregorio Bernardi	Directeur de recherche (LPNHE)	Rapporteur
M. Stan Lai	Professeur (Goettingen)	Rapporteur
M. Florian Beaudette	Chargé de recherche (LLR)	Examinateur
M. Fabrice Hubaut	Directeur de recherche (CPPM)	Examinateur
M. Luc Poggioli	Directeur de recherche (LAL)	Directeur de thèse

Laboratoire de l'Accélérateur Linéaire LAL 16-224

"Wisdom is not a product of schooling but of the lifelong attempt to acquire it"

Albert Einstein

université PARIS-SACLAY | ÉCOLE DOCTORALE PHENIICS

Titre : Recherche du boson de Higgs se désintégrant en deux leptons tau dans le canal $\tau_{lep}\tau_{had}$ dans l'expérience ATLAS avec les données à 13 TeV du LHC.

Mots clés : Modèle Standard, boson de Higgs, LHC, ATLAS, H→ττ

Résumé : Dans cette thèse, je présente ma contribution à la recherche du boson de Higgs du Modèle Standard dans son canal de désintégration en deux leptons taus dans le sous-canal $\tau_{lep}\tau_{had}$. J'ai contribué aux différentes étapes de cette analyse. Premièrement, j'ai travaillé sur le développement du framework utilisé pour produire les fichiers d'analyse qui contiennent les informations nécessaires à cette étude. J'ai également participé au développement du framework utilisé pour introduire les prédictions des bruits de fond pour ce canal, tester l'accord entre ces prédictions et les données d'ATLAS, et à la production des fichiers utilisés dans l'étude statistique finale. J'ai également travaillé sur le modèle statistique, qui prend en compte les erreurs statistiques et systématiques, pour en extraire une mesure de la force du signal pour ce canal du couplage du Higgs aux leptons. Ma contribution à l'amélioration de la reconstruction d'un tau hadronique, à l'aide des algorithmes qui identifient les traces de conversion des photons provenant de la désintégration des pions neutres, est également détaillée.

Title : Search for the Higgs boson decaying into two tau leptons in the $\tau_{lep}\tau_{had}$ channel in ATLAS experiment with the 13 TeV data of the LHC

Keywords : Standard Model, Higgs, LHC, ATLAS, H→ττ

Abstract : In this thesis, I show my contribution to the search for the Standard Model Higgs Boson decaying into two tau leptons in the $\tau_{lep}\tau_{had}$ sub-channel. I contributed to the different stages of this analysis. First, I worked on the development of the framework used to produce analysis files that contain the information necessary for this study. I also participated in the development of the framework used to introduce the predictions of the background for that channel, test the agreement between the predictions and the ATLAS data, and on the production of files used in the final statistical analysis. I also worked on the statistical model, which takes into account the statistical and systematic errors to extract a measurement of the signal strength for the Higgs coupling channel to leptons. My contribution to the improvement of reconstruction of a hadronic tau, using algorithms that identify photon conversion traces from the decay of neutral pions, is also detailed.

Acknowledgments

First of all, I would like to thank very much my wonderful supervisor, Luc Poggioli. Thanks for all your time, your support. You gave me the opportunity to have a really nice scientific and human experience. Without you Luc, this thesis would not have been completed.

A big thanks goes to David Rousseau, the group leader during my PhD. Thanks for being always very nice and helpful to me.

I am equally grateful to Achille Stocchi who gave me the opportunity to do the master NPAC. This has opened the door for me to enter in the great particle physics world, the LHC, and work in ATLAS group, which was like a dream when I was at school.
I want to thank all ATLAS-LAL members who I spent three years with. A special thanks goes to Jean Baptiste de Vivie and Laurent Duflot for being always there to answer my questions. Thanks also to my friends in the group for all the "soirée" and the good times with you, especially Steven, Baptiste, Christophe, and Charle, and all the new students. I want to especially thank David Delgove for all the fruitful discussions we had since we were NPAC students.

I am also grateful to all ATLAS people I have worked with, Dimitris Varouchas, Quentin Buat, Zinonas Zinonos, Clara Nellist, Antonio Di Maria and Brian Le.

A big thanks goes to my Lebanese friends who always supported me.

I want to thank all my professors in the Lebanese university who gave me the essential background to continue in this field.

A very big emotional thanks goes to my family. As we say in Lebanon, you are the "Light of my eyes and the soul of my heart". Thanks my parents, Rima and Ali, my grandmother Zalfa, my aunt Sawsan and my friend Catherine Bourge, my brothers and sisters who were helping and supporting me all the time, Fatima, Hussein, Rabab, Ghadir, Taghrid and Abdallah. Without you, I would not be here.

Finally, I want to dedicate this work to my grandmother Khadija who planned to come to Paris to attend my defense but she passed away in the last period of my thesis.

Contents

Chapter 1

The Standard Model of particle physics

Contents

1.1 Introduction

1.1.1 The nature in the view of particle physics

What is the world around us made of? How we can describe the world in terms of particle physics? These questions are what we try to answer in the elementary

particle physics domain.
Let's start with a quick historical introduction. The Greeks gave much to the world of physics by developing the basis of fundamental modern principles as the conservation of matter, atomic theory, etc. Atoms were postulated long ago by the Greek philosopher Democritus, and until the beginning of the 20^{th} century, atoms were thought to be the fundamental indivisible building blocks of all forms of matter. Protons, neutrons and electrons came to be regarded as the fundamental particles of nature when we learned in the 1900's through the experiments of Rutherford and others that atoms consist of mostly empty space with electrons surrounding a dense central nucleus made up of protons and neutrons. In this period, atoms were solid building blocks of nature and people trusted Newtonian laws of motion. However, scientists gradually realized that their knowledge was far from complete when they started with Einstein's theory of relativity which replaced Newtonian mechanics.
Of particular interest was the growing field of quantum mechanics, which completely altered the fundamental precepts of physics at the begining of the 20^{th} century. In quantum mechanics, the point-like scheme of particles with defined momentum and position is no more valid. A wave function is associated now to particles where its modulus square is defined as the probability of presence in a given position. The formalism of quantum mechanics was done between 1925 and 1927, and was the fruit of an exceptional conjunction of talents of physicists and mathematicians like Schrödinger, Heisenberg, Born, Bohr, Dirac, Pauli, Hilbert, Von Neumann, etc.
Let's speak now with more recent way about particle physics. With the development of accelerator physics and the advent of particle accelerators that could accelerate protons and electrons to high energies, a great progress of science of particle physics has followed and a rich spectrum of new particles were produced in these collison experiments.
We distinguish two types of elementary particles: the fondamental constituents of matter called "Fermions", and the quanta of fields called "Bosons". The interaction between fermions is thus mediated by the exchange of these bosons. In the following sections, we will see more details about the nature of these sub-atomic constituants.

1.1.2 Fermions

The matter particles are fermions. They have an intrinsic angular momentum, called spin, J=1/2. They obey the Fermi-Dirac statistics. Fermions are divided into two categories: leptons and quarks. There is for every fermion an anti-fermion that has the same mass but opposite quantum numbers. Fermions and anti-fermions can annihilate or be created when enough energy is available.

1.1.2.1 Leptons

The leptons (comes from the Greek word meaning "light"). There are three families or generations of leptons formed by three charged leptons (electron e, muon μ and tau τ) and the respective neutral leptons, the neutrinos (ν_e, ν_μ and ν_τ) as it is

shown in Figure 1.1. For each leptonic family, we associate a quantum number called leptonic number, L. Only electron and neutrinos are stable. The electron anti-particle, the positron, has identical mass but has a positive charge. The muon is a lepton which could decay to an electron or a positron ($\mu^- \longrightarrow e^- + \bar{\nu_e} + \nu_\mu$ or $\mu^+ \longrightarrow e^+ + \nu_e + \bar{\nu_\mu}$). The lifetime of the muon is 2.2 μs. It can be produced for example in the upper atmosphere by the decay of pions produced by cosmic rays ($\pi^+ \longrightarrow \mu^+ + \nu_\mu$ or $\pi^- \longrightarrow \mu^- + \bar{\nu_\mu}$). The tau is the most massive lepton. It has a rest mass of 3477 times the mass of the electron and 17 times the one of the muon [1].

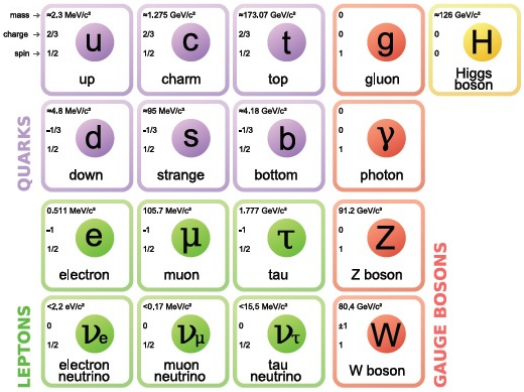

Figure 1.1: Elementary particles of the Standard Model.

1.1.2.2 Quarks

There are six known quarks. As for leptons, quarks are grouped in three families as it is detailed in Figure 1.1 For each family, we associate a quantum number of baryonic flavor, B. For each quark, there is an anti-quark having the same mass but with opposite charge and other internal quantum numbers. Quarks cannot exist in a free state [1].
The hadrons are not elementary particles. They are bound states of quarks and anti-quarks. And as it is shown in Figure 1.2, we can divide also the hadrons into two categories, baryons and mesons.

1.1.3 Bosons

The Quantum mechanics describe the non-relativistic motion of particles in an external field. In quantum field theory, there is the mechanism of force transmission by emission of a quanta of field.

The interaction between matter particles is done by exchange of a boson. It is a particle of integer spin and obeys the Bose-Einstein statistics. Through an interaction, a boson is emitted by a matter particle and then absorbed by another particle.

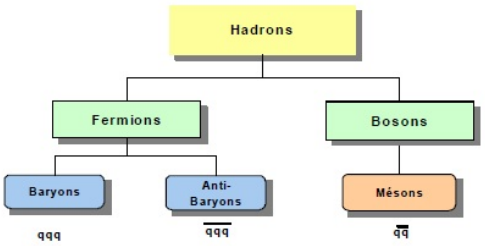

Hadrons	
p	proton
n	neutron
π^+, π^0, π^+	pions
ρ^+, ρ^0, ρ^-	mésons ρ
Λ	lambda
$K^+, K^0, \bar{K}^0, K^-$	mésons K

Figure 1.2: List of the most frequently observed hadrons

A good way to visualize the interactions is the Feynman diagrams (Figure 1.3). In these diagrams, the external lines are the real particles and at each vertex, the energy and momentum are conserved, and there is a coupling "g" which characterizes the different types of forces.

1.1.4 Interactions

There are four type of forces in nature: electromagnetic force, weak force, strong force and gravitational force. The interactions relates to matter (fermions) by the transmission of a boson.

Figure 1.3: Feynman diagram example.

- Electromagnetic interaction:
  * Interaction between charged particles (leptons and quarks).
  * Mediated by massless photons γ of spin one.
  * It is an ∞ range interaction.

- Weak interaction:
  * It is an interaction between left handed component of fermions.
  * Mediated by the massive weak gauge bosons Z^0 and $W^{\pm}$ of spin 1.
  * β-decay is an example of this interaction (p + e^- $\longrightarrow$ n + ν_e).
  * It is a limited range interaction.

- Strong interaction:
  * Mediated by massless gluon g of spin 1.
  * There is a self interaction between gluons.
  * Responsible for bounding of quarks inside nuclei.
  * It is a limited range interaction.

- Gravity:
  * An interaction between all massives particles.
  * Mediated by massless graviton of spin 2 (not yet observed).
  * Possible theories: M-theory, superstring theory, ...

1.2 The gauge theories

1.2.1 symmetries and invariance

Today, we have a unified description of the electromagnetic, weak and strong interactions. It is a gauge theory called Standard Model. The formulation of this framework was done by Glashow[2], Salam and Ward[3], and Weinberg[4] in the 1960's. We will discuss also in this chapter the Brout-Englert-Higgs mechanism introduced in 1964 to give mass to elementary particles [5] [6] [7]. In this theory, all particles are described by a dynamical quantum field ϕ(x) depending on the four dimensional space-time system of coordinates x=(x^0, x^1, x^2, x^3)) and **globally** respecting the symmetries of special relativity: spatial translation, spatial rotations and boosts of the reference frame. The kinematics of particles can be described by a Lagrangian function that we can construct by using fundamental symmetries of nature and the dynamics can be probed by introducing **local** symmetries.

Is is known that the symmetry properties of a mechanical system expressed as invariance under the transformations of a group, lead the physical implications for the quantum mechanical states of the system and to conservations laws. The relation between these conservations laws and symmetry properties represent an important application of group theory in particle physics. For example, the invariance under space translations of the coordinate frame of reference leads to the conservation of momentum, the invariance with time translation implies the conservation of energy and the invariance under rotation of the system leads to the conservation of angular momentum.
These invariance properties are important in relating observed particle states to

representations of certain Lie groups and in connecting some dynamical aspects of particle interactions.
Let's now consider a physical system described by a Lagrangian L (in local field theory, L is interpreted as a spatial integral of a Lagrangian density $\mathcal{L}$ (ϕ,$\partial_\mu\phi$), which is a function of a single field ϕ(x) and its derivatives.
We define a fundamental quantity in physics which is the action by

$$S = \int L dt \tag{1.1}$$

One of the fundamental principles is the least action principle. It is based on choosing the path that minimizes the variation of the action. So the evolution of the system between two times t_1 and t_2 correspond to a minimum, which means

$$\delta S = 0 \tag{1.2}$$

This gives rise of the equation of motion of the system which is the Euler-Lagrange equation

$$\partial_\mu(\frac{\partial \mathcal{L}}{\partial(\partial_\mu\phi)}) - \frac{\partial \mathcal{L}}{\partial\phi} = 0 \tag{1.3}$$

The analysis of the continuous transformation of the field ϕ(x) is the base of Noether's theorem [10] . An infinitesimal deformation of the field can be expressed as

$$\phi(x) \longrightarrow \phi'(x) = \phi(x) + \delta\phi(x) \tag{1.4}$$

This transformation can be considered as a symmetry of the system if it leaves the Euler-Lagrange equation invariant. This leads to the relation of current conservation

$$\partial_\mu j^\mu(x) = 0 \tag{1.5}$$

Where $j^\mu = \dfrac{\partial L}{\partial(\partial_\mu\phi)}\ \delta\phi$.
The vanishing of the four-divergence of the current j^μ leads to a conservation law.
In space-time translation, where the transformation is

$$x^\mu \longrightarrow x^\mu + e^\mu \tag{1.6}$$

leads to the conservation of the Hamiltonian H and the three components of the linear momentum P.
In phase transformation, where the transformation is expressed as

$$\phi \longrightarrow e^i\alpha\phi, \phi^* \longrightarrow e^-i\alpha\phi^* \tag{1.7}$$

leads to the conservation of the electric charge.

1.2.2 The gauge symmetries

The introduction of gauge transformations has a fundamental importance in particle physics to build a dynamical theory of elementary particles. They are **local** transformation such that the invariance under them requires the introduction of gauge vector fields that we can interpret as the quanta mediating the interactions among the fundamental constituents of matter, the fermions.
As discussed in a previous section, we have four types of fundamental interactions: electromagnetic, strong, weak and gravity. Only the first three are not negligible at scale reachable today ($\sim$ TeV), much below the Planck energy scale, $\mathrm{M_{Planck}}$, which represents the order of magnitude of the energy at which gravitational interactions become of the same order as other forces.

$$\mathrm{M_{Planck}} = (\frac{G_N}{hc})^{-1/2} = 1.22 \times 10^{19} \quad GeV \tag{1.8}$$

In the next part, we will discuss the gauge field theory we use in particle physics. Historically, the first one is the Quantum Electrodynamics (QED) [11]. It is based on the Abelian group U(1). It is a very successful theory tested with high precision. In order to describe the other interactions of particles, we will need to replace the group U(1) by larger non-Abelian group to allow more vector particles. The Non-Abelian gauge field theories are introduced by Yang and Mills [12]. We will discuss the case of Quantum Chromodynamics (QCD) which is based on the gauged version of the color SU(3) group [13] [14].

QED and QCD are exact symmetries. The Standard Model of particle physics, which will be described in Section 1.3, is a gauge theory reconstructed on the group SU(2)$\bigotimes$U(1), where the electroweak symmetry is spontaneously broken according to the Higgs mechanism (see Section 1.3.2.2) in order to give mass to the messenger, the gauge bosons [15].

1.2.2.1 The Quantum Electrodynamics (QED)

The Quantum Electrodynamics describes the dynamics of electromagnetically charged particles [11]. Let's start by a quick reminder on the Dirac Lagrangian. A charged particle of mass m can be described by the Dirac field ψ(x), a four component spinor. The Dirac Lagrangian density for this charged particle field can be written as

$$\mathcal{L}(x) = \bar{\psi}(i\gamma_\mu \partial_\mu - m)\psi(x) \tag{1.9}$$

where γ^μ are Dirac matrices and μ are indices from 0 to 3 representing the four space-time coordinates.
$\mathcal{L}$ is invariant under a global phase transformation

$$\psi(x) \longrightarrow e^{i\alpha}\psi(x) \tag{1.10}$$

where α is a real constant. For the conjugate field $\bar{\psi}$(x), the conjugate transformation is applied. But if the constant α is now a function of a space-time coordinate x, α(x), the invariance under the local transformation

$$\psi(x) \longrightarrow e^{i\alpha(x)}\psi(x) \tag{1.11}$$

require the replacement of the usual derivative ∂_μ by the covariant derivative D_μ

$$\partial_\mu\psi(x) \longrightarrow D_\mu\psi(x) = [\partial_\mu - ieA_\mu(x)]\psi(x) \tag{1.12}$$

e is the electron charge and A_μ (x) is a four vector field that transform as

$$A_\mu(x) \longrightarrow A_\mu(x) + \frac{1}{e}\partial_\mu\alpha(x) \tag{1.13}$$

So we have now a new term in the Lagrangian,

$$e\bar{\psi}(x)\gamma^\mu\psi(x)A_\mu \tag{1.14}$$

This term correspond to an interaction which couples the electron current to the field A_μ(x). The expression of the Lagrangian is now of the form

$$\mathcal{L}(x) = \bar{\psi}(x)(i\gamma^\mu\partial_\mu - m)\psi(x) - \frac{1}{4}F_{\mu\nu}(x)F^{\mu\nu}(x) + e\bar{\psi}\mu\psi(x)A^\mu \tag{1.15}$$

where $F_{\mu\nu} = \partial_\mu A_\nu$ - $\partial_\nu A_\mu$ is the electromagnetic field tensor. This is the Quantum Electrodynamics Lagrangian, i.e. charged spinor field in interaction with the electromagnetic field.
A mass term for the four vector gauge field A of the form

$$m^2 A_\mu A^\mu \tag{1.16}$$

is not allowed because it break the gauge symmetry. So the field A is massless. This is in agreement with the fact that A_μ is the photon field in this theory which is massless.
So the invariance under a local transformation in QED leads to the apparition of a massless vector field which carries the interaction with charged fermionic spinor field.

1.2.2.2 The Quantum Chromodynamics (QCD)

The Quantum Chromodynamics is a non-Abelian gauge theory in which the Lagrangian is invariant under local transformations of a non-Abelian group SU(3) (non-commutative group). It is the theory of the strong interaction [13] [14]. SU(3) is a unitary group of degree 3. The Lie algebra of these groups is defined by the commutation relation:

$$[t^A, t^B] = if^{ABC}t^C \tag{1.17}$$

where t^A is the generator of the group.

The Lagrangian of QCD is:

$$\mathcal{L} = \bar{\psi}_i(i\gamma_\mu D^\mu_{ij} - m_f\delta_{ij})\psi_i - \frac{1}{4}F^a_{\mu\nu}F^{\mu\nu}_a \tag{1.18}$$

In this theory, the quarks are represented by a fermionic field ψ_i (i runs from 1 to 3). This label is associated to a new quantum number which is the color.
The covariant derivative looks similar to the QED one but acting now in color space

$$D^\mu_{ij} = \partial_\mu\delta_{ij} + ig_s t^a_{ij}A^\mu_a \tag{1.19}$$

a=1,8 is the color index in the adjoint representation of SU(3). The field-strength tensor for QCD has an important difference with respect to the QED, it is the self-interaction of gauge bosons

$$F^a_{\mu\nu} = \partial_\mu A^a_\nu - \partial_\nu A^a_\mu - g_s f_{abc}A^b_\mu A^c_\nu \tag{1.20}$$

f_{abc}, a,b,c=1...8 are the structure constants of SU(3).
Eight gauge bosons need to be introduced in order to preserve the local gauge invariance. They are the eight gluons. The strong interaction is mediated by these gluons in the same way as the electromagnetic interaction is mediated by photons. Figure 1.4 shows some examples of gluons-gluons self interaction and gluon-quark vertices.

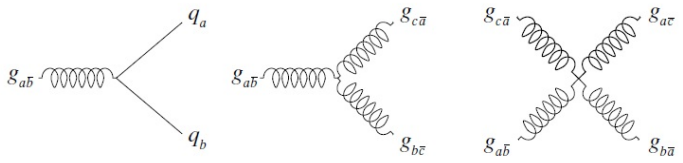

Figure 1.4: Gluon verticies in QCD.

All the interaction in QCD are proportional to the strong coupling constant g_s.It is expressed in terms of α_s such that $\alpha_s = \frac{g_s^2}{4\pi}$

α_s is demonstrated to be a running coupling constant which decreases when the momentum scale of the external particles coming into the vertex is increased [1]. This allows to carry out reliable perturbative calculations for QCD processes.

1.3 The Standard Model of particle physics

1.3.1 The electro-weak sector

The weak interactions of elementary particles are distinguished from other interactions by some characteristic properties like lifetimes, strength of coupling, cross-sections, and violation of symmetries. Some processes of weak interactions are muon decay ($\mu^- \longrightarrow e^- + \bar{\nu_e} + \nu_\mu$), e$\nu$ scattering ($e^- \ \nu_\mu \longrightarrow \mu^- + \nu_e$).
In 1932, Enrico Fermi formulated a theory for the β-decay of the neutron as a four fermion process governed by $G_F \sim 10^{-5}\ GeV - 2$ [16] [17] [18] . The discovery of parity violation in the β-decay of Cobalt by Wu in 1956 [19] and then the measurement of the helicity of the neutrino in 1957 by Goldhaber [20], assess that only the left-handed fermions are considered.
The non renormalizability of the Fermi theory makes compulsory to find a renormalizable Lagrangian in such a way the Fermi theory become an effective theory. The electro-weak theory introduce the gauge groupe $SU(2)_L$ that can describe the charged current interaction for doublets of left-handed fermions (d_L,u_L), (e_L^-,ν_L^e) and their equivalents in the other generation of fermions.
The gauge group of the electro-weak theory, elaborated by Salam, Weinberg and Glashow is $SU(2)_L \times U(1)_Y$. Here L refers to left-handed fields, and the U(1) charge is the hypercharge Y. Four vectorial fields have been then introduced. Two of them, the $W^\pm$ are carrying the charged current interactions. The photon is a linear combination of the third degree of freedomof the field associated to $SU(2)_L$ and the field associated to U(1). The second combination give the neutral current interaction field, the Z^0 boson.

1.3.2 Spontaneous symmetry breaking and electroweak theory

The introduction of gauge local transformations in the electroweak theory brings up new interaction mediator particles such as the photon and the two vector bosons, W and Z, without giving them masses (consequence of Yang-Mills theory). However, the experimental observations have shown that the W and Z bosons have non zero mass, since the interaction has a limited range. The solutions of this issue was found by introducing the mechanism of "spontaneous symmetry breaking" (SSB) [21] [22]. The physicist and theoretician Peter Higgs has introduced (with Brout and Englert) this mechanism to explain first specific phenomena in condensed matter physics, then it has been extended to build a renormalizable field theory of electro-weak interactions in a renormalizable Yang Mills theory with massive bosons.
In the next sections, we will see first in details the SSB for a global symmetry and then extend it to the gauge symmetry.

1.3.2.1 Spontaneous symmetry breaking of a global symmetry

Let's start with the Lagrangian density of a complex scalar field ϕ(x) and add a self-coupling term $\lambda(\phi^*\phi)^2$

$$\mathcal{L} = \partial_\mu \phi^* \partial^\mu \phi - \mu^2 \phi^* \phi - \lambda(\phi^* \phi)^2 \tag{1.21}$$

It is invariant under the global transformtions of U(1) (1.7).

Let's define the last two terms in the Lagrangian density as the potential of the system:

$$V(\phi) = \mu^2 |\phi|^2 + \lambda |\phi|^4 \tag{1.22}$$

We aim to analyse the properties of the ground state which corresponds to the lowest energy state of the system, it is the vacuum state.

For $\mu^2 > 0$, one obtains the minimum of the potential from the equation

$$\frac{dV}{d|\phi|} = 2\mu^2 |\phi| + 4\lambda |\phi|^3 = 0 \tag{1.23}$$

So the minimum is given by $|\phi|_{min} = 0$ as we see in Figure 1.5

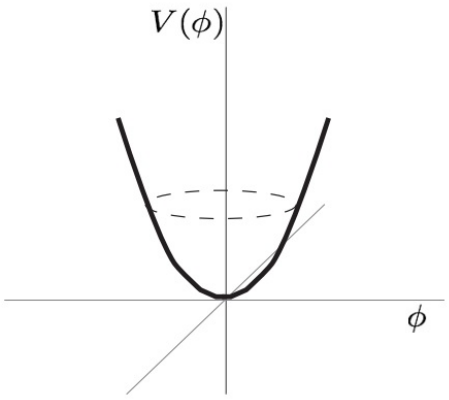

Figure 1.5: For $\mu^2 > 0$ there is a unique ground state at $\phi = 0$

For $\mu^2 < 0$, $|\phi|$ would become a relative maximum and the minimum could correspond to

$$|\phi|^2_{min} = -\frac{\mu^2}{2\lambda} \tag{1.24}$$

A continum set of solutions can be associated to the above equation since the phase of ϕ at the minimum is completely arbitrary.

As we can see in Figure 1.6, there is an infinite set of degenerate vacuum states and if we choose a particular one, we end up with the "spontaneous symmetry

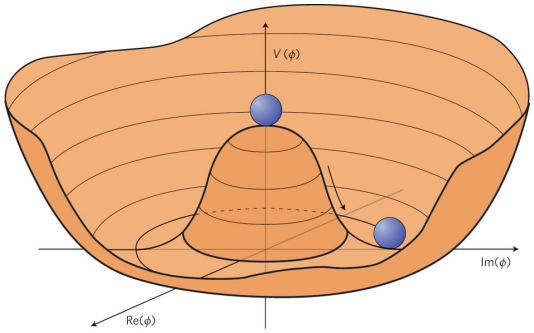

Figure 1.6: For $\mu^2 < 0$ the ground state is degenerate[15]

breaking" [15].

The equation 1.22 is invariant under phase transformation, so the complex field can be written as follows

$$\phi = \frac{1}{\sqrt{2}}\phi_1(x) + i\phi_2(x) \tag{1.25}$$

And then the minimun is

$$(\phi_1)_m in = \sqrt{\frac{-\mu^2}{\lambda}} = v \tag{1.26}$$

v is the vacuum expectation value (vev) of the scalar field ϕ_1.
In order to describe the spectrum of the system after choosing one of the ground states, we apply a small perturbation to the system starting from the minimum we have chosen. So let us now shift the two fields ϕ_1 and ϕ_2:

$$\phi_1(x) = \eta(x) + v \tag{1.27}$$

$$\phi_1(x) = \chi(x) \tag{1.28}$$

This leads to the following Lagrangian density at leading order

$$\mathcal{L} = \frac{1}{2}\partial_\mu\eta\partial^\mu\eta + \frac{1}{2}\partial_\mu\chi\partial^\mu\chi - \frac{1}{2}(-2\mu^2)\eta^2 \tag{1.29}$$

This Lagrangian is used in the case $\mu^2 < 0$ to treat the interaction terms by perturbation around the stable configuration ϕ(x) = $(\phi_1)_{min}$. It contains a real scalar field η(x) with squared mass m_η^2 = -2μ^2 = 2 λv^2 and a massless real scalar field χ (x). η(x) is a quantum excitations above v along the radial direction and χ(x) is a massless mode corresponding to excitations along the flat direction of the potential (these massless bosons are the so-called Goldstone Bosons).
The presence of massless bosons, which is the consequence of Goldstone theorem [22], makes things difficult to apply the SSB to a realistic theory of weak interactions

which is mediated by massive vector bosons. We will see in the next section that the way to evade the Goldstone theorem is by promoting the global symmetry to a local gauge symmetry.

1.3.2.2 Higgs mechanism - SSB of a gauge symmetry

Let us start with the Lagrangian (1.23), and consider the local transformation:

$$\phi(x) \longrightarrow e^{i\alpha(x)}\phi(x) \tag{1.30}$$

As we have seen before, the Lagrangian is invariant under these transformation if we introduce the covariant derivative

$$\partial_\mu\phi(x) \longrightarrow D_\mu\phi(x) = [\partial_\mu + ieA_\mu(x)]\phi(x) \tag{1.31}$$

A_μ(x) is the vector field. The Lagrangian is then

$$\mathcal{L}(\phi, A_\mu) = (D_\mu\phi)^* D^\mu\phi - V(\phi) - \frac{1}{4}F_{\mu\nu}F^{\mu\nu} \tag{1.32}$$

where $F_{\mu\nu} = \partial_\mu A_\nu - \partial_\nu A_\mu$.

The mechanism of SSB can be applied again here for $\mu^2 < 0$ as it was explained in the previous section. So the Lagrangian without the interaction terms can be written now in the form

$$\mathcal{L} = \frac{1}{2}\partial_\mu\eta\partial^\mu\eta + \frac{1}{2}\partial_\mu\chi\partial^\mu\chi - \frac{1}{2}m_\eta^2\eta^2 + \frac{1}{2}e^2v^2A_\mu A^\mu + ev\partial_\mu\chi A^\mu \tag{1.33}$$

So the vector field A_μ, that is massless without the SSB , has now a non zero mass. The value of this mass is

$$m_A = ev \tag{1.34}$$

where e is the coupling constant and v is the vev.
Before applying the SSB, A_μ is massless and has only transversal component. After the SSB, A_μ become massive and it acquires a longitudinal component (three degrees of freedom). The third degree of freedom corresponds to the χ field which is unphysical. So the Goldstone boson is absorbed by the longitudinal component of the vector field. And the η field is a massive physical field: it is the famous Higgs boson field.
Note that a different parametrization for the scalar field ϕ(x) is used to eliminate the unphysical field:

$$\phi(x) = \frac{1}{\sqrt{2}}e^{i\chi(x)/v}[\eta(x) + v] \tag{1.35}$$

So by applying the local gauge transformations

$$\phi(x) \longrightarrow e^{-i\chi(x)/v}\phi(x) = \frac{1}{\sqrt{2}}[\eta(x) + v] \tag{1.36}$$

$$A_\mu(x) \longrightarrow A_\mu(x) + \frac{1}{ev}\partial_\mu\chi(x) \tag{1.37}$$

The Lagrangian then takes a form where the unphysical field χ(x) disappear.

1.3.2.3 Gauge bosons properties

The spontaneous symmetry breaking is applied to the model of electroweak interactions by breaking the local gauge invariance of $SU(2)_L \otimes U(1)_Y$ [23].
The assignment of quantum numbers, which corresponds to the grouping into representations of the gauge group, is obtained as follows: The non-Abelian group SU(2) has a chargeless one-dimensional singlet representation and charged multidimensional representations, starting with the two-dimensional doublet representation. The U(1) group is Abelian, so it only has one-dimensional representations.

Let us now call A^i_μ (i=1,2,3) and B_μ the gauge field corresponding respectively to the generators of isospin and hypercharge.
The weak interaction is a short range interaction, so the vector bosons need to be massive. To resolve this issue, we introduce the SSB and the Higgs mechanism and a successful gauge field theory was formulated by Glashow, Salam and Weinberg. This theory is the famous so-called "the Standard Model of electroweak interactions. It is built by including both weak and electromagnetic currents.
Concerning now the four gauge fields cited before, three linear combinations of them acquire mass and identified as the physical bosons $W^\pm$ and Z^0. And the fourth combination represent the photon and must be massless.
The Lagrangian containing the gauge vectors and the scalar field terms can be written like

$$\mathcal{L}_{gauge} = (D_\mu\phi)^\dagger D^\mu\phi - V(\phi^\dagger\phi) - \frac{1}{4}F^i_{\mu\nu}F^{i\mu\nu} - \frac{1}{4}B_{\mu\nu}B^{\mu\nu} \tag{1.38}$$

where ϕ is a minimun choice consists in a doublet of complex fields

$$\begin{pmatrix}\phi^\dagger \\ \phi^0\end{pmatrix}$$

and

$$V(\phi^\dagger\phi) = \mu^2\phi^\dagger\phi + \lambda(\phi^\dagger\phi)^2 \tag{1.39}$$

$$F^i_{\mu\nu} = \partial_\mu A^i_\nu - \partial_\nu A^i_\mu + g\varepsilon_{ijk}A^j_\mu A^k_\nu \tag{1.40}$$

$$B_{\mu\nu} = \partial_\mu B_\nu - \partial_\nu B_\mu \tag{1.41}$$

$$D_\mu = \partial_\mu - igI_iA^i_\mu - ig'\frac{1}{2}YB_\mu \tag{1.42}$$

g and g' are the coupling constants of the gauge fields of $SU(2)_L$ and $U(1)_Y$ respectively to the other fields of the theory.

The potential has a minima for $\mu^2 < 0$ at

$$(\phi^\dagger\phi)_{min} = -\frac{\mu^2}{2\lambda} = \frac{1}{2}v^2 \tag{1.43}$$

The complex field ϕ can have the form

$$\phi = \frac{1}{\sqrt{2}}\begin{pmatrix}\phi_1^\dagger + i\phi_2^\dagger \\ \phi_1^0 + i\phi_2^0\end{pmatrix} \tag{1.44}$$

In the Higgs mechanism, the Goldstone bosons corresponding to $\phi_1^\dagger$, $\phi_2^\dagger$ and ϕ_2^0 are absorbed by the gauge fields that acquire masses. So a convenient choice among the infinity of minima can have the form

$$\phi = \frac{1}{\sqrt{2}}\begin{pmatrix}0 \\ v + h(x)\end{pmatrix} \tag{1.45}$$

where only the physical field h(x) is left.
So the Lagrangian 1.38 is now:

$$\begin{aligned}\mathcal{L}_{gauge} = \frac{1}{2}\partial_\mu h\partial^\mu h - \frac{1}{2}m^2h^2 - \frac{1}{4}B_{\mu\nu}B^{\mu\nu} \\ + \frac{1}{8}v^2g^2(A_\mu^{(1)}A^{(1)\mu} + A_\mu^{(2)}A^{(2)\mu}) + \\ \frac{1}{8}v^2(g^2A_\mu^{(3)}A^{(3)\mu} + g'^2B_\mu B^\mu - gg'A_\mu^{(3)}B_\mu + interaction \quad terms\end{aligned} \tag{1.46}$$

The gauge fields acquire masses as we see in the Lagrangian. First, concerning the charged fields, we can define new fields as

$$W_\mu^{(\mp)} = \frac{1}{\sqrt{2}}(A_\mu^{(1)} \mp iA_\mu^{(2)}) \tag{1.47}$$

The squared mass term expected for a charged vector field is $M_W^2W_\mu^{(+)}W^{(-)\mu}$, so the mass of the vector bosons W is

$$M_W = \frac{1}{2}vg \tag{1.48}$$

The last term in the Lagrangian 1.46 is corresponding to the two neutral vector bosons. And we see the fields $A_\mu^{(3)}$ and B_μ get mixed, so to get the physical fields, we need to diagonalize the matrix

$$\frac{1}{4}v^2\begin{pmatrix}g^2 & -gg' \\ -gg' & g'^2\end{pmatrix} \tag{1.49}$$

The mass term expected for the neutral vector field is $M_Z^2Z_\mu Z^\mu$. One eigenvalue is zero, but the other one gives a mass of

$$M_Z = \frac{1}{2} v \sqrt{g^2 + g'^2} \tag{1.50}$$

The eigenvectors corresponding to the zero and M_Z eigenvalues can be written in the form

$$A_\mu = cos\theta_w B_\mu + sin\theta_w A_\mu^{(3)} \tag{1.51}$$

$$Z_\mu = -sin\theta_w B_\mu + cos\theta_w A_\mu^{(3)} \tag{1.52}$$

The Weinberg angle θ_w is the weak mixing angle. It is a free parameter of the theory and it can be expressed as $cos\theta_w = \frac{g}{\sqrt{g^2 + g'^2}}$.
We can also conclude the $M_Z > M_W$ since $\frac{M_W}{M_Z} = \cos\theta_w$.

And finally we consider the existence of the scalar boson h, called the Higgs boson with a mass given by

$$m_h^2 = 2v^2\lambda \tag{1.53}$$

where v, the vacuum expectation value, can be estimated from the Fermi constant with a value of 246 GeV.

1.3.2.4 Yukawa coupling and fermions mass

In order to generate masses for fermions, a additional terms is added to the Lagrangian to couple fermions to the scalar field. It is the so-called Yukawa coupling. The Yukawa Lagrangian in the Standard Model electroweak Lagrangian is

$$\mathcal{L}_{YuK} = \Gamma^u_{mn} \bar{q}_{m,L} \tilde{\phi} u_{n,R} + \Gamma^d_{mn} \bar{q}_{m,L} \phi d_{n,R} + \Gamma^e_{mn} \bar{l}_{m,L} \phi e_{n,R} + \Gamma^\nu_{mn} \bar{l}_{m,L} \tilde{\phi} \nu_{n,R} + h.c \tag{1.54}$$

with the implicit loop over leptons and quarks family indices m and n. The matrices Γ_{mn} contain the Yukawa coupling between the fermions and the Higgs doublet field ϕ.
There are two representations of Higgs fields needed with Y $= \frac{1}{2}$ and $-\frac{1}{2}$ to give masses to the down quarks and leptons and to the up quarks ans neutrinos. (Note that, as the neurino has no right-handed partner in the SM, so it can not acquire a mass via Yukawa coupling).
The two representations of the Higgs field are:

$$\phi = \begin{pmatrix} \phi^\dagger \\ \phi^0 \end{pmatrix} \tag{1.55}$$

$$\tilde{\phi} = \begin{pmatrix} \phi^{0*} \\ -\phi^- \end{pmatrix} \tag{1.56}$$

All fermions can acquire masses with a single Higgs doublet by using ϕ and $\tilde{\phi}$. Let us do this for a simple example by taking only the first family. The Lagragian is

$$\mathcal{L}_{YuK} = f_e \bar{l}_L \phi e_R + f_u \bar{q}_L \tilde{\phi} u_R + f_d \bar{q}_L \phi d_R + h.c. \tag{1.57}$$

So no by applying again the spontaneous symmetry breaking and then choosing

$$\phi = \frac{1}{\sqrt{2}} \begin{pmatrix} 0 \\ v+h \end{pmatrix} \tag{1.58}$$

$$\phi = \frac{1}{\sqrt{2}} \begin{pmatrix} v+h \\ 0 \end{pmatrix} \tag{1.59}$$

The mass terms of the Lagrangian take the form

$$\mathcal{L}_{YuK} = -\frac{\lambda_e v}{\sqrt{2}}(\bar{e}_L e_R + \bar{e}_R e_L) - \frac{\lambda_u v}{\sqrt{2}}(\bar{u}_L u_R + \bar{u}_R u_L) - \frac{\lambda_d v}{\sqrt{2}}(\bar{d}_L d_R + \bar{d}_R d_L) \tag{1.60}$$

From this terms, we can conclude that the mass of fermions can be written as

$$m_i = -\frac{\lambda_i v}{2} \tag{1.61}$$

where i refers to e,u and d. And $\frac{\lambda_i}{\sqrt{2}}$ is found in the Lagrangian to be the coupling between the Higgs and the fermions.
In the same way, the mass of all other fermions (μ and τ) can be generated. As we can see, the coupling to the Higgs is proportionnel to the mass of the fermions. So especially, in the leptonic sector, giving the fact that the tau is the heaviest lepton, the Higgs decaying into two leptons taus is very important to study the Higgs Yukawa coupling to fermions.

1.3.3 Successes and weaknesses of the Standard Model

The Standard Model has been quite successful in describing all the fundamental particles and their interactions. The gauge bosons W and Z have been discovered in 1983 by the UA1 and UA2 experiments [24]. The LEP electron-positron collider at CERN and the Tevatron proton-antiproton collider at Fermilab have established many results validating the Standard Model. For example, the masses of W and Z bosons were measured by the LEP with at a precision level of 2.10^{-4} and 2.10^{-5} respectively [25] and the ratio $\frac{m_W}{m_Z} = \cos\theta_W$ was in agreement with the value predicted by the electroweak theory, and the top quark was discovered at the Tevatron [26][27].

The most recent big success of the SM is the discovery of the missing part, the scalar Higgs boson particle. On 2012 July 4^{th}, the ATLAS and CMS experiments at the CERN's Large Hadron Collider announced they had each observed a new particle in the mass region around 126 GeV [28]. This particle is consistent with the Higgs boson predicted by the SM (see Chapter 2). On 2013 October 8^{th} the Nobel prize in physics was awarded jointly to Francois Englert and Peter Higgs "for the theoretical discovery of a mechanism that contributes to our understanding of the origin of mass of subatomic particles, and which recently was confirmed through the discovery of the predicted fundamental particle, by the ATLAS and CMS experiments at CERN's Large Hadron Collider."

Another aspect of the success of the SM can be seen in Figure 1.7 where we have the comparison between the SM parameters measurements and the expectation values [29]. This represents the precision measurements on those parameters versus the accurate prediction of the SM via **radiative corrections**. We can see that differences between experimental and expected parameters are within 2σ for almost all of them. An example on the importance of these precision measurements is the indirect determination of a parameter, like the Higgs boson mass, by combining measurements that depend indirectly on it (cross sections, masses, coupling). For example, the Higgs boson appear in the radiative corrections on the mass and width of the W and Z bosons (however, constraints are quite weak because the dependence on the Higgs mass is only logarithmic). Therefore, improving the precision measurements on these masses (mainly for W) can improve the prediction of the Higgs mass with more precision and then verify its consistency with the boson discovered at the LHC.

Figure 1.8 shows the good agreement between the predicted and measured cross sections for most of the Standard Model processes [30].

Despite the big experimental success of the Standard Model, it can not describe everything in nature. Some of its shortcomings are related to the theoretical point of view and others come from experimental observations that can not be described in the context of the Standard Model.
Let us mention some of these limitations:

Number of free parameters There is 19 free parameters in the Standard Model that can not be estimated by the theory. The 3 masses of leptons, 6 masses of quarks, the electroweak mixing angle, the 4 parameters of the CKM matrix, the 2 parameters of the Higgs potential and the 3 coupling constants.

The neutrinos The Standard Model expects the neutrinos to be massless. However, the discovery of neutrinos oscillation implies massive neutrinos.
On the other hand, the neutrino mass is found to be very small (order of 1 eV), so there is a need to understand why we have this difference with the lepton masses

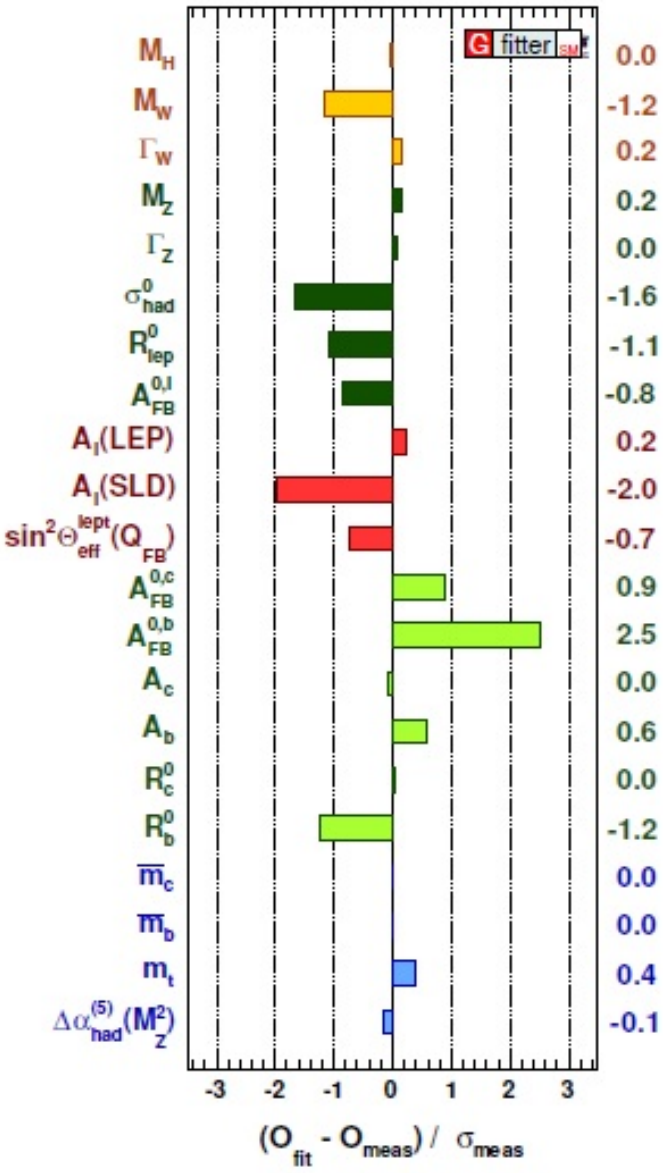

Figure 1.7: Comparison between experimentale and expected values of principle parameters of the Standard Model from a global fit [29]

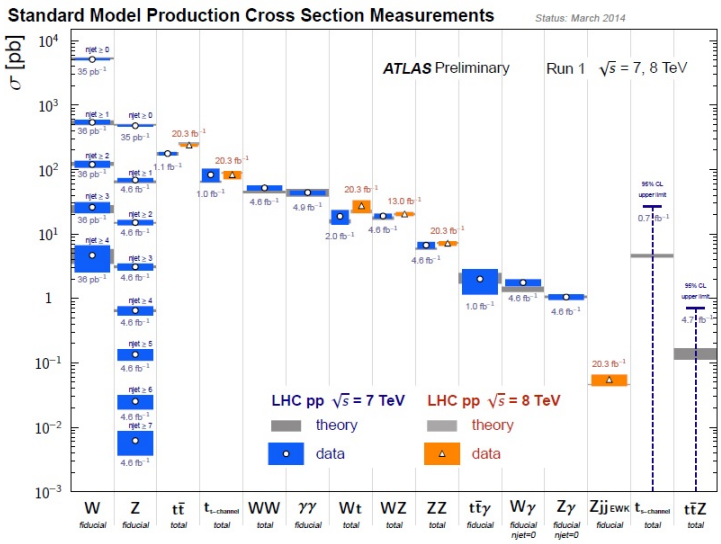

Figure 1.8: Overview on the cross section of several processes measured by ATLAS compared to the SM prediction [30]

(511 keV). A solution for this problem can be introduced by the so-called see-saw mechanism which we will not discuss here [31].

Cosmological observations The ordinary matter that is described in the Standard Model constitute only 5% of the universe contents. However, 27% of the universe matter is called dark matter, and 66% is called dark energy which is needed to explain the universe expansion. And this is not described in the SM [32].

The Gravity The gravity is described by the General Relativity while, in the Standard Model, the three interactions, electromagnetic, weak and strong, are unified in the same formalism.
At the Planck level, the gravity is no more negligible as it becomes of the same order as the other fundamental interactions. So a new theory is needed for gravity. One of the more fashionable theory is the so-called string theory. This last one unifies the four interactions by considering the particles not like fundamental particles but like vibrating strings [33].

Asymmetry matter/anti-matter The Universe is made essentially of matter. However, in the Standard Model, the matter and anti-matter have been created in an equal amount, and no mechanism in the Standard Model can describe an asymmetry as observed [34].

The hierarchy problem The radiative corrections on the Higgs boson mass contain quadratic divergence on Λ (the energy scale). So for high Λ (Planck scale),

the Higgs boson mass become comparable to the Planck mass. To compensate this effect, a mechanism called fine tuning is required to stabilize the Higgs boson mass, which is not a natural solution.

1.3.4 Theory Beyond the Standard Model

The theoretical physics, many proposition have been established to resolve these problems in the Standard Model. Many of them are based on an extension of the SM, where the SM will be a limit at low energy of a more complete theory, so it is an efficient theory valid up to a given scale. Beyond this scale, there will be a new physics which the SM is not able to explain.
In the following, we mention two theories beyond the SM.

Supersymmetry (SUSY) In Supersymmetry [35] , the fermionic and bosonic degrees of freedom are identical. A supersymmetric transformation Q change a fermion to a boson and vice-versa (Q| fermion >=| boson > *and* Q | boson >=| fermion >).
As a consequence, in Supersymmetry, each fermion has a superpartner which is a boson. And the same way for bosons. In SUSY, The scale of symmetry breaking is assumed to be smaller than the Planck mass, and often close to the electroweak scale in order to solve the hierarchy problem. Another important feature of this theory is the unification of the interaction couplings at high energy scale $\sim 10^{16}$ GeV (Grand Unification). In addition, String theory gives SUSY at the O(TeV) scale.
In most of SUSY theoretical models, there is a conserved number, the R-parity [36]. It is 1 for SM particles and -1 for super-partners. In that case, the Lightest Supersymmetric Particle (LSP) is a neutral and sterile particle and it appears in all supersymmetric processes as missing transverse energy. This particle provides also a good candidate for dark matter.
In the simplest Supersymmetric extension of the SM, called MSSM (Minimal Supersymmetric Standard Model), two Higgs doublets with two vacuum expectation values v_1 and v_2 have to be introduced and after symmetry breaking [37], five physical fields appear:
Two charged fields H^+ and H^- and three neutral bosons h^0, H^0, and A^0.

Extra-dimensions Extra-dimensions allow to handle the hierarchy problem. The gravitation is as strong as EM, weak and strong interactions but diluted in extra-dimensions. This allows to stabilize the model up to Planck scale [38].
At the Planck scale, in models that predict the existence of extra-dimensions, the gravitational force shows its quantum nature and the search at the LHC for black holes is an example of how this can be probed [39]. It also predicts a rich phenomenology in the O(TeV) mass region.

1.3.5 Conclusion

In this chapter, we have seen how the Standard Model theory of particle physics was built. The numerous predictions that were found to be compatible with the experimental observations and the discovery of the SM Higgs boson in 2012, confirm the real experimental success of this theory. However, a set of arguments and issues mentioned also in this chapter, give a hint that the SM might be just an effective theory in a more global one.
In the next chapter, we will focus more on the Higgs sector of the SM, and we will see in details the production and the decay modes of the Higgs Boson, and its properties.

Bibliography

[1] J. Beringer et al. Review of Particle Physics (RPP). In: Phys. Rev. D86 (2012), p. 010001. DOI: 10.1103/PhysRevD.86.010001 (Cited on pages 3 and 9.)

[2] S. L. Glashow. Partial Symmetries of Weak Interactions. In:Nucl.Phys.22(1961),pages 579-588. DOI: 10.1016/0029-5582(61)90469-2 (Cited on page 5.)

[3] A. Salam and J.C.Ward. Electromagnetic and weak interactions. In PhysicsLetters 13.2(1964). pages 168-171. ISSN: 0031-9163. DOI: http://dx.doi.org/10.1016/0031-9163(64)90711-5 (Cited on page 5.)

[4] S. Weinberg. Precise Relations between the Spectra of Vector and Axial-Vector Mesons. In:Phys.Rev.Lett. 18(13Mar.1967), pages 507-509. DOI: 10.1103/PhysRevLett.18.507 (Cited on page 5.)

[5] F.Englert and R.Brout. Broken symmetry and the mass of gauge vector mesons. Phys.Rev. Lett., 13:321-323, Aug 19 (Cited on page 5.)

[6] P. W. Higgs. Broken symmetries, massless particles and gauge fields. In: Phys.Lett. 12(1964).pages 132-133. DOI:10.1016/0031-9163(64)91136-9 (Cited on page 5.)

[7] P.W. Higgs. Broken symmetries and the masses of gauge bosons. In: Phys.Rev.Lett.13(1964). pages 508-509.DOI: 10.1103/PhysRevLett.13.508 (Cited on page 5.)

[8] P. W. Higgs. Spontaneous symmetry breakdown without massless bosons.In:Phys. ReV. 145(1966), pages 1156-1163. DOI:6410.1103/PhysRev.145.1156 (Not cited.)

[9] T.W.B.Kibble. Symmetry breaking in non-abelian gauge theories. Phys.Rev., 155:1554-1561, Mar 1967 (Not cited.)

[10] E. Noether : Invariant Variation Problems. Gott.Nachr., pages 235-257, 1918 (Cited on page 6.)

[11] F. J. Dyson, The Radiation Theories of Tomonaga, Schwinger, and Feynman, Phys. Rev 75, 486 - Published 1 February 1949 (Cited on page 7.)

[12] C.-N. Yang and R. L. Mills. Conservation of Isotopic Spin and Isotopic Gauge Invariance, Phys.Rev. 96(1954),pages 191-195. DOI: 10.1103/PhysRev.96.191 (Cited on page 7.)

[13] (Cited on pages 7 and 8.)

M. Gell-Mann. A schematic model of baryons and mesons. Physics Letters, 8(3):214-215, 1964

[14] H. Fritzsch, M. Gell-Mann, and H.Leutwyler. Advantages of the color octet gluon picture. Physics Letters B, 47(4):365 - 368, 1973. (Cited on pages 7 and 8.)

[15] A. Pich, The Standard Model of Electroweak Interactions, (arXiv:0705.4264). (Cited on pages 7 and 12.)

[16] E.Fermi. Tentativo di una teoria dell'emissione dei raggi 'beta'. In: La Ricerca Scientifica 4.2(1933), pp. 491-495 (Cited on page 10.)

[17] E.Fermi. Tentativo di una Teoria Dei Raggi β. In: Il Nuovo Cimento (8) 11.1 (1934), pp. 1-19 (Cited on page 10.)

[18] E.Fermi. Versuch einer Theorie der β-Strahlen. I. In: Z-Phys. 88.3-4(1934),pp. 161-177 (Cited on page 10.)

[19] C. S. Wu, E. Ambler, R. W. Hayward, D. D. Hoppes, and R. P. Hudson, Experimental Test of Parity Conservation in Beta Decay. Phys. Rev. 105, 1413 - Published 15 February 1957. (Cited on page 10.)

[20] M. Goldhaber, L. Grodzins, and A. W. Sunyar, Helicity of Neutrinos , Phys. Rev. 109, 1015 - Published 1 February 1958 (Cited on page 10.)

[21] J. Goldstone. Field theories with superconductor solutions. Il Nuovo Cimento (1955-1965), 19:154-164, 1961. 10.1007/BF02812722 (Cited on page 10.)

[22] Jeffry Goldstone, Abdus Salam, and Steven Weinberg. Broken symmetries. Phys. Rev.,127:965-970, Aug 1962 (Cited on pages 10 and 12.)

[23] S. Weinberg. A Model of Leptons. In: Phys. Rev. Lett. 19(1967), pp. 1264-1266. DOI: 10.1103/PhysRevLett.19.1264 (Cited on page 14.)

[24] The experimental discovery of the intermediate vector bosons W^+, W^-, and Z^0 at the CERN $p\bar{p}$ collider, Prog. Part. Nucl. Phys. 14 (1985) 231-328. http://cds.cern.ch/record/151272 (Cited on page 17.)

[25] S. Schael et al. Electroweak Measurements in Electron-Positron Collisions at W-Boson-Pair Energies at LEP. In: Phys. Rept .532 (2013), pp. 119-244. DOI: 10.1016/j.physrep.2013.07.004. arXiv:1302.3415 [hep-ex] (Cited on page 17.)

[26] CDF Collaboration. Observation of Top Quark Production in $p\bar{p}$ Collisions with the Collider Detector at Fermilab. In: Phys. Rev. Lett. 74 (14 Apr. 1995), pp. 2626-2631. DOI: 10 . 1103 / PhysRevLett.74.2626 (Cited on page 17.)

[27] D0 Collaboration. Search for High Mass Top Quark Production in $p\bar{p}$ collisions at $\sqrt{s} = 1.8$ TeV. In: Phys. Rev. Lett. 74 (13 Mar. 1995), pp. 2626-2631. DOI: 10 . 1103 /PhysRevLett.74.2626 (Cited on page 17.)

[28] PRESS CONFERENCE Update on the search for the Higgs boson at CERN on the eve of the ICHEP 2012 Conference, http://cds.cern.ch/record/1459604 (Cited on page 18.)

[29] M. Baak et al. The Electroweak Fit of the Standard Model after the Discovery of a New Boson at the LHC. In: Eur. Phys. J. C72 (2012), p. 2205. DOI: 10.1140/epjc/s10052-012-2205-9.arXiv:1209.2716 [hep-ph] (Cited on pages 18 and 19.)

[30] twiki https ://atlas.web.cern.ch/Atlas/GROUPS/PHYSICS/ CombinedSummaryPlots/SM/ (Cited on pages 18 and 20.)

[31] Manfred Lindner, Tommy Ohlsson, Gerhart Seidl, See-saw Mechanisms for Dirac and Majorana Neutrino Masses, arXiv:hep-ph/0109264 (Cited on page 20.)

[32] P.A.R. Ade et al. Planck 2013 results. I. Overview of products and scientific results. In: (2013). arXiv:1303.5062 [astro-ph.CO] (Cited on page 20.)

[33] Recent Developments in String Theory, W. Lerche. Theoretical Physics Division, CERN, Geneva, Switzerland (Cited on page 20.)

[34] E. Sather, The Mystery of the matter asymmetry, SLAC Beam Line 26N1 (1996) 31-37. (Cited on page 20.)

[35] S. P. Martin. A Supersymmetry primer. In: (1997). arXiv:hep-ph/9709356 [hep-ph] Cited on page 29. (Cited on page 21.)

[36] G. R. Farrar and P. Fayet. Phenomenology of the Production, Decay and Detection of New Hadronic States Associated with Supersymmetry. In: Phys. Lett. B76 (1978), pp. 575-579. DOI: 10.1016/0370-2693(78)90858-4 10.1016/0370-2693(78)90858-4 (Cited on page 21.)

[37] P. Fayet. Spontaneously Broken Supersymmetric Theories ofWeak, Electromagnetic and Strong Interactions. In: Phys. Lett. B69 (1977), p. 489. DOI: 10.1016/0370-2693(77)90852-8 (Cited on page 21.)

[38] Randall, Lisa; Sundrum, Raman (1999). "Large Mass Hierarchy from a Small Extra Dimension". Physical Review Letters. 83(17): 3370-3373 (Cited on page 21.)

[39] Savas Dimopoulos and Greg L. Landsberg. Black holes at the LHC. Phys. Rev. Lett., 87:161602,2001 (Cited on page 21.)

Chapter 2

The Higgs boson phenomenology

Contents

2.1 Higgs production mechanisms

The Standard Model Higgs boson can be produced in several ways in a hadron collider like the Large Hadron Collider (LHC). The main production mechanisms are the gluon fusion (ggH) which is the dominant production mode, the vector boson fusion (VBF), the associated production with a gauge boson (WH and ZH) and the associated production with top quarks ($t\bar{t}H$). The corresponding Feynman diagrams are shown in Figure 2.1.

The production cross section of the Standard Model Higgs boson is a function of the centre of mass energy $\sqrt{s}$ of the proton-proton collisions at the LHC. This dependency is shown in Figure 2.2. We can see that the Higgs production cross section increases with the centre of mass energy [1].

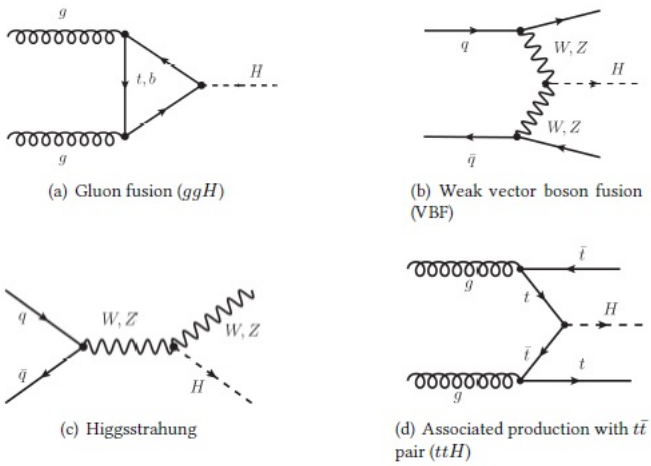

Figure 2.1: The different production modes of the Higgs Boson at the LHC.

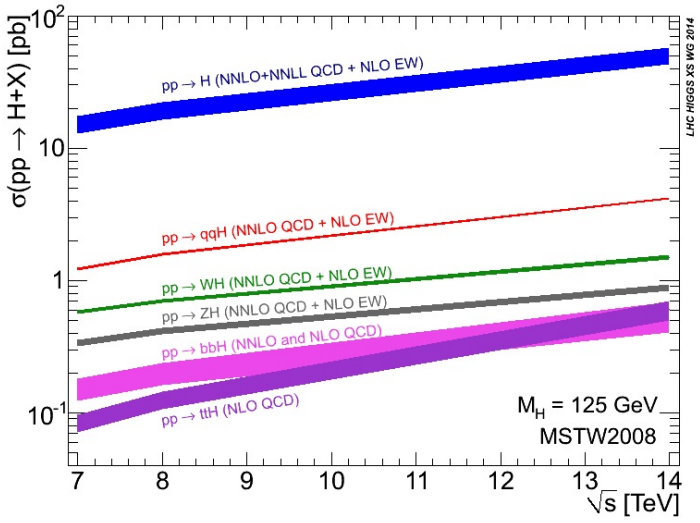

Figure 2.2: The SM Higgs boson production cross sections as a function of the center of mass energy for proton-proton collision. The colored bands represent the theoretical uncertainties. [1]

2.1.1 The gluon fusion production mode

The dominant production mode at the hadronic collider is the gluon-gluon fusion [1] gg $\longrightarrow$ H + X. The gluon is a massless boson and so it does not couple directly to the Higgs Boson. Therefore, this production is mainly mediated by a virtual loop of heavy quarks. The amplitude of the gluon-gluon fusion process is evaluated using an effective Lagrangian which contains the local operator: $HG^a_{\mu\nu}G^{a\mu\nu}$, under the approximation that the leading top-quark contribution is evaluated in the limit $m_t \longrightarrow \infty$ in such a way the SM is matched to an effective theory.
In this approximation, the cross section is calculated at the next-to-leading order and the next-to-next-to-leading order. An important feature related to the gluon fusion process is the QCD corrections. The leading order prediction of the cross section is increased by $\sim$ 80% when adding the NLO QCD corrections and by $\sim$ 20% with the NNLO corrections. And the electroweak radiative corrections are computed at the NLO level and increase the cross section by $\sim$ 5% for $m_H = 125$ GeV [2] [3].

2.1.2 The vector boson fusion production mode

The vector boson fusion (VBF) is also an important production mechanism at the LHC [1]. Its cross section is about 10 times smaller than the one of ggH. In this process, there is a scattering of two quarks (anti-quarks), mediated by t- or u-channel exchange of a vector boson (W or Z), and the Higgs boson is radiated by the fusion of the weak bosons.
Two hard jets are present in the forward-backward region of the detector coming from the quarks scattering. And it is important to mention that the gluon radiation from the central rapidity η regions is negligible (because of the color-singlet nature of the vector gauge boson exchange).
The presence of the two additionnal jets and the suppression of QCD activities in the central η region are important to discriminate between this process and other QCD backgrounds. So the VBF mode is an important and sensitive channel for the Higgs boson searches and coupling and characteristics measurement at the LHC.

2.1.3 Higgs production associated to a vector boson (W or Z)

In this mechanism [1], the Higgs boson is produced in association with an electroweak vector boson W or Z. The name of this mechanism is Higgsstrahlung where the Higgs boson is radiated by a vector boson.
There are corrections to the cross section of this production mode at NLO and NNLO from QCD and at NLO from electroweak. The WH and ZH production mechanisms (with the Higgs production associated to top quark pair, that we will see in the next paragraph) provide a relatively clean environment to study the Higgs decay to a pair of bottom quark, at the expense of a cross section which is $\sim$ 3-6 times smaller than VBF.

2.1.4 Higgs production associated to a pair of top quarks

Finally, the Higgs boson can be produced in association with a top and anti-top quark [1] with a rate that is almost two orders of magnitude smaller than the direct production (ggH). The cross section of this mechanism has corrections at NLO from QCD. This leads to an increase of the cross section of about 20 %.
An important feature of this mechanism is that it gives informations about the Higgs Yukawa coupling to fermions and can provide access to the Higgs decay into bottom quarks.

2.2 Higgs boson decay

As we have seen in the first chapter, the Higgs boson of the Standard Model couples to vector bosons and fermions (leptons and quarks). So different decay modes exist for the Higgs boson, where the branching ratios are completely predicted by the Standard Model.
A branching ratio has to be estimated for each decay channel. They depend on some parameters, mainly the Higgs boson mass and the coupling constants with the vector bosons W and Z and with the fermions.
To calculate the branching ratio of a given Higgs boson decay process, we define the so-called decay width Γ which is the inverse of the lifetime. It is a measure of the probability of a specific decay process occuring within a given amount of time in the parent particle's rest frame.
When multiple decay modes are available, as it is the case for the Higgs boson, one can associate a decay rate for each mode, and the total rate will be the sum of the rates of the individual modes:

$$\Gamma_{total} = \sum \Gamma_i \tag{2.1}$$

The particle's lifetime is given by

$$\tau = \frac{1}{\Gamma_{total}} \tag{2.2}$$

So the branching ratio, which is the probability of a decay by an individual mode i, is

$$B_i = \frac{\Gamma_i}{\Gamma total} \tag{2.3}$$

Given the fact that the dimension of Γ is the inverse of time, in our system of units, it has the same dimension as mass (or energy). When the mass of an elementary particle is measured, the total rate shows up as the irreducible "width" of the shape of the distribution. Hence the name decay width.
The decay width is determined for the Higgs boson for the different decay modes. It is predicted by the quantum field theory and can be written as [4] (respectively for H $\longrightarrow$ l^+l^-, $q\bar{q}$, $W^\pm$ and Z^0)

$$\Gamma(H \longrightarrow l^+l^-) = \frac{G_F m_l^2}{4\sqrt{2}\pi} m_H \tag{2.4}$$

$$\Gamma(H \longrightarrow q\bar{q}) = \frac{3G_F^2}{4\sqrt{2}\pi} m_q^2(m_H) m_H [1 + 5.67(\frac{\alpha_s}{\pi}) + (35.94 - 1.36N_F)(\frac{\alpha_s}{\pi})^2] \tag{2.5}$$

$$\Gamma(H \longrightarrow W^+W^-) = \frac{G_F^2}{8\sqrt{2}\pi} m_H^3 \beta [\beta^2 - \frac{3}{4}(1-\beta^2)^2] \tag{2.6}$$

$$\Gamma(H \longrightarrow ZZ) = \frac{G_F^2}{16\sqrt{2}\pi} m_H^3 \beta [\beta^2 - \frac{3}{4}(1-\beta^2)^2] \tag{2.7}$$

where G_F is the Fermi constant

$$G_F = \frac{\sqrt{2}g^2}{8m_W^2} \tag{2.8}$$

α_s is the strong coupling constant. β is given by

$$\beta = 1 - 4\frac{m_{W,Z}^2}{m_H^2} \tag{2.9}$$

The term inside the brackets in the equation (2.5) is determined by taking into account the radiative corrections at NLO and NNLO level.

The branching ratios of the different decay modes are calculated using HDECAY [5]. They are shown in Figure 2.3 for the most relevant decay channels as a function of the Higgs mass.

The theoretical uncertainties in the branching ratios include the higher order corrections on the theoretical calculations. They include also the errors in the SM input parameters in particular gauge couplings and fermions masses.
We see in Figure 2.3 that for a Higgs boson mass of about 125 GeV, the dominant decay channels are H$\longrightarrow b\bar{b}$, H$\longrightarrow$WW* and H$\longrightarrow$gg, then the H$\longrightarrow \tau^+\tau^-$, H$\longrightarrow c\bar{c}$ and H$\longrightarrow$ZZ*. The other channels, H$\longrightarrow \gamma\gamma$, H$\longrightarrow$Z$\gamma$ and H$\longrightarrow \mu^+\mu^-$, have much smaller rates of decay. Since gluons and photons are massless particles, so the Higgs decay to di-gluons, diphotons and Zγ are loop induced where the loop is performed by W, Z and top (Figure 2.4). This provides indirectly informations about the Higgs coupling to WW, ZZ and $t\bar{t}$.
In order to determine the promising channels for the Higgs boson research, the branching ratios have to be multiplied by the cross section of the production for each final state ($\sigma \times BR$) [6]. Figure 2.5 shows this product for the various decay channels. In addition, the potential observation for each channel depends also on the efficiency of reconstruction of the final state and the signal to background ratio. According to this fact, the important Higgs search channels are the following:
In the H$\longrightarrow \gamma\gamma$ channel, at low energies up to 140 GeV, the mass peak can be

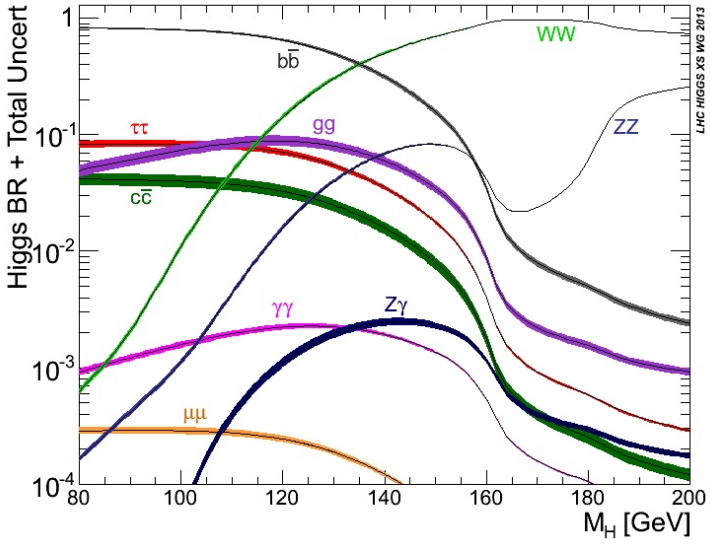

Figure 2.3: The branching ratios of the relevant SM Higgs boson decay modes. [1]

reconstructed with very good resolution, and this is why this channel has been used for the discovery of the Higgs boson as we will see in the next section, despite the very high background.
Starting around 120 GeV, to some hundreds of GeV, the promising decay channels are the H$\longrightarrow$WW and the H$\longrightarrow$ZZ$\longrightarrow$4l (where l is an electron or muon). The first one has a large σ $\times$BR (but presence of neutrinos in the final state from the W decay affect the precision on the reconstructed Higgs boson mass). For the second one, the very good mass resolution with the four leptons in the final state, and the lower background, makes it an important channel for the Higgs boson discovery.
The fermionic channels, H$\longrightarrow$ $\tau^+\tau^-$ and $\longrightarrow$ $b\bar{b}$ are also considered. They suffer from a lower mass resolution but are very important to test the Yukawa sector of the Standard Model.

2.3 The Higgs boson discovery

Let's start with a historical overview of the Higgs boson searches. The ALEPH, DELPHI , L3 and OPAL experiments at the LEP e^+ e^- collider have conducted direct searches for the Higgs boson in the Higgsshtrahlung process. The combination of LEP data at a center-of-mass energies of up to 209 GeV yielded a lower bound of 114.4 GeV for the mass of the Standard Model Higgs boson at 95% Confidence level [7].
The Tevatron p$\bar{p}$ collider at Fermilab has continued the searches for the Higgs boson after the shutdown of the LEP collider in 2000. After recording approximately 10 fb^{-1}, the combination of the results by the CDF and D0 experiments excluded two mass ranges for m_H, between 90 GeV and 109 GeV and between 149 GeV and 182

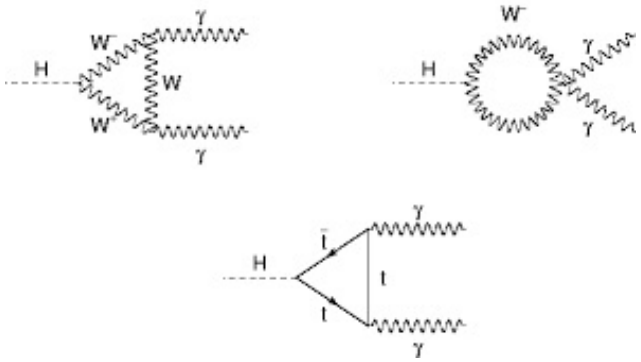

Figure 2.4: The loop induced decays at lowest order of the Higgs boson in the di-photon channel.

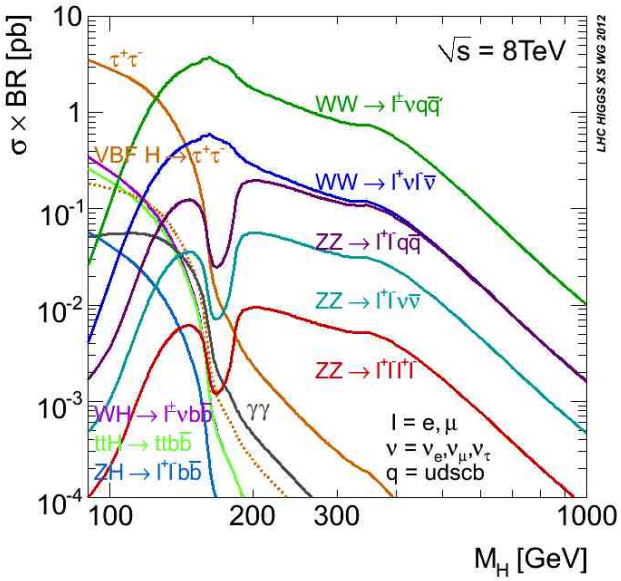

Figure 2.5: The Higgs production cross section multiplied by the branching ratio for various final states[1] [6].

GeV. And an excess of data has been seen in the mass range between 115 GeV and 140 GeV, in the Wb$\bar{b}$ associated mode [8].
In 2010, LHC at CERN was commissioned and a high intensity run started in 2011 with a center-of-mass energy of 7 TeV followed by a run with 8 TeV in 2012. This correspond to the Run I of the LHC and has opened the door for a new era of Higgs boson searches.
On 2012 July 4^{th}, the observation of a narrow resonance with a mass around 125 GeV was announced [9] after analysing the 2011 and 2012 LHC data with respectively 4.8 (5.1) fb^{-1} at $\sqrt{s}$ = 7 TeV and 5.9(5.3) fb^{-1} at $\sqrt{s}$ = 8 TeV as integrated luminosities recorded by the ATLAS and CMS experiments, respectively. The evidence was strong that the new particle was decaying into $\gamma\gamma$ and ZZ with rates consistent with those predicted for the Standard Model (SM) Higgs boson. There were indications that the new particle could also decay to W^+W^-. Although the experiments searched for decays to $b\bar{b}$ and $\tau^+\tau^-$, no statistically significant signal was found.
After combining the results from the two years data taking (2011-2012) and for all the decay channels that we will see in details in the next sections, ATLAS collaboration observed the largest excess with a local significance of 5.9 σ at a mass m_H = 126.5 GeV, to be compared with an expected significance of 4.6 σ if a SM Higgs boson were present at such a mass [10]. CMS observed an excess with a local significance of 4.9 σ at a mass of 125.5 GeV, to be compared with an expected significance of 5.9 σ in this dataset [11].
A total luminosity of 25 fb^{-1} had been collected by ATLAS and CMS in Run I of the LHC.
Figure 2.6 illustrates the p-value and the signal significance near 125 GeV observed by ATLAS and CMS after analysing the full datasets from Run I with a full luminosity of 25 fb^{-1} [12] [13].

2.3.1 The observation channels

For a Higgs boson of a mass between 110 and 150 GeV, the dominating decay channel are shown in Table 2.1, with emphasis for discovery on narrow mass spectrum. The final state can be examined very well and the resolution of reconstructed mass is good for the H$\longrightarrow \gamma\gamma$, H$\longrightarrow$ZZ$\longrightarrow$4l channels. However, the reconstructed mass resolution is rather poor for the H$\longrightarrow W^+W^-$ but it has a relatively large branching ratio. And concerning the fermionic channels, H$\longrightarrow \tau^+\tau^-$ and H$\longrightarrow b\bar{b}$, they have a huge background (from QCD and top quark processes) and rather poor mass resolution.

2.3.1.1 H$\longrightarrow \gamma\ \gamma$

The search for the H$\longrightarrow \gamma\ \gamma$ channel looks for a narrow peak over the background in the distribution of the invariant mass of two high transverse momentum photons [14]. There is a high background for this channel from $\gamma\ \gamma$ (irreducible), γ+jet

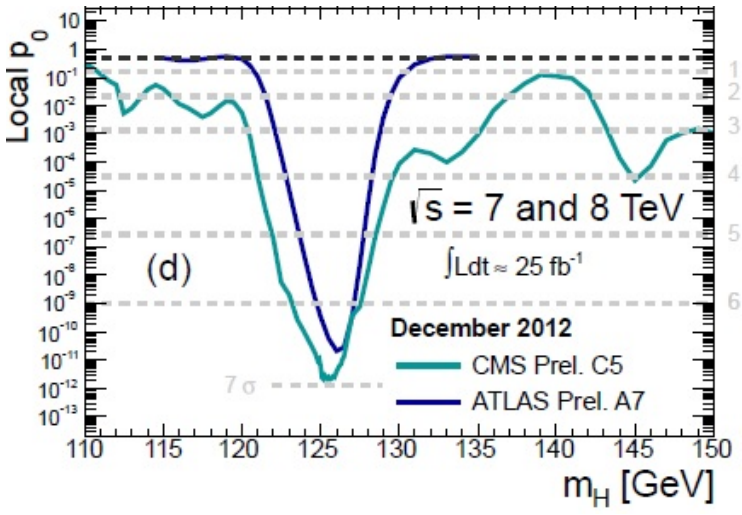

Figure 2.6: The p-value and the signal significance observed by ATLAS and CMS experiments using the Run I datasets with a luminosity of 25 fb^{-1} [12] [13].

Decay channel	Mass resolution
H$\longrightarrow \gamma\gamma$	1-2%
H$\longrightarrow$ZZ$\longrightarrow$4l	1-2%
H$\longrightarrow W^+W^-$	20%
H$\longrightarrow \tau^+\tau^-$	15%
H$\longrightarrow b\bar{b}$	10%

Table 2.1: The different Higgs boson decay channel with the associated mass resolution.

and di-jet processes (reducible) and in order to optimize the analysis sensitivity, the Higgs production modes are separated and the events are split into different exclusive categories. A categorisation based on the final states configurations is also used. For example, an event with diphoton system and a high p_T electron, muon , dijets or missing energy, which is consistent with the decay of a vector boson W or Z, is tagged in the associated production category. While events with energetic dijets with a large mass and pseudorapidity difference, are assigned as vector boson fusion (VBF) category.
Using the full ATLAS dataset of 2011 and 2012, the obtained mass distribution $m_{\gamma\gamma}$ is shown in Figure 2.7.
An excess of events over the background is observed at $m_H = 126.8$ GeV with a significance of 5.2 σ compared to 4.6 σ expected for a SM Higgs boson at that mass [14].
Another parameter is calculated in order to evaluate the consistence with the SM,

which is the signal strength $\mu = \frac{(\sigma.BR)_{obs}}{(\sigma.BR)_{SM}}$, i.e. the observed product of the Higgs boson production cross section σ and the branching ratio BR in units of the corresponding SM values. It was found to be 1.17 ± 0.27, so consistent with the SM.

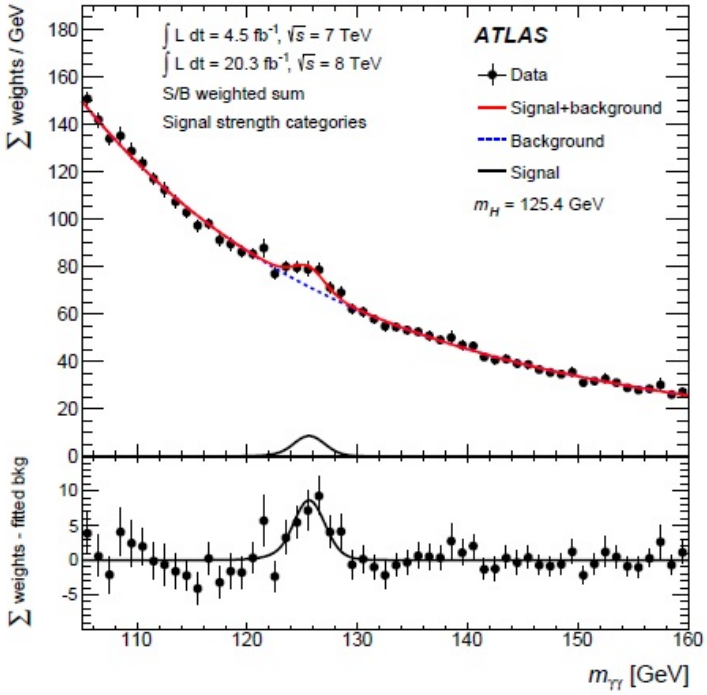

Figure 2.7: The weighted invariant mass distribution of the diphoton system [14].

2.3.1.2 H$\longrightarrow$ ZZ*

Over a small continuum of irreducible background dominated by non-resonant ZZ* production from $q\bar{q}$ annihilation and gg fusion processes, and a small contribution from reducible Z+$b\bar{b}$, t$\bar{t}$ and Z+jets events, the search for the H$\longrightarrow$ ZZ* $\longrightarrow$ $l^+l^-l'^+l'^-$ looks for a narrow mass peak [15]. For the background treatment, the contribution and the shape is taken from simulated events. To optimize the analysis sensitivity, the events are split into two categories, VBF with the existence of 2 jets with high mass and pseudorapidity, and associated production with the requirement of an additional lepton.
The level of the reducible background and the mass resolution of the 4 leptons system are different in the 4μ, 4e and 2e2μ sub-channels, so the analysis is performed separately and then the results are combined.
The m_{4l} distribution after combining the sub-channels is shown in Figure 2.8.
After analysing and combining the full 7 and 8 TeV data, The largest deviation from the SM background-only expectation is observed at $m_H = 124.3$ GeV where the significance of the peak is 6.7 σ knowing that the expected significance for the

SM Higgs boson at this mass is 4.4 σ. And as it is clear in Figure 2.8, a peak at $m_{4l} = 91$ GeV from Z/γ^* production at the expected rate is observed [15].
The signal strength μ for the inclusive H⟶4l channel measured by ATLAS is $1.43^{+0.40}_{-0.35}$, which is consistent with the SM prediction.

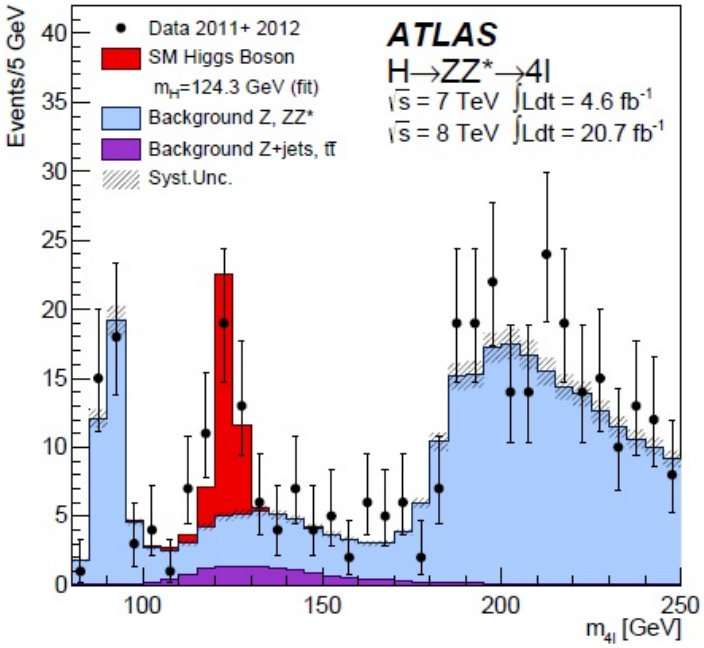

Figure 2.8: The ATLAS combined m_{4l} distribution [15]

2.3.2 H⟶ W^+ W^-

In the H ⟶ W^+ W^- ⟶ l^+ ν l^- $\bar{\nu}$ channel, the analysis is performed by searching for an excess of events with two leptons of opposite charge accompanied by a large missing energy and up to two jets [15].
Despite the large production rate in this channel, the presence of two neutrinos in the final state make the m_H resolution quite modest.
As for the two previous channels, the events are split in several categories depending on the number of jets (0, 1 or ≥2) and of the lepton flavor combination (e^+e^-, $\mu^+\mu^-$ and $e^\pm\mu^\mp$). The VBF category is selected by requiring N_{jet} ≥2 and the two leading jets have to have a large mass $m_{jj} > 500$ GeV and a large pseudorapidity separation.
The background in this channel is important and vary with the analysis category. For example, for events events with opposite flavor lepton and without a high p_T jets, the background is dominated by the non-resonant WW production and for events with same-flavor leptons, the dominant background is from the Drell-Yan contamination. In addition, background from $t\bar{t}$, Wt and W+jets, where the jet is

misidentified as a lepton, is contaminating all categories.
In the same lepton flavor category (e^+e^- and $\mu^+\mu^-$), events with m_{ll} consistent with the Z mass are vetoed. And in order to reduce the Drell-Yan and multi-jet background, a requirement of large missing transverse energy is applied. A veto against identified b-jets or a requirement of low p_T muons (assuming that they come from semileptonic b-hadron decays within jets) are used to suppress $t\bar{t}$ background.
In this channel, the transverse mass m_T constructed from the dilepton p_T^{ll}, the missing transverse energy E_T^{miss} and the azimuthal angle between p_T^{ll} and E_T^{miss} is used as an important variable to discriminate between signal and background. This variable is sensitive also to the Higgs boson mass but with a poor resolution. Figure 2.9 show the m_T distribution for ATLAS for the category with ≤ 1 jets. After fitting the m_T distributions, ATLAS observes the most significant excess for $m_H = 140$ GeV and the significance of the observed excess for $m_H = 125$ GeV is 3.8 σ. The measured inclusive signal strength is $\mu = 1.01 \pm 0.31$ for $m_H = 125$ GeV.

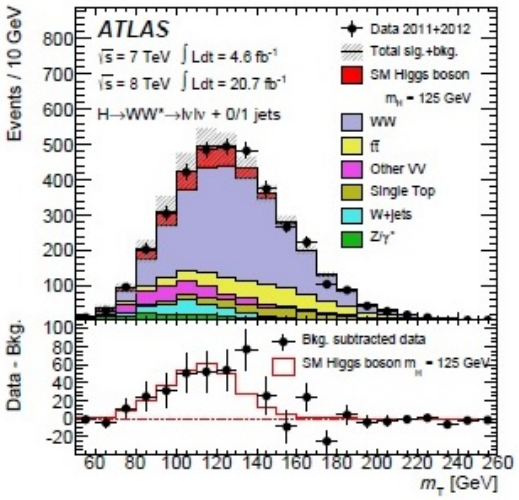

Figure 2.9: The ATLAS m_T distributions in the WW^* channel in category with $\leq$ 1 associated jets. The lower panel shows the observed excess over the estimated SM background and the expectation from a SM Higgs boson at $m_H = 125$ GeV [15].

2.3.3 The fermionic decay channels

As has been described in Chapter 1, the Higgs boson is responsible for fermions mass generation via Yukawa coupling.
The most prominent candidate channels to search for the Higgs field coupling to leptons and quarks at the hadron colliders are the decays into tau leptons, and two bottom quarks (b-quarks), since, for a Higgs boson of $m_H \sim 125$ GeV, the branching fraction to $b\bar{b}$ is $\sim 57\%$ and to $\tau^+\tau^-$ is $\sim 6\%$. However, the presence of a very large background for these channels make their rate really small and their detections a

challenging search. More favourable signal-to-background conditions are expected a priori in the H$\longrightarrow \tau^+\tau^-$ channel.

2.3.3.1 The H$\longrightarrow \tau^+\tau^-$ channel

The tau lepton is the heaviest lepton. It decays leptonically to electron or muon (τ_{lep} where l = e or μ) and hadronically (τ_{had}). The Higgs decay into a pair of tau leptons is the only mode accessible today to probe the coupling to leptons. In this analysis, all the sub-channels corresponding to all tau decay modes are analysed (H$\longrightarrow \tau_{lep}\tau_{lep}$, $\tau_{lep}\tau_{had}$ and $\tau_{had}\tau_{had}$). In Chapter 6, the details on the Higgs analysis strategy in the ditau channels will be presented in detail.

The dominant backgrounds for this channel are the Drell-Yan Z$\longrightarrow \tau^+\tau^-$, the multijet production from QCD processes (a major background for the $\tau_{lep}\tau_{had}$ and $\tau_{had}\tau_{had}$ channels), the Z$\longrightarrow e^+e^-$, the W+jets and t$\bar{t}$.
Sophisticated methods are developed to estimate the different type of background. This will be shown in detail later.

Let's present briefly here the H$\longrightarrow \tau^+\tau^-$ analysis that has been done using the data recorded by the ATLAS experiment during the Run I.
The events in each the sub-channels are divided into categories in order to increase the sensitivity of the search. Two categories are defined for this purpose, the VBF category which is for events with a Higgs boson produced via vector boson fusion and characterized by the presence of two additional jets with a high p_T and large pseudorapidity separation $\Delta\eta$ and the Boosted category for events with a boosted Higgs boson produced via gluon fusion where the Higgs boson candidates are required to have a transverse momentum greater than 100 GeV.
The mass reconstruction of the ditau system requires a sophisticated method as we will see in the following due to the presence of neutrinos in the final state and given the fact that the reconstruction of a hadronic tau is not a trivial thing to do.
In order to extract the Higgs boson signal from the large number of backgrounds, a multivariate analysis MVA [16] has been used in this search. In this approach, all the discriminating variables between signal and background are combined in a single variable using the Boosted Decision Tree BDT [17]. The excess of signal events above the expected background is located at high BDT bins.
Concerning the final results from the Run I analysis, an excess of events over the expected background from other Standard Model processes is found with an observed (expected) significance of 4.5 (3.4) standard deviations. This excess is consistent with a H$\longrightarrow \tau^+\tau^-$ decay with $m_H = 125$ GeV. The measured signal strength, normalised to the Standard Model expectation for a Higgs boson of $m_H = 125.36$ GeV is $\mu = 1.43^{+0.43}_{-0.37}$ [18].
The LHC Run I data of ATLAS and CMS collabarations has been combined and a significance of 5.5 σ(5.0 σ) expected(observed) is achieved [19]. Thus, the discovery

in $\tau^+\tau^-$ channel is assessed, but not individually per experiment.

2.3.3.2 The H$\longrightarrow b\bar{b}$ channel

Despite the high signal yield in H$\longrightarrow b\bar{b}$ decay mode, the ggH production mode is overwhelmed by the background from strong interaction processe pp $\longrightarrow$ b$\bar{\text{b}}$+X .
In the associated production modes with a vector boson VH (V = W,Z), the W is reconstructed via the leptonic decay channel W$\longrightarrow l\bar{\nu_l}$ ($l = e, \mu$ or τ), and the Z is reconstructed in the di-leptonic or di-neutrino modes Z$\longrightarrow e^+e^-$, $\mu^+\mu^-$ or $\nu\bar{\nu}$. The Higgs boson is reconstructed using two b-tagged jets.
The main backgrounds for this decay channel are from vector bosons (W or Z) associated to jets, $t\bar{t}$, QCD multijets and non-resonant diboson ZZ or WZ where Z$\longrightarrow b\bar{b}$.
In this analysis, the most important elements are the efficiency of tagging a b-quark, the accurate measurement of the b-jet momentum and a good estimate of the different backgrounds.
Th H$\longrightarrow b\bar{b}$ analysis has been performed first by the CDF and D0 experiments at the Tevatron. The combination of data between the two experiments has shown an excess of events with respect to the predicted background in the 115-140 GeV mass range such that for m_H = 125 GeV, the local significance of the excess is 3.0 standard deviations [8] [20].

ATLAS has performed a search in the $b\bar{b}$ decay mode of the SM Higgs boson using the full dataset recorded in Run I. The processes considered are in association to a vector boson (W or Z) (from the associated production mode). An excess of events over the expected background from other Standard Model processes is found with an observed (expected) deviation from the background-only hypothesis with a significance of 1.4 (2.6) standard deviations and the ratio of the measured signal yield to the Standard Model expectation is found to be $\mu = 0.52\pm0.56$ for a Higgs boson mass of 125.36 GeV [21].
The ATLAS collaboration also performed recently an analysis for this Higgs decay channel in the production mode where the Higgs boson is asscociated with top quarks. No significant excess of events above the background expectation is found and the ratio of the measured signal yield to the Standard Model expectation is found to be $\mu = 1.5\pm1.1$ for a Higgs boson mass of 125 GeV [22].
The combined ATLAS and CMS results give a significance of 2.6 σ(3.7 σ) observed(expected) [19].

2.4 Higgs boson parameters

2.4.1 Higgs boson production and decay rates

In this section, the compatibility of the experimental data with the SM predictions will be shown from the combined results of ATLAS and CMS collaborations. This

is based on the combinations results of the data at $\sqrt{s} = 7$ TeV and $\sqrt{s} = 8$ TeV in 2011 and 2012 respectively [19].

The simplest test of this compatibility can be provided by the parametrisation of the signal strength μ with the assumption that the μ_i (the μ's of the different production modes) and μ^f (the μ's of the different decay modes) values are the same for all production processes and decay channels. In this case, the SM predictions of signal yields in all categories are scaled by a global signal strength μ.
Using μ as the parameter of interest, the best fit value of combined ATLAS and CMS data is:

$$\mu = 1.09^{+0.11}_{-0.10} \tag{2.10}$$

This result is consistent with the SM expectation of $\mu = 1$ within less than 1 σ and the p-value of the compatibility between the data and the SM predictions is 34%.
This simple parametrisation of the signal strength is very model dependent, since all Higgs boson production and decay measurements are combined with the assumption mentioned before. Another less model-dependent way of measuring the compatibility of the measured data with the SM can be done by relaxing these assumptions separately for the production cross sections and the decay branching ratios.
The five main Higgs boson production processes are explored with independent signal strengths:μ_{ggF}, μ_{VBF}, μ_{WH}, μ_{ZH} and μ_{ttH}, with the assumption that the SM values for the Higgs boson branching ratios is $\mu^f = 1$. The ATLAS and CMS measurements are combined with these five signal strengths as the parameters of interest. The results are shown in Figure 2.10.

On the other hand, the Higgs boson decays can be studied similarly with five independent signal strengths, one for each decay channel included in the combination, assuming that the Higgs boson production cross sections are the same as in the SM. Figure 2.11 shows the best-fit values for μ's, where the consistency with the SM can be observed.

2.4.2 The Higgs boson mass and width measurements

In the Standard Model, the Higgs boson mass is the only non predicted parameter of the Higgs sector. Therefore, its measurement is necessary for precise calculations of electroweak observables including the production and decay properties of the Higgs boson itself. In the LHC collaborations, a model-independent approach has been chosen to measure the Higgs boson mass based on fitting the mass spectra of the two "precision" modes H$\longrightarrow \gamma\gamma$ and H$\longrightarrow ZZ^* \longrightarrow 4l$. In these two channels, the Higgs boson produces a narrow mass peak with a typical experiemental resolution of 1.6 to 2 GeV over a smooth background from which the mass can be extracted without assumptions on the signal production and decay yields.

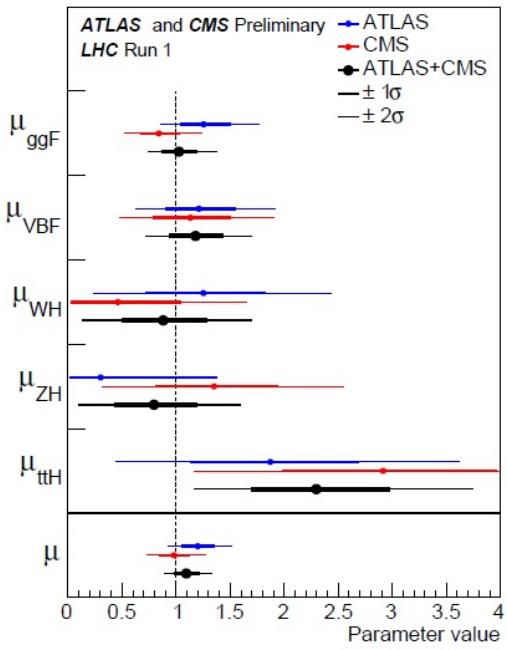

Figure 2.10: Best-fit results for the production signal strengths for the combination of ATLAS and CMS and for each experiment separately. The error bars indicate the 1 σ (thick lines) and 2 σ (thin lines) intervals [19].

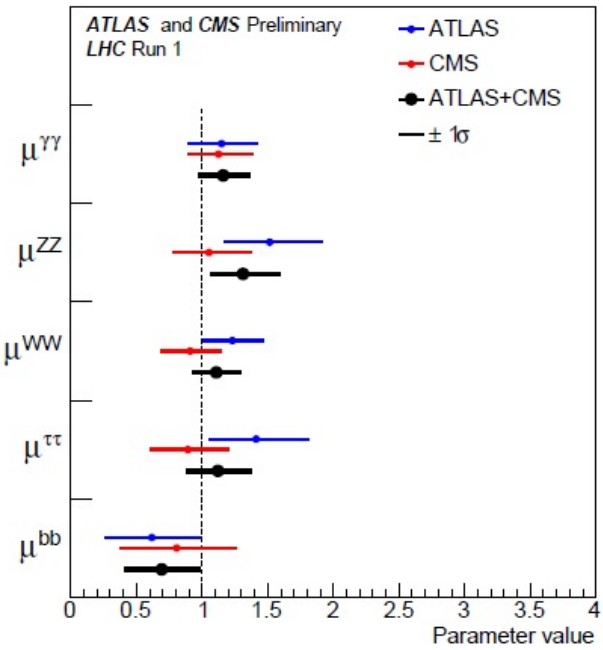

Figure 2.11: Best-fit results for the decay signal strengths for the combination of ATLAS and CMS and separately. The error bars represent the 1 σ intervals. [19].

The ATLAS measurement of the Higgs boson mass is based on LHC data corresponding to the full integrated luminosity of 4.5 fb^{-1} at $\sqrt{s}$ = 7 TeV and of 20.3 fb^{-1} at $\sqrt{s}$ = 8 TeV.

- H$\longrightarrow \gamma\gamma$ channel:
  As was mentioned before, in the H$\longrightarrow \gamma\gamma$, a good sensitivity to the Higgs boson mass is provided [23]. In order to improve the accuracy of the mass measurements, the selected events are split into ten exclusive categories with different signal-to-background ratios and different diphoton invariant mass resolutions. The categorization is based only on the two photon candidates in order to keep the analysis simple.
  The mass spectra for the 10 data categories and the two center-of-mass energies are fitted simultaneously assuming the signal-plus-background hypothesis, using an unbinned maximum likelihood fit. The fitted parameters of interest for the signal are the Higgs boson mass and the signal strength, defined as the yield normalized to the SM prediction. The parameters describing the background mass distributions for each category and center-of-mass energy are also free in the fit.
  The measured Higgs boson mass in the H$\longrightarrow \gamma\gamma$ decay channel is m_H = 125.98 $\pm$ 0.50 GeV.
  A direct limit on the decay width of the Higgs boson is set from the observed width of the invariant mass peak. The observed (expected for μ = 1) 95% confidence level upper limit on the width is 5.0 (6.2) GeV.

- H$\longrightarrow ZZ^*$ channel:
  The high signal-to-background ratio (about two in the signal mass window 120-130 GeV) and the excellent mass resolution in the H$\longrightarrow$ ZZ* $\longrightarrow$4l channel provides a good sensitivity to the measurement of the Higgs boson mass [23].
  A multivariate discriminant is used to reduce the impact of the ZZ^* background on the fitted mass. It is based on a boosted decision tree (BDT). To measure the Higgs boson mass in the H$\longrightarrow$ ZZ* $\longrightarrow$4l , several methods are used. A two dimensional fit to the m_{4l} and the BDT is chosen as the baseline because it has the smallest expected uncertainty among the different methods.
  The measured Higgs boson in the H$\longrightarrow$ ZZ* $\longrightarrow$4l decay channel obtained with this method is m_H = 124.51 $\pm$ 0.52 GeV.
  A direct limit on the total width of the Higgs boson of $\Gamma_H < 2.6$ GeV at 95% CL is obtained.

2.4.3 Higgs boson spin-CP measurement

The measurement of the spin and parity of the Higgs boson can be performed by studying the angular distribution of the decay products. The search in ATLAS for

this parameter is based on the data collected at the Run I.

The recent results of ATLAS for the spin and parity of the Higgs boson are based on the three bosonic decay channels: H$\longrightarrow \gamma\gamma$, H$\longrightarrow$ ZZ* $\longrightarrow$4l and H$\longrightarrow$WW [24]. The SM Higgs boson hypothesis, corresponding to the quantum numbers $J^P = 0^+$, is tested against several alternative spin and parity models. The models considered include non-SM spin-0 and spin-2 models with universal and non-universal couplings to quarks and gluons. The combination of the three decay processes allows the exclusion of all considered non-SM spin hypotheses at a more than 99.9% CL in favour of the SM spin-0 hypothesis.

2.5 Conclusion

The first years of LHC (2010 - 2012) were very fruitful for Higgs searches in particular. It has been observed in the bosonic decay channels (H$\longrightarrow ZZ^*$, $\gamma\gamma$ and W^+W^-) and a strong indication in the leptonic mode (H$\longrightarrow \tau^+\tau^-$) has been obtained. With the Run II data (2015-2018), we aim for an unambiguous signal (i.e. $> 5\ \sigma$) per experiment in H$\longrightarrow \tau^+\tau^-$, and hopefully in b$\bar{\text{b}}$.

Bibliography

[1] LHC Higgs Cross Section Working Group, S. Heinemeyer, C. Mariotti, G. Passarino, and R. Tanaka (Eds.), *Handbook of LHC Higgs Cross Sections: 3. Higgs Properties*, CERN-2013-004 (CERN, Geneva, 2013), `arXiv:1307.1347 [hep-ph]`. (Cited on pages 27, 28, 29, 30, 32 and 33.)

[2] A. Djouadi and P. Gambino, Phys. Rev. Lett. 73, 2528 (1994);
S. Actis et al., Phys. Lett. B670, 12 (2008);
U. Aglietti et al., Phys. Lett. B595, 432 (2004);
G. Degrassi and F. Maltoni, Phys. Lett. B600, 255 (2004).
(Cited on page 29.)

[3] C. Anastasiou, R. Boughezal, and F. Petriello, JHEP 0904, 003 (2009). (Cited on page 29.)

[4] Abdelhak DJOUADI, Decays of the Higgs Bosons , arXiv:hep-ph/9712334v1 10 Dec 1997 (Cited on page 30.)

[5] A. Djouadi, J. Kalinowski, et M. Spira, HDECAY: A Program for Higgs boson decays in the standard model and its supersymmetric extension, Comput.Phys.Commun. 108, 56 (1998), arXiv:hep-ph/9704448 [hep-ph]. (Cited on page 31.)

[6] https://twiki.cern.ch/twiki/bin/view/LHCPhysics/LHCHXSWGCrossSectionsFigures. (Cited on pages 31 and 33.)

[7] ALEPH, DELPHI, L3, and OPAL Collaborations, The LEP Working Group for Higgs Boson Searches, Phys. Lett. B565, 61 (2003). (Cited on page 32.)

[8] CDF and D0 Collaborations, Phys. Rev. D 88 ,052014 (2013). (Cited on pages 34 and 40.)

[9] PRESS CONFERENCE Update on the search for the Higgs boson at CERN on the eve of the ICHEP 2012 Conference, http://cds.cern.ch/record/1459604 (Cited on page 34.)

[10] G. Aad et al., [ATLAS Collab.], Phys. Lett. B716, 1 (2012). (Cited on page 34.)

[11] S. Chatrchyan et al., [CMS Collab.], CMS Collab., Phys. Lett. B716, 30 (2012). (Cited on page 34.)

[12] ATLAS Collab., ATLAS-CONF-2013-034 (2013). (Cited on pages 34 and 35.)

[13] CMS Collab., CMS-HIG-12-045 (2012). (Cited on pages 34 and 35.)

[14] G. Aad et al., arXiv:1408.7084v2 [hep-ex] 9 Sep 2014 (Cited on pages 34, 35 and 36.)

[15] G. Aad et al., [ATLAS Collab.], Phys. Lett. B726, 88 (2013). (Cited on pages 36, 37 and 38.)

[16] A. Hoecker, P. Speckmayer, J. Stelzer, J. Therhaag, et al., TMVA: Toolkit for Multivariate Data Analysis, PoS ACAT, 040 (2007), arXiv:physics/0703039. (Cited on page 39.)

[17] L. Breiman, J. Friedman, R. Olshen, and C. Stone, Classification and Regression Trees. Chapman and Hall, New York, 1984. (Cited on page 39.)

[18] G. Aad et al., arXiv:1501.04943v3 [hep-ex] 27 Apr 2015 (Cited on page 39.)

[19] ATLAS-CONF-2015-044, Measurements of the Higgs boson production and decay rates and constraints on its couplings from a combined ATLAS and CMS analysis of the LHC pp collision data at $\sqrt{s} = 7$ and 8 TeV, 15 September 2015 (Cited on pages 39, 40, 41 and 42.)

[20] CDF and D0 Collaborations, Phys. Rev. Lett. 109, 071804 (2012) (Cited on page 40.)

[21] G. Aad et al., arXiv:1409.6212 [hep-ex] (Cited on page 40.)

[22] G. Aad et al., arXiv:1503.05066 [hep-ex] (Cited on page 40.)

[23] G. Aad et al., arXiv:1406.3827v1 [hep-ex] 15 Jun 2014 (Cited on page 43.)

[24] G. Aad et al., arXiv:1506.05669v2 [hep-ex] 23 Oct 2015 (Cited on page 44.)

Chapter 3

The LHC and the ATLAS detector

Contents

3.1 The Large Hadron Collider

3.1.1 Introduction

The Large Hadron collider (LHC)[1] is the most advanced collider that enables the experimental study of particle physics by colliding protons-protons at the highest energy achieved so far.
It is operated by the European Organization for Nuclear Research (CERN) at the border between Switzerland and France. It was first conceived in the 1980s with the purpose of finding the Higgs boson and discovering physics beyond our current understanding. After LEP (Large Electron-Positron Collider) [2] which was operated until the year 2000 and the TeVatron [3], which stopped working in September 2011, the LHC is the new particles collider devoted to new searches and discoveries. In 2011, the LHC started running at the center of mass energy of $\sqrt{s} = 7$ TeV followed by a run with $\sqrt{s} = 8$ TeV in 2012.
The LHC occupies the underground tunnel originally constructed for the LEP for use in the 1990s. It is a circular hadron collider with 27 kilometers of circumference and 100 meters underground, near Geneva, Switzerland.

Along the LHC ring, there are four interaction points where hadrons are collided at high energies. The experiments at these collision points are: ATLAS (A Toroidal LHC ApparatuS)[4], CMS (Compact Muon Solenoid)[5], ALICE (A Large Ion Collider Experiment)[6] and LHCb (LHC beauty experiment)[7]. ATLAS and CMS are the two biggest experiments dedicated for understanding physics of the Standard Model and beyond. ALICE is built to study heavy ion collisions (lead nuclei) and probe the physics of gluon-quark plasma. LHCb is specialized on b-hadrons physics. Figure 3.1 shows a view of the underground LHC experiments.

3.1.2 Description of the accelerator

The CERN accelerator complex is a succession of machines with increasingly higher energies [8]. The beam is injected from a machine to a next one to bring the beam to the nominal energy.
The LHC is the last part in that chain where proton beams are accelerated to the final energy.

Most of the other accelerators in the chain have their own experimental halls, where the beams are used for experiments at lower energies.
The story of the accelerated proton beam [9] through the accelerator complex at CERN starts from hydrogen atoms taken from a bottle containing hydrogen. The proton are obtained by stripping electrons from hydrogen atoms. The protons are then injected into the PS Booster (PSB) at an energy of 50 MeV from Linac2. It accelerates them up to 1.4 GeV. The beam is then fed to the proton synchrotron (PS) which accelerates it up to 25 GeV. After that, the protons are injected in the Super Proton Synchrotron (SPS) where they are accelerated up to 450 GeV. Finally,

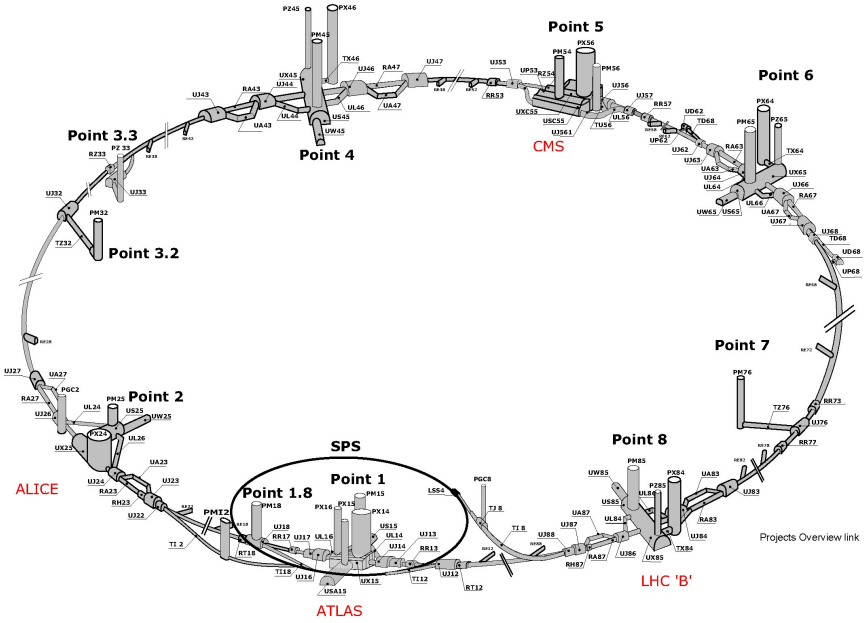

Figure 3.1: The Large Hadron Collider (LHC) with its four detector experiments (ATLAS, CMS, LHCb and ALICE) sits in a 27-km-long circular tunnel, 100m below the ground at the European Organization for Nuclear Research (CERN) on the French-Swiss border, North of Geneva.

the beam is transferred to the LHC (both in a clockwise and an anticlockwise direction) where they are accelerated for 20 minutes up to their nominal energy. Beams will circulate for many hours inside the LHC beam pipes under normal operating conditions. Protons are injected at the LHC in bunches, which are prepared in the upstream machines.
In addition to the proton beam acceleration, the CERN complex accelerator also accelerates lead ions for a program of research of heavy ion collisons.
The main caracteristics of the LHC are listed in Table 3.1 [10].
In the accelerator, the particles circulate in a vacuum tube and electromagnetic devices are used to steer them. The beam and its trajectory are controlled by a large variety of magnets including dipoles, quadripoles, sextupoles... (∼9600 magnets). They are supraconducting magnets and cooled down to 1.9 K by pumping superfluid helium into the magnet systems. Each 2 in 1 dipole is 15 m long and weighs around 35 t. The dipoles (∼ 1230) are able to produce a field of 8.33 Tesla to keep the circular trajectory of protons. The quadrupoles (∼ 390) control the beam size to focus it.
Accelerating cavities, electromagnetic resonators, are used to accelerate particles and then keep them at a constant energy by compensating for energy losses. A major role of the cavities is to keep the proton bunches tightly bunched to ensure high luminosity at the collision points and hence, maximize the number of collisions. They also deliver radiofrequency (RF) power to the beam during acceleration to the top energy. The LHC use eight cavities per beam, each delivering 2 MV (an accelerating field of 5 MV/m) at 400 MHz. The cavities operate at 4.5 K.
In the LHC, the beam vacuum pressure is 10^{-13}atm (ultrahigh vacuum) in order to avoid collisions with gas molecules.

Quantity	Design	2011	2012	2015	September-2016
$\sqrt{s}$(TeV)	14	7	8	13	13
Luminosity peak($cm^{-2}s^{-1}$)	10^{34}	3.5×10^{33}	7.5×10^{33}	5×10^{33}	11.6×10^{33}
Integrated luminosity	-	4.5	20	3.2	13
No. of bunches per proton beam	2808	1380	1380	2232	2220
No. of protons per bunch ($\times10^{11}$)	1.15	1.45	1.7	1.21	1.25
$\Delta t(ns)$	25	50	50	25	25
$< \mu >$	20	9	20.7	13	23.2

Table 3.1: Evolution of some relevant LHC parameters between 2011, 2012 and today [10].

3.1.3 The LHC parameters

3.1.3.1 The luminosity

The instantaneous luminosity L is a crucial parameter to measure the performance of a collider:

$$N_{process} = \sigma_{process}.L \tag{3.1}$$

where $\sigma_{process}$ is the cross section of a given process and $N_{process}$ is the event yield for this process.

The expression of the luminosity in terms of the beam parameters is [11]:

$$L = \frac{N_b^2 n_b f_{rev} \gamma_r}{4\pi\varepsilon_n \beta^*} F \tag{3.2}$$

where:

- N_b: the number of particles per bunch.
- n_b: the number of bunches per beam.
- f_{rev}: the revolution frequency (40 MHz).
- γ_r: the relativistic gamma factor of the proton.
- ε_n: the normalised transverse beam emittance.
- β^*: the beta function at the collision point.
- F: the geometric luminosity reduction factor due to the non-zero crossing angle at the interaction point, to limit beam-beam interactions.

The evolution of the luminosity in the LHC during the different runs will be described in the next LHC-operation section.

3.1.3.2 The centre-of-mass energy

The LHC was commissioned in September 2008. It is designed to collide protons with a design center-of-mass energy $\sqrt{s} = 14$ TeV, a luminosity of 10^{34} cm^{-2}s^{-1} and 2808 bunches per beam. Shortly after the initial operation of the LHC, a fault occurred in a superconducting interconnection between two magnets (splices), a dipole and a quadrupole, resulting in mechanical damage and release of helium from the magnet cold mass into the tunnel. An explosion involving helium gas damaged about 57 LHC magnets [12].
Until November 2009, major repairs were made to replace the magnets and to prevent a recurrence. First beams circulated in the LHC in the same year, followed by first collisions at 900 GeV (450 GeV per beam with no acceleration in the LHC for

this test).
In 2010, as a precaution, beams in the LHC were accelerated below the LHC design limit where the LHC achieved collisions with energy of 7 TeV in the center-of-mass. In 2011, the LHC continued colliding protons at 7 TeV, then at 8 TeV in 2012. CERN originally planned that the LHC would run through to the end of 2012, but in late 2012, thanks to the discovery of the Higgs boson, the shutdown was postponed for some weeks into early 2013, to allow additional data to be obtained prior to shutdown.
After two years of upgrade, the LHC restarted commissioning in June 2015 at the new energy of 6.5 TeV per beam so a total collision energy of 13 TeV.

3.1.3.3 Pileup and bunch spacing

Pileup The pileup is the average number of proton-proton collisions per bunch crossing $< \mu >$, knowing that, in the LHC, there is a non-negligible probability that one single bunch crossing may produce several separate events, due to the high proton-proton inelastic cross section ($\sim$ 70 mb).
The mean number of interactions per crossing corresponds to the mean of the Poisson distribution on the number of interactions per crossing calculated for each bunch. It is calculated from the instantaneous per bunch luminosity as $\mu = L_{bunch} \times \sigma_i nel / f_r$ where L_{bunch} is the per bunch instantaneous luminosity, σ_{inel} is the inelastic cross section which we take to be 71.5 mb for 7 TeV collisions and 73.0 mb for 8 TeV collisions, n_{bunch} is the number of colliding bunches and f_r is the LHC revolution frequency.
These pileup events add detector noise to potential high-p_T events.

Bunch spacing The nominal bunch spacing for the LHC is 25 ns in order to minimize the pileup. During the period between 2010 and 2013, the luminosity production mainly used beams with 50 ns spacing, while 25 ns beams were only employed for short periods in 2011 and 2012 for test purposes. Electron Cloud (EC) [13] effects have been identified as a major performance limitation for the LHC when operating with the nominal bunch spacing of 25 ns. To briefly remind the EC effect, Synchrotron radiation from proton bunches in the LHC creates photoelectrons at the beam screen wall. These photoelectrons are pulled toward the positively charged proton bunch. When they hit the opposite wall, they generate secondary electrons which can in turn be accelerated by the next bunch. Depending on several assumptions about surface reflectivity, photoelectron and secondary electron yield, this mechanism can lead to the fast build-up of an electron cloud [13]. A beam induced strategy, called scrubbing, is used in order to mitigate the electron cloud effects.
After the startup in 2015, apart from the LHC collision energy which is raised to 6.5 TeV per beam, the LHC starts operations with the nominal 25 ns bunch spacing in order to maximise the integrated luminosity in this for the limited event pileup acceptable by the LHC experiments (see Table 3.1).

3.1.4 Operations

In this section, we will see the different runs of the LHC and the evolution of the machine parameters throughout the different periods of data taking.

3.1.4.1 Run I

The Run I of the LHC referred to the data taking from 2011 until the shutdown in March 2013. As mentioned before, the corresponding energies of this period are respectively 7 TeV and 8 TeV.
The peak instantaneous luminosity achieved in 2012 was 7.7×10^{33} cm^{-2}s^{-1}, which is almost the double of the peak luminosity of 2011 data taking (3.5×10^{33} cm^{-2}s^{-1}) [14]. Figure 3.2 shows the luminosity peak as a function of the day in 2010, 2011 and 2012.
In physics analysis, the integrated luminosity, $\int$Ldt, over a given period is used. It is expressed in fb^{-1} where 1b = 10^{-24} cm^2. Figure 3.3 (Left) shows the integrated luminosity of the LHC versus time in 2011 and 2012. The luminosity recorded by ATLAS is also shown. We see that the data certified to be good quality data for physics analysis is 4.57 fb^{-1} in 2011 and 20.3 fb^{-1}.
Profiles of the pileup are shown in Figure 3.3 (Right). The integrated luminosity and the mean μ values are given in this figure. The $<\mu>$ in 2012 is around 20 collisions per crossing and can reach 35-40 [15].

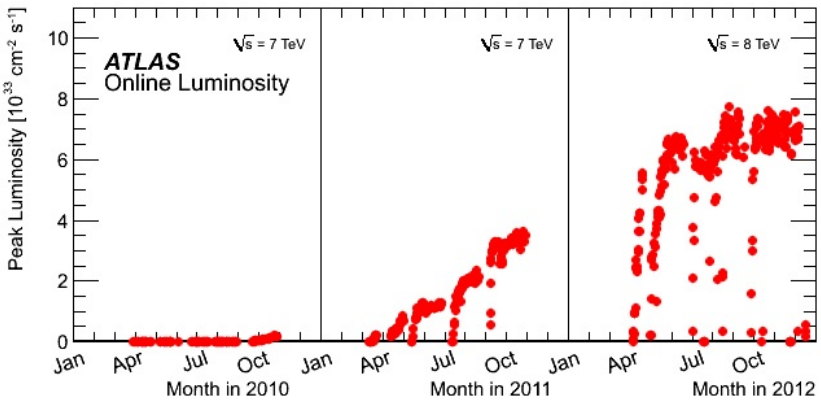

Figure 3.2: The peak of luminosity as measured during the Run I [15].

3.1.4.2 Run II

The run period between 2015 and 2018 is referred as the Run II of the LHC. Apart from the LHC energy which is raised to 6.5 TeV, the integrated luminosity expected from this run is around 100-120 fb^{-1} at a nominal peak luminosity of 10^{34} cm^{-2}s^{-1}. Figure 3.4 shows the running plan for the Run II between 2015 and 2018, including the shutdown and technical stops, the proton-proton collision schedule for physics,

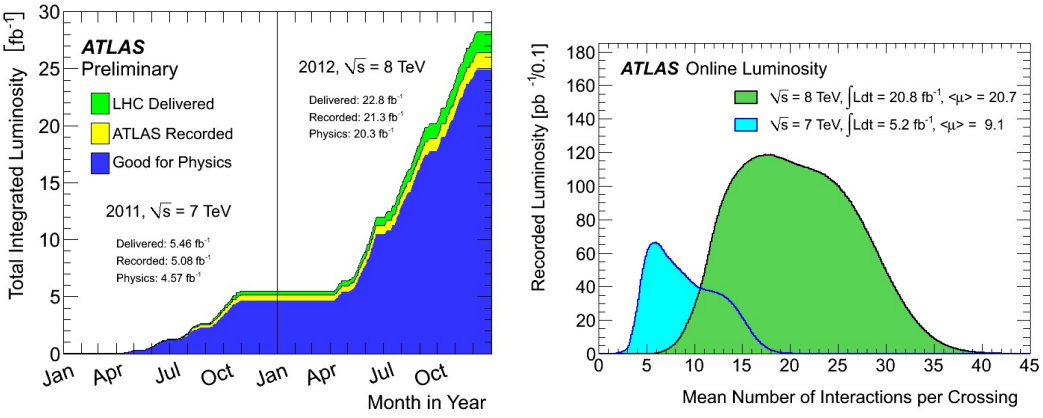

Figure 3.3: Left: Integrated luminosity versus time delivered to (green), recorded by ATLAS (yellow), and certified to be good quality data (blue) during stable beams and for pp collisions at 7 and 8 TeV centre-of-mass energy in 2011 and 2012. Right: and the mean number of interactions per bunch crossing (right) [15].

the commisioning time, and the heavy ions collision schedule.

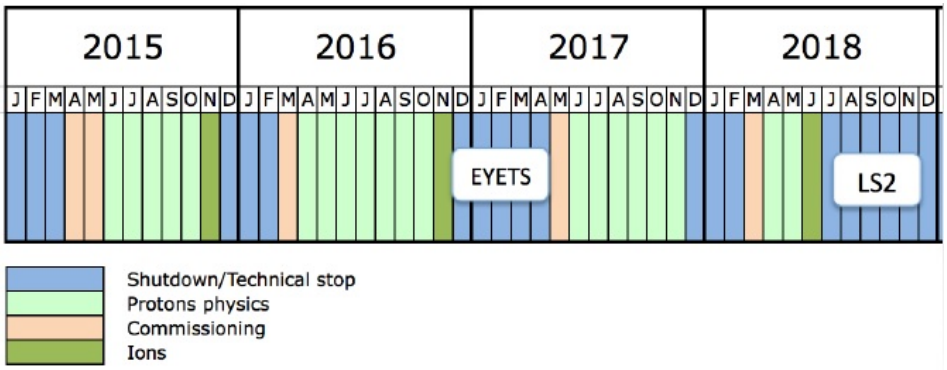

Figure 3.4: The plan of LHC Run II during the period 2015-2018.

Many improvements have been introduced to the machine during more than two years of shutdown including the performance of the system. In the following cited a few examples of what have been improved for the Run II are quoted:

- The magnetic system has been improved and in particular the superconducting interconnection between magnets, responsible of the incident in 2008, have been fixed.
- Better focusing and smaller β^*. This means more interactions and collision to study.
- The bunches of protons are separated in time by 25 ns compared to 50 ns in

order to maximize the integrated luminosity in Run II and to limit the pileup.

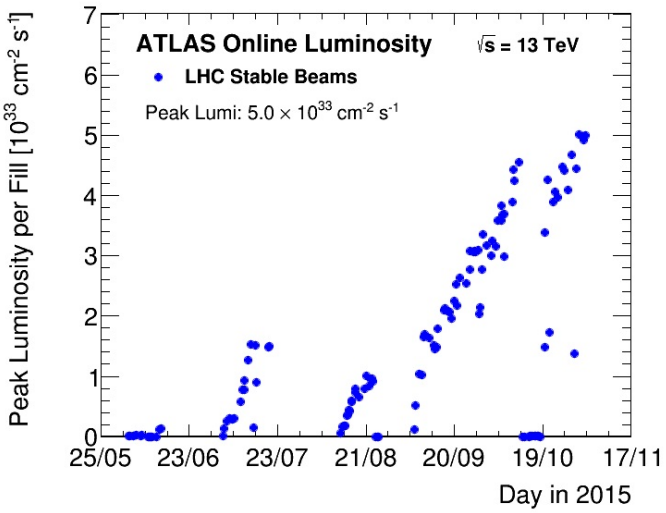

Figure 3.5: The peak luminosity as measured during the 2015 data-taking period [16].

In 2015, as shown in Figure 3.5, the LHC started with a tuning period, with luminosity peak of 10^{33} and a bunch spacing of 50 ns. This was followed by a run with 25 ns of bunch spacing and a luminosity peak of 5×10^{33} has been achieved. Figure 3.6 shows the total integrated luminosity recorded by ATLAS in this year (~ 3.9 fb^{-1}) and the luminosity-weighted distribution of the mean number of interactions per crossing [16].
During the period between 2016 and 2018, the LHC will run with 25 ns bunch spacing and an expected luminosity peak of 10^{34} cm^{-2}s^{-1}.

The new phase of an LHC operating at 13 TeV centre-of-mass energy allow the LHC experiments to explore the Nature and probe the physical laws governing it

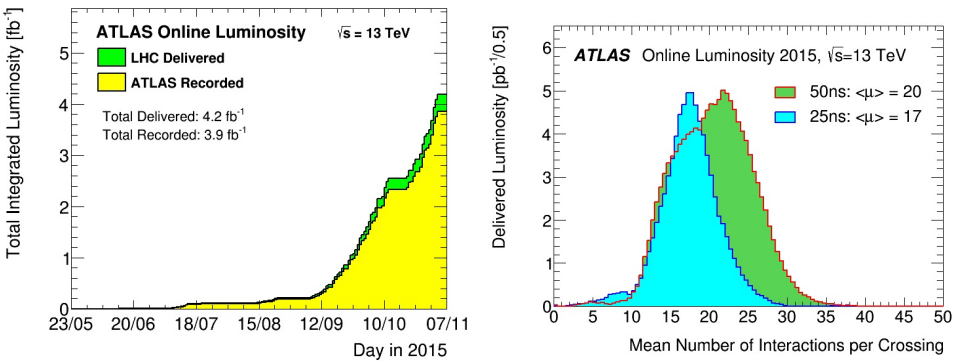

Figure 3.6: Distributions of the integrated luminosity in 2015 (left) and the recorded luminosity in bins of $< \mu >$ for two runs 50 ns and 25 ns (right)[16].

at scales never reached before. Figure 3.7 shows the cross section ratios between the Run II at 13 TeV and Run I at 8 TeV for a set of physics processes. The higher energy leads to a hugely increased potential for discovery of heavy particles (SUSY, QBH,..). And the gain in luminosity allows to study processes with low cross section (H$\longrightarrow \tau\tau$ for example).

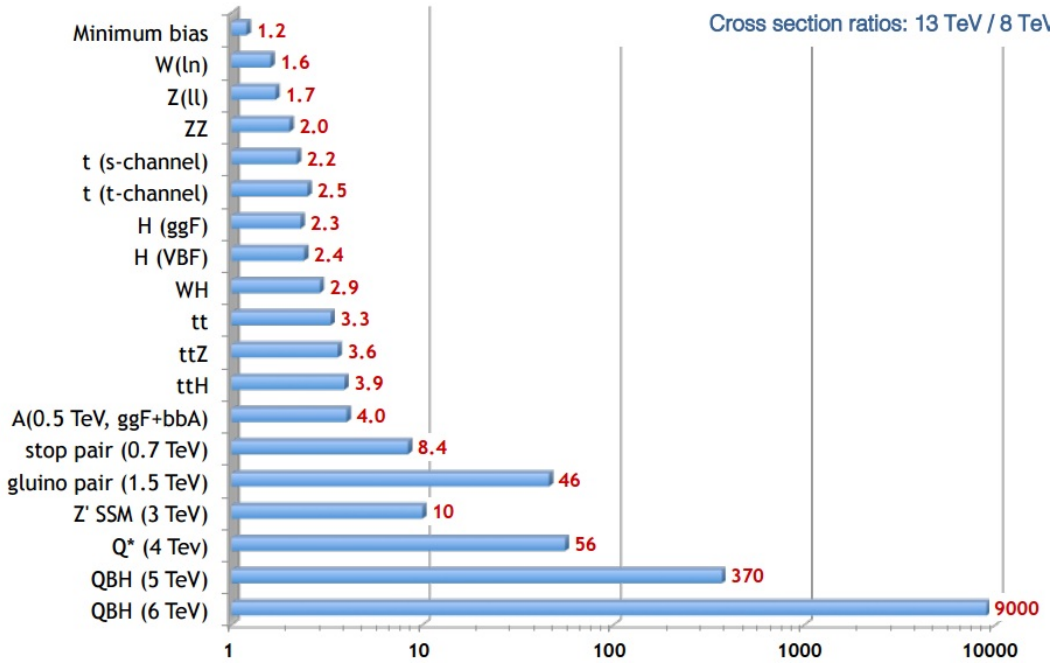

Figure 3.7: The cross section ratio between Run I and Run II for some physics processes [17].

3.1.5 The future of the LHC

To exploit the full potential of the Large Hadron Collider, the machine will operate in the future with a higher luminosity. The Run 3 of the LHC will start in 2020 after an upgrade stage in 2018 and 2019 and continue until the end 2022. The collision energy is 13 TeV and the expected total integrated luminosity is 300fb^{-1}.
The next step is what is called the HL-LHC (high luminosity LHC). The goal is to operate from 2025 up to 2035. The scenario for this run is to get an integrated luminosity of 3000 fb^{-1} in around 10 to 12 years, always with 13 TeV centre-of-mass collision energy.
The higher luminosity will allow more accurate precision measurements, the observation of very rare processes, and increase the discovery reach with rare events at the high-energy frontier.

3.2 The ATLAS detector

3.2.1 Introduction

The ATLAS (A Toroidal LHC Apparatus) detector is one of the four experiments dedicated to study the proton-proton (and Pb ions) collisions at the LHC. This huge detector is the result of the work of a international collaboration including several thousand physicists, engineers, technicians, and students over a period of 25 years of dedicated design, development, fabrication, and installation.
ATLAS is a multi-purpose particle physics detector that should be able to measure the signatures of all the possible final states we expect to observe from proton-proton (or heavy ion) collisions.
Placed at 90 m underground, at the collision point 1, ATLAS is a 4π detector measuring approximately 44 m in length and 25 m in height.
The ATLAS detector is shown in Figure 3.8. It uses a cylindrical geometry with one end-cap on each side to ensure full coverage in solid angle. It is divided into three main parts and organized in layers from the interaction point outwards:

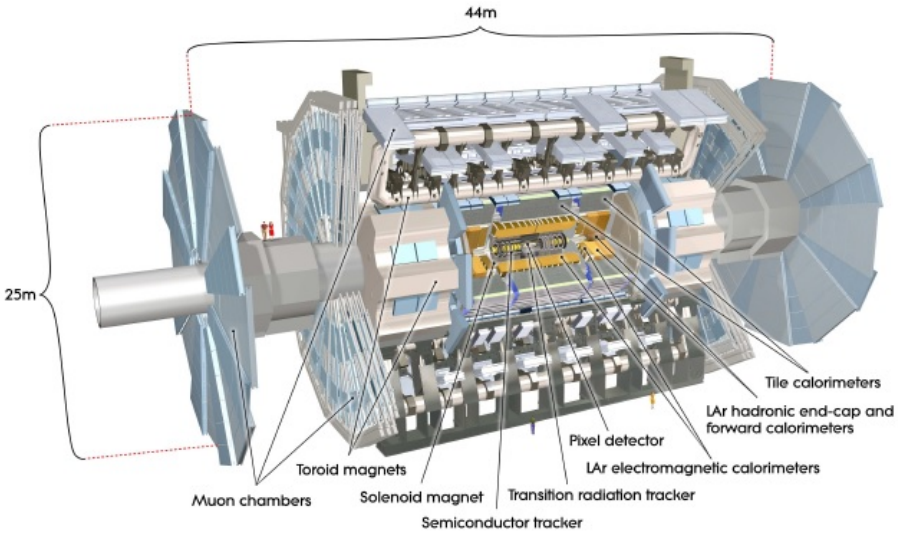

Figure 3.8: The ATLAS detector.

- The inner detector dedicated to measure the trajectory of charged particles in the central volume. A solenoidal magnetic field curves the trajectory of charged particles and provides a precise measurement of their momentum.
- The calorimetric system to provide the measurement of energies of charged and neutral particles. It is subdivided into electromagnetic calorimeter to measure the energies of electrons and photons, and a hadronic calorimeter that absorb the particles shower and provides the reconstruction of jets and missing transverse momentum.

- The muon spectrometer bathed in a toroidal magnetic field. It provides a precise measurement of muon momentum.

Coordinate system Concerning the coordinate system of the ATLAS detector, the nominal interaction point is defined as the origin of the coordinate system, while the beam direction defines the z-axis and the x-y plane is transverse to the beam direction. The positive x-axis is defined as pointing from the interaction point to the centre of the LHC ring and the positive y-axis is defined as pointing upwards. These coordinate are illustrated in Figure 3.9.

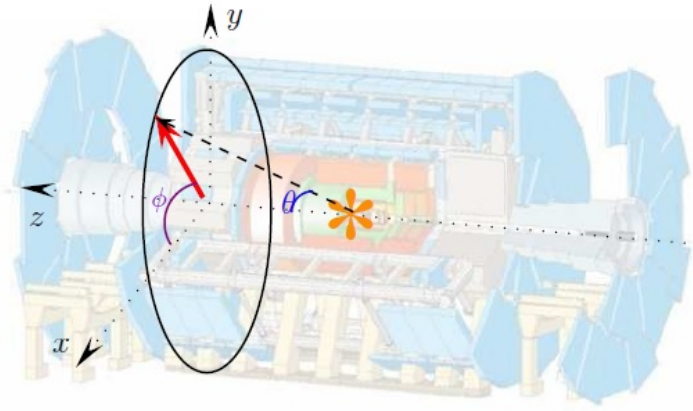

Figure 3.9: the coordinate system in ATLAS

The pseudorapidity is defined as:

$$\eta = -ln \quad tan(\theta/2) \tag{3.3}$$

It is equivalent to the rapidity for relativistic particles. The definition of rapidity used in experimental particle physics is:

$$y = \frac{1}{2} ln(\frac{E + p_L}{E - p_L}) \tag{3.4}$$

In the limit where the particle is travelling close to the speed of light, or equivalently in the approximation that the mass of the particle is negligible, one can make the substitution m<<p $\Longrightarrow$ E$\sim$P $\Longrightarrow$ $\eta = y$. The most interesting property of the rapidity is to be shifted by the same amount for all particles with the same boost along the z axis. That means that the rapidity difference between two particles is a Lorentz invariant under such boosts, which is convenient.
The range of the pseudorapidity is from -∞ to +∞ and is 0 when $\theta = \frac{\pi}{2}$. The limit of coverage of the ATLAS detector is $|\eta| = 4.9$ corresponding to $\theta \approx 0.85$ degrees.

The distance ΔR in the pseudorapidity-azimuthal angle space is defined as $\Delta R = \sqrt{\Delta\eta^2 + \Delta\phi^2}$.

3.2.2 Physics requirements and performances

As discussed in the previous section, the LHC provides a rich physics potential, ranging from precise measurements of Standard Model parameters to the search for new physics phenomena. The high energy, high luminosity and increased cross-sections at the LHC allow the discovery of new heavy particles and enable further high precision tests of QCD, electroweak interactions, and flavor physics. As an example, the top quark is produced at the LHC at a rate of a few tens of Hz, providing the opportunity to test its couplings and spin.
The search for the Standard Model Higgs boson constitutes a very important part of ATLAS activities. And as we have seen in the last chapter, ATLAS searches (with CMS) covers a wide area of Higgs boson searches in different decay channels.
The decays of supersymmetric particles, such as squarks and gluinos, would involve cascades which contains a lightest stable supersymmetric particle (LSP). As the LSP would interact very weakly with the detector, the experiment would measure a significant missing transverse energy in the final state. The rest of the cascade would result in a number of leptons and jets. In schemes where the LSP decays into a photon and a gravitino, an increased number of hard isolated photons is expected. So a good and precise measurements of all the objects including jets, and a high pseudorapidity coverage are required in order to achieve a good resolution on missing transverse energy.
Several models propose the existence of extra dimensions [18] leading to a characteristic energy scale of quantum gravity in the TeV region. In terms of experimental signatures, this could lead to the emission of gravitons which escape into extra dimensions and therefore generate E_T^{miss}, or of Kaluza-Klein excitations which manifest themselves as Z-like resonances with ~TeV separation in mass. Other experimental signatures could be anomalous high-mass di-jet production, and miniature black-hole production with spectacular decays involving democratic production of fundamental final states such as jets, leptons, photons, neutrinos, W's and Z's.
Given the fact that the LHC collides protons, the QCD jet production cross sections dominate over the rare processes mentioned above, requiring the identification of experimental signatures characteristic of the physics processes in question. To achieve the rich physics program, ATLAS has to fulfill very stringent requirements:

- A high granularity is needed to handle the particle fluxes and to reduce the influence of overlapping events from pileup.
- Fast, radiation-hard electronics and sensor elements are required due to the experimental conditions of the LHC.
- Good charged-particle momentum resolution and reconstruction efficiency in

the inner tracker are essential. For offline tagging of τ-leptons and b-jets, vertex detectors close to the interaction region are required to observe secondary vertices.

- A very good calorimetric system. The electromagnetic calorimeter, for identifying and measuring electrons and photons, and the hadronic calorimeter for accurate jet and missing transverse energy measurements. A good acceptance in pseudorapidity is required in the detector in order to minimize the number of escaping particles and improve the missing transverse energy measurement.

- Good muon identification and momentum resolution over a wide range of momenta and the ability to determine unambiguously the charge of high p_T muons are fundamental requirements.

- Highly efficient triggering (down to low p_T objects) with sufficient background rejection, is a prerequisite to achieve an acceptable trigger rate for most physics processes of interest.

In the next sections, we will see in details all the components of ATLAS detector designed with a very high accuracy in order to achieve all the goals and performances mentioned above.

3.2.3 The magnetic system

The ATLAS magnetic system consists of one solenoid and three toroids. It features a unique hybrid system of four large superconducting magnets [19] .
The ATLAS magnetic system is 22 m in diameter and 26 m in length, with a stored energy of 1.6 GJ. The magnets provide magnetic field over a volume of approximately 12000 m^3. Figure 3.10 shows the spatial arrangement of the coil windings. So the ATLAS magnets system can be presented as:

- A central solenoid, located between the tracker and the electromagnetic calorimeter. It provides an axial magnetic field of 2T for the inner detector when supplied with a current of 7.73 KA.

- A barrel toroid and two end-cap toroids. they extend over 26 m long and 22 m in diameter. It is traversed by a current of 22.3 KA and provides a magnetic field of 0.5 T and 1 T for the muon detectors in the central and end-cap regions, respectively.

3.2.4 The inner detector

The ATLAS inner detector (ID) [20] is the closest part of the apparatus to the beampipe. It is designed as a tracker to provide the excellent momentum resolution, primary and secondary vertex measurements for charged particles above a

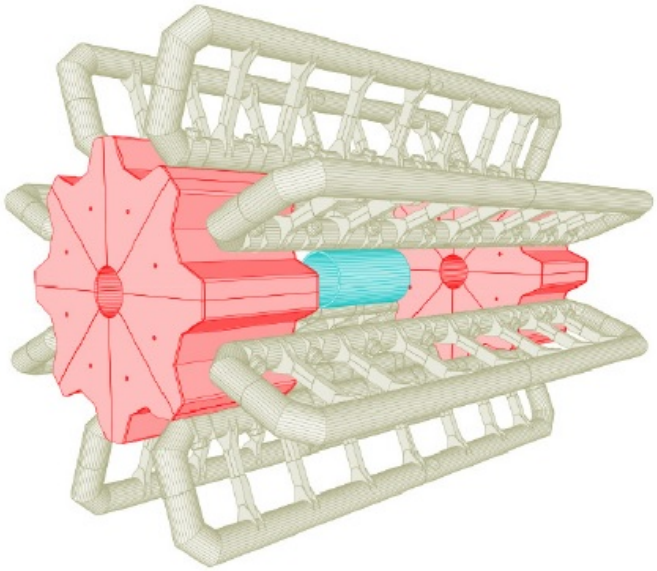

Figure 3.10: Geometry of magnet windings and tile calorimeter steel. The solenoide in blue, the cryostats of eight coils of the barrel of the toroid in gray, and the toroid cryostats plugs in red.

given p_T threshold and within the pseudorapidity range $|\eta| < 2.5$, tagging of b-quarks and tau-leptons and discrimination between electrons and photons.
The ID spans 6.2 m of length and 2.1 m of diameter where reigns an axial magnetic field of 2 T.
It is composed of three sub-detectors, split into barrel and endcap components, have full 2π coverage in ϕ, and a good coverage in $|\eta|$ up to 2.0. Figure 3.11 shows the layout of the three sub-detectors starting from the interaction point to the outside:

- The pixel detector
- The SemiConductor Tracker (SCT)
- The Transition Radiation Tracker (TRT)

3.2.4.1 The pixel detector

The pixel detector is the closest part to the collision point. It is designed with fine granularity and good spatial resolution in order to reconstruct with high precision the primary and secondary vertices. The intrinsic resolution in the barrel part is 10 μm in Rϕ and 115 μm in z [21] [22] [23].

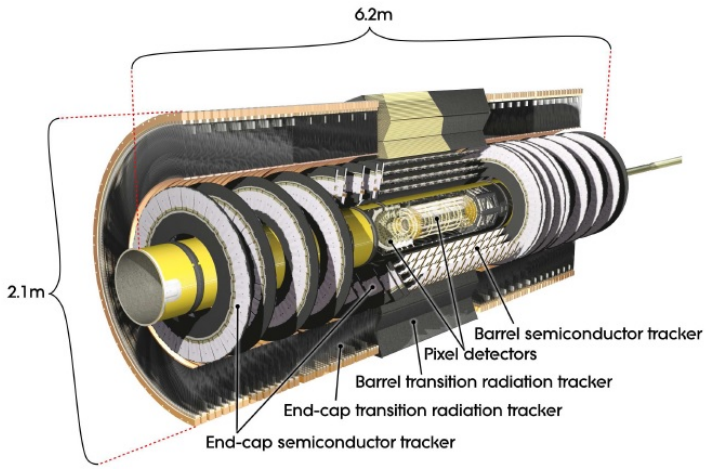

Figure 3.11: The layout of the ATLAS inner detector with the three sub-components.

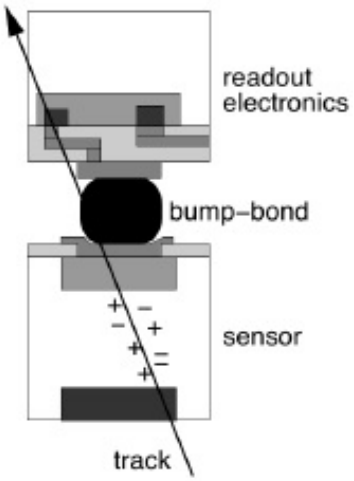

Figure 3.12: Operation principle of a pixel.

- Run I: During the Run I of the LHC, to have a coverage of the region $|\eta| < 2.5$, the pixel detector was composed of three concentric cylinders located at 50.5, 88.5 and 122,5 mm of the beam axis in the barrel region. In each end cap, there are three disks centered on the axis of the beam. It consists of 1744 modules where each one is composed of 47232 silicon pixels with dimensions of 50 μm $\times$ 400 μm (z) so leading in total to more than 80 million readout channels.
  The operation of a single pixel is shown in Figure 3.12. The active zone of the pixel is made of silicon semi-conductor enriched with oxygen to increase its resistivity to radiation [24]. When a charged particle ionises the silicon, the liberated electrons drift towards to the readout electronic when applying a voltage. The charges are collected by an electrode. The measurement of a current higher than a threshold indicate the passage of a charged particle.

- Run II: In the heart of ATLAS, and closest to the beam pipe where the proton collisions occur, a new pixel layer, the Insertable B-Layer (IBL) [25], was inserted in the detector during the shutdown in 2013-2014. The mean radius of the IBL is 33 mm from the beam axis. Figure 3.13 shows the IBL during the insertion procedure.

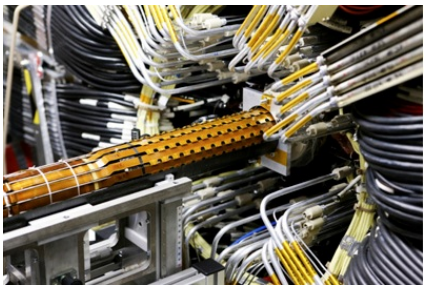

Figure 3.13: The insertion of the IBL sub-detector at the midpoint of its installation journey [25].

3.2.4.2 The semiconductor tracker (SCT)

The SCT is located around the pixel detector [26], it provides at least 4 measurement points per track. It is divided into 4 concentric cylinders in the barrel at fixed radii and 9 disks in the end-caps.
Instead of pixels, it uses silicon strips with 80 μm pitch assembled in double-sided modules with a stereo angle of 40 mrad between the two sides as we can see in Figure 3.14.
The thickness of the silicon sensor in the SCT is 285$\pm$15 μm. This accounts for about 6 million read-out channels in the detector and covers a surface of silicon of 63 m^2, making the SCT one of the largest existing silicon detectors.

The spatial resolution of the SCT is about 17 μm in rϕ and 580 μm in z. It has a pseudorapidity coverage up to $|\eta| = 2.5$.

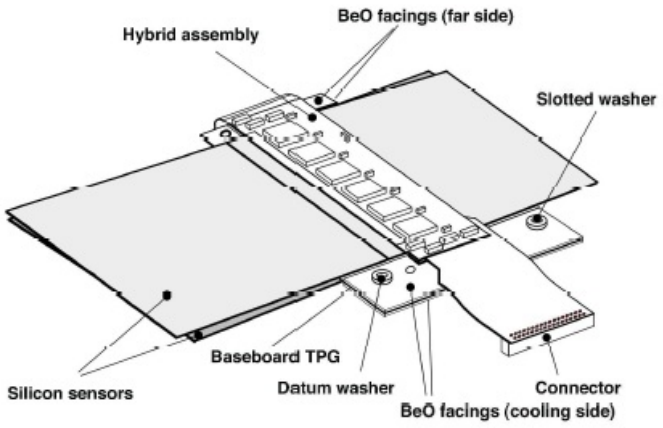

Figure 3.14: An SCT module. The stereo angle is 40mrad between the two sides

3.2.4.3 The Transition Radiation Tracker (TRT)

The TRT [27] is the outermost component of the ATLAS inner detector. It is based on the use of drift-tube detectors (straws), each 4 mm in diameter and up to 144 cm long and equipped with a 30 μm diameter central wire. There are about 50000 straws in the barrel and 320000 radial straws in the end-caps. Inside the drift-tubes, there is a mixture of nonflammable gas with a total volume of 3 m^3. The anode is a tungsten wire located at the center of each straw and provides more than 30 points on each particle track when it ionizes the gas. The intrinsic single point resolution of the TRT in the barrel is 130 μm in ϕ. This is not as precise as those for the other two detectors but provides many measurement points (30 hits per track).
The straws are organized in layers (Figure 3.15), parallel to the beams axis in the barrel and radially in the end-caps.

In addition, between the straws, there are polypropylene fibers with different optical index than the air surrounding them. Therefore, the TRT can collect electrons resulting from the absorption by the gas of transition photons (X-rays) emitted when a charged particle crosses the boundary between two media of different dielectric constants. This radiation is proportional to the Lorentz factor γ of the charged particle. The TRT is in an operating mode with two thresholds, a lower one which indicates the passage of a charged particle and the high threshold that indicates the passage of a high γ factor particle. This allows the identification of charged particles as electrons or pions knowing that a pion is much heavier than an electron and for the same impulsion, an electron has a Lorentz factor 270 times larger than the one of a pion.

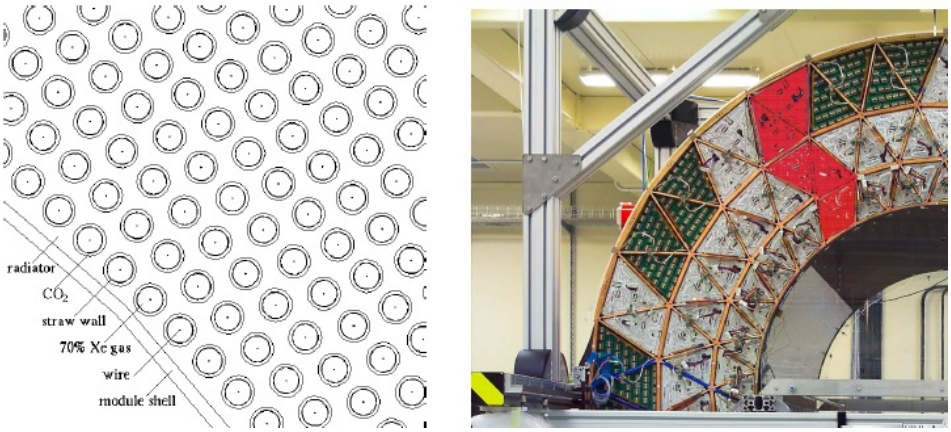

Figure 3.15: Organisation of the TRT components with its straws, radiator and wires (left) [28] and a Photography of the detector system during the installation (right) [29].

3.2.5 The calorimeters

The ATLAS calorimeters sit arround the inner detector (Figure 3.16). The calorimeter system is composed of two main parts: the electromagnetic (ECAL) and the hadronic calorimeter (HCAL). The name of each part reflect the nature of particle it is designed to measure.
Both ECAL and HCAL are sampling calorimeters with an $|\eta| < 4.9$ coverage. Both consist of alternating layers of passive material which develop the showers, the absorber, and active material layers where the detection takes place. The detectors are based on a liquid argon technology (yellow color parts in Figure 3.16) and tiles scintillators (gray parts), and organized as follows:

- The electromagnetic calorimeter (EM) composed by the barrel ($|\eta| < 1.475$) and two end-caps ($1.375 < |\eta| < 3.2$).
- The hadronic calorimenter composed by the barrel ($|\eta < 1.7|$ and two end-caps ($1.375 < |\eta| < 3.2$).
- The forward calorimeter ($3.2 < |\eta| < 4.9$).

The fine segmentation of the EM calorimeter provides good and precise measurements of electrons and photons. And the coarser of the hadronic calorimeter is sufficient to satisfy the physics requirements for jets and missing energy transverse E_T^{miss} measurements.

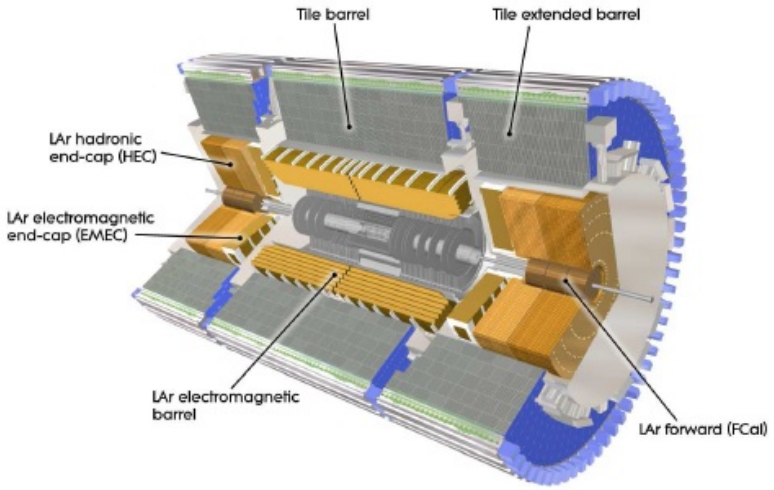

Figure 3.16: The ATLAS calorimeter system [29].

3.2.5.1 The EM calorimeters

An accordion design has been employed for the absorbers and the electrodes of the barrel and endcap electromagnetic calorimeters as shown in Figure 3.17. This design provides a full coverage in ϕ by avoiding the readout gap between the modules.

The detector is segmented into three longitudinal layers (Figure 3.18). The front one has the higher granularity and finely segmented along η with dimension $\delta\eta \times \delta\phi = 0.0031 \times 0.1$ in the barrel. For the middle layer, the largest fraction of the energy of the electromagntic shower is collected. The size of the cells is this layer is $\delta\eta \times \delta\phi = 0.025 \times 0.025$. The third layer is less segmented and collect the tail of the electromagnetic shower.

The absorber is made by lead plates with high density allowing the development of the electromagnetic showers, and the active medium is made by liquid argon. when an electron or a photon penetrates in the detector, it initiates an electromagnetic shower in the absorber (through the bremsstrahlung $e^{\pm} \longrightarrow e^{\pm}\gamma$ and conversion $\gamma \longrightarrow e^{+}e^{-}$ processes), thus creating secondary particles with lower energy, that will ionize the liquid argon. The ionization electrons drift and are collected by electrodes. The charge collected is converted into a current of intensity proportional to the deposited energy.

In front of these three layers, a thin presampler with $\delta\eta \times \delta\phi = 0.025 \times 0.1$ is used in the region $|\eta| < 1.8$ to quantify the energy losses before the calorimeter.

The barrel part is composed of two half barrels (cylinders) with internal radius of 1.4 m and external radius of 2.0 m and each half-barrel weighs 57 tons. The length of each half-barrel is 3.2 m.

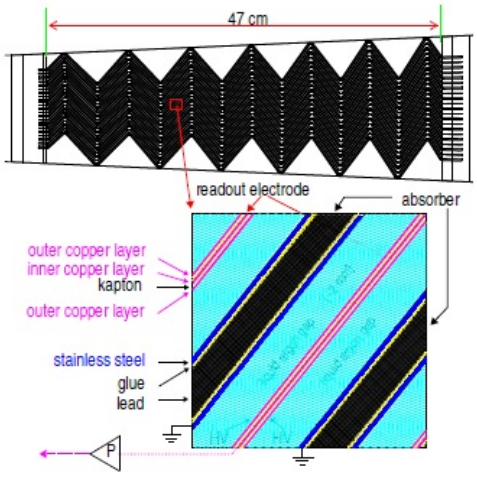

Figure 3.17: Accordion design of the EM calorimeter (up) and the arrangement of the different layers absorber, liquid argon and electrodes (down). The gap between layers is 2.1 mm in the barrel region and goes from 0.9 mm up to 3.1 mm in the end-cap regions [30].

A half-barrel is made of 1024 accordion-shaped absorbers, interleaved with readout electrodes. Each half-barrel has been divided into 16 modules. The thickness of a module is at least 22 radiation lengths (X_0). It varies depending on η and increases from 22 X_0 to 30 X_0 between $|\eta| = 0$ and $|\eta| = 0.8$ and from 24 X_0 to 33 X_0 between $|\eta| = 0.8$ and $|\eta| = 1.3$.

The end-caps are made of two concentric wheels. The boundary between the inner and the outer wheel, which is 3 mm wide and located at $|\eta| = 2.5$, is mostly filled with low density material. This boundary is approximately projective and matches the acceptance of the inner detector. The total active thickness of an end-cap calorimeter is greater than 24 X_0 except for $\eta < 1.475$.

3.2.5.2 The hadronic calorimeters

The goal of the hadronic calorimeter is to reconstruct and measure the energy of hadrons, i.e jets.
It is composed of three parts:

- The Tile Cal.
- The Liquid Argon hadronic end-cap calorimeter HEC.
- The liquid Argon forward calorimeter FCAL.

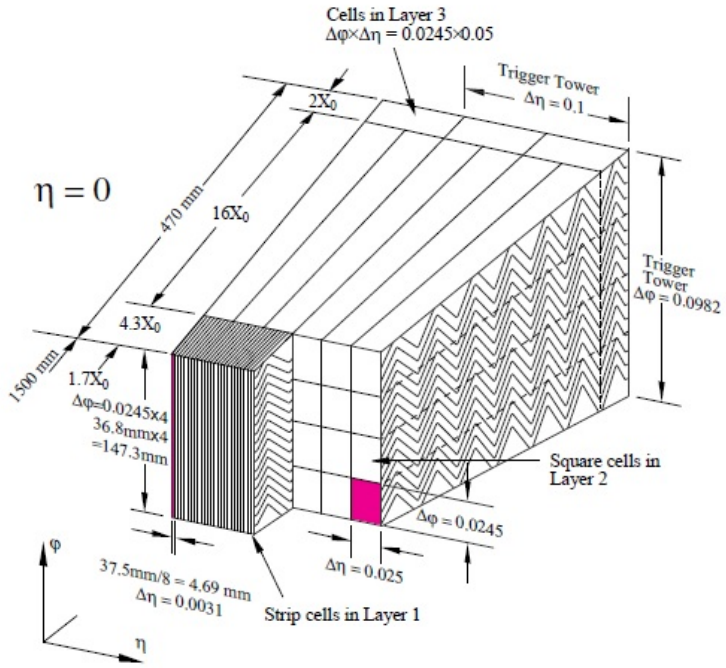

Figure 3.18: The barrel module with the three different layers with the granularity in η and ϕ of the cells [31].

The Tile Cal The hadronic tile calorimeter sits outside the EM calorimeter envelope [32]. It is made of a central barrel that use scintillator tiles and covering the region $|\eta|$ <1.0, and two extensions, also with scintillator tiles, and covers the region 0.8< $|\eta|$ <1.7. It use steel for the absorber part.
The total number of modules in the tile calorimeter is 64 with $\delta\phi = 0.1$ for each one. A module is shown in Figure 3.19.

The central barrel is 5.8 m long and the two extensions are 2.6 m. The tile calorimeter extends radially from an inner radius of 2.28 m to the outer one of 4.25 m.
It is segmented in depth in three layers, approximately 1.5, 4.1 and 1.8 interaction lengths (λ) thick for the barrel and 1.5, 2.6, and 3.3 λ for the extended barrel. The total depth is 7 λ which is enough to limit the hadronic leakage in the muon detectors.
When a charged particle penetrates the detector, the polystyrene doped with fluorine (tiles component) emits ultraviolet scintillation light. This light is collected on both sides with wave-length shifting fibers (WSF) that extract the signal to the back of the module. The fibers that belong to the same cell are grouped. The total light is then detected by a photomultipliers (PMT) which provides a current proportional to the energy deposited.

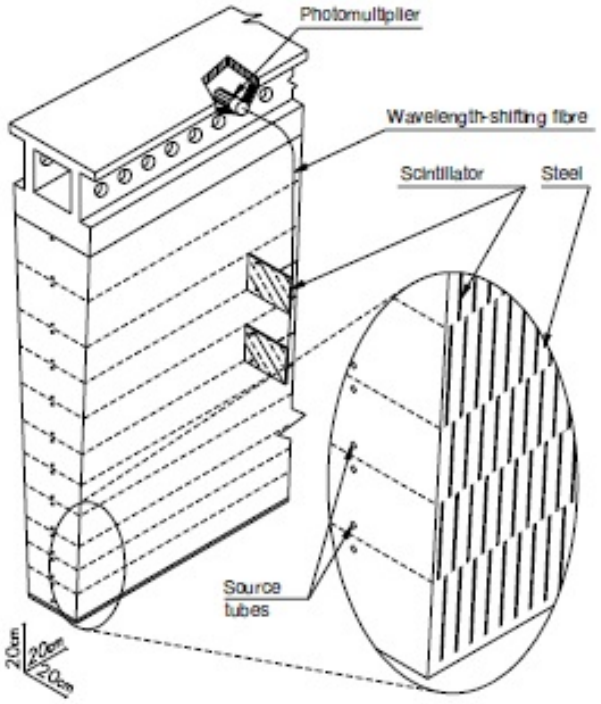

Figure 3.19: Diagram of a tile calorimeter module showing the arrangement of scintillator tiles and absorber.

HEC The hadronic end-cap calorimeter (HEC) [33] is located directly behind the electromagnetic calorimeter end-cap. Similarly to the EM end-cap, this sub-detector use the liquid argon as active medium. However, the absorber use copper and it has a classical sandwich design of parallel planes and perpendicularly to the beam.

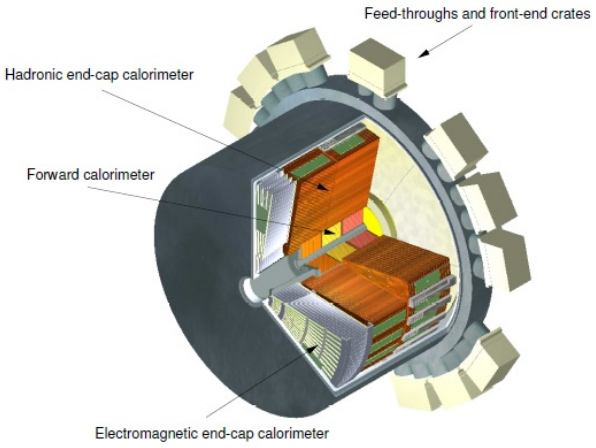

Figure 3.20: Diagram of the end-cap calorimeter showing the wheels of electromagnetic and hadronic end-caps, the forward calorimeter and the front-end electronics.

The HEC is formed by two wheels. Each wheels contain two layers. The wheels are cylindrical with an outer radius of 2030 mm. The HEC shares each of the two liquid-argon end-cap cryostats with the electromagnetic end-cap (see Figure 3.20). This detector covers the range $1.5 < |\eta| < 3.2$.

FCAL The forward calorimeter (FCAL) covers the region $3.1 < |\eta| < 4.9$. It allows to increase the hermiticity of the ATLAS detector by retrieving forward particles and thus improving the measurement of the missing transverse energy.
As shown in Figure 3.20, the FCAL is composed of three modules with 45 cm of thickness for each one. They are sampling calorimeters and use the liquid argon as active medium. The 1^{st} one uses copper as absorber for better energy resolution and the two others uses tungsten as absorber to obtain short and narrow showers. Each module consists of a metal matrix, with regularly spaced longitudinal channels filled with the electrode structure consisting of concentric rods and tubes parallel to the beam axis.
This structure allows for small gaps (~ 300 μm) to handle the large particle flux in the forward region.

3.2.6 The muon spectrometer

The muon spectrometer MS is designed to allow a precise measurement of muon momentum in a wide p_T range up to 1 TeV [34]. The expected resolution on the muon

momentum measurement is around 3% for a $p_T = 100$ GeV muon and increases up to 10% at 1 TeV. For low p_T muons, the precision comes essentially from the inner detector information.
The design is shown in Figure 3.21. It is composed of a barrel part for pseudorapidities up to 1.4 and an end-cap detector for the pseudorapidity range $1.6 < |\eta| < 2.7$. It is based on the magnetic deflection of muon tracks thanks to a toroidal magnetic field of about 0.5 T in the barrel and 1 T in the end-cap (curvature in R-Z plane). In the barrel part, the magnetic field is provided by 8 supraconducting coils and in the end-cap it is created by another coil system. In the transition region $1.4 < |\eta| < 1.6$, magnetic deflection is provided by a combination of barrel and end-cap fields.

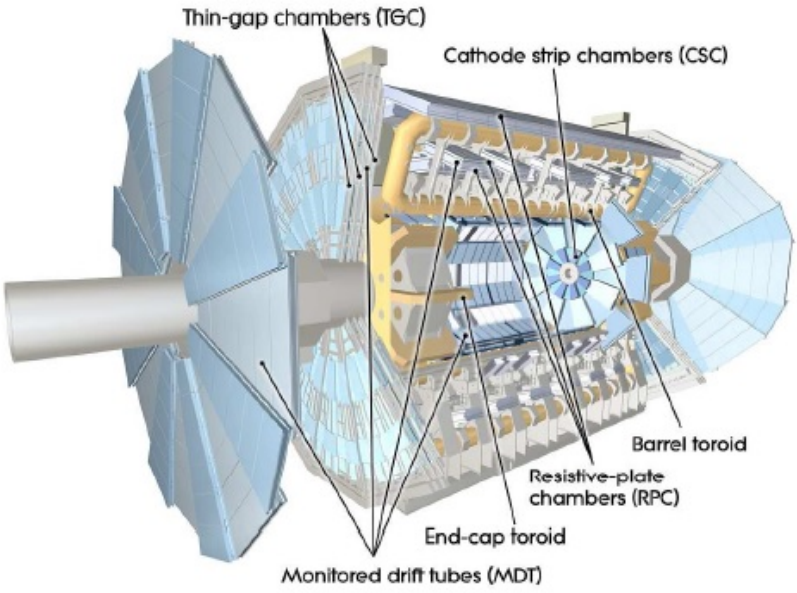

Figure 3.21: The muon spectrometer system.

As shown in Figure 3.21 and 3.22, there are four technologies of detectors used in the MS:

- The Monitored Drift Tubes (MDTs), used for precision measurements of the muon trajectory and momentum, and over the full range of the MS, $|\eta| < 2.7$. are made of several layers of 30 mm diameter tubes filled with gas with an anode in their centre. The position reconstruction is based on the drift time in the tube and a 80 μm resolution can be achieved with a single tube.
- The Cathode Strip Chambers (CSCs) deployed in the forward region $|\eta| > 2.0$ with higher granularity due to their higher resistance to high rates beam background.
- The Resistive Plate Chambers (RPCs), and the Thin Gap Chambers (TGCs), in the barrel and end-cap respectively, used in the hardware trigger where fast

processing is required.

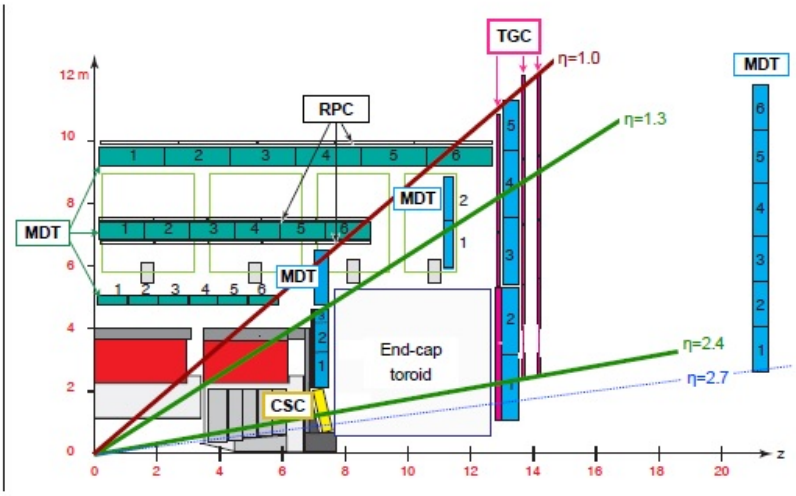

Figure 3.22: A diagram of the ATLAS muon system [35].

3.2.7 The trigger and data acquisition system

The trigger is the system allowing to reduce the amount of data produced by the pp collisions, given the fact that, at hadron colliders like the LHC, there is a huge amount of uninteresting events for physics searches (low p_T processes).
The computing resources of ATLAS do not allow to recorde all the raw data and then a selection has to be applied in order to keep only interesting events for physics. The goal is to maximize the acquisition efficiency of interesting events that will used in the analysis and reject the large number of so-called minimum bias events.
The ATLAS trigger system is subdivided into three levels: Level-1 (L1), Level-2 (L2), and event filter (EF). The L2 and event filter together form the High-Level Trigger (HLT). The output of the L1 trigger is limited to 100 KHz maximum to allow the High-Level triggers to treat properly the data.
One distinguishes two types of triggers: the online trigger which refers to the reconstruction and decision-making during the data taking, and the offline trigger where the nominal ATLAS reconstruction occurs on stored data.
During Run I, the input rate at the L1 trigger was about 20 MHz, reduced to about 75 KHz entering the HLT and the rate at the EF is about 700 Hz on average, so a factor of rejection of about 30000 [36] [37].
In Run II, the higher center-of-mass energy and higher luminosity lead to higher trigger rates. The input rate at the L1 trigger is 40 MHz, reduced to about 1 KHz entering the HLT and the output rate at the EF is about 1 KHz. A schematic of the trigger performance and data acquisition in Run II is shown in Figure 3.23.

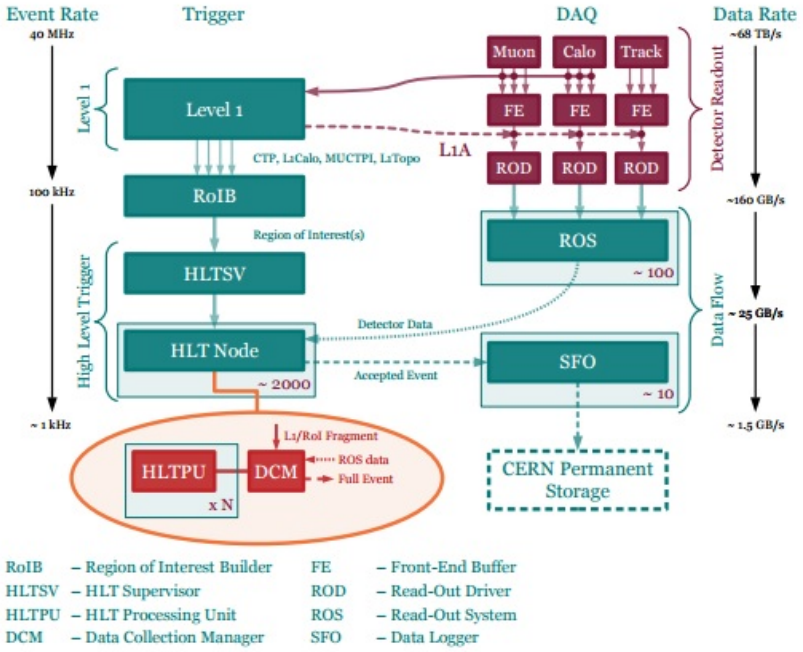

Figure 3.23: Schematic of ATLAS Trigger system and data acquisition for Run II [38].

- The level-1 trigger (L1)
  The L1 trigger performs the first event selection based on the calormeters and muons system informations. It makes a decision on whether to accept or reject an event within 2.5 μs
  The calorimeters information is based on all the components of this detector (electromagnetic and hadronic; barrel, end-cap and forward). It uses a coarse granularity ($\Delta\eta \times \Delta\phi = 0.1 \times 0.1$ for faster processing), as shown in Figure 3.24, to identify clusters compatible with an electron, a photon, a tau or a jet. Simple isolation conditions can be checked on these clusters. Finally, the total transverse energy of the event is also calculated.
  The L1 muon trigger is based on signals in the muon trigger chambers: RPC in the barrel and TGC in the end-caps. The trigger searches for patterns of hits consistent with high-p_T muons originating from the interaction region. A reconstruction of the muon parameters (p_T, η, ϕ) is made by reconstucting hits in these detectors as shown in Figure 3.25.
  The central processor of the L1 trigger has to identify for the L2 trigger the so-called regions of interest (RoI). These are regions of the detector where the L1 trigger has identified possible trigger objects within the event.

- The level-2 trigger (L2)
  The L2 trigger uses the RoI informations identified at the L1 trigger (in

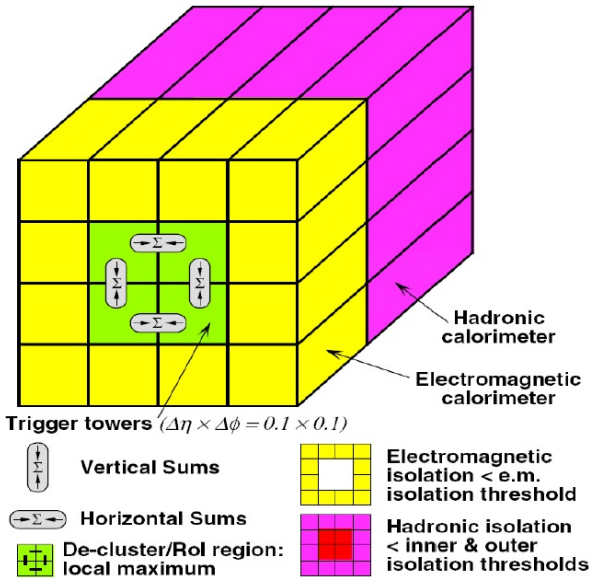

Figure 3.24: Schematic showing the calorimeter granularity at L1 trigger [39]

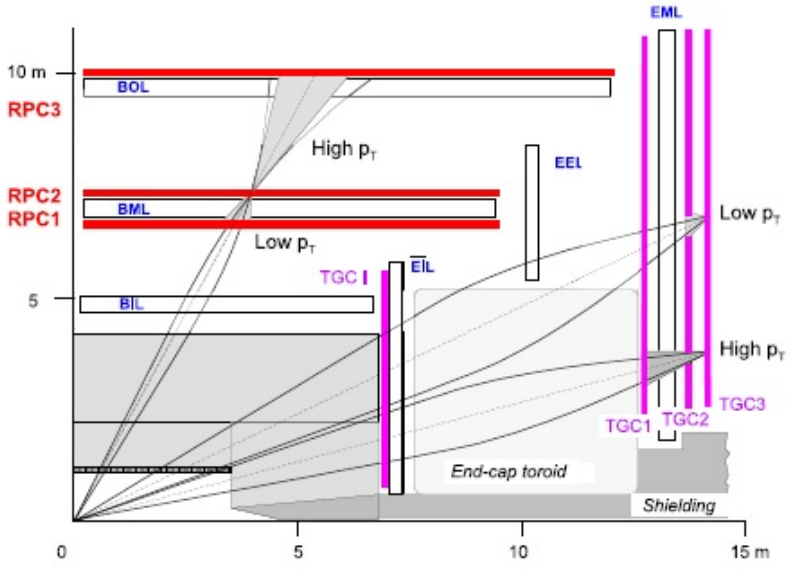

Figure 3.25: Schematic showing the L1 trigger for the muon detector.

addidtion to the tracker informations). This represent 1 to 2 % of the event data. The L2 trigger uses RoI information on coordinates, energy, and type of signatures to limit the amount of data which must be transferred from the detector readout. It is a software based trigger that reconstruct the objetcs in the RoI using dedicated algorithms, and using the full detector information, with an average event processing time of approximately 40 ms.

- The Event Filter (EF)
  The EF trigger analyse the events seeded by the L2 trigger. It is an offline software trigger that uses the standard reconstruction algorithms. It reduces the event rate to $\simeq$ 1000 Hz ($\simeq$ 700 Hz in Run I) and after the event is accepted by the EF, it is saved and ready to go to the full event reconstruction.

Trigger upgrade for Run II The ATLAS trigger system has been upgraded to cope with the new conditions of the LHC Run II [40] [41]. The increase in peak luminosity expected in Run II, as well as the increase in beam energy, is expected to lead to a factor of 5 increase in interaction rate (a factor of 2 from the luminosity and a rough factor of 2.5 from the increase in total cross-section). The higher interaction rates will directly impact the operation of the trigger: The Level 1 rate has been increased from 75 kHz to 100 kHz, and the HLT rate has been increased from $\sim$ 500 Hz to 1 kHz.

3.3 Conclusion

During LHC Run I, the ATLAS subdetectors operated with a high performance and the physics program yield was a real success. For Run II, and with all the new conditions of energy, pileup and events rates, major updates have been inluded in the detector and a new component has been added to the tracker system (the IBL). This new era of the LHC is a promising and exciting period in term of physics program given the new energy scale and the high luminosity achieved.

Bibliography

[1] L. Evans and P. Bryant, LHC Machine, Journal of Instrumentation 3 (2008) S08001. jinst.sissa.it/LHC/. 3.1 (Cited on page 48.)

[2] ALEPH, DELPHI, L3, and OPAL Collaborations, The LEP Working Group for Higgs Boson Searches, Phys. Lett. B565, 61 (2003). (Cited on page 48.)

[3] CDF and D0 Collaborations, Phys. Rev. D 88 ,052014 (2013). (Cited on page 48.)

[4] ATLAS Collaboration, The ATLAS Experiment at the CERN Large Hadron Collider , Journal of Instrumentation 3 (2008) S08003. jinst.sissa.it/LHC/. 3.1, 3.2.1, 3.2.1.1, 3.11, 3.15, 3.3 (Cited on page 48.)

[5] CMS Collaboration, The CMS experiment at the CERN LHC, Journal of Instrumentation 3 (2008) S08004. jinst.sissa.it/LHC/. 3.1 (Cited on page 48.)

[6] ALICE Collaboration, The ALICE experiment at the CERN LHC, Journal of Instrumentation 3 (2008) S08002. jinst.sissa.it/LHC/. 3.1 (Cited on page 48.)

[7] LHCb Collaboration, The LHCb Detector at the LHC, Journal of Instrumentation 3 (2008) S08005. jinst.sissa.it/LHC/. 3.1 (Cited on page 48.)

[8] C. Lefevre, LHC: The Guide, Brochure, 2009. 3.2, 3.1 (Cited on page 48.)

[9] CERN, The Accelerator Complex, home.web.cern.ch/about/accelerators, 2015. 3.1. (Cited on page 48.)

[10] http://press.web.cern.ch/backgrounders/lhc-season-2-facts-figures (Cited on page 50.)

[11] L. Evans and P. Bryant, LHC Machine, JINST 3 (2008) S08001 (Cited on page 51.)

[12] CERN, CERN releases analysis of LHC incident, CERN Press Release, 2008. 3.1.2 (Cited on page 51.)

[13] Proceedings of IPAC2014, Dresden, Germany, Analysis of the electron cloud observations with 25 ns bunch spacing at the LHC (Cited on page 52.)

[14] CERN, The first LHC protons run ends with new milestone, CERN Press Release, 2012. 3.1.2 (Cited on page 53.)

[15] ATLAS Collaboration, Luminosity public results, 2012. 3.3, 3.4 (https://twiki.cern.ch/twiki/bin/view/AtlasPublic/LuminosityPublicResults) (Cited on pages 53 and 54.)

[16] ATLAS Collaboration, Luminosity public results, LuminosityPublicResults, 2012. 3.3, 3.4 (https://twiki.cern.ch/twiki/bin/view/AtlasPublic LuminosityPublicResultsRun2) (Cited on page 55.)

[17] Workshop Physique Atlas France 2014, Talk of Andreas Hoecker "Trigger and Physics for Run-2", https://indico.cern.ch/event/318822/contributions/737623/ (Cited on page 56.)

[18] M. Shifman, LARGE EXTRA DIMENSIONS: Becoming acquainted with an alternative paradigm, Int.J.Mod.Phys. A25, 199 (2010), arXiv:0907.3074v2 (Cited on page 59.)

[19] A. Yamamoto et al., The ATLAS central solenoid, Nucl. Instrum. Meth. A 584 (2008) 53. (Cited on page 60.)

[20] ATLAS collaboration, ATLAS Inner detector: technical design report. 1, CERN-LHCC-97-016, http://cdsweb.cern.ch/record/331063; ATLAS Inner detector: technical design report. 2, CERN-LHCC-97-017, http://cdsweb.cern.ch/record/331064. (Cited on page 60.)

[21] ATLAS Collaboration, The ATLAS Inner Detetor commissioning and calibration, Eur.Phys. J. C 70 (2010),787-821 arxiv:1004.5293 [physics.ins-det] (Cited on page 61.)

[22] A.Andreazza, Status of the ATLAS Pixel Detector at the LHC and its performance after three years of operation, Proceeding of the 6^{th} International Workshop on Semiconductor Pixel Detectors for Particles and Imaging, PIXEL (2012) (Cited on page 61.)

[23] ATLAS Collaboration, ATLAS pixel detector electronics and sensors, JINST3(2008) P07007 (Cited on page 61.)

[24] H. Feick et E.R. Weber : Radiation-induced defects in oxygen-enriched silicon detector materials. NIM A : Accelerator, Spectrometers, Detectors and Associated Equipment, 473(1-2):114-118, 2001. Proceedings of the 9th International Workshop on Vertex Detectors. (Cited on page 63.)

[25] http://www.atlas.ch/news/2014/a-new-sub-detector-for-ATLAS.html (Cited on page 63.)

[26] A. Ahmad et al., The silicon microstrip sensors of the ATLAS semiconductor tracker, Nucl. Instrum. Meth. A 578 (2007) 98. (Cited on page 63.)

[27] ATLAS Collaboration, Particle Identification Performance of the ATLAS Transition Radiation Tracker, ATLAS-CONF-2011-128, 2011. 3.2.1.1 (Cited on page 64.)

[28] ATLAS Collaboration, ATLAS inner detector : Technical design report. Vol. 2, (1997), CERN-LHCC-97-17. (Cited on page 65.)

[29] G. Aad et al. (ATLAS Collaboration), The ATLAS Experiment at the CERN Large Hadron Collider, JINST 3, S08003 (2008). (Cited on pages 65 and 66.)

[30] A. Airapetian et al. (ATLAS Collaboration), ATLAS calorimeter performance Tech- nical Design Report, (1996), CERN-LHCC-96-40. (Cited on page 67.)

[31] ATLAS Public Results. LArCaloPublicResults twiki page. Twiki page. https://twiki.cern. ch/twiki/bin/view/AtlasPublic/LArCaloPublicResultsDetStatus. 2012 (Cited on page 68.)

[32] ATLAS collaboration, Tile calorimeter technical design report, CERN-LHCC-96-042, http://cdsweb.cern.ch/record/331062. (Cited on page 68.)

[33] [ATLAS Collaboration], ATLAS liquid argon calorimeter: Technical design report, CERN-LHCC-96-41 (Cited on page 70.)

[34] ATLAS Collaboration, Commissioning of the ATLAS Muon Spectrometer with Cosmic Rays, Eur. Phys. J. C70 (2010) 875-915, arXiv:1006.4384 [hep-ex]. cds.cern.ch/record/1275998. 3.2.3 (Cited on page 70.)

[35] ATLAS Collaboration, Performance of the ATLAS muon trigger in pp collisions at $\sqrt{s}$ = 8 TeV , arXiv:1408-3179 [hep-ex]. TRIG-2012-03. Submitted to Eur. Phys. J. 3.14, 3.3, 3.22 (Cited on page 72.)

[36] ATLAS Collaboration, TriggerOperationPublicResults, TriggerOperationPublicResults, 2015.3.3 (Cited on page 72.)

[37] ATLAS Collaboration (F. Pastore for the collaboration), the ATLAS Trigger System: Past, Present and Future, Proceedings of the 37^{th} International Conference on High Energy Physics, Nucl. Phys. B Proceedings Supplement 00 (2014) 1-7 (Cited on page 72.)

[38] Gorm Galster, ATLAS Trigger: Preparations for Run II, June 30, 2015. (Cited on page 73.)

[39] ATLAS Collaboration, Level-1 Trigger Technical Design Report, http://atlas.web.cern.ch/Atlas/GROUPS/DAQTRIG/TDR/tdr.html, 1998. 3.21 (Cited on page 74.)

[40] The ATLAS Trigger System, ATLAS Software and Computing Workshop, https://indico.cern.ch/event/352570/session/5/contribution/16/materiel/slides/0.pdf (Cited on page 75.)

[41] CERN Press, LHC Season 2: Major work at the experiments for Run 2, http://press.web.cern.ch/backgrounders/lhc-season-2-major-work-experiments-run-2 (Cited on page 75.)

Chapter 4

Data simulation and objects reconstruction

Contents

In this chapter, the reconstruction of physics objects in ATLAS needed for H $\longrightarrow \tau\tau$ analysis will be described.
A general overview on the Monte Carlo simulation chain is discussed first. The reconstruction process, from the information of the detector to the identification and measurement of final objects is described.

4.1 The simulation chain

The MC simulation [1] is an important and essential step in particle physics analysis. It aims at reproducing as well as possible the genuine pp collisions in ATLAS. It is show in Figure 4.1 and described as follows:

Events generation An events generator simulates the complete chain of a proton-proton collision and describe the interaction, including the hard scattering, hard scattering, hadronisation and underlying event.

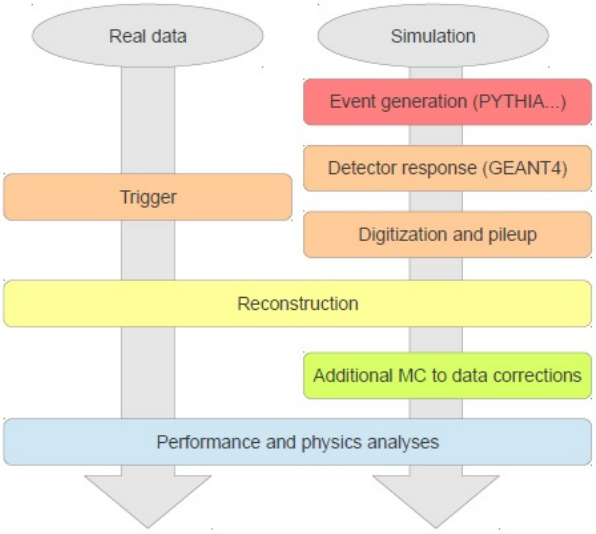

Figure 4.1: Analysis flow for real data and simulation events.

There are two approaches used in the generators. First, the matrix element computations (ME) for the hard scattering processes. It is a full calculation of Feynman diagrams for each perturbative order (Leading-order LO, Next to LO NLO,...). The alternative approach is called "Parton shower PS" which is a full LO calculation and then the PS calculation for higher order. It is a probabilistic method that uses Markov chain, and is useful for phase space regions where appear infrared and collinear divergence, but less efficient for the hard radiations.
Finally, since protons are made of many partons, a hard (or semi-hard) scattering can occur from the remnants of the protons and this is the so-called 'underlying event'.
Here are some examples of events generators used in particle physics:

- PYTHIA [2] [3]: It is a LO generator used for pp, $p\bar{p}$ and ep collisions. It

performs the event generation, the initial and final shower, the hadronization and the underlying event.

- POWHEG (Positive Weight Hardest Emission Generator) [4]: It is an NLO generator. It performs the generation of Higgs production modes gluon-gluon fusion and VBF. It is interfaced with Pythia to add the PS, the hadronization and underlying events.
- SHERPA [5]: The latest Sherpa version includes NLO calculations. This generator contains processes of the SM, the MSSM and extra-dimensions.
- MADGRAPH [6]: It is a generator that creates automatically the matrix elements and provides processes for SM and BSM phenomenology. The MadGraph5-aMCNLO program combines LO and NLO calculation from MadGraph5 and aMCNLO respectively.

Detector simulation Once the event is generated, the outgoing particles are passed through a simulation of the detector response to simulate the hits and energy deposits in the various part of the detector. In ATLAS, this is done in an integrated simulation framework (ISF) [8]:

- Full simulation (FullSim): Done using Geant4 [7] for all detector parts. It is a time-consuming method but very accurate.
- Fast simulation (ATLFAST-II): In order to overcome the computing limitations of full simulation imposed by the complicated detector geometry, fast simulation is needed. Its goal is to speed up the simulation process while allowing to run the standard ATLAS reconstruction.

ISF optimizes the computer resources by optimizing the relative use of fast and full simulation.

Digitization This step transforms the simulation hits into detector signal, similar to the one induced by real data. All this truth information is stored in the event and can, afterwards, be compared to the reconstructed data to study the detector performances.
A modeling of MC Pile-up is also needed for more accurate analysis. It is simulated at the digitization level using a list of Minimum Bias (MB) events generated with PYTHIA. The number of superimposed MB events is based on a Poisson distribution (function of luminosity).

Reconstruction The reconstruction is a set of software algorithms that run on data and Monte Carlo (MC) samples to convert the basic signals recorded by the detector into collections of measurements associated to particles produced in the collision. After digitization of simulated data, the reconstruction of physics objects is performed in the same way as for real data. More details on this reconstruction, used for Run II physics analysis, will be given on the following sections.

4.2 Tracks and vertex reconstruction

4.2.1 Tracks reconstruction

The reconstruction of charged tracks is used at multiple stages in the definition and the reconstruction of the physics objects used in the analyses [9] [10]. They are used as an input to the reconstruction of muons and electrons, and are an important ingredient for the calculation of lepton isolation, identification of b-quark jets, as well as for the pile-up suppression in jets.
In ATLAS, a track is reconstructed starting from clusters and space points defined using the information from the sub-detectors composing the inner detector. It is caracterized by a set of parameters in the transverse plane x-y.

- The curvature $\frac{q}{p}$: ratio between charge and momentum of particle.
- θ_0: the polar angle with the z-axis in the r-z plane.
- ϕ_0: the azimuthal angle with the z-axis in the r-z plane.
- d_0: the impact parameter in the transverse plane (its sign is opposite to the angular momentum of the track about the z axis.
- z_0: the impact parameter in the r-z plane.

The impact parameters d_0 and z_0 represent the minimum distance to the centre of the detector in the transverse plane and in the longitudinal direction respectively. Impact parameters and direction are expressed with respect to the main primary vertex in the event [12] [13].

To reconstruct a track, two approaches are used:

- Inside-out:
  The inside-out algorithm performs the search for a track and its reconstruction starting from the pixel layers and adding hits from the other detectors moving away from the interaction point. It is designed for the efficient reconstruction of primary charged particles. In this approach, a track seed is formed using a combination of space points from three pixel layers and the first SCT layer and then extended to all the other SCT layers in order to search for additional hits. The hits are ranked in three ways: a hit with good properties, an outlier that provides a reduction of the fit quality and a hole, a hit not found when expected. According to this classification, a track candidate has to satisfy a set of quality cuts. An example of some of these cuts used is shown in Table 4.1 [14]. At the next stages, the ambiguities between the tracks are resolved (by placing a score on the track quality) and more refined fitting is performed. It includes global χ^2 and Kalman-fitting techniques. In the final stage a track is completed with the TRT hits.

Cut	Value
Minimum p_T	400 MeV
Maximum η	2.5
$N_{SCThits}$	$\geqslant 7$
$N_{SharedHits}$	$\leqslant 1$
$N_{SCTholes}$	$\leqslant 2$

Table 4.1: Example of some tracking cuts of the inside-out algorithm for loose selection. A shared hit is either a hit in the pixel detector which is used by more than one track, or in the case of the SCT two shared hits in the same SCT layer. [14].

- Outside-in:
  It is a complementary track-finding algorithm [14], called back-tracking used to reconstruct secondary particles that result from interactions (photon conversion for example) or decays of primary particles or decays of other secondaries. This algorithm allows to reconstruct long-lived particles which may not leave any hits in the Pixel Detector. In this case, there is no seed for the inside-out algorithm. It searches for unused track segments in the TRT. Such segments are extended into the SCT and pixel detectors to improve the tracking efficiency for secondary tracks.

  A second inside-out algorithm with looser requirements on pattern recognition is executed after the back-tracking in order to recover tracks with $p_T > 150$ MeV (low p_T tracking).

4.2.2 Vertex reconstruction

:

The location of the hard pp collision, the origin of the particles produced in the collision, is called primary vertex (Figure 4.2).

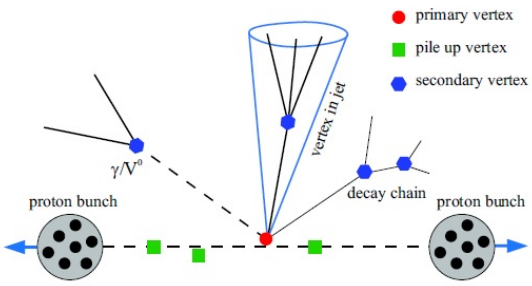

Figure 4.2: Different vertices in ATLAS.

Two algorithms are used to identify the vertices [13]:

- The vertex finding algorithm:
  it associates tracks to the vertex candidate. It selects the reconstructed tracks that are consistent with originating from the interaction region and selects a vertex seed based on different criteria:

  $p_T > 400$ MeV.
  $d_0 < 4$mm, $\sigma(d_0) < 5$mm and $\sigma(d_0) < 10$mm.
  4 associated hits in the SCT.
  6 silicon (pixel+SCT) hits.

- The vertex fitting algorithm:
  It takes as an input the seed position and the tracks around it and performs a χ^2 based fit. Any track that does not satisfy the fit is then used to set a new seed and the procedure starts again until no tracks are left. It is clearly possible that an event has more than one vertex: in this case, the primary vertex is defined as the one that has the highest sum of p_T^2 of the associated tracks [15].

4.2.3 Tracks and vertex reconstruction performances in Run II

Figure 4.3 shows the primary track reconstruction efficiency parametrized in two-dimensional bins of p_T and η. This quantity, ε_{trk} is determined from the simulation and defined as:

$$\varepsilon_{trk}(p_T, \eta) = \frac{N_{rec}^{matched}(p_T, \eta)}{N_{gen}(p_T, \eta)} \tag{4.1}$$

where p_T and η are generated particle properties, $N_{rec}^{matched}(p_T, \eta)$ is the number of reconstructed tracks matched to a generated charged particle and $N_{gen}(p_T, \eta)$ is the number of generated charged particles in that bin.
As we can see in the Figure 4.3 (Left), The track reconstruction efficiency is lower in the region $|\eta| > 1$ due to particles passing through more material in that region. The slight increase in efficiency at $|\eta| \backsim 2.2$ is due to the particles passing through an increasing number of layers in the ID end-cap.

As mentioned before, a new layer in the pixel detector, the IBL was inserted. Figure 4.4 shows the improvement of the transverse impact parameter resolution ($\sigma(d_0)$) between the 2012 data and the 2015. We see the clear gain thanks to the IBL usage.

In a high pile-up scenario the detector occupancy increases and this affects the number of reconstructed tracks without corresponding primary or secondary particles, called fake tracks. The dependance of the number of reconstructed tracks as a function of the number of interaction per beam crossing is shown in Figure 4.5.

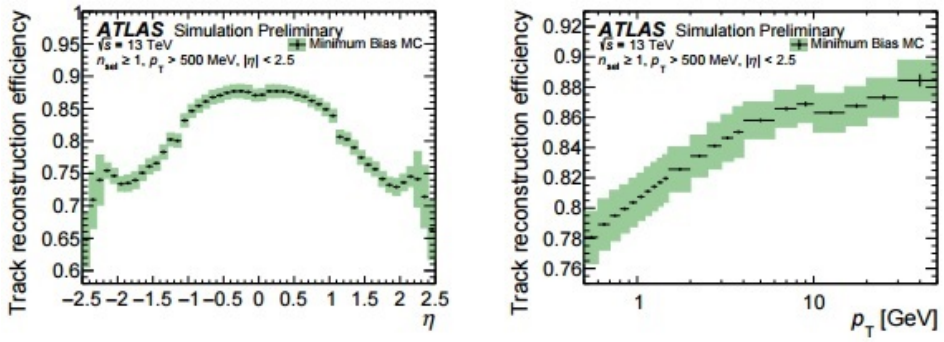

Figure 4.3: The track reconstruction efficiency as a function of η (Left) and p_T (Right) [16].

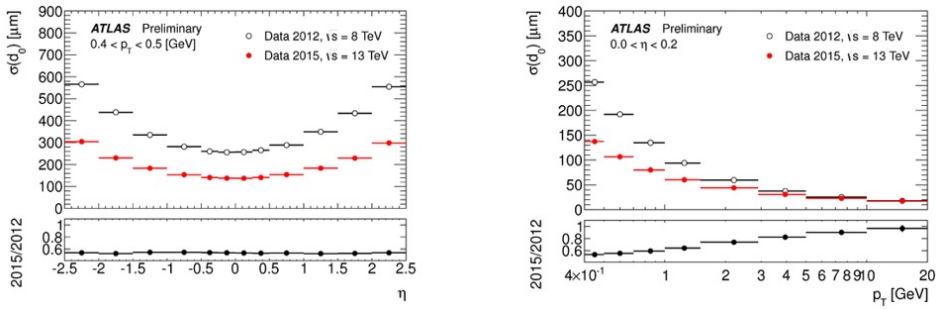

Figure 4.4: The transverse impact parameter resolution in 2015 (with IBL) and 2012 (without IBL) as function of η (Left) and p_T (Right) [17].

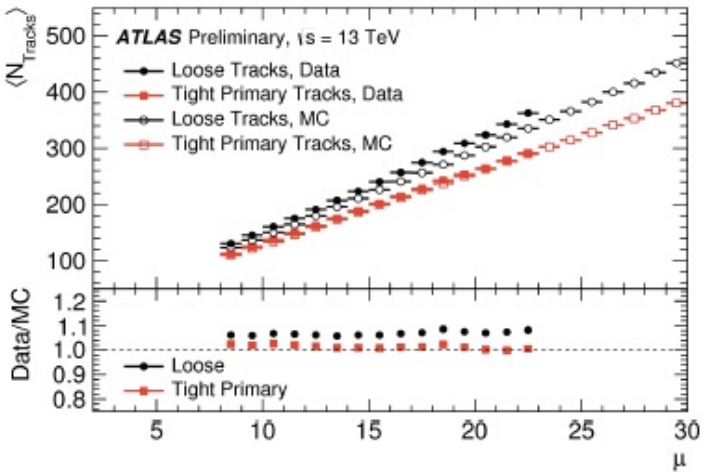

Figure 4.5: Average number of reconstructed tracks as a function of μ for data and MC with loose and tight selections [17].

The vertex reconstruction efficiency is determined from data by taking the ratio between events with a reconstructed vertex and events with at least two reconstructed tracks. Concerning the dependence of the vertex reconstruction on pile-up conditions, as the number of interaction per bunch crossing increase, the fraction of fake tracks increase. This implies the degradation of the vertex reconstruction efficiency at high value of $< \mu >$.

4.3 Electrons and photons

4.3.1 Reconstruction

The electrons and photons reconstruction algorithm starts from an energetic cluster in the electromagnetic calorimeter (ECAL). For an electron, once an EM cluster is identified, a search for an associated track in the inner detector (ID) is performed. Using informations from both ECAL and ID allows the reduction of noise and a good separation between electrons and photons [21] [22].
The reconstruction algorithm is a "sliding window" algorithm [23] used for the central part of the detector ($|\eta| < 2.47$). It is based on summing energy deposits in cells within a fixed-size rectangular window (3×5 cells in $\eta \times \phi$, with each cell having a size of $\Delta\eta \times \Delta\phi = 0.025 \times 0.025$). The seed clusters are required to have a transverse energy above 2.5 GeV and the final cluster size is defined by a collection of seed clusters with a typical size of 3×7 longitudinal towers in $\eta \times \phi$ in the barrel and 5×5 towers in the end-caps. After building the clusters, duplicates from neighboring seeds are removed by the algorithm.
From the inner detector, tracks with a transverse momentum greater than 0.5 GeV are extrapolated to the middle layer of the EM calorimeter associated to the EM cluster. A cluster-track matching is then performed. The matching criteria are very loose, since they have to take into account all the radiative effects, such as bremsstrahlung for high energy electrons. These losses in energy can change the trajectories of the electrons across the magnetic field. In the fitting track procedure used in ATLAS, electrons are reconstructed using the Gaussian Sum Filter (GSF) algorithm [24] which takes into account the non-Gaussian noise by modeling it as a weighted sum of Gaussian components. In an event, all tracks with transverse momentum $p_T > 400$ MeV and $|\eta| < 2.5$ that are identified as electrons can be refitted. The redefined track parameters are then used in the matching with the calorimeter clusters. If a track matches the cluster within a $\Delta\eta \times \Delta\phi$ of 0.05×0.10, the object is considered as an electron (or converted photon). Otherwise, it is considered to be an unconverted photon.
The EM is optimized to minimize the lateral leakage of energy lost by the particle, without adding too much electronic noise to the cluster. Basically, unconverted photons clusters are smaller than electrons (or converted photons) in the ϕ direction due to the bending of tracks in the magnetic field from the Inner Detector and bremsstrahlung radiations that expand the electrons clusters. This argument is not

valid for the end-caps region and a fixed window size is used.
From the reconstruction stage, two object "containers" are created: one for electrons and one for photons. From now on, let's concentrate on electrons for analysis.

4.3.2 Electron identification

In addition to true electrons, one is left with jets/hadrons or photons faking electrons. To reduce this fake rate, further identification criteria are applied to the track and the cluster shower of the electron candidate [22].
Three identification criteria, called working points, are defined: loose, medium and tight. Each one is based on a set of selections and provides different electron efficiency and jet rejection (ε,Rej). These working points, described hereafter, are ordered according to the decreasing of signal efficiency and thus increasing of background rejection.

- Loose: uses cuts on the shower shape in the middle layer of the EM calorimeter (lateral shower shape and width) and cuts on the hadronic leakage (the ratio of the E_T in the first compartment of the HCAL and in the ECAL). It provides the best efficiency but the lowest background rejection.

- Medium: in addition to the loose criteria, this selection includes cuts on the shower shape based on the first layer of the EM calorimeter. Cuts on the track quality from the inner detector are used, in particular on the number of hits in the Pixel and SCT subdetectors and on the transverse impact parameter d_0. The medium selection increases the jet rejection by a factor 3-4 with respect to the loose identification and reduces the selection effciency by $\sim$ 10 %.

- Tight: on top of the medium selection, additional cuts on the tracking variables are applied (on the hits in the b-layer of the inner detector, the transverse impact parameter, and the matching between cluster and track). Additional isolation cut is applied to the cluster using all cell energies within a cone of ΔR < 0.2 around the electron candidate.
  This working point is the best compromise between the electron identification and jet rejection.

Electrons Isolation In addition to these identification criteria, electrons are required to be isolated to further reduce the rate of hadrons/jets being mis-identified as electrons.
There are two types of isolation variables:

- Calorimeter Isolation: etCone30, (etCone20) is the sum of the transverse energy of topological clusters calibrated at the electromagnetic scale within a cone of radius ΔR = 0.3 (0.2) around the lepton.

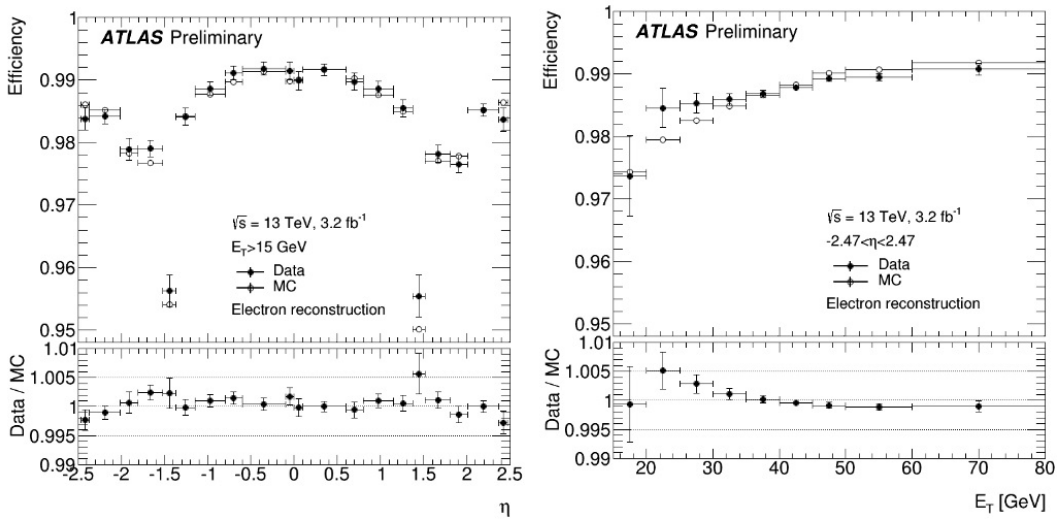

Figure 4.6: The electron reconstruction efficiency as a function of η (left) and E_T (right) using Z $\longrightarrow$ ee and $J/\psi \longrightarrow$ ee samples [26].

- Track Isolation: ptCone30 (ptCone20) is the sum of the transverse momenta of tracks with $p_T > 400$ MeV found within a cone of radius ΔR = 0.3 (0.2) around the lepton.

There are seven defined isolation selection criteria (isolation working points). Each optimised for different physics analyses (LooseTrackOnly, Loose, Tight, Gradient, GradientLoose, FixedCutTightTrackOnly, FixedCutLoose).

Finally, for more accurate measurement of the energy from the EM calorimeter, further energy calibration is applied. The energy response of electrons is calibrated in several steps using a combination of MC-based and data-driven methods [25].

4.3.3 Performances

The reconstruction and identification electron efficiencies are measured using a tag-and-probe method using Z $\longrightarrow$ ee and $J/\psi \longrightarrow$ ee samples as described in [22]. Figure 4.6 (left) shows the reconstruction efficiency as a function of the transverse energy E_T integrated over the full pseudo-rapidity range. This is measured using the data recorded by ATLAS in 2015. The reconstruction efficiency as a function of the pseudo-rapidity η is shown in the left plot for $E_T > 15$ GeV [26].

The identification efficiency is shown in Figure 4.7 as a function of η (left) and the transverse energy E_T (right) for the different identification working points (loose, tight and medium). The integrated efficiency over η and E_T are $\sim 95\%$, 90% and 85% for the loose, medium and tight operating points respectively.

A difference in the measured efficiency between data and MC can be observed for the reconstruction and identification efficiency due to the known mismodeling of shower shapes and other identification variables in the simulation. This difference results in the use of a scale factor (SF) which corrects the MC simulation for what

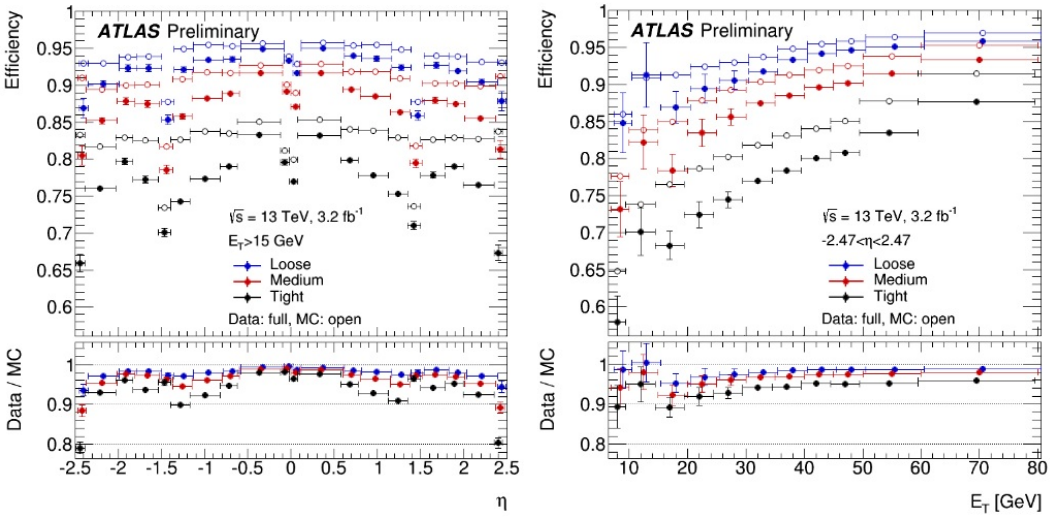

Figure 4.7: The electron identification efficiency as a function of η (left) and E_T (right) for the data recorded by ATLAS in 2015, for the three identification working points (loose, medium and tight), and for data (full circles) and MC (open circles) [26].

is actually observed in data. It is close to 1 with deviations larger than a couple of percent occurring only for low E_T or high η regions.

4.4 Muons

4.4.1 Reconstruction

As explained in the previous chapter, the muon spectrometer (MS) is designed to detect muons after they traverse all other subdetectors. The inner detector (ID) and the calorimeter informations are also used for muon reconstruction. First, the reconstruction is performed independently in the ID and the MS. A combination of the information from each component is then performed in order to provide the best performance in terms of resolution over the entire p_T range.

Depending on which subdetectors are used in the reconstruction, one distinguishes 4 types of muons [27]:

- Combined (CB) muons: the muon track is reconstructed using the MS and the ID. The informations from both detectors are then combined using a global refit that uses hits from the two subdetectors. Most of these muons are reconstructed first in the MS and then extrapolated back to match an ID track. The inverse is used as a complementary approach. The muon momentum is defined as a weighted combination of the two momenta measured by the MS and the ID. These muons cover the $|\eta|$ region below 2.5 given the limited

acceptance of the ID. They are the standard muon objects for physics analysis and provide candidates of highest purity.

- Extrapolated (ME) muons: The muon track is reconstructed using only the MS and then extrapolated to the beam line to define the track parameters and momentum, taking into account the energy losses in the calorimeters. To perform a track measurement, the muon is required to traverse 2 layers of the MS chambers (3 layers in the forward region). These muons are used to extend the muon reconstruction acceptance into the region not covered by the ID ($2.5 < |\eta| < 2.7$).

- Segment-tagged (ST) muons: when a track from the ID is found to be matched to at least one local track segment in the Monitor Drift Tubes (MDT) or the Cathod Strip Chambers (CSC) when extrapolated to the MS, it is tagged a ST muon. This algorithm is used for low p_T muons and/or for muons that fall in regions with reduced MS acceptance.

- Calorimeter-tagged (CT) muons: if a track reconstructed in the ID is matched to an energy deposit in the calorimeter compatible with a minimum-ionizing particle, it is identified as a muon. Although this type of muons has the lowest purity with respect to all other muon types, it allows to recover acceptance in the region with no MS coverage. The identification criteria for these muons are optimized for that region ($|\eta| < 0.1$) and a momentum range of $15 < p_T < 100$ GeV.

4.4.2 Identification

In order to identify prompt muons and suppress background, mainly from light hadron decays, a set of quality requirements is applied.
For CB muons, the identification uses the following variables:

- $\frac{q}{p}$: the absolute value of the difference between the ratio of the charge and momentum of the muons measured in the ID and MS divided by the sum in quadrature of the corresponding uncertainties.

- ρ': the absolute value of the difference between the transverse momentum measurements in the ID and MS divided by the p_T of the combined track.

- normalised χ^2 of the combined track fit.

- requirements on the number of hits in the ID and MS are used.

There are four muon identification working points [27]:

Loose this criteria maximize the reconstruction efficiency keeping a good quality muon track. All the muon types are used and about 97.5 % of the loose muons are CB muons in the region $|\eta| < 2.5$. All CB muons satisfying the medium requirements are included in the loose selection.

Medium It is the default working point for muons in ATLAS. Only CB and ME muon candidates are used. There is a specific requirement for each type of these two types of candidates according to the number of hits in the MS. To supress contamination from hadrons misidentified as muons, a loose selection on the compatibility between ID and MS momentum measurements is applied.

Tight It is the category with the best purity of muons with loss of some efficiency. Only CB muons satisfying the medium selection criteria and with hits in at least two stations of the MS are considered. Additional cuts on χ^2, $\frac{q}{p}$ and ρ' are applied.

High-p_T this selection is performed to maximize the momentum resolution for tracks with transverse momentum above 100 GeV. This is optimized for high mass Z' and W' resonances searches [28]. The selection includes CB muons passing the medium selection and having at least three hits in three MS stations.

4.4.3 Isolation

As for electrons, the muon isolation is a powerful tool to reject background in many physics analysis. Muon coming from heavy particles decays (W, Z or Higgs boson) are isolated and well separated from other particles, unlike muons from semileptonic decays, which are often embedded in jets.
There are two variables for muon isolation, $P_T^{varcone30}$ and $E_T^{topocone20}$, defined similarly as for electrons as described in Section 4.3.2.

- $P_T^{varcone30}$: it is a track-based isolation variable defined as the scalar sum of the transverse momenta of the tracks with $p_T > 1$ GeV in a cone of size ΔR around the muon, excluding the muon track itself. (ΔR is p_T-dependent to improve the performance for muons produced in the decay of particles with a large transverse momentum).
- $E_T^{topocone20}$: it is a calorimeter-based isolation variable defined as the sum of the transverse energy of topological clusters in a cone of size $\Delta\text{R} = 0.2$ around the muon, after subtracting the contribution from the energy deposit of the muon itself and correcting for pile-up effects.

The isolation selection criteria are determined using the relative isolation variables, which are defined as the ratio of the track- or calorimeter-based isolation variables to the transverse momentum of the muon. As for electrons, there are the same seven isolation working points, each optimized for different physics analyses.

4.4.4 Reconstruction efficiency

The muon reconstruction efficiency is the product of the reconstruction efficiency in the ID, the reconstruction efficiency in the MS, and the matching efficiency between

the ID and MS measurements [27].

As for electrons, a tag-and-probe method is used to measure the efficiency for muons in the acceptance covered by the ID ($|\eta| < 2.5$). Muon samples from $Z \longrightarrow \mu\mu$ for muons with $p_T > 10$ GeV are used ($J/\Psi \longrightarrow \mu\mu$ for low p_T muons).
In this method, the tag muon is identified as a medium muon that fires the trigger, and the probe muon is then scrutinized to study performances. A selection based on the event topology is used to reduce the background contamination.
To measure the muon efficiencies, three kinds of probes are used. To measure the efficiency in the MS, ID tracks and CT muons can be used. Compared to ID tracks, CT muons offer a more powerful rejection of backgrounds, especially at low transverse momenta, and are therefore the preferred probe type for this part of the measurement, and ID tracks are used as a cross-check and for measurements not directly accessible to CT muons. To measure the complementary efficiency of the muon reconstruction in the ID, MS tracks are used.
To measure the efficiency for medium, tight and High-p_T muons, two stages are needed:

- ε(X|CT): where X = Medium/Tight/High-p_T. It is the efficiency of reconstructing these muons in MS assuming a reconstructed ID track is measured using a CT muon as probe.
- ε(ID|MS): the efficiency of the ID track reconstruction, measured using MS probes.

The efficiency is then expressed as: $\varepsilon(\text{X}) = \varepsilon(\text{X|CT}) \ . \ \varepsilon(\text{ID|MS})$.

The muons selected by the loose identification requirements are decomposed into two samples: CT muons within $|\eta| < 0.1$ and all other muons. The CT muon efficiency is measured using MS probe tracks, while the efficiency of other muons is evaluated using CT probe muons in a way similar to the medium, tight, and High-p_T categories.
The level of agreement between measured muons efficiency on data ε^{Data} and predicted muon effciencies on simulation ε^{MC} is evaluated, and the ratio of these two numbers is called "efficiency scale factor" (SF). It describes the deviation of the simulation from the real detector behavior, and is of particular interest for physics analyses. Figure 4.8 shows the muon reconstruction efficiency as a function of η measured using $Z \longrightarrow \mu\mu$ samples for the different muon selections [27].

4.5 Jets

High energy quarks and gluons produced from the interactions between partons during the pp collision radiate other quarks and gluons, which then hadronize into mesons or baryons. A jet is a cluster of many of these particles produced by the

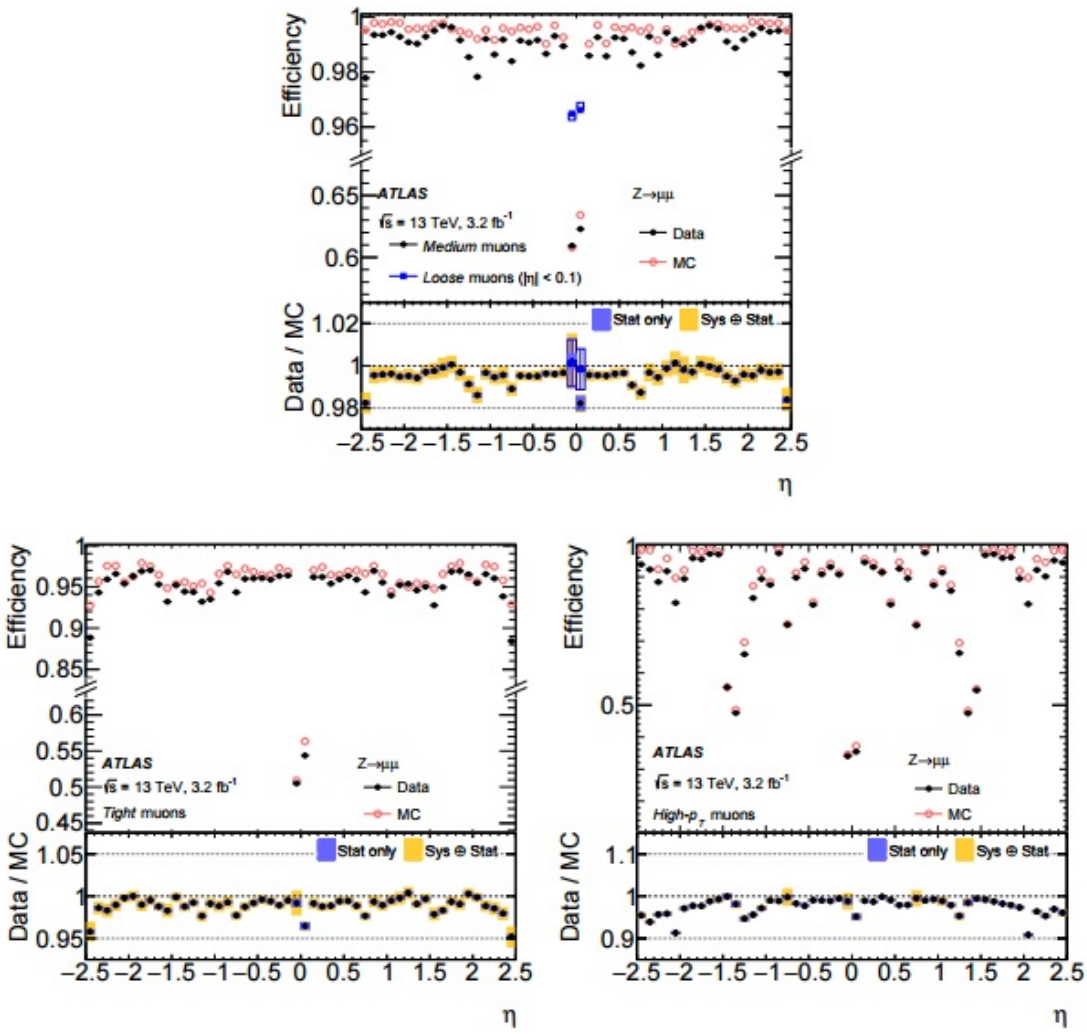

Figure 4.8: Muon reconstruction efficiency as a function of η for muons with $p_T >$ 10 GeV using Z $\longrightarrow \mu\mu$ sample, shown for medium and loose (top), tight (bottom left), and High-pT (bottom right) muon selections. In addition, the top plot also shows the efficiency of the loose selection (squares) in the region $|\eta| < 0.1$ where the loose and medium selections differ significantly. Data is in black, MC in red [27].

hadronisation of initial quarks and gluons coming from the hard scattering. Figure 4.9 illustrates the jet formation in a pp collision.

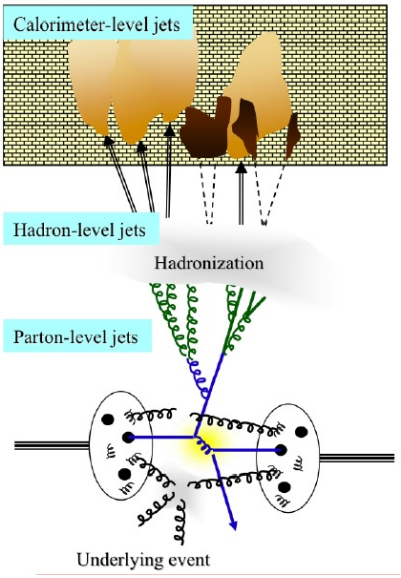

Figure 4.9: Jet formation in the pp collision in ATLAS.

The jet signature in the detector is formed of clusters in the calorimeters and of non-isolated tracks in the Inner Detector. In the jet reconstruction algorithm, it is important that the kinematic properties of the reconstructed jet match as closely as possible those of the original quark or gluon.

4.5.1 Reconstruction

There is a variety of algorithms to reconstruct a jet. The basic one is the fixed cone algorithm that consists in moving a fixed size cone on the calorimeter surface to find area with maximum energy. It was found to be infrared unsafe [29] [30] which means that if a soft gluon is emitted between two partons, the reconstructed jet will change.

In ATLAS, the soft and collinear safe anti-k_t jet clustering algorithm is used [31]. This algorithm uses as input topological clusters, called proto-jets, and the objects are reconstructed by grouping together calorimeter cells with energy greater than 4σ where σ represent the mean electronic and pile-up noise in the electromagnetic calorimeter. It is based on the sequential recombination of the input objects based on a distance between them, d_{ij} , and a distance between the beam and the object, d_{iB}:

$$d_{ij} = min(\frac{1}{k_{iT}^{2p}}, \frac{1}{k_{jT}^{2p}})\frac{\Delta R_{ij}^2}{R^2} \tag{4.2}$$

$$d_{iB} = \frac{1}{k_{iT}^{2p}} \tag{4.3}$$

where R is the radius parameter (cone size) set to 0.4, k_{iT} is the transverse momentum of an object i, $\Delta R_{ij}^2 = (y_i^2 - y_j^2) + (\phi_i^2 - \phi_j^2)$is the distance between i and j measured using the rapidity y.
When calculating the minimum of all d_{ij} and d_{iB}, if d_{ij} is found to be the smallest distance, object i and i are combined together and their quadrivectors combined to form a new proto-jet. While if d_{iB} is selected as minimum, the object i is called a jet and removed from the list of input objects.

The key feature of the anti-k_t algorithm is that soft particles will tend to cluster with hard ones, rather than among themselves, so soft particles do not modify the shape of the jet (infrared safety).

4.5.2 Calibration

The goal of the jets calibration is to infer the initial parton energy from the reconstructed jet energy. This correction, so-called jet energy scale (JES) correction, is done at different levels:

Calibration at parton level this calibration applies corrections from physical sources, like the hadronisation, the initial and final radiations,...

Calibration at particle level this calibration takes into account the detector effects, such as the different calorimetric response between hadrons and electromagnetic particles (electrons and photons), the loss in the transition (or dead) detector region, etc... Jets contain $\sim$ 60 % of hadronic charged particles ($\pi^{\pm}$, $K^{\pm}$), 25 % of photons (mainly from π^0 decay) and 10 % protons and neutrons. The main part of the energy is deposited in the EM calorimeter, and since the electromagnetic energy scale is not suitable for hadrons, energy corrections have to be applied. Therefore, the topoclusters are reconstructed at the EM scale and are later calibrated using the Local Custer Weighting (LCW) [32] method to improve the resolution. This method labels first the topoclusters as either electromagnetic or hadronic, based on the measured energy density and the longitudinal shower depth. Energy corrections are derived according to this classification from single charged and neutral pion Monte Carlo simulations.

Calibration of the energy scale (JES) As shown in Figure 4.10, the jets, already calibrated at particle scale (EM or LCW), undergo additional corrections to obtain the final jet energy. This is done in different steps:

- The calibration by applying a correction to account for the energy offset caused by pile-up interactions. This correction is obtained from Monte Carlo

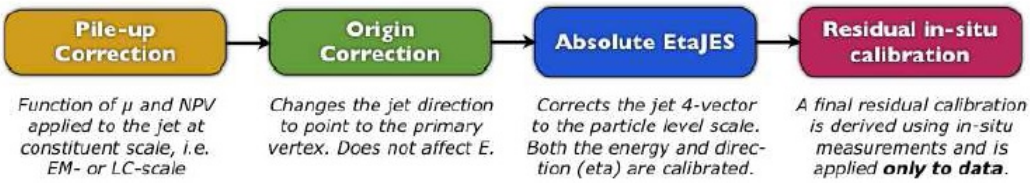

Figure 4.10: Jet energy calibration chain.

simulations as a function of the number of primary vertices in the event and $< \mu >$, in bins of jet p_T and $|\eta|$.

- The jet direction is corrected such that the jet points back to the reconstructed primary vertex instead of the geometrical centre of the ATLAS detector.
- A Monte Carlo based p_T and $|\eta|$ dependent calibration is then applied to the jets to bring the measured jet p_T to the truth jet energy (particle level in the simulations). Figure 4.11 illustrates the average energy response R(p_T,η) = $\frac{p_T^{EM/LCWjet}}{p_T^{truth}}$ (the inverse of the jet calibration correction), for various jet energies as a function of the jet rapidity [33]. These corrections can be applied to jets formed from topoclusters at EM or LCW scale with the resulting jets being referred to as calibrated with the EM+JES or LCW+JES scheme.
- As a last step, to consider the differences between data and Monte Carlo, a residual correction is applied to jets reconstructed in data (in-situ calibration).

4.5.3 Jet quality

In Run I analysis, in order to reject pile-up jets, a cut on a variable called Jet Vertex Fraction (JVF) is applied [34]. It is defined as the sum p_T of all tracks from the primary vertex matched to a jet divided by the total jet-matched track p_T from all vertices (a track is considered matched to a jet if the angular distance to the jet direction ΔR is smaller than 0.4). For the 2012 dataset, the selection on the jets required |JVF| > 0.50. The cut is applied only to jets with p_T < 50 GeV since the pile-up contribution at high p_T is negligible and with $|\eta| < 2.4$ since tracking information is required.
For Run II analysis, two new variables are used for this purpose [35]. The corrJVF which is a variable similar to JVF, but corrected for the NV_{tx} dependent average scalar sum p_T from pileup tracks associated to a jet, and the variable R_{pT} which is defined as the scalar p_T sum of the tracks that are associated to the jet and originate from the hard-scattering vertex divided by the fully calibrated jet p_T, which includes pileup subtraction.
These two variables are used to reconstruct a new discriminant called the jet-vertex-tagger (JVT) as a 2-dimensional likelihood based on a "k-nearest neighbor" (kNN)

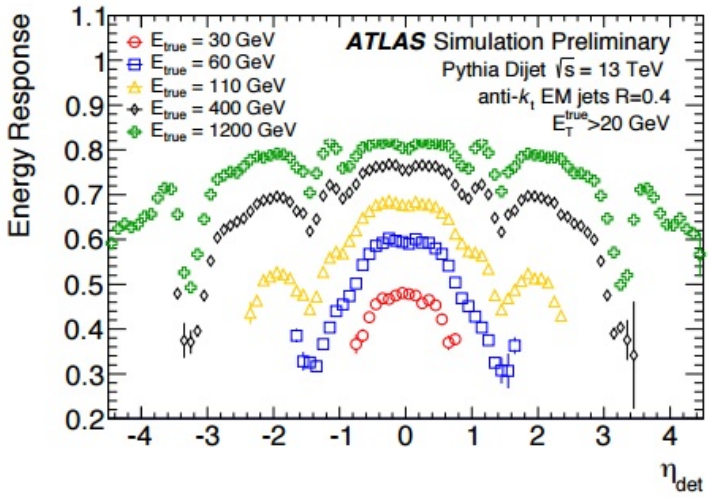

Figure 4.11: Energy response $\frac{p_T^{EM/LCWjet}}{p_T^{truth}}$ (inverse of the jet calibration correction) as a function of η for EM scale anti-k_t, R=0.4 jets, and for various jets energies [33].

algorithm [36].

Figure 4.12 shows the JVT distribution for hard-scattered and pileup jets with $20 < \text{pT} < 30$ GeV (left) and the hard-scattered jet efficiency as a function of the number of reconstructed primary vertices in the event when imposing a minimal JVT and JVF requirement (right). The hard-scattered jet efficiency after a selection based on JVT is stable at 90% ± 1%, where the average number of vertex in Run II is about 25. The JVT is thus much more robust than JVF with respect to pile-up.

4.5.4 b-jet tagging

The identification of jets originating from b-quark decay, called b-tagging, is not only important for many B physics channels, but also for all analyses that involves b quarks (t$\longrightarrow$Wb, H $\longrightarrow b\bar{b}$).
In the H$\longrightarrow \tau\ \tau$ analysis, the b-jet tagging is important to reject the background from $t\bar{t}$ or single top production processes.
The relatively long life time (1.5 ps) of B mesons produced in the hadronisation of b-quark allows them to travel a few millimeters from the production vertex in the detector before decaying. So a secondary vertex can be identified as shown in Figure 4.13.

In Run I analysis, several b-tagging algorithms have been used in ATLAS [37]. They are either impact parameter-based algorithm using informations of transverse and longitudinal impact parameter (d_0 and z_0 tends to be larger for particles originating from a B decay) or secondary vertex-based algorithms which use tracks to

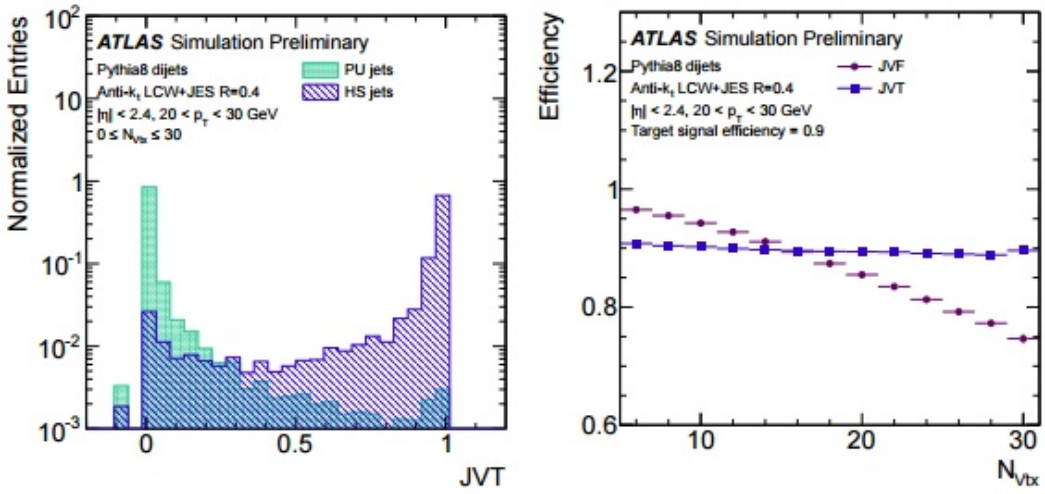

Figure 4.12: The JVT distribution for pile-up and and hard-scattered jets (left), and the primary-vertex dependence of the hard-scattered jet efficiency for fixed cuts of JVT (blue) and JVF (purple) (right) [35].

build an inclusive vertex formed by the decay products of a b-hadron.
This collection of algorithms was combined in a neural network MultiVariate tagger, called MV1 [38], which takes as input, the output weights of the different single algorithms.
For the analysis presented in this thesis, an updated tagger, called MV2c20, is used. This tagger uses an updated version of the different algorithm mentioned for Run I, in a BDT MultiVariate method [39].

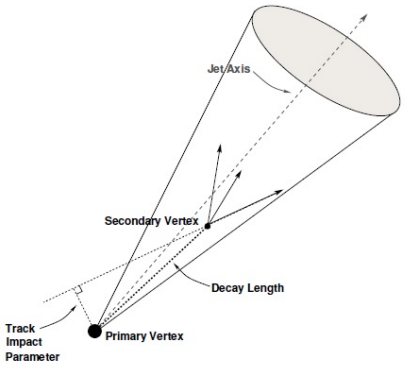

Figure 4.13: Illustration of primary and secondary vertex in b quark decay and the most relevant variables used for b-tagging.

4.6 Taus

The tau-lepton is reconstructed using its decay products given its short life time (3 $.10^{-13}$ s). There are two possibles decay modes: the leptonic mode ($\sim$ 35 %) where the tau lepton is reconstructed similarly as the other leptons, and the hadronic mode ($\sim$ 65 %), with mainly charged and neutral pions in the final state, where the reconstruction is based on searching for a collimated hadronic particles in the calorimeter using the anti-k_t algorithm, and associate tracks to it within a cone of $\Delta R < 0.4$.
The reconstruction of hadronic tau decay and its identification against the large QCD jets background in the LHC environment, is a challenging part of the tau-related physics analyses, like the H$\longrightarrow \tau\tau$ analysis described in this thesis. In the next Chapter, we will see in details the reconstruction and identification, used in Run I analysis, and the new algorithms developed for Run II.

4.7 Missing transverse energy MET

4.7.1 Reconstruction

Given the fact that there is no momentum in the transverse plane before the hard collision, and due to the momentum conservation law, any momentum imbalance in the transverse plane is referred to the missing transverse momentum $\overrightarrow{E_T^{miss}}$ [40].
The neutral weakly interacting particles with matter, such as neutrinos, are considered to be the dominant source of real $\overrightarrow{E_T^{miss}}$. Other source of fake E_T^{miss} like mis-reconstructed objects, imperfect resolution or detector inefficiencies can degrading the performance of the measurement.
A good measurement of $\overrightarrow{E_T^{miss}}$ is essential for many analysis, mainly for channels where neutrinos are expected to be in the final state, such as the analysis presented in this thesis.

$\overrightarrow{E_T^{miss}}$ can be calculated as the negative sum of all calibrated reconstructed objects in the event in addition to the energy deposits and tracks which are not associated to any object (the soft-term E_T^{miss}) [40]:

$$E_{x(y)}^{miss} = E_{x(y)}^{miss,e} + E_{x(y)}^{miss,\gamma} + E_{x(y)}^{miss,\mu} + E_{x(y)}^{miss,\tau} + E_{x(y)}^{miss,jets} + E_{x(y)}^{miss,SoftTerm} \quad (4.4)$$

Objects selections The selection of objects that enter the $\overrightarrow{E_T^{miss}}$ calculation can be summarized as follows [40]:

- Muons are required to pass medium working point selection (see Section 4.4.2) and to have $p_T > 10$ GeV.
- Electrons are selected using the medium criteria (see Section 4.3.2) and are required to have $p_T > 10$ GeV $|\eta| < 1.37$ or $1.52 < |\eta| < 2.47$ to avoid the

transition region between the central and end-cap electromagnetic calorimeters.

- Photons are required to pass the tight selection and must have $p_T > 25$ GeV and $|\eta| < 1.37$ or $1.52 < |\eta| < 2.37$ for the same reason as for electrons.

- Taus candidates have to pass the medium criteria (see next section) and a p_T cut above 20 GeV is applied. Tame cut in $|\eta|$ as for photons is applied.

- Jets are calibrated using the EM+JES scheme (see Section 4.5.2) and a correction for pile-up, and required to have a calibrated $p_T > 20$ GeV. To remove jets originating from pile-up, a JVT > 0.64 cut is applied.

E_T^{miss} soft term To measure this term, different algorithms have been developed [40]. In order to reduce the impact of pile-up interactions, methods that make use of ID tracks which can be matched to the primary vertex corresponding to the hard interaction are used.
The track soft term (TST) is calculated using tracks satisfying the selection criteria but not matched to any hard object (electrons, muons,...). And tracks not associated to the primary vertex are not included. Furthermore, an overlap removal between tracks and calorimeter clusters is applied: for example, tracks within ΔR(track, electron/photon cluster) < 0.05 and tracks within ΔR(track, τ-lepton) < 0.02 are removed.

4.7.2 Performance

The performance of the E_T^{miss} reconstruction is evaluated using Z $\longrightarrow \mu\mu$ events. In these events, neutrinos are only coming from heavy-flavor meson decays, so there is very little genuine E_T^{miss} making the resolution measured by the width of the $E_{x(y)}^{miss}$ distribution indicative of the E_T^{miss} reconstruction quality.
The W $\longrightarrow$ eν is an another good metric to validate the scale and direction of the reconstructed E_T^{miss}, since the event topology contains genuine E_T^{miss}.
To select Z $\longrightarrow \mu\mu$ events, exactly two muons with opposite charge and $p_T > 25$ GeV are required, and the reconstructed invariant mass of the dimuon system is required to be consistent with the Z boson mass. Figure 4.14 shows the E_T^{miss} distributions for the jets, muons and soft terms for TST E_T^{miss} as compared to MC prediction of signal and background [40].
For W $\longrightarrow$ eν events, exactly one electron is required. Cuts on E_T^{miss} and the reconstructed transverse mass are applied in order to reduce the multijet background with one jet emulating an isolated electron from the W boson. The reconstructed transverse mass is given by:

$$m_T = \sqrt{2p_T^l E_T^{miss}(1 - cos\Delta\phi)} \tag{4.5}$$

where p_T^l is the transverse momentum of the electron and $\Delta\phi$ is the azimuthal angle between the electron momentum and E_T^{miss}.

Figure 4.15 shows the overall TST E_T^{miss} distribution and the soft term of the TST E_T^{miss} for the W$\longrightarrow e\nu$ process [40]. The agreement between data and MC simulation is slightly worse compared to the Z $\longrightarrow \mu\mu$ events in the low E_T^{miss} region. This is likely due to the multi-jet background which is not included in the MC simulation.

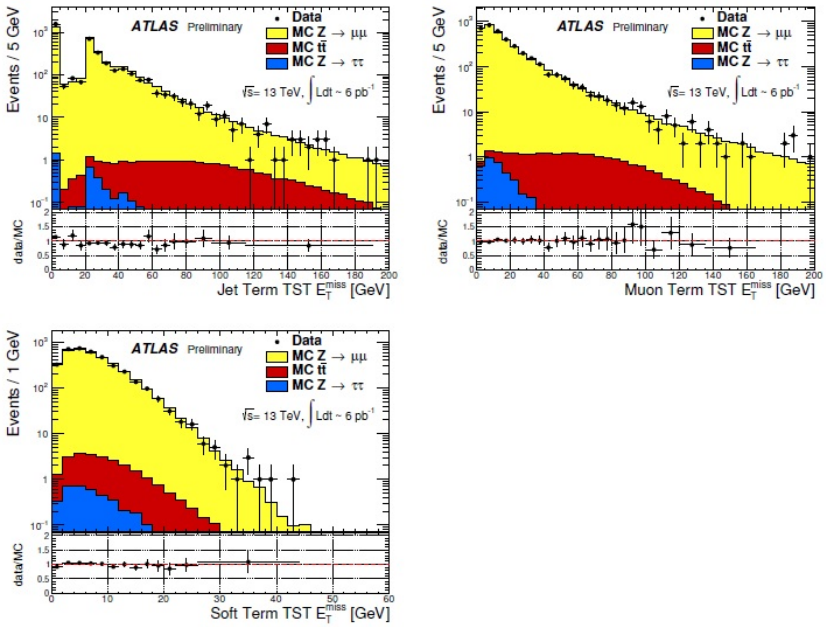

Figure 4.14: Distributions of jet term, muon term and soft term for TST E_T^{miss} in Z $\longrightarrow \mu\mu$ events [40]. Data are compared to MC signal and backgrounds.

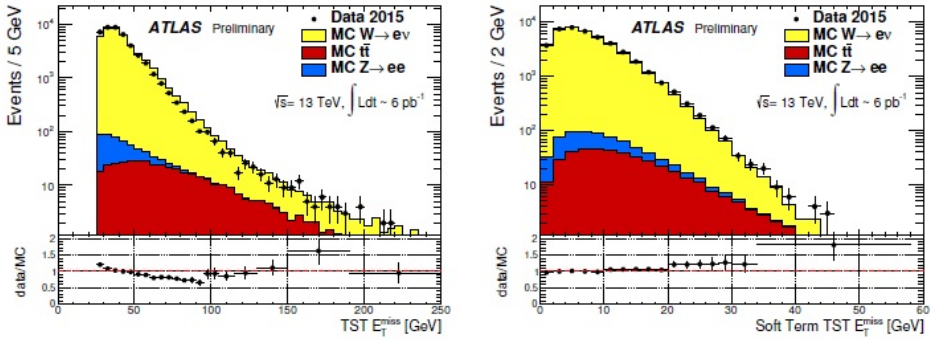

Figure 4.15: Distributions of TST total and soft term E_T^{miss} in W $\longrightarrow$ eν events [40]. Data are compared to MC signal and backgrounds.

Bibliography

[1] N. Metropolis, The beginning of the Monte Carlo method, volume 15, Cambridge University Press, 1987. (Cited on page 82.)

[2] T. Sjostrand, S. Mrenna and P. Z. Skands, PYTHIA 6.4 Physics and Manual, JHEP 0605, 026 (2006), arXiv:0603175 [hep-ph]. (Cited on page 82.)

[3] T. Sjostrand, S. Mrenna and P. Z. Skands, A Brief Introduction to PYTHIA 8.1, Comput. Phys. Commun. 178, 852-867 (2008), arXiv :0710.3820 [hep-ph], CERN-LCGAPP-2007-04, LU-TP-07-28, FERMILAB-PUB-07-512-CD-T. (Cited on page 82.)

[4] S. Alioli, P. Nason, C. Oleari and E. Re, A general framework for implementing NLO calculations in shower Monte Carlo programs : the POWHEG BOX, JHEP 1006, 043 (2010), arXiv:1002.2581 [hep-ph], DESY-10-018, SFB-CPP-10-22, IPPP-10-11, DCPT-10-22. (Cited on page 83.)

[5] HepForge project, Sherpa wiki, https://sherpa.hepforge.org/trac/wiki/SherpaDownloads/ Sherpa-2.2.0. (Cited on page 83.)

[6] J. Alwall, R. Frederix, S. Frixione, V. Hirschi, F. Maltoni et al., The automated computation of tree-level and next-to-leading order differential cross sections, and their matching to parton shower simulations, (2014), arXiv:1405.0301 [hep-ph], CERN-PH-TH-2014-064, CP3-14-18, LPN14-066, MCNET-14-09, ZU-TH-14-14. (Cited on page 83.)

[7] S.Agostinelli et al., Geant4: a simulation toolkit, Nucl. Instr. Meth. A 506 no.3, (2003) 250 (Cited on page 83.)

[8] ATLAS Collaboration, The ATLAS Simulation Infrastructure, Eur. Phys. J. C70 (2010) 823-874, arXiv:1005.4568 (Cited on page 83.)

[9] T. Cornelissen, M. Elsing, I. Gavrilenko, W. Liebig, A. Salzburger, Single Track Performance of the Inner Detector New Track Reconstruction (NEWT), ATL-INDET-PUB-2008-002 (Cited on page 84.)

[10] ATLAS Collaboration, Performance of the ATLAS silicon pattern recognition algorithm in data and simulation at p $\sqrt{s}$ = 7 TeV, ATLAS-CONF-2010-072 (2010). (Cited on page 84.)

[11] ATLAS Collaboration, Performance of the ATLAS Inner Detector track and vertex recon- struction in the high pile-up LHC environment, ATLAS-CONF-2012-042 (2012). (Not cited.)

[12] The ATLAS Collaboration, Performance of impact Parameter-Based b-tagging Algorithms with the ATLAS Detector using Proton-Proton Collision at $\sqrt{s}$=7 TeV, ATLAS-CONF-2010-091. (Cited on page 84.)

[13] The ATLAS Collaboration, Performance of primary vertex reconstruction in proton-proton collision at $\sqrt{s}$=7TeV in the ATLAS experiment, ATLAS-CONF-2010-069. (Cited on pages 84 and 86.)

[14] ATLAS Collaboration, Track Reconstruction Performance of the ATLAS Inner Detector at $\sqrt{s}$= 13 TeV. http://cds.cern.ch/record/2037683. (Cited on pages 84 and 85.)

[15] R. Fruhwirth, W. Waltenberger, P. Vanlaer, Adaptive vertex fitting, J. Phys. G34 (2007). (Cited on page 86.)

[16] ATLAS Collaboration, Charged-particle distributions in $\sqrt{s}$=13 TeV p p interactions measured with the ATLAS detector at the LHC, ATLAS-CONF-2015-028. (Cited on page 87.)

[17] ATLAS Public Plots, https://atlas.web.cern.ch/Atlas/GROUPS/PHYSICS/PLOTS/IDTR-2015-007/ (Cited on page 87.)

[18] ATLAS Collaboration, Performance of the ATLAS Inner Detector track and vertex recon- struction in the high pile-up LHC environment, ATLAS-CONF-2012-042 (2012). (Not cited.)

[19] ATLAS Collaboration, Performance of primary vertex reconstruction in proton-proton colli- sions at $\sqrt{s}$ = 7 TeV in the ATLAS experiment, ATLAS-CONF-2010-069 (2010). (Not cited.)

[20] ATLAS NOTE, Vertex Reconstruction Performance of the ATLAS Detector at $\sqrt{s}$ = 13 TeV, ATL-PHYS-PUB-2015-026 (Not cited.)

[21] ATLAS Collaboration, Expected electron performance in the ATLAS experiment. (Cited on page 88.)

[22] ATLAS Collaboration, G. Aad et al., Electron performance measurements with the ATLAS detector using the 2010 LHC proton-proton collision data, Eur.Phys.J. C72 (2012) 1909, arXiv:1110.3174 [hep-ex]. (Cited on pages 88, 89 and 90.)

[23] W. Lampl, S. Laplace, D. Lelas, P. Loch, H. Ma et al., Calorimeter clustering algorithms : Description and performance, (2008), ATL-LARG-PUB-2008-002, ATL-COM-LARG-2008-003. (Cited on page 88.)

[24] ATLAS Collaboration, Improved electron reconstruction in ATLAS using the Gaussian Sum Filter-based model for bremsstrahlung, ATLAS-CONF-2012-047 (2012). (Cited on page 88.)

[25] ATLAS Collaboration, Electron and photon energy calibration with the ATLAS detector using LHC Run 1 data, submitted to EPJC, http://arxiv.org/abs/1407.5063. (Cited on page 90.)

[26] https://atlas.web.cern.ch/Atlas/GROUPS/PHYSICS/PLOTS/EGAM-2015-006/index.html (Cited on pages 90 and 91.)

[27] ATLAS Collaboration, Muon reconstruction performance of the ATLAS detector in proton-proton collision data at $\sqrt{s}$ = 13 TeV. arXiv:1603.05598v1 [hep-ex] 17 Mar 2016 (Cited on pages 91, 92, 94 and 95.)

[28] ATLAS Collaboration, Search for high-mass dilepton resonances in pp collisions at $\sqrt{s}$ = 8 TeV with the ATLAS detector, Phys. Rev. D 90 (2014) 052005, arXiv:1405.4123 [hep-ex]. (Cited on page 93.)

[29] G. P. Salam and G. Soyez. "A Practical Seedless Infrared-Safe Cone jet algorithm". In: JHEP 0705 (2007), p. 086. DOI: 10.1088/1126-6708/2007/05/086. arXiv:0704.0292 [hep-ph] (Cited on page 96.)

[30] G. P. Salam. "Towards Jetography". In: Eur. Phys. J. C67 (2010), pp. 637-686. DOI: 10.1140/ epjc/s10052-010-1314-6. arXiv:0906.1833 [hep-ph] (Cited on page 96.)

[31] M. Cacciari, G. P. Salam, and G. Soyez, The anti-kt jet clustering algorithm, J. High Energy Phys. 04 (2008), arXiv:0802.1189 [hep-ph]. (Cited on page 96.)

[32] ATLAS Collaboration, Monte Carlo Calibration and Combination of In-situ Measurements of Jets in ATLAS, ATL-COM-PHYS-2015-071 (2015), url: https://cds.cern.ch/record/1987296. (Cited on page 97.)

[33] ATLAS Collaboration, Jet Calibration and Systematic Uncertainties for Jets Reconstructed in the ATLAS Detector at $\sqrt{s}$ = 13 TeV. ATL-PHYS-PUB-2015-015 24 July 2015 (Cited on pages 98 and 99.)

[34] The ATLAS Collaboration, Pile-up subtraction and suppression for jets in ATLAS, ATL-COM-PHYS-2013-083 (Cited on page 98.)

[35] ATLAS Note, ATL-PHYS-PUB-2014-001. Tagging and suppression of pileup jets. (Cited on pages 98 and 100.)

[36] A. Hoecker, P. Speckmayer, J. Stelzer, J. Therhaag, E. von Toerne, and H. Voss, TMVA: Toolkit for Multivariate Data Analysis, PoS ACAT (2007) 040, arXiv:physics/0703039. (Cited on page 99.)

[37] ATLAS Collaboration, Commissioning of the ATLAS high-performance b-tagging algorithms in the 7 TeV collision data, ATLAS-CONF-2011-102, http://cds.cern.ch/record/1369219. (Cited on page 99.)

[38] The ATLAS Collaboration, Calibration of the performance of b-tagging for c and light-flavour jets in the 2012 ATLAS data, ATLAS-CONF-2014-046. (Cited on page 100.)

[39] https://twiki.cern.ch/twiki/bin/view/AtlasProtected/BTaggingBenchmarks (Cited on page 100.)

[40] ATLAS Collaboration, Performance of missing transverse momentum reconstruction with the ATLAS detector in the first proton-proton collisions at $\sqrt{s}$ = 13 TeV,ATL-PHYS-PUB-2015-027 27 July 2015 (Cited on pages 101, 102 and 103.)

Chapter 5

Tau reconstruction and conversion tracks in hadronic tau decay

Contents

Tau leptons play an important role for a variety of different studies at the LHC, within a wide momentum range from 10 GeV to 500 GeV. They provide an excellent probe in searches for the Standard Model Higgs boson coupling to leptons, as well as in searches for MSSM Higgs boson or SUSY. In this thesis, the search for the SM Higgs boson decaying in two tau leptons with ATLAS experiment is studied.

5.1 Hadronic tau in ATLAS

5.1.1 Tau decay modes

Taus are the heaviest leptons with a mass $m_\tau = 1.77$ GeV and proper decay length of 87 μm so they decay before leaving the beam pipe.
There are two possibles decay modes:

- Leptonic mode: with a branching ration BR = 35 %. In this mode, the visible decay products, the electrons or muons, are reconstructed like primary electrons or muons.
- Hadronic mode: with BR = 65 %, where the taus are the only leptons decaying to hadrons due to their relatively high mass. This decay is divided into two categories, one including one charged tracks and called "1-prong " tau ($\sim$ 52 %), and the other category includes three charged tracks and called "3-prong" taus ($\sim$ 14 %). Charged tracks include pions or kaons where the latter contributes to only 3 % of the total hadronic branching ratio [1].
  In addition to the charged hadrons, the hadronic decay includes neutral pions in about 40 % of cases. Figure 5.1 illustrates the different tau decay modes where the hadronic modes are separated depending on the number of prongs and of neutral charged pions.

The reconstruction and identification of hadronic modes of tau leptons are the challenging part of tau performance studies due to the large background in the LHC environment coming from the production of jets. Figure 5.2 shows a sketch of a hadronic tau (left) and a QCD jet (right). Two geometrical regions are defined for the reconstruction (tau and QCD jets), the core cone (blue region) with $0 < \Delta R < 0.2$ (which should contain the decay products in case of a hadronic tau decay), and the isolation cone with $0.2 < \Delta R < 0.4$.

5.1.2 Tau reconstruction

The reconstruction algorithm of tau decaying hadronically (indicated as τ_{had} in the following) is seeded by jets formed using the anti-k_T algorithm described in Section

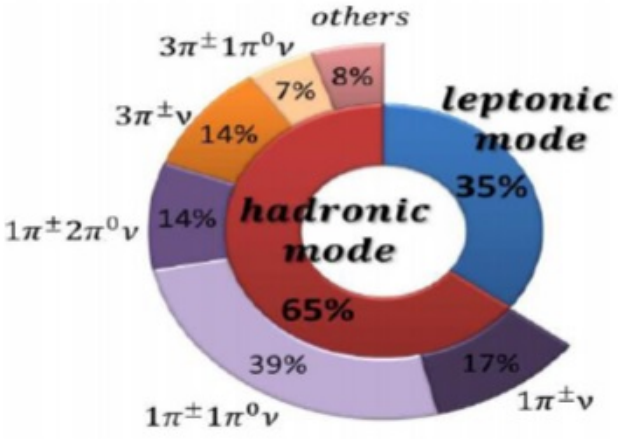

Figure 5.1: The different decay modes of the tau lepton.

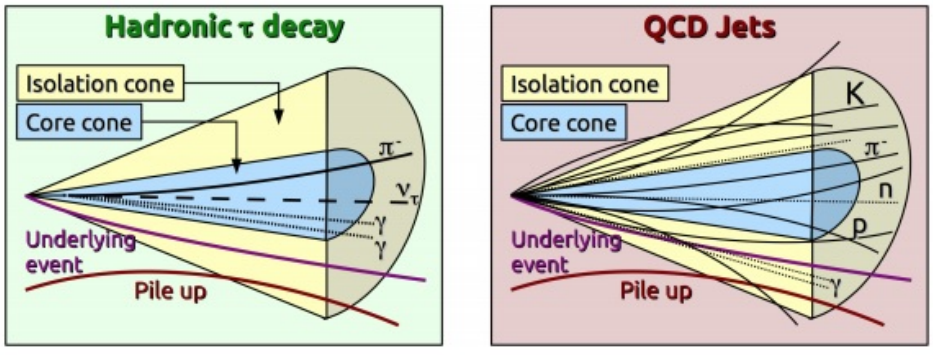

Figure 5.2: Decay cones of hadronically decaying tau (left) and a QCD jet (right).

4.6.1 with a cone radius parameter R = 0.4 and clusters of calorimeter cells, using the local hadronic calibration LCW (see Section 4.5) as inputs [2]. Jets are required to have $p_T > 10$ GeV and $|\eta| < 2.5$. where the τ_{had} p_T is set to the total energy of topoclusters within $\Delta R < 0.2$ at the LCW scale.
In addition, events are required to have a reconstructed primary vertex with at least three associated tracks.
The vertex candidates with highest $\Sigma\, p^2_{T,tracks}$ associated is chosen to be the primary vertex. However, the tau lepton is not always produced from the chosen primary vertex. To identify this vertex, among the previously reconstructed primary vertex candidates in the event, a tau lepton algorithm (TV) is used. It takes as inputs all tau candidate tracks. The p_T of these tracks are then summed and the primary vertex candidate to which the largest fraction of the p_T sum is selected [3]. This vertex is used to find the direction of τ_{had}, tracks are associated to it and a coordinate system is built in which identification variables are calculated (see next section).

4-momentum reconstruction : The τ_{had} p_T at the LC scale is set to the total energy of topoclusters within $\Delta R < 0.2$ [4]. This is also the base value for the final energy calibration discussed in Section 4.5.2. The hadronic component of the topoclusters consists of the cells in the last layer of the electromagnetic calorimeter and of the hadronic calorimeter, while the electromagnetic component is referred to the energy deposited in the other layers of the ECAL.
The barycenter of the jet seed topocluster calibrated at the LCW scale is used to get the τ_{had} 3-momentum components.

The associated tracks have to pass the following selections:

- Tracks $p_T > 1$ GeV.
- Be in the core region $\Delta R < 0.2$ around the τ_{had} direction
- At least two associated hits in the pixel detector (including the IBL), and at least seven hits in total in the pixel and the SCT detectors.
- $|d_0| < 1.0$ mm (the distance of closest approach of the track to the TV in the transverse plane). And in the longitudinal plane, $|\Delta z_0 sin\theta| < 1.5$ mm.

Figure 5.3 shows the distribution of numbers of reconstructed tracks associated to τ_{had} candidates, separately for true 1-prong and 3-prong decays [2].

The tracking inefficiency due to nuclear interactions in the inner detector are the dominant cause of underestimation of the number of prongs. The overestimation of the numbers of prongs comes mainly from conversion tracks that pass track criteria (will be detailed in this Chapter).

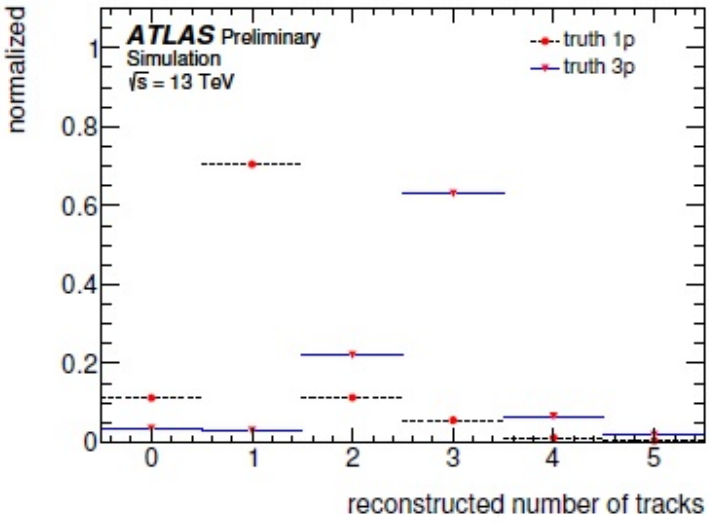

Figure 5.3: Distribution of number of reconstructed tracks for τ_{had} candidates from true 1-prong and 3-prong decays [2].

π^0 reconstruction in Run I analysis The current π^0 reconstruction algorithm is made in two steps:

- Measurement of the number of neutral pions, N_{π^0}, which can be 0, 1 or 2, in the core region by using a combined BDT algorithm which takes as inputs the global tau features measured using the strip layer and calorimeter quantities, and tracks momenta.

- The kinematic information of tracks and of clusters likely originating from π^0 decays are then combined in this algorithm. A candidate π^0 decay is composed of up to two clusters among those found in the core region of τ_{had} candidates. Contributions from pileup, underlying event and electronic noise are subtracted and a π^0 likelihood score for each cluster found in the core region using cluster properties is provided.

5.1.3 Tau identification

Rejection against the huge QCD jet background needs a further identification step after the reconstruction of τ_{had} candidates. There are two types of jets, quark-like and gluon-like jets, depending on the dominant parton initiating the jet (defined often as as the parton initiating the jet or the highest-p_T parton within a jet). The rejection against quark-like jets is less effective than gluon-like jets, since the first ones are usually more collimated and have fewer tracks, so they look more like tau-jets.
The identification is based on tracks and topoclusters (and cells linked to them)

in the core or isolation region around the τ_{had} direction. Information about the longitudinal and lateral shower shape are provided by the calorimetric system, and the π^0 content of a tau candidate is provided by the ECAL.
A Boosted Decision Trees (BDT) method is used in this identification. Some of the discriminating variables used in as inputs for the tau identification are listed below [2]:

- Central energy fraction (f_{cent}): The shower shape in the calorimeter provides good discrimination since QCD jets are wider than typical τ_{had}. This shower shape is described by the core transverse energy fraction in the region $\Delta R < 0.1$ with respect to all the energy deposited in the region $\Delta R < 0.2$ around the τ_{had} candidate. It is obtained by summing the energy deposited in all cells belonging to topoclusters with a barycentre in this region, calibrated at the EM energy scale. A correction based on the number of reconstructed primary vertices in the event is used to remove biases due to pileup contributions.

- Leading track momentum fraction ($f^{-1}_{leadtrack}$): the transverse energy sum, calibrated at the EM energy scale, deposited in all cells belonging to topoclusters in the core region and divided by the transverse momentum of the highest-p_T charged particle in the core region of the τ_{had} candidate.

- p_T-weighted distance of the associated tracks to the τ_{had} direction, using all tracks in the core and isolation regions.

- Track radius ($R^{0.2}_{track}$): p_T-weighted ΔR distance of the associated tracks to the τ_{had} direction, using only tracks in the core region.

- Fraction of tracks p_T in the isolation region (f^{track}_{iso}): Scalar sum of the p_T of tracks associated with the τ_{had} candidate in the region $0.2 < \Delta R < 0.4$ divided by the sum of the p_T of all tracks associated with the τ_{had} candidate.

- Fraction of EM energy from charged pions ($f^{track-HAD}_{EM}$): It is defined as the fraction of the electromagnetic energy of tracks associated with the τ_{had} candidate in the core region. The numerator is defined as the difference between the sum of the momentum of tracks in the core region and the sum of cluster energy deposited in the hadronic part of each topocluster (including the third layer of the EM calorimeter) associated with the τ_{had} candidate. The denominator is the sum of cluster energy deposited in the electromagnetic part of each topocluster (presampler and first two layers of the EM calorimeter) associated with the τ_{had} candidate. All clusters are calibrated at the LCW energy scale.

Figure 5.4 illustrates one discriminating variable, the f^{track}_{iso}, for both signal (real taus) and multi-jet background. We see that for hadronic taus, most of the events are at low value of f^{track}_{iso} which is expected (most tracks are in the core region).

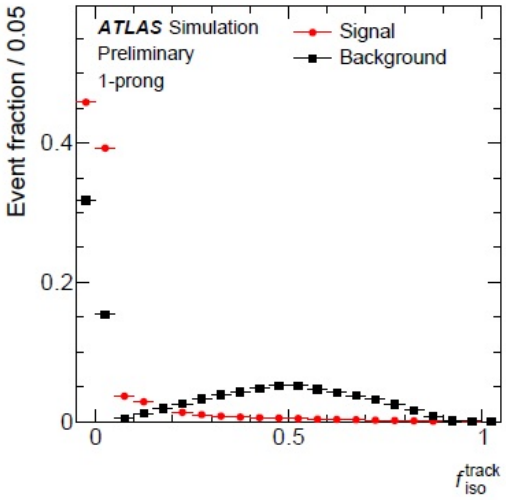

Figure 5.4: Distribution of the f_{iso}^{track} variable for signal (hadronic tau decays) and background (multi-jet events)[2].

Boosted Decision Tree (BDT) algorithms are trained separately for 1-track and 3-track τ_{had} p_T decays using $Z/\gamma^* \longrightarrow \tau\tau$ sample for signal and di-jet sample for background.

5.1.4 Performance

Reconstruction efficiency It is determined by calculating the fraction of true 1-prong (3-prong) hadronic taus which are reconstructed as 1-track (3-track) τ_{had} candidates.
The tracks and vertex association, described in Section 5.1, has a dominant effect on the reconstruction efficiency, knowing that the detector is almost fully efficient for finding a jet-seed for a τ_{had} candidate with $p_T > 20$ GeV in the pseudorapidity acceptance range.

Figure 5.5 shows the efficiency to reconstruct the correct number of tracks of a true tau lepton as a function of true τ_{had} p_T.

For 1-prong τ, the reconstruction efficiency looks almost constant. There is a small drop at high p_T due to the fact that very high-p_T taus decay sometimes after the first pixel detector, so it fails the requirement on the number of hits mentioned in Section 5.1. Also, with high-p_T taus, there is an increase of the probability to wrongly assign an electron from photon conversion (from π^0 decay) as a charged track from hadronic tau decay, leading to an incorrect counting of the number of tracks of a hadronic tau decay.
For 3-prong taus, we see a drop of the efficiency at low-p_T due to charged decay tracks that do not pass the minimum p_T requirement, and a reduction at high p_T

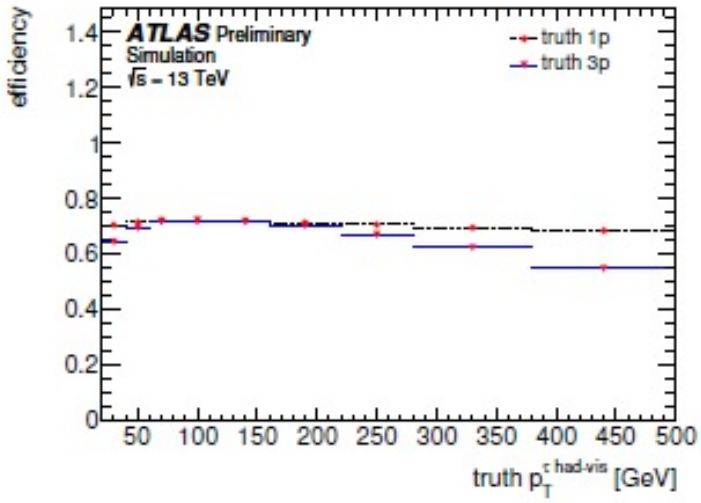

Figure 5.5: Reconstruction efficiency of the correct number of tracks of true τ leptons as a function of τ_{had} p_T [2].

is seen due to the increased probability of missing a track because of the overlap between different tracks trajectories (decay products are collimated at high p_T).

The data to MC differences in τ_{had} reconstruction efficiencies is corrected using the so-called "scale-factors". These quantities are applied to simulated MC samples. They are defined as the ratio of data to MC efficiencies: SF $= \frac{\varepsilon_{data}}{\varepsilon_{MC}}$. Scale factors are determined by studying the tau reconstruction efficiency in data and in MC samples using tag and probe method [5], using Z $\longrightarrow \tau\tau$, W $\longrightarrow \tau\nu$ and $t\bar{t} \longrightarrow \tau$ + jets samples.

Identification and combined efficiency The tau identification efficiency is the fraction of 1-prong (3-prong) taus reconstructed correctly as 1-track (3-track) τ_{had} candidates that passes the BDT identification cuts. And three working points (Tight, Medium and Loose) are defined. For each point corresponds an identification efficiency value.
The combined efficiency is the product of the reconstruction and identification efficiency, and the BDT requirements are chosen such that the combined efficiency almost does not depend on the τ_{had} p_T. Pileup corrections are also applied to reduce the dependency of the combined efficiency on the average number of interactions. Figure 5.6 shows the residual dependency of the combined efficiency on p_T. It seems to be uniform, compensating the p_T-dependence of the reconstruction efficiency shown in Figure 5.5. And Figure 5.7 shows the stability of the combined efficiency with respect to $< \mu >$.

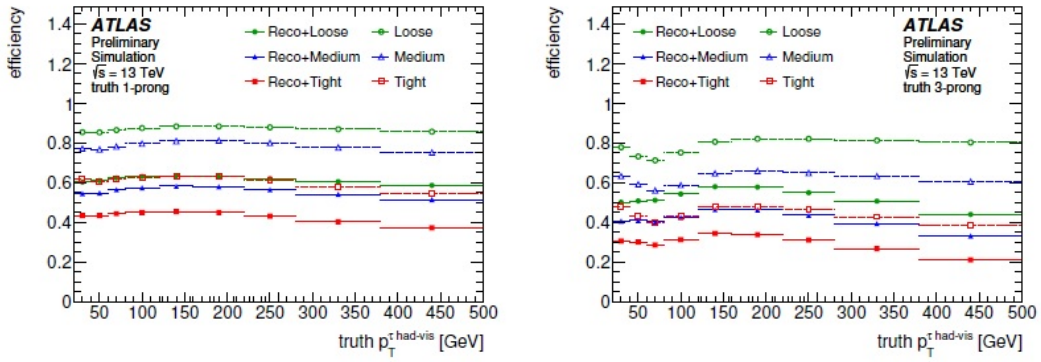

Figure 5.6: Identification efficiency of τ_{had} (open symbols) and combined reconstruction and identification efficiency (full symbols) versus the τ_{had} p_T, for τ_{had} candidates (for 1-track (a) and 3-track (b)) [2].

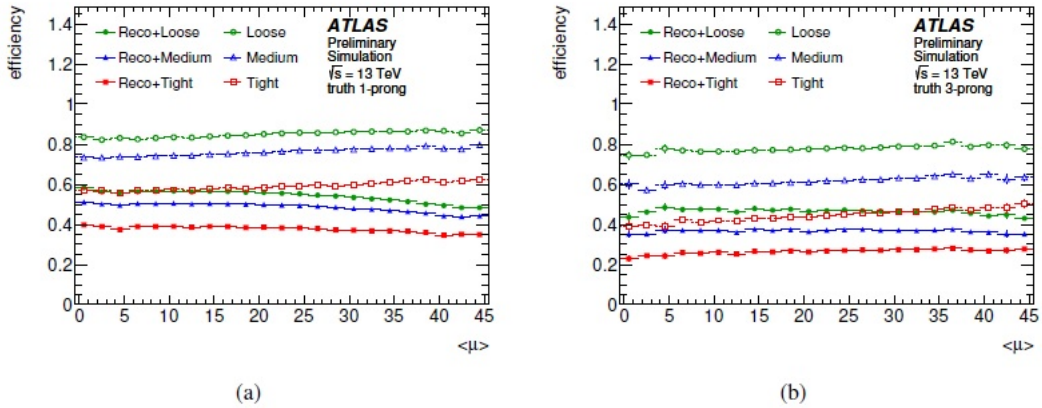

Figure 5.7: Identification efficiency of τ_{had} (open symbols) and combined reconstruction and identification efficiency (full symbols) versus the average number of interactions per event, for τ_{had} candidates (for 1-track (a) and 3-track (b)) [2].

5.1.5 Discrimination against electrons

In addition to QCD jets faking τ's, another contribution from electrons faking 1-prong τ's must be reduced. A powerful likelihood discriminator algorithm developed in the context of ATLAS electron reconstruction and identification effort is used [6], (since charged pions are one of the major backgrounds of electrons ID).
The discriminator uses the:

- Shower shape information from the calorimeter measurements.
- Information from tracking detector (reconstructed hits including transition radiation informations from the TRT).

A full list of variables used in this discriminator can be found here [5].

Figure 5.8 shows the likelihood score distribution for a sample of true 1-prong hadronic tau decays ($Z \longrightarrow \tau\tau$) and a sample of true electrons ($Z \longrightarrow ee$). The discrimination between is provided by a geometrical matching between the reconstructed tau candidates and electrons with $p_T > 5$ GeV, within a cone of $\Delta R < 0.4$. Reconstructed 1-prong tau candidates which are matched to an electron candidate with a large Likelihood score value are rejected. A parametrization of the electron Likelihood score cut values is done in order to provide a constant tau efficiency of 95% for a sample of tau candidates passing the Loose identification working point [2].

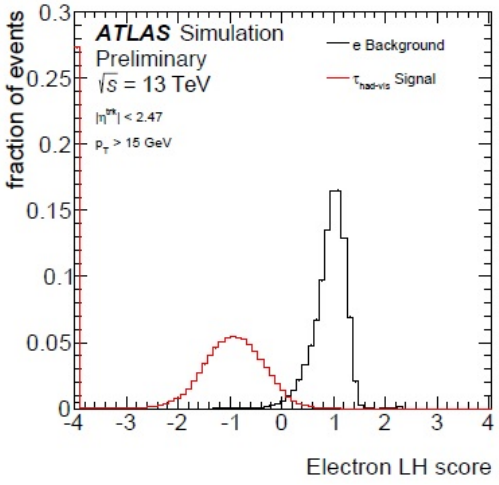

Figure 5.8: Electron likelihood score for hadronic tau decays and prompt electrons of $Z \longrightarrow ee$ sample [2].

5.1.6 Tau energy calibration

The tau energy is calibrated first after the reconstruction at the LCW scale. This takes into account the calorimeter non-compensation and the energy deposited in

dead material or outside topoclusters.
The tau energy scale (TES) [2] consists of two additional corrections which calibrate the tau energy back to the true visible energy. This relies on Monte Carlo samples with hadronic tau lepton decays ($Z \longrightarrow \tau\tau$), and applies multiplicative factors based on the p_T of the reconstructed tau lepton to the energy measurements in the calorimeters.

- There is an energy contribution coming from pileup interactions. This needs to be subtracted.
- A set of possible effects for the τ_{had} particles needs to be considered: decay products not detected within $\Delta R = 0.2$ of the reconstructed τ_{had} candidate, too small energy deposit in the calorimeter to create topoclusters or even not reaching the calorimeter. A response correction is applied to take into account these effects.

5.2 Improvement for Run II - Tau Particle Flow

5.2.1 Method and concept

A new hadronic tau reconstruction method, called "Tau Particle Flow" [7], has been developed for the Run II.
This algorithm aims to identify the five dominant decay modes ($h^{\pm}$, $h^{\pm}\pi^0$, $h^{\pm} \geq 2\pi^0$, 3 $h^{\pm}$, $3h^{\pm} \geq 1\pi^0$) and reconstruct properly the decay products.
The charged hadrons ($h^{\pm}$) are reconstructed using the tracking system, from which the charge and momentum are determined. In the current implementation, the association of charged tracks to the hadronic tau is done by considering each track in the core region to be a $\pi^{\pm}$. However, some of these tracks are misclassified as $\pi^{\pm}$ and could be from another sources like charged tracks from photons conversion (see next section), pileup or underlying events.
A dedicated algorithm has been developed in order to tag these charged tracks but it has not yet been implemented in the Tau Particle Flow code. Neutral pions are reconstructed from their energy in the EM calorimeter.
The reconstructed charged and neutral hadrons (the visible tau decay products) are then used to infer the decay mode and to calculate the four-momentum of the reconstructed τ_{had} candidates.
We will see in the following the improvement introduced by this algorithm on the tau energy and direction resolution. This improvement, coupled with the ability to better identify the hadronic tau decay modes, can lead to a better resolution of the di-tau mass reconstruction.
The individual steps of the Tau Particle Flow method will be detailed in the following sections [2]. First, we will see how the neutral pions are reconstructed and identified to be used in the tau decay mode classification. Next, since photons from π^0 decays are highly collimated, a reconstruction of energy deposits from individual photons in the finely segmented innermost layer of the EM calorimeter (EM1) is done to identify

cases where two π^0 are contained within a single cluster. The decay mode is then tagged by exploiting the available information from the reconstructed $h^{\pm}$ and π^0 and the photons reconstructed in EM1. The four-momentum is then reconstructed using the individual hadrons.

5.2.2 Neutral pions reconstruction and identification

The neutral pion candidates are reconstructed and identified as described in the following steps:

- Clustering cells in the EM calorimeter in the core region of the τ_{had} are used first to create π^0 candidates (π^0_{cand}).

- The energy of the π^0_{cand} is then corrected for contamination from charged hadrons $h^{\pm'}$s. This is done by estimating the energy that each $h^{\pm}$ deposits in the EM calorimeter ($E^{EM}_{h^{\pm}}$) as the difference between the energy of the $h^{\pm}$ from the tracking system ($E^{trk}_{h^{\pm}}$) and the energy deposited in the HCAL which is associated with the $h^{\pm}$ ($E^{HAD}_{h^{\pm}}$).
  The $E^{EM}_{h^{\pm}}$ of each $h^{\pm}$ is then subtracted from the energy of the closest π^0_{cand} if it is within $\Delta R = 0.04$ of the $h^{\pm}$.

- A p_T requirement and an identification selection is then applied in order to reject π^0 candidates that may come from $h^{\pm}$ remnants, pileup or other sources. A BDT is used for the π^0 identification and it takes as inputs the properties of π^0_{cand} clusters, such as the energy density and the width and depth of the shower. A full list of the variables used in this BDT can be found in [7]. The p_T and identification score thresholds are optimised in five $|\eta|$ ranges, corresponding to structurally different regions of the calorimeter, to maximise the number of τ_{had} with the correct number of reconstructed $h^{\pm}$ and identified π^0_{cand}. The p_T thresholds are in the range 2.1-2.7 GeV.

The performance of the $h^{\pm}$ and π^0 counting achieved at this level is shown in Figure 5.9. This decay mode classification matrix illustrates the probability to reconstruct properly the true tau decay modes, using $Z \longrightarrow \tau\tau$ MC samples. We can see that for τ_{had} with one $h^{\pm}$, the separation of modes, at the reconstruction level, with and without π^0 is reasonable, but the distinction between $h^{\pm}$ π^0 and $h^{\pm} \geqslant 2\pi^0$ is difficult.
The $h^{\pm} \geqslant 2\pi^0$ case shows the largest misclassification and this is due to one of the two following reasons: either one the two π^0 failed selection or the energy deposits of both $\pi^{0'}$s merge into a single cluster, falling in the $h^{\pm}\pi_0$ category.
The distinction is also difficult between $3h^{\pm}$ and $3h^{\pm} \geqslant \pi^0$ decays, and this is due to the fact that $\geqslant 2\pi^0$ are typically soft with large overlapping $h^{\pm}$ deposits, thus missing the π^0 identification.

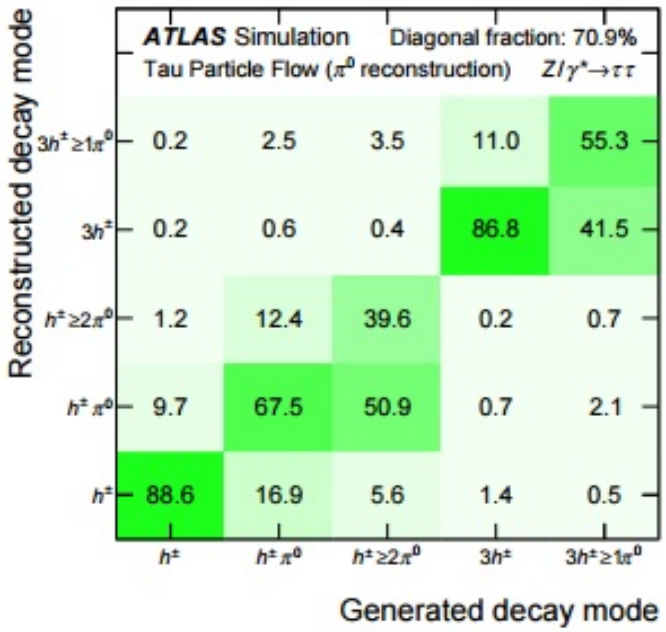

Figure 5.9: Decay mode classification efficiency matrix showing the probability for a given generated mode to be reconstructed as a particular mode by the Tau Particle Flow after π^0 reconstruction in simulated Z $\longrightarrow \tau\tau$ events [7].

5.2.3 Individual photons reconstruction

To improve the π^0 reconstruction and counting in the tau decay, a reconstruction of the individual photons from π^0 decay is needed. When the two photons from π^0 decay deposit their energy in the ECAL, they may be merged into one cluster during the π^0 reconstruction. Therefore, a important fraction of $h^\pm \geqslant 2\pi^0$ is mistagged as $h^\pm \geqslant \pi^0$, as mentioned before.
This individual photon identification can be achieved using the informations from EM1 where 30 % of the photon energy is deposited, and profiting from its high segmentation in η ($\Delta\eta = 0.0031$ in the barrel).

The energy deposited by photons in EM1 is reconstructed by searching for an energy maximum within the core region of the tau decay. Detailed information about this procedure can be found in the reference [7].
The counting of the number of maximum associated to π^0 candidates improves the $h^\pm \geqslant 2\pi^0$ tau decay mode classification depending on the number of π^0. And a maxima is assigned to a π^0 candidate if its cell is within the π^0 cluster and passes a given energy threshold optimized to maximize the total number of correctly classified tau decays.
The correction of decay mode classification of τ_{had} candidates is performed as follows:

- τ_{had} candidates tagged as $h^\pm \geqslant \pi^0$, where the π^0 candidate has three associ-

ated maxima, are then tagged as $h^{\pm} \geqslant 2\pi^0$.

- A recovery of 16% of mistagged $h^{\pm} \geqslant 2\pi^0$ is achieved (with 2.5% misclassification of $h^{\pm} \geqslant \pi^0$).

5.2.4 Tau decay mode classification

A Boosted Decision Tree (BDT) method is used to determine the tau decay mode taking as inputs the following informations: the kinematic of the tau decay products, the π^0 identification scores and the number of identified photons as described in the previous paragraphs.
The classification is based on three decay mode tests performed to distinguish between the different following decay modes: ($h^{\pm}$, $h^{\pm}\pi^0$) , ($h^{\pm}\pi^0$, $h^{\pm} \geq 2\pi^0$) and ($3h^{\pm}$, $3h^{\pm} \geq \pi^0$).
The tests are performed as follows:

- τ_{had} candidates with one or three reconstructed tracks and without any π^0 candidate are directly classified as $h^{\pm}$ and $3h^{\pm}$ respectively.

- τ_{had} candidates with one associated track and at least two π^0 candidates, where one at least is an identified π^0 enter the test ($h^{\pm}\pi^0$, $h^{\pm} \geq 2\pi^0$).

- τ_{had} candidates with one identified π^0 and then classified as $h^{\pm} \geqslant 2\pi^0$ because of the individual photons counting in the cluster, keep the same classifications and do not enter the test.

- Remaining τ_{had} candidates with 1 or 3 associated tracks enter the tests ($h^{\pm}$, $h^{\pm}\pi^0$) and $3h^{\pm} \geq \pi^0$), respectively.

The training of the BDT for each decay mode test is done using a $Z \longrightarrow \tau\tau$ MC sample. And the τ_{had} candidates entering each decay mode test are then further categorised based on the number of identified π^0's.
The detailed list of input variables used in the BDT can be found if Ref [7]. They are chosen to discriminate against additional misidentified π^0 candidates (from imperfect $h^{\pm}$ subtraction, pileup or underlying events). For example, the clusters associated to these misidentified π^0 have low energy and low π^0 identification score. Figure 5.10 shows the final classification efficiency matrix by decay mode. It shows the efficiency for each generated true decay mode to be correctly reconstructed by the Tau Particle Flow algorithm. Compared to the efficiencies shown in Figure 5.9, an improvement is achieved in the $h^{\pm}\pi^0$ mode, while there is always difficulties in the $h^{\pm} \geq 2\pi^0$.
The overall classification efficiency achieved is 74.7% (diagonal fraction), which shows an improvement compare to the 70.9 % efficiency of Figure 5.9.

5.2.5 τ_{had} 4-momentum reconstruction

The 4-momentum reconstruction described in Section 5.1.2 constitutes the so-called "baseline" 4-momentum calculation of the hadronically decaying taus. This is the one used in Run I analysis and in the current Run II analysis presented in this thesis.
In the new reconstruction software, described in Section 5.2, there are two levels of 4-momentum reconstruction:

- The "Constituent-based" 4-momentum calculation where the τ_{had} 4-momentum reconstruction begins with summing the 4-momenta of the $h^{\pm}$ and π^0 candidates.
- A further calibration is applied to the Constituent-based τ_{had} energy in each decay mode as a function of the Constituent-based E_T. The resulting four-momentum is used to set the τ_{had} direction in the Tau Particle Flow. For the final energy calibration of the Tau Particle Flow, the Constituent-based calculation is combined with the Baseline calibration.

Figure 5.11 shows the τ_{had} η and ϕ residuals (difference between true generated and reconstructed values for these quantities) of the Tau Particle Flow and the baseline reconstruction. A significant improvement can be observed.

Figure 5.12 shows the E_T residual (a) and the core and tail resolutions (half-widths spanned by the 68% and 95% quantities), of the relative E_T residual distributions as a function of the generated τ_{had} E_T [7]. The resolution of the Tau Particle Flow is superior in both the core and tails at low E_T and it is as good at high E_T.

5.3 Conversion tracks tagging in hadronic tau decay

In about 40 % of cases, there is at least one neutral pion ($\pi^0 \longrightarrow \gamma\gamma$) in the final state of hadronic tau decays, as shown in Figure 5.1. Passing through the ATLAS inner detector, before depositing their energy in the Liquid Argon Calorimeter, the interaction of the photon will be dominated by e^+e^- pair production in the presence of material. This phenomena is called photon conversion [8] [9].

The probability for a photon to convert as a function of the transverse radius from the interaction point is given in Figure 5.13. This shows that the probability of conversion is not negligible and it varies greatly with the pseudorapidity [10]. It is lowest in the most central region $|\eta| < 0.5$, where the amount of tracker material is reduced. And about 20 % of photons with $|\eta| > 1.5$ convert within the first 200 mm radius of the inner detector.

This conversion process leads to extra-charged tracks (e^+e^-) in the final state of a hadronic tau decay and then may shift the tau track multiplicity towards larger

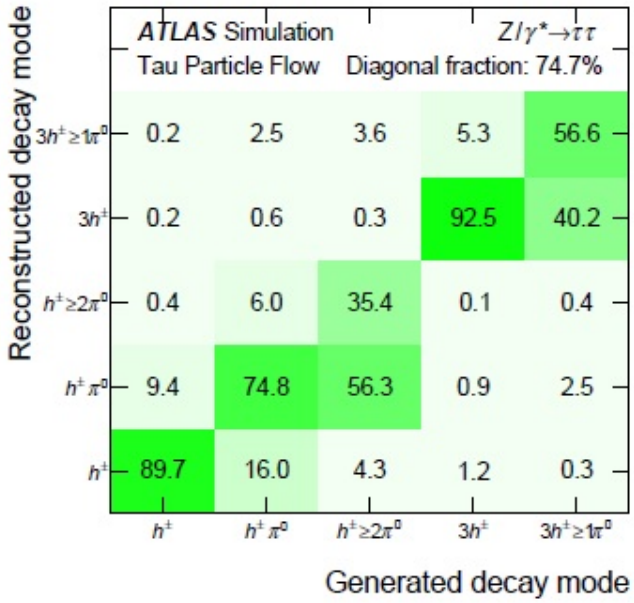

Figure 5.10: Decay mode classification efficiency matrix. The numbers show the probability for a given generated mode (true tau mode) to be reconstructed as a particular mode by the Tau Particle Flow after the final decay mode classification in simulated Z$\longrightarrow \tau\tau$ sample. Decays containing neutral kaons are omitted [7].

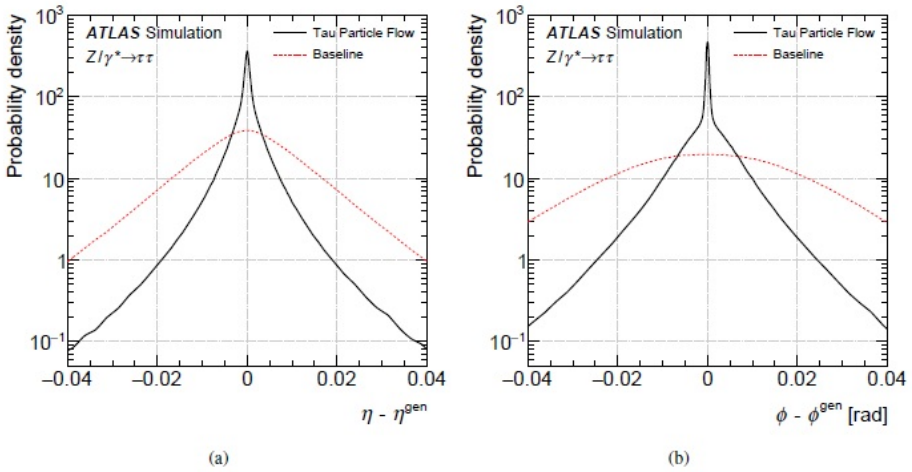

Figure 5.11: The distributions of the τ_{had} η and ϕ residuals of the Tau Particle Flow compared to the Baseline reconstruction. [7].

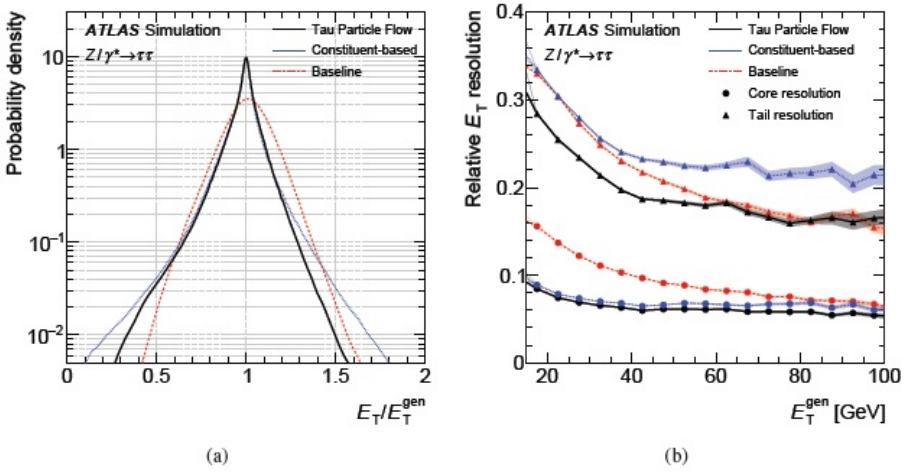

Figure 5.12: The distribution of the τ_{had} relative E_T residual (a) and the core and tail resolutions (half-widths spanned by the 68% and 95% quantities) (b), of the relative E_T residual distributions as a function of the generated τ_{had} E_T, for the baseline (red), the constituent-based (blue) and the particle flow approaches (black) [7].

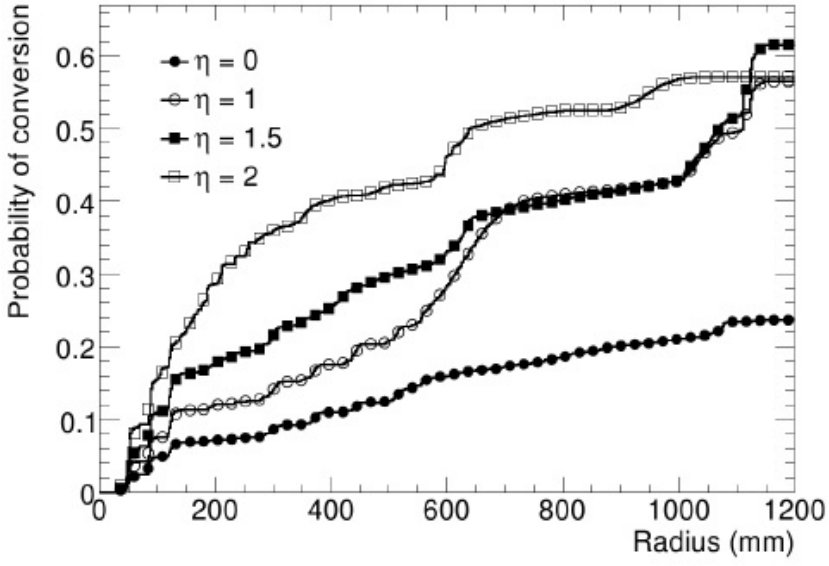

Figure 5.13: Conversion probability of photons with $p_T > 1$ GeV as a function of transverse radius from the interaction point [10].

values. Figure 5.14 shows a sketch of a true 3-prong hadronic tau decay (left) with three real charged pions and a true 1-prong decay with a converted photon from π^0 decay leading to two extra-charged tracks. In the 2 cases, there is the same number of charged tracks so the 1-prong τ could be mis-identified as 3- prong. Another example is when there is true 1-prong τ with only one reconstructed conversion tracks, the event is reconstructed as 2-prong. For the official ATLAS analysis, τ candidates reconstructed as 2-prong are currently rejected.

Figure 5.14: Sketch of true 3-prong hadronic tau decay (left) and true 1-prong decay with the conversion of one photon (right).

This $\pi^{\pm}/e^{\pm}$ mis-identification, leading to wrong tau track multiplicity, makes the tagging of photon conversion tracks an important step in the hadronic tau reconstruction.
Various photon conversion algorithms, called conversion taggers, have been developed in ATLAS. In the following section, we will describe two conversion algorithms, the "Single track tagger" and the "Double track tagger", to decide for each track of reconstructed τ candidate if it is a track from a photon conversion or not.

5.3.1 Single Track Tagger (STT)

It is an algorithm aiming at finding conversion tracks in the hadronic tau decay products using only tracking variables from the inner detector ID.
At the beginning, this algorithm was developed to recover the tau candidate reconstructed as 2-prong (taus with two reconstructed tracks). These taus are usually rejected. In some cases, they are true 1-prong (or 3-prong) taus but with an extra-charged track (mainly from photon conversion) in case of true 1-prong and with one missing track in case of 3-prong decay. For the conversion related study, we will focus on the 1-prong case where the extra-track could originate from photon conversion in true 1-prong ($+\pi^0$) which constitutes the major part of hadronic tau decay ($\sim$ 70 %) as shown in Figure 5.1.
Table 5.1 shows, for each true tau decay mode, the different reconstructed n-prong cases with their relative fractions. For example, looking at the true 1-prong+$1\pi^0$ mode, with the highest hadronic tau decay branching ratio, and with the presence of π^0 which will leads to two photons and so probably conversion tracks, we see that 10 % are reconstructed as 2-prong decay and then are rejected. The conversion

tracks are not the only source of extra charged tracks leading to 2-prong reconstruction, they can originate also from pileup and underlying events. An illustration of this false reconstruction can be seen in Figure 5.15 with the sketch of a true 1-prong+$1\pi^0$ decay (left) reconstructed as 2-prong (right). The reconstructed tracks are divided into two categories:

- Signal tracks: Matched to a true charged pion from the hadronic tau decay.
- Background tracks: Not matched to a true charged pion from the tau decay but originating from conversion, pileup or underlying events.

True tau decay	1p+$0\pi^0$ (20%)	1p+$1\pi^0$ (42%)	1p+$2\pi^0$ (14%)
Nprong=0	6	7	7
Nprong=1	86	79	74
Nprong=2	5	10	13
Nprong=3	1	3	5
Nprong=4	<1	<1	1
Nprong=5	<1	<1	<1

Table 5.1: The different reconstructed n-prong modes for each true hadronic tau decay channel determined using H$\longrightarrow \tau\tau$ MC sample.

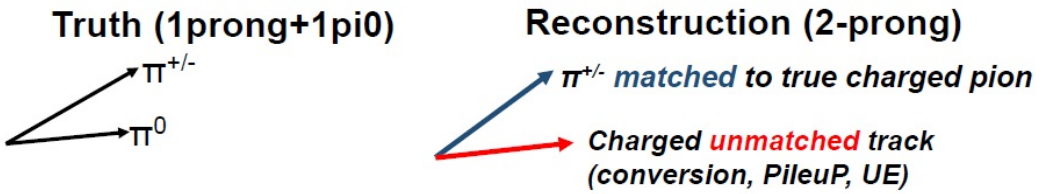

Figure 5.15: Sketch of a true 1-prong+$1\pi^0$ tau decay (left) and its reconstruction as 2-prong decay (right) with one track matched to a charged pion and an extra charged track from conversion, pileup or underlying event.

5.3.1.1 Discrimination variables between signal and background tracks

The study of discrimination power between signal and background tracks has been done using a H$\longrightarrow \tau\tau$ MC sample.
The taus reconstructed as 2-prong and matched to a true hadronic tau ($\Delta R < 0.2$) are selected and used for this study. A ΔR matching is then performed at the track level where one of the two tracks has to be matched to a true tau track ($\Delta R < 0.01$) and the other one is unmatched to a tau track. Using variables only from the inner detector, three of them have shown a discrimating power:

- TRT (transition radiation tracker) high threshold outliers ratio (TRT HTR): It is the fraction of high threshold hits per track. Given the fact that the emission of transition radiation is much more likely for an electron than for a pion of the same momentum, an important discrimination between electron-pion is expected from this variable. Figure 5.16 shows the the probability of a TRT high-threshold (HT) hit as a function of the Lorentz factor, γ, for the TRT barrel and end-cap regions, as measured in 7 TeV collision events. As expected from the production of transition radiation (TR), we see that the probability of a HT hit increases for particles with a gamma-factor above 1000, which enables the TRT to separate electrons from pions over a momentum range between 1 GeV and 150 GeV [12].

- Conversion radius R_{conv}: It is the distance in the transverse plane between the interaction point and the place where the conversion occurs [11]. Rconv is expressed by $\sqrt{\frac{d_0 p_T}{0.15B}}$ Where d_0 is the impact parameter defined as the shortest in r-ϕ plane distance between the beam line and the trajectory of the particle. p_T is the transverse momentum and B is the magnetic field. An geometrical illustration of this variable is shown in Figure 5.17.

- nBlayer Hits: It is the number of hits in the innermost detector B-Layer. This variable can help on tagging conversion tracks because the conversion happens in most cases after the B-Layer thus leaving no hits.

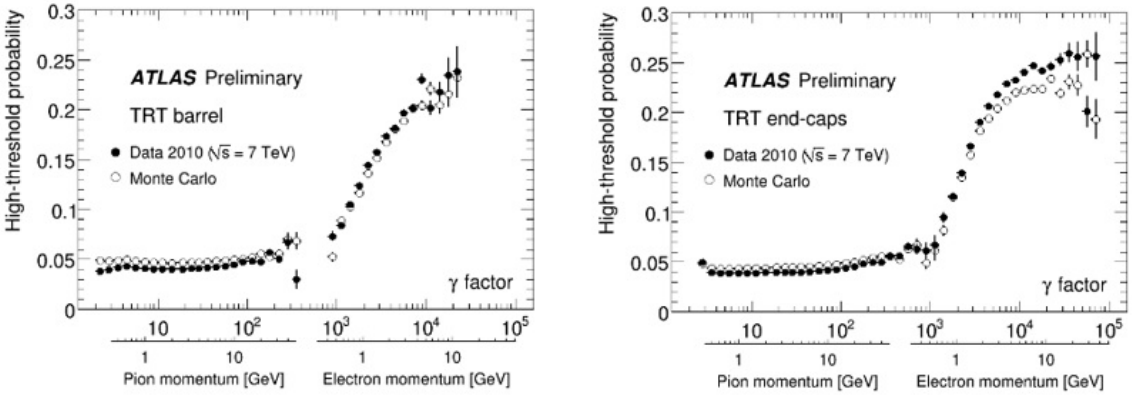

Figure 5.16: Plots showing the probability of a TRT high-threshold hit as a function of the Lorentz factor, $\gamma = \frac{E}{m}$, for the TRT barrel (left) and end-cap (right) regions, as measured in 7 TeV collision events.

The distributions of the TRT HTR for signal and background tracks in the reconstructed 2-prong taus matched to true 1-prong real taus are shown in Figure 5.18 for the different bins on true π^0 number. We see that for the background

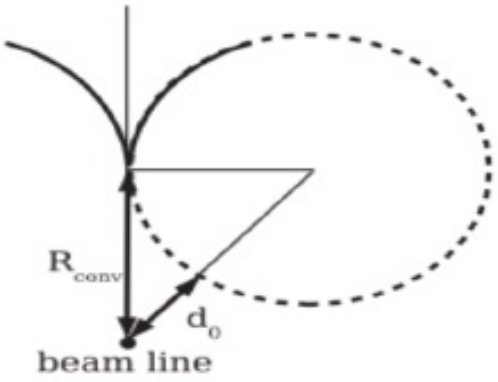

Figure 5.17: Schematic illustration of the distance R_{conv} from the beam line to the point where the conversion occured. Here d_0 is the impact parameter.

tracks, in cases with more than one π^0, there are more events at high values. This is expected since the background track is more likely coming from photon conversion, while signal tracks (charged pions) are at lower values.
Figure 5.19 shows the distribution of the absolute value of R_{conv} for the signal and background tracks of the reconstructed 2-prong taus in the true 1-prong decay bin for the different bins on true π^0 number (left). We see that at high value of R_{conv}, there are more background tracks than signal, and this is expected because conversion tracks are supposed to have high R_{conv} values compared to pion tracks from tau decay.

The same kind of distributions are shown for the nBlayer hits variable in Figure 5.20. In the true 1-prong bin (left), there is more background tracks at nBlayer Hits = 0 than signal, when produced with more than one true π^0, which is expected since photon conversion could occur after the B-Layer.

5.3.1.2 Variables combination

The discriminating variables between signal and background tracks, are then combined in two dimension plots. This is done using the following strategy:

- Combine the two variables TRT HTR and R_{conv} in a 2-dimension plot separately for signal and background tracks.
- Do this for nBlayer = 0 and nBlayer > 0 cases separately.

Figure 5.21 (a) shows the 2-dimensional plot for signal tracks for nBlayer Hits = 0. Most of signal tracks (charged pions) are in the low TRT HTR and R_{conv} regions. Figure 5.21 (b) shows the same plot for background tracks where we can

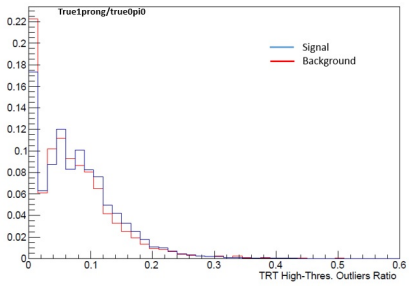

(a) True1prong+$0\pi^0$

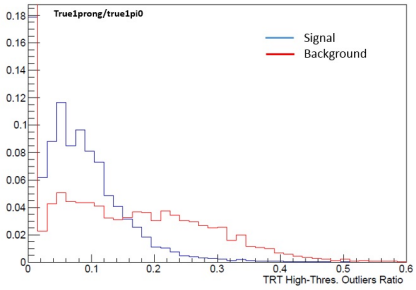

(b) True1prong+$1\pi^0$

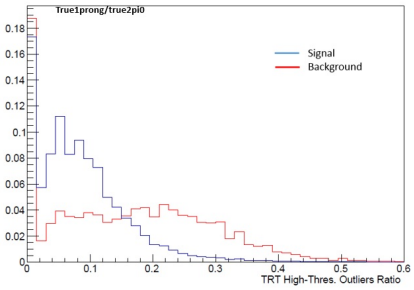

(c) True1prong+$2\pi^0$

Figure 5.18: TRT HTR distribution for signal (blue) and background (red) tracks in true 1-prong bin ($n_{\pi^0} = 0$ (a),1 (b),2 (c)).

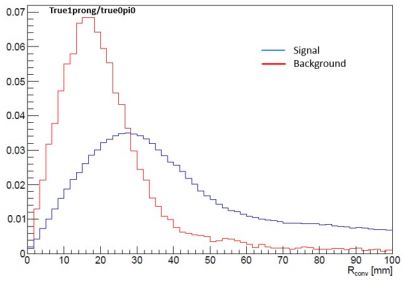

(a) True1prong+$0\pi^0$

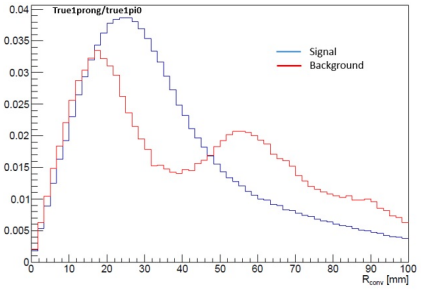

(b) True1prong+$1\pi^0$

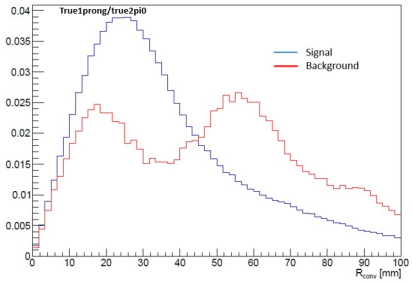

(c) True1prong+$2\pi^0$

Figure 5.19: R_{conv} distribution (absolute value) for signal (blue) and background (red) tracks in true 1-prong bin ($n_{\pi^0} = 0$ (a),1 (b),2 (c)).

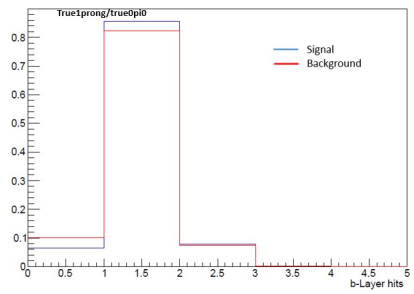

(a) True1prong+$0\pi^0$

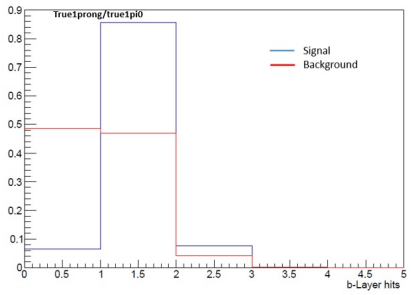

(b) True1prong+$1\pi^0$

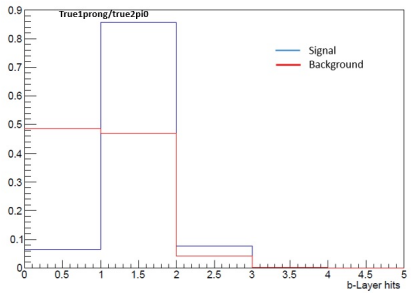

(c) True1prong+$2\pi^0$

Figure 5.20: Left: nBlayer hits distribution for signal (blue) and background (red) tracks in true 1-prong bin ($n_{\pi^0} = 0$ (a),1 (b),2 (c)).

see two families: Low TRT HTR and R_{conv} which corresponds to signal-like tracks and the high TRT HTR and R_{conv} which corresponds to conversion-like tracks.

A linear cut is then applied to separate the phase space between signal and background. A two dimension scan of the parameters a and b has been performed in order to optimize the separation between signal and background tracks provided by the cut line. Figure 5.21 shows different cut lines that correspond to different metric that have been tested ($\frac{S}{\sqrt{B}}$, LLH). No important difference was seen from the different metrics, and a likelihood one was chosen.
Figure 5.22 shows the same plots but for tracks with nBlayer > 0, where an extra sensitivity can be gained. A 2-dimensional scan of the a and b parameters are done also for this case.

5.3.1.3 Methodology

As mentioned previously, the performance of this algorithm has been first tested on hadronic taus reconstructed as 2-prong using H $\longrightarrow \tau\tau$ MC sample, in order to see how efficient is this method in recovering real 1-prong taus reconstructed as 2-prong mainly because of an extra-charged track from a photon conversion.
To exploit the discrimination power between signal (charged pions) and background (mainly conversions) from the 2-dimensional cut method described in the previous

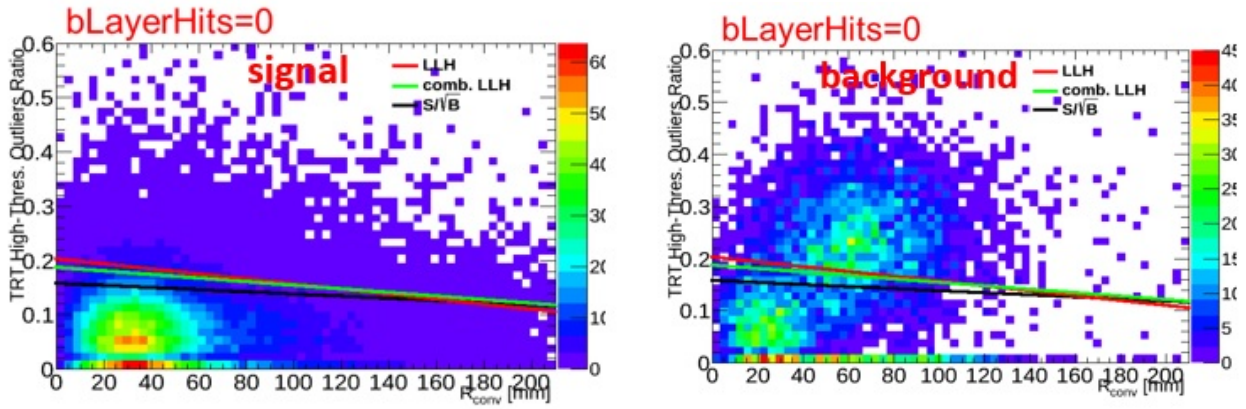

(a) (b)

Figure 5.21: Plot showing the two dimensional combination of TRT HTR and R_{conv} for signal tracks (matched to true pions) (a) and for background tracks (not matched to charged pions) (b) for tracks with nblayer=0. The different lines corresponds to 2-dimensional polynomial cuts performed by a scan which optimize the separation between signal and background.

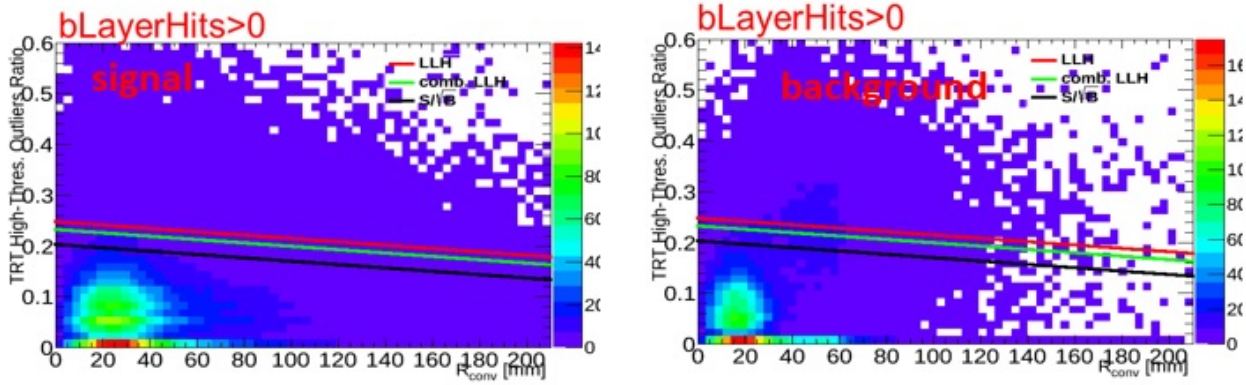

(a) True1prong+0π^0 (b) True3prong+0π^0

Figure 5.22: Plot showing the two dimensional combination of TRT HTR and R_{conv} for signal tracks (matched to true pions) (a) and for background tracks (not matched to charged pions) (b) for tracks with nblayer=1. The different lines corresponds to 2-dimensional linear cuts performed by a scan which optimizes the separation between signal and background.

paragraph, the following methodology has been used:

- Select tau candidates reconstructed as 2-prong taus.
- Run over the two tracks of these candidates. For each track, the TRT HTR, the nBlayer Hits and the R_{conv} variables are available.

- Test for each track if it has a TRT HTR lower than aR_{conv} + b (which means that the track is in the signal-like region below the triangle cut line). If the track passes this selection, it will be considered as "good" track (charged pion). Otherwise, it will be considered as "bad" track (potentially a conversion).

- If one of the two reconstructed tracks is "good" and the other one is "bad", the tau candidate is corrected from 2-prong reconstructed tau to 1-prong. Otherwise, the tau candidate is kept as 2-prong.

Table 5.2 shows, for 2-prong reconstructed taus, the proportion of candidates where the 2-prong bin is corrected to 1-prong, and the proportion where the two tracks are found to be good or bad.
This is shown for different 1-prong configurations.
The results are given separately with and without applying an identification requirement on the tau candidate (see Section 5.1.3).
We can see that the correction increases with the number of π^0. Table 5.3 shows the same results but only on reconstructed 2-prong taus without any truth matching.

1pr+$0\pi^0$	No TauID (%)	With TauID (%)
Correction	11	10
2 good tracks	88	88.5
2 bad tracks	0.7	1

1pr+$1\pi^0$	No TauID (%)	With TauID (%)
Correction	33	42
2 good tracks	62	51
2 bad tracks	5	7

1pr+$2\pi^0$	No TauID (%)	With TauID (%)
Correction	39	45
2 good tracks	55	47
2 bad tracks	6	8

Table 5.2: Three tables showing the proportion of reconstructed 2-prong tau candidates corrected to 1-prong, or having two signal or two background tracks, after applying the 2-dimensional cut. This is shown for different true 1-prong configurations.

In order to further discriminate between signal pions tracks and background tracks (especially conversion tracks), additional information from the variable R_{conv} has been exploited. Actually, this information is related to the sign of R_{conv} which

	No TauID (%)	With TauID (%)
Correction	17	23
2 good tracks	81	74
2 bad tracks	2	3

Table 5.3: Proportion of reconstructed 2-prong tau candidates corrected to 1-prong, or having two signal or two background tracks, after applying the 2-dimensional cut. No truth matching is applied on these recontructed taus.

is the sign of the product $d_0 \times p_T$. Geometrically, for tracks originating from a photon conversion, this product has a given sign (positive in our case). This can be shown in Figure 5.23 where the tracks labeled "1" and "4" represent tracks from a photon conversion vertex. We can see that the product of the sign of the impact parameter (d_0 in the Figure) and the charge of conversion track is always the same. Figure 5.24 shows the signed R_{conv} (R_{convII}) distribution for signal and background tracks for 2-prong reconstructed taus with different number of π^0. One observes an asymmetric peak of background tracks in the positive region. This peak corresponds to conversion tracks since R_{convII} has always a unique sign in case of conversion. It becomes more important when the true number of π^0 increases.
In addition to the two dimensional method, a cut on R_{convII} has been added to the algorithm. Tracks found in the signal-like region by the two-dimensional cut need to have an R_{convII} lower than 40 mm to be tagged as signal tracks, otherwise they will be considered as background.

Table 5.4 shows again the same results as Table 5.3 on reconstructed 2-prong taus without matching to truth but adding the cut on R_{convII}. This shows a net improvement as compared to Table 5.3.

	No TauID (%)	With TauID (%)
Correction	32	44
2 good tracks	60	41
2 bad tracks	8	15

Table 5.4: Proportion of reconstructed 2-prong tau candidates corrected to 1-prong, or having two signal or two background tracks, after applying the 2-dimensional cut and the cut on R_{convII}. No truth matching is applied on these recontructed taus.

The performance of this algorithm has been tested to correct the 2-prong reconstructed taus to 1-prong by rejecting non pion tracks, mainly conversion tracks. We will see in this chapter how this algorithm has been then used as a finder of photon conversion tracks in the reconstructed taus.
In the next paragraph, we will see another algorithm that has been also developed to tag conversion tracks in hadronic tau decays.

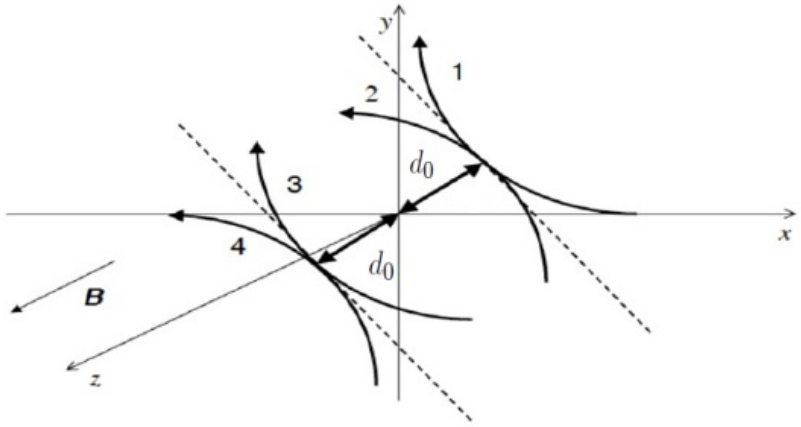

Figure 5.23: A geometrical illustration showing the correlation between the sign of the conversion track (tracks 1 and 2) and the sign of the impact parameter (d_0). The product has always the same sign.

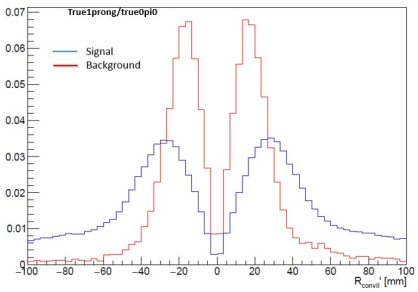

(a) True1prong+$0\pi^0$

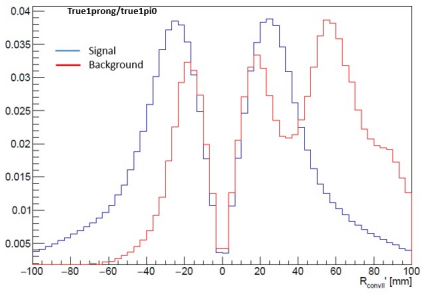

(b) True1prong+$1\pi^0$

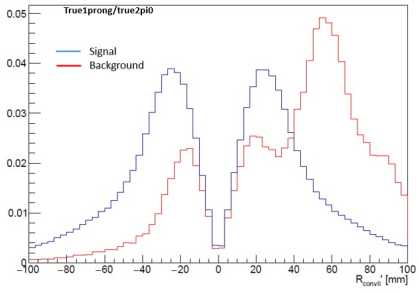

(c) True1prong+$2\pi^0$

Figure 5.24: Signed R_{conv} distribution for signal (blue) and background (red) tracks in true 1-prong bin ($n_{\pi^0} = 0$ (a),1 (b),2 (c)).

5.3.2 Double Track Tagger (DTT)

The DTT is an algorithm based on finding the conversion vertices in hadronic tau decays. This vertex is usually produced far away from the interaction point, and it is possible to reconstruct a secondary vertex distinct from the primary vertex.
An ATLAS algorithm, called "Conversion Finder Tool", has been used in this tagger to find conversion vertices candidates using the reconstructed charged tracks. It enumerates all oppositely charged track pairs. For each track pair, a vertex is fitted and a selection is made on the parameters of the fitted vertex [13] [14]. The vertex fitting is based on fast Kalman filtering as described in detail in [15]. Some of parameters used by this algorithm to find the conversion vertices are the following:

- M_{vertex}: The invariant mass of the fitted vertex. It is the mass of the parent particle of the track pair. And since the photon is the parent particle of a pair of conversion tracks, the reconstructed invariant mass should be close to zero.
- R_{conv}: The conversion radius as described before.
- $\Delta\phi_{direction}$: The opening angle which is the difference of the track pair initial ϕ direction. In the case of conversion photons, both tracks are expected to move initially in the same direction. Thus this variable should be close to zero.
- $\Delta\eta_{direction}$ The difference of the track pair initial η direction.
- $\frac{\chi^2}{ndf}$: The fit quality derived using least squares minimization.

In order to improve the performance of the "conversion finder tool" to find conversions in hadronic tau decays, the DTT provides an optimization to create a new set of conversion vertices candidates optimized for taus [16]. This is done by:

1. Tune the parameters previously described to search for conversion vertices especially from taus. This tuning is done using a $Z \longrightarrow \tau\tau$ sample. The parameters are plotted for vertices with correctly paired tau conversion tracks (called "signal S") and for vertices with all other track pairs, which could be tau primary track pairs, other conversions in the region, or fake vertices that are formed from incorrectly paired tracks (called "background B"). Figure 5.25 shows the distribution of signal and background vertices for some conversion finding parameters. The dotted vertical lines are the location of the new selection criteria applied to provide an optimised set of conversion vertices for taus based on maximising the "Figure of Merit", $\frac{S}{\sqrt{S+B}}$.
2. Since more than 99.9 % of tau conversion tracks are contained within the region ΔR <0.5, only that region of any reconstructed tau is considered.

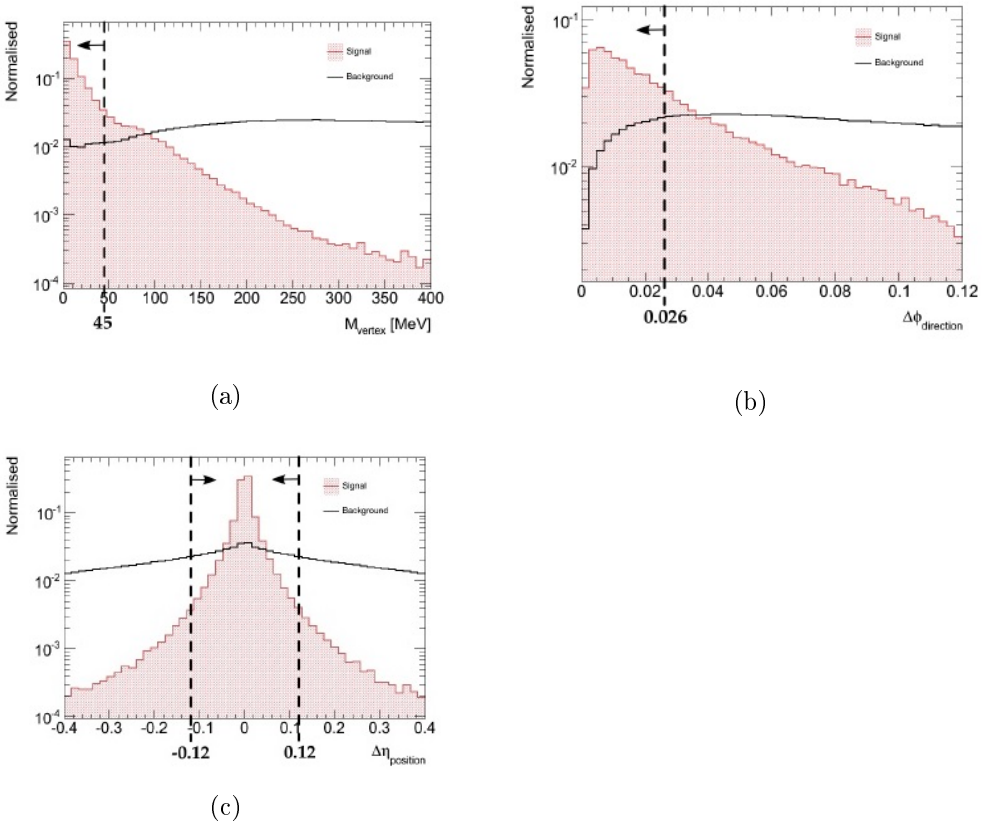

(a) (b)

(c)

Figure 5.25: Signal and background distributions for Conversion Finder parameters (M_{vertex}, $\Delta\phi$ and $\Delta\eta$) before any selection criteria are applied. The dotted line represents the cut used for each variable [16].

In order to tag the conversion tracks by this algorithm, the reconstructed tau tracks are compared to tracks from the vertex found by the vertex fitter already before. If a track is found to belong to these two subsets of tracks, i.e. reconstructed tau tracks and tracks found by the vertex fitter, it is tagged as a conversion.
In the next section we will describe the performance of the two taggers when integrated in ATLAS software.

5.4 Conversion taggers performances

5.4.1 Overview of ATLAS Software framework

As described in the previous Chapter (Section 4.1), the reconstruction of ATLAS events is done using a set of algorithms running of both data and MC simulation.
The ATLAS reconstruction software is called "ATHENA". There are successive versions, called releases, where improvements are introduced to the software with each new version (new reconstruction and identification functionality, new calibrations, bugs fixes,...).
During Run I analysis, the technical reconstruction chain of physics objects is shown in Figure 5.26. Starting from raw data, the reconstruction algorithms run to produce files called ESD (Event Summary Data) [17]. These files contain the physics objects and additional information, such as tracks, cells and calorimeter clusters. The information is then reduced by moving from ESD to the so-called AOD (Analysis Object Data), where only physics objects are kept. Derived files are then produced, called DPD (Derived Physics Data), enabling faster access to stored information. A specific DPD format, called D3PD was used in this study. These are root files that can be used for the final physics analysis.

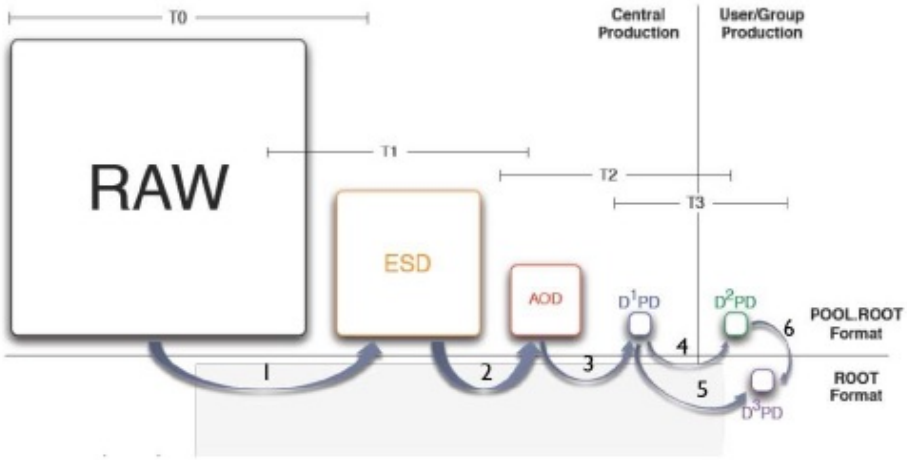

Figure 5.26: Different format of files for analysis in ATLAS during Run I [17].

A new infrastructure has been developed for the Run II analysis. It merges the AOD and D3PD steps into one format file called "xAOD" and will be discussed in more details in Chapter 6.

5.4.2 Conversion taggers in Athena

Both taggers have been implemented in the tau reconstruction part of Athena, called "tauRec".
The first test and validation of the new implemented STT inside Athena, and then a full performance study has been done using first the Run I analysis environment. After moving to the new ATLAS software infrastructure, the performance study has been redone since all algorithms needed to be validated after this migration.
The conversion taggers performance results are shown first using 8 TeV MC samples, then recalculated using 13 TeV samples.

5.4.3 Performance

The performance of the two conversion taggers STT and DTT has been evaluated as follows:

1. Produce two samples, D3PD or xAOD, depending on the environment (Run I or Run II). Each one by activating one of the two conversion taggers in Athena. This dumps the conversion information track by track obtained from the corresponding conversion tagger.

2. Run over all the taus inside the files and over all the reconstructed tau tracks.

3. Calculate the two following performance quantities:

   - Conversion tagging efficiency:

   $$E_{ff}^{conv} = \mathrm{N}_{\mathrm{Conv}}^{\mathrm{flagged}} / \mathrm{N}_{\mathrm{Tot}}^{\mathrm{Conv}} \tag{5.1}$$

   which is the efficiency of tagging a reconstructed track as conversion when it is a true conversion, where:

   – $\mathrm{N}_{\mathrm{Conv}}^{\mathrm{flagged}}$: Number of tracks matched to true conversion tracks and flagged as conversion by the given tagger.
   – $\mathrm{N}_{\mathrm{Tot}}^{\mathrm{Conv}}$: Total number of tracks matched to true conversions

   - Fake rate:

   $$F_r^x = \mathrm{N}_{\mathrm{x}}^{\mathrm{flagged}} / \mathrm{N}_{\mathrm{Tot}}^{\mathrm{x}} \tag{5.2}$$

x can be a charged pion, pileup or underlying event track (but not a conversion track). This is the rate to tag a track as conversion by the tagger when it is not a true conversion, where:

- $N_x^{flagged}$: Number of tracks matched to x type of particle and flagged as conversion by the tagger
- N_{Tot}^{x}: Total number of tracks matched to x type of particles.

A truth matching tool [18] has been used in order to know the true origin of each reconstructed track (conversion, charged pion, pileup or underlying event).

5.4.3.1 Performances in Run I environment

The STT is activated when producing a D3PD from an AOD input file. The first format of the conversion information dumped to the D3PD is a container for each reconstructed tau, containing the number of tracks classified as conversion by the STT.
A validation of the implementation has been performed using a Higgs$\longrightarrow \tau\tau$ 8 TeV MC sample. This was done by producing the same results as in Table 5.3. The numbers have shown a compatibility between the results from the standalone analysis and from the STT inside Athena.
After validating the STT, in order to perform a more dedicated performance measurement of the two conversion taggers, some modifications have been introduced in the software in order to produce the information per each reconstructed tau track. This means that for a given reconstructed hadronic tau, we have in the D3PD an information associated to each tau track deciding if it is a conversion or not.
The performances have been calculated for core tracks ($\Delta R < 0.2$) since most of prompt pions and conversion tracks are within this region. The $|\eta|$ >2 region has been also excluded given the acceptance of the TRT detector.
Table 5.5 shows the conversion tagging efficiency on reconstructed hadronic taus, for 1 and 3 prong combined and separately. The performance is comparable between the two taggers with a slightly better efficiency from the DTT.
Table 5.6 shows the global fake rate and separately for the three types on non-conversion tracks: charged pions, pileup and underlying events. The STT has shown a clearly higher fake rate compared to the DTT. This is due to the fact that the STT does not use a vertex information as it is the case with the DTT and therefore the rejection power between conversion and other type of tracks is less good. We can see that the global fake rate is highly dominated by the one with charged pions (F_r^{pions}) since most of the charged tracks inside the core region, for reconstructed 1 or 3 prong taus that passed the identification selection, are charged pions.

Fake rate reduction in STT The reduction of the fake rate in the STT is a critical thing to do in order to mainly reduce the rejection of true charged pions from the tau track multiplicity when they are mis-identified as conversion tracks by

E_{ff}^{conv}	STT	DTT
1 and 3 prong (%)	65 ± 0.8	68 ± 0.8
1 prong (%)	67 ± 0.85	71.5 ± 0.85
3 prong (%)	50 ± 2.4	44.5 ± 2.4

Table 5.5: Conversion tagging efficiency for combined 1 and 3 prong reconstructed taus bin and for each bin separately. This is obtained using a $Z \longrightarrow \tau\tau$ events.

F_r^x	STT	DTT
F_r^{global} (%)	7.5 ± 0.1	0.5 ± 0.1
F_r^{pions} (%)	7 ± 0.1	0.36 ± 0.1
F_r^{pileup} (%)	4 ± 0.5	0.6 ± 0.5
F_r^{UE} (%)	13 ± 0.6	2.4 ± 0.6

Table 5.6: Fake rate calculated using 1 and 3 reconstructed hadronic taus. This is given globally (fake rate with all the type of non-conversion tracks combined): F_r^{global}, and separately: F_r^{pions}, F_r^{pileup}, F_r^{UE}.

the conversion tagger.
Two variables have been exploited to further reduce the relatively high fake rate of the STT:

- The transverse momentum of the track (p_T^{trk}): Figure 5.27 shows the transverse momentum distributions of reconstructed hadronic tau decay tracks. This is shown for tracks matched to true charged pions (blue) and true conversion tracks (red). Truth-matched conversion tracks are at low p_T^{trk} values compared to charged pions. Almost all of them are at p_T^{trk} below 20 GeV. A cut at this value is also tested to reduce the mis-identification of all charged pion tracks that have a p_T^{trk} greater than 20 GeV.

- The signed R_{conv}: As we have already seen in Section 5.3.1.1, the conversion tracks have higher signed R_{conv} compare to pion tracks (see Figure 5.19). An explicit cut on this variable can be applied in order to reduce the fake rate. This means that a track should have a signed R_{conv} >40 mm to be tagged as conversion track by the STT.

The STT performance has been studied after applying these additional two cuts on top the main 2-dimensional cut already described. Table 5.7 shows E_{ff}^{conv} and F_r^x after applying the p_T^{trk} cut. The efficiency loss is very limited (65 % to 62 %), while a very good reduction of the global fake rate is achieved (40 %). This is dominated by the reduction of fake rate with charged pions, while pileup and underlying events fakes rates remain almost unchanged. This is expected since

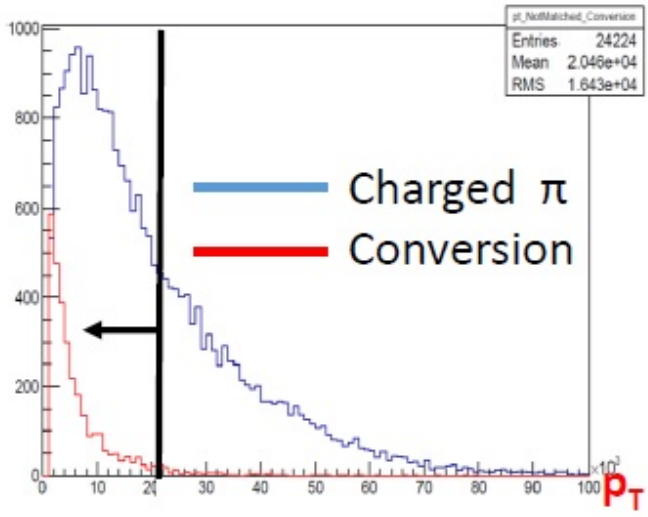

Figure 5.27: The transverse momentum distribution of tracks for reconstructed hadronic taus. Red: Tracks matched to true conversion. Blue: Tracks matched to true charged pions.

these tracks are supposed to have also low p_T^{trk} values.
Table 5.8 shows the performance obtained after applying the cut on signed R_{conv}. The fake rate is reduced by almost factor 2 for charged pions and a high reduction of pileup (PU) and underlying events (UE) fakes rates, but with about 20 % of loss on conversion tagging efficiency. The performance by applying both cuts is shown in Table 5.9 where we see the loss on efficiency caused by the signed R_{conv} cut, with a very good reduction of global fake rate which become in the same order as for the other tagger.

E_{ff}^{conv}	No p_T^{trk} cut	With p_T^{trk} cut
1 and 3 prong (%)	65	62
1 prong (%)	67	64
3 prong (%)	50	48

F_r^x	No p_T^{trk} cut	With p_T^{trk} cut
F_r^{global} (%)	7.5	4.7
F_r^{pions} (%)	7	4.2
F_r^{pileup} (%)	4	4
F_r^{UE} (%)	13	12

Table 5.7: The STT conversion tagging efficiency and fake rate compared before and after applying the p_T^{trk} on top of the main 2-dimensional cut.

E_{ff}^{conv}	No additional cuts	With signed R_{conv} and p_T^{trk} cuts
1 and 3 prong(%)	65	54
1 prong(%)	67	55
3 prong(%)	50	43

F_r^x	No additional cuts	With signed R_{conv} and p_T^{trk} cuts
F_r^{global} (%)	7.5	3.6
F_r^{pions} (%)	7	3.7
F_r^{pileup} (%)	4	0.17
F_r^{UE} (%)	13	2.1

Table 5.8: The STT conversion tagging efficiency and fake rate compared before and after applying the signed R_{conv} cut on top of the main 2-dimensional cut.

E_{ff}^{conv}	No signed R_{conv} cut	With signed R_{conv} cut
1 and 3 prong (%)	65	49
1 prong (%)	67	50
3 prong (%)	50	38

F_r^x	No signed R_{conv} cut	With signed R_{conv} cut
F_r^{global} (%)	7.5	1
F_r^{pions} (%)	7	1
F_r^{pileup} (%)	4	0.17
F_r^{UE} (%)	13	2

Table 5.9: The STT conversion tagging efficiency and fake rate compared before and after applying the p_T^{trk} and signed R_{conv} cuts on top of the main 2-dimensional cut.

Despite the better performance shown by the DTT compared to the STT, a CPU timing study (average time needed to process an event, number of time the algorithm is called,...) has been performed and shown a CPU overhead of the DTT compared to the STT. This is expected since the DTT loops over all the combination of paired charged tracks to fit the conversion vertices and this is supposed to be time consuming.

5.4.3.2 Performances in Run II environment

To reevaluate the performance after moving to the new Athena ATLAS software, the conversion taggers have been migrated and tested.

STT in the new software Table 5.10 shows the comparison of performances between old - 8 TeV and new - 8 TeV for the STT, using the baseline 2-dimensional cut. The conversion tagging efficiency is almost similar. The fake rate has shown a small reduction for charged pions and an important one for UE, while no PU was available yet in the used sample at that moment.
In order to understand the fake rate difference between the two frameworks, the input variables used in the STT have been investigated.

STT	Old - 8 TeV	New - 8 TeV
E_{ff}^{conv} (%)	65	66
F_r^{pions} (%)	7	5
F_r^{pileup} (%)	-	4
F_r^{UE} (%)	13	4

Table 5.10: The performance of the STT (efficiency and fake rates) compared between Athena old - 8 TeV and new - 8 TeV.

Figure 5.28 shows the R_{conv} and TRT HTR ratio distributions for reconstructed hadronic tau tracks matched to true pion tracks, for the old environment (blue) and the new one (red). We see that R_{conv} is almost similar, while the TRT HTR distribution shows that, in the new environment, there is more pion tracks at low values, and since low TRT HTR tracks are not tagged by the STT as conversion, so this explain the reduced charged pion fake rates in the new environment. Figure 5.29 shows the same distributions for reconstructed tracks matched to true UE where R_{conv} is also similar between the two frameworks while TRT HTR is lower in the new framework, thus explaining why we have lower UE fake rate in the new framework. The difference on TRT HTR between the two frameworks is due to an updated calculation of this track variable in the new xAOD samples.
Distribution for reconstructed tracks matched to true conversions show similar behavior in the two frameworks, thus explaining why the conversion tagging efficiency is similar.

DTT in the new software The evaluation of the DTT performance after moving to the new ATLAS software has shown a clear discrepancy compared to the original performance in the old framework. This mainly shows up in the fake rate as can be seen in Table 5.11 where the charged pion fake rate increases from 0.36 to 12 %.

5.4.3.3 Performance on 13 TeV samples

After studying the performance of the STT on 8 TeV MC samples, the performance has been re-evaluated on 13 TeV produced xAOD for Z$\longrightarrow \tau\tau$ MC sample.
Using the main 2-dimensional cut only, the conversion tagging efficiency and the

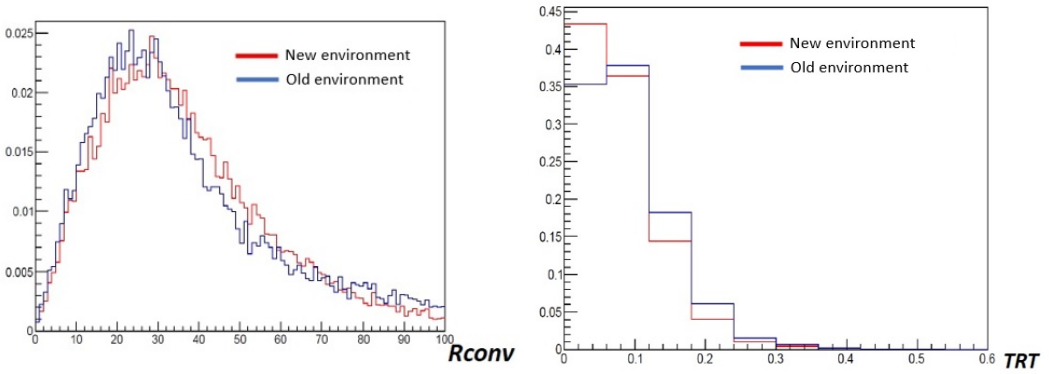

(a) (b)

Figure 5.28: Distributions of R_{conv} (a) and TRT HTR (b) for reconstructed tau tracks matched to true charged pions in old - 8TeV (blue) and new - 8TeV (red) environments.

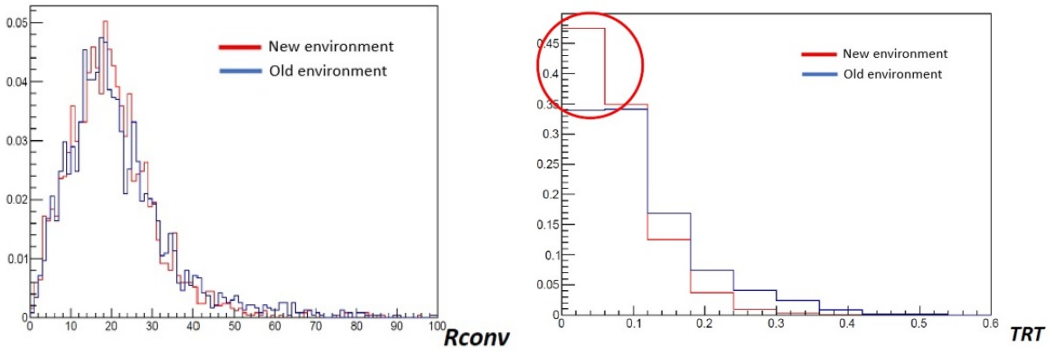

(a) (b)

Figure 5.29: Distributions of R_{conv} (a) and TRT HTR (b) for reconstructed tau tracks matched to true underlying event tracks in old - 8TeV (blue) and new - 8TeV (red) environments.

STT	Old - 8 TeV	New - 8 TeV
E_{ff}^{conv} (%)	68	70
F_r^{pions} (%)	0.36	12

Table 5.11: The performance of the DTT (efficiency and fake rates) compared between the old - 8 TeV and new - 8 TeV environments.

charged pion fake rate are shown in Table 5.12. The efficiency and the fake rate show an important increase by moving to 13 TeV. This is understood by looking again at the TRT HTR distributions for reconstructed tracks (Figure 5.30) matched

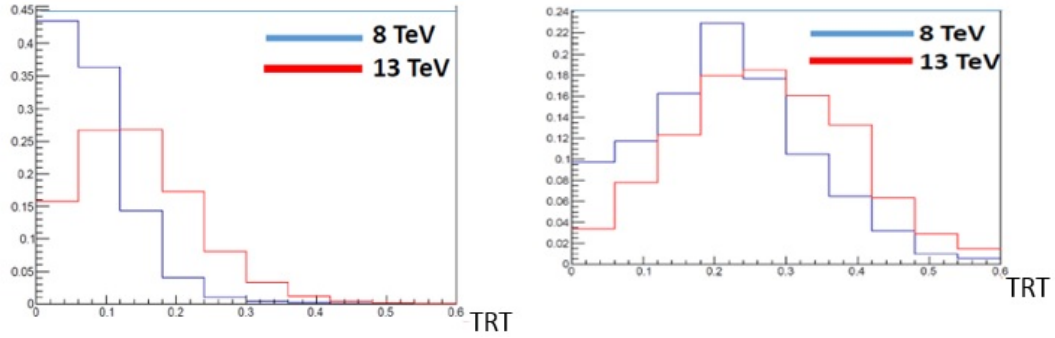

(a) pion-truth-matched (b) conversion-truth-matched

Figure 5.30: Distributions of TRT tracks matched to true charged pions on 8 TeV (blue) and 13 TeV (red) sample (a), and the same distribution for tracks matched to true conversions (b).

to true charged pions (a) and true conversions (b). The distributions shows clearly that the higher center-of-mass energy leads to higher track TRT HTR. This appears then in the increasing of both efficiency and fake rate, since the higher TRT HTR values lead to higher probability for the track to be tagged as conversion by the STT.

STT	8 TeV	13 TeV
E_{ff}^{conv} (%)	65	81
F_r^{pions} (%)	5	39

Table 5.12: The performance of the STT (efficiency and fake rates) compared between 8 TeV and 13 TeV on Z $\longrightarrow \tau\tau$ MC sample after applying the new cuts on top of the 2-dimensional method.

In order to improve the new performance results of the STT obtained for 13 TeV samples, i.e. reduce the very high fake rate compare to the 8 TeV numbers, a tuning of the 2-dimensional cut parameters has been tested but the results did not show a clear improvement on the fake rate reduction.
By using the exclusive cuts on signed R_{conv} and the transverse momentum p_T^{trk} of the reconstructed tau track (described in Section 5.4.3.1) on top of the 2-dimensional algorithm, a very good reduction of the fake rate has been achieved with some loss on the efficiency. The final performance results are shown in Table 5.13 where we can see that by using this method, E_{ff}^{conv} and F_r^{pions} become comparable to the basic performances (only 2-dimensional cut) achieved in 8 TeV case (see Table 5.5) .

13 TeV	STT	STT with new cuts
E_{ff}^{conv} (%)	81	60
F_r^{pions} (%)	39	5

Table 5.13: The performance of the STT (efficiency and fake rates), for 13 TeV samples, compared before and after applying the new cuts on top of the 2-dimensional method, using $Z \longrightarrow \tau\tau$ sample.

5.5 Track classification status

The STT described in the previous section is implemented as the default track conversion tagger in Athena by providing, for each reconstructed tau track, a information deciding if it is tagged or not as a conversion. However, the output information of this algorithm is not used in the current tau reconstruction algorithm developed for the Run II analysis, the Tau Particle Flow, described in Section 5.2.1, where the charged tracks classification of the reconstructed tau tracks is not yet incorporated in this algorithm.
In the last two years, a new global track classification algorithm has been developed. It uses a multivariate method BDT (Boosted Decision Tree) to categorizes the tracks into four categories: Tau-pion tracks, conversion tracks, isolation tracks (tracks from the same interaction) and fake tracks (including pileup). Many variables are used as inputs in the BDT such as the track rapidity, the impact parameter, the conversion radius,...
This algorithm has shown a good performance on correctly tagging the charged tracks, hence improve the tau reconstruction efficiency (by reconstructing a tau with correct number of prongs), and it is targeted to be implemented into the new reconstruction algorithm quite soon.
A further targeted goal, using the MVA track classification method, is to adapt the tau identification algorithm to use the pion and isolation tracks to improve the rejection against fake QCD jet background, and the tagged conversion tracks to help on π^0 reconstruction.

Bibliography

[1] J. Beringer et al. (Particle Data Group Collaboration), Review of Particle Physics (RPP), Phys. Rev. D86, 010001 (2012). (Cited on page 110.)

[2] ATLAS NOTE. ATL-PHYS-PUB-2015-045 2nd November 2015. Reconstruction, Energy Calibration, and Identification of Hadronically Decaying Tau Leptons in the ATLAS Experiment for Run-2 of the LHC (Cited on pages 112, 113, 114, 115, 116, 117, 118 and 119.)

[3] http://cds.cern.ch/record/1700870, ATLAS Collaboration, ATLAS-CONF-2014-018 (2014) (Cited on page 112.)

[4] ATLAS Collaboration, Monte Carlo Calibration and Combination of In-situ Measurements of Jets in ATLAS,ATL-COM-PHYS-2015-071 (2015), url: https://cds.cern.ch/record/1987296. (Cited on page 112.)

[5] The ATLAS Collaboration, Identification of Hadronic Decays of Tau Leptons in 2012 Data with the ATLAS Detector, ATLAS-CONF-2013-064 (Cited on pages 116 and 118.)

[6] ATLAS Collaboration, Electron efficiency measurements with the ATLAS detector using the 2012 LHC proton-proton collision data, ATLAS-CONF-2014-032,2014, url: http://cdsweb.cern.ch/record/1706245. (Cited on page 118.)

[7] The ATLAS Collaboration, Reconstruction of hadronic decay products of tau leptons with the ATLAS experiment, (Eur. Phys. J. C76(5) (2016) 1-26) (6 November 2015) (Cited on pages 119, 120, 121, 122, 123, 124 and 125.)

[8] Y.S. Tsai, Rev. Mod. Phys. 46 (1974) 815. (Cited on page 123.)

[9] S.R. Klein, Radiat. Phys. Chem. 75 (2006) 696 (Cited on page 123.)

[10] The ATLAS Collaboration, "Photon Conversions in ATLAS" 2008. (Cited on pages 123 and 125.)

[11] T. Aaltonen et al. (CDF Collaboration) Phys. Rev. D 77, 092001 - Published 16 May 2008. (Cited on page 128.)

[12] https://twiki.cern.ch/twiki/bin/view/AtlasPublic/TRTPublicResults (Cited on page 128.)

[13] H. Zhu, Photon conversion reconstruction and its application to the Higgs search in the ATLAS experiment at the Large Hadron Collider. PhD thesis, University of Sheffield, 2009. (Cited on page 136.)

[14] The ATLAS Collaboration, Photon Conversions in ATLAS, 2008. (Cited on page 136.)

[15] V. Kostyukhin, VKalVrt-package for vertex reconstruction in ATLAS, vol. ATLPHYS- 2003-031, 2003. (Cited on page 136.)

[16] Improving the Reconstruction of Tracks from Hadronic Tau Decays at ATLAS, Kong Guan Tan, Master Thesis. (Cited on pages 136 and 137.)

[17] https ://twiki.cern.ch/twiki/bin/viewauth/Atlas/CoreSoftware. (Cited on page 138.)

[18] https://svnweb.cern.ch/trac/atlasoff/browser/PhysicsAnalysis/TauID/TauAnalysisTools/trunk/doc/README-TauTruthTrackMatchingTool.rst (Cited on page 140.)

Chapter 6

H$\longrightarrow \tau\tau$ analysis in the $\tau_{lep}\tau_{had}$ decay mode

Contents

6.1 Introduction

6.1.1 Overview

After discovering the Standard Model (SM) Higgs boson by ATLAS and CMS collaborations at the LHC Run I in the bosonic decay channels (H$\longrightarrow \gamma\gamma$, H$\longrightarrow$ZZ$\longrightarrow$4l, H$\longrightarrow$WW) [1] [2] as described in Chapter 2, one of the very challenging Higgs boson decay channels is into a pair of tau leptons, H$\longrightarrow \tau^+\tau^-$ with a branching ratio of 6.3 % for a 125 GeV Higgs mass [3]. The motivation of this study is to check the compatibility of the Higgs boson Yukawa coupling to fermions with the SM prediction, and the H$\longrightarrow \tau^+\tau^-$ is the only accessible channel today for the direct observation of this Higgs coupling to leptons. It is also relevant for the measurement of the Higgs boson CP quantum numbers. There is another promising fermionic decay mode to probe this Yukawa coupling, the decay into a pair of bottom quarks, H$\longrightarrow b\bar{b}$, but more favorable signal-to-background conditions are expected for H$\longrightarrow \tau\tau$ decays.

As described in Chapter 5, there are two tau main decay categories, leptonic and hadronic. This leads to three H$\longrightarrow \tau^+\tau^-$ final states:

- $\tau_{lep}\tau_{lep}$: it is a fully leptonic decay final state, H$\longrightarrow \tau^\pm\tau^\pm \longrightarrow l^\pm l'^\pm + 4\nu$, where both taus decay into leptons (l= μ,e). The small branching ratio of this mode (12.4 %) [4] and the worse mass resolution due to the presence of four neutrinos in the final state makes it the less sensitive decay mode despite the high lepton detection efficiency.

- $\tau_{had}\tau_{had}$: it is a fully-hadronic mode, H$\longrightarrow \tau^\pm\tau^\pm \longrightarrow \tau^\mp_{had}\tau^\mp_{had} + 2\nu$, where both taus decay into a hadronic jet. The high branching ratio of 42 % is

affected by the necessity of reconstructing two hadronic jets, and makes it the second most sensitive decay mode.

- $\tau_{lep}\tau_{had}$: H$\longrightarrow \tau^{\pm}\tau^{\pm} \longrightarrow \tau^{\mp}_{lep}\tau^{\mp}_{had} + 3\nu$, where one τ decays leptonically and the other one hadronically. Having the largest branching ratio of 45.6 % and requiring only one τ_{had} makes it the most sensitive final state.

In this thesis, the current status of the H$\longrightarrow \tau_{lep}\tau_{had}$ analysis with the Run II data will be presented. It follows naturally the same lines of the Run I analysis presented here [5]. We will see explicitly in the following sections the main changes of the current analysis with respect to Run I.

6.1.2 Signal and backgrounds

6.1.2.1 Signal

The Higgs production mechanism and the tau decay product specify the experimental event signature of the H$\longrightarrow \tau_{lep}\tau_{had}$ events.
The two dominant Higgs production mechanism contributing to the H$\longrightarrow \tau\tau$ analysis are the ggH and VBF modes (see Chapter 2). The Higgs production associated to a vector boson (VH) and the top-pair associated production mechanisms have lower contribution to this analysis.
The ggH mode has the largest cross-section. Concerning the jet activity for this process, there is a non-negligible multi-jet ggH events due to the higher order QCD corrections for the gluon radiation and top loop.
The VBF mode has the second largest cross-section and has two additional jets in the final state at leading order (the QCD corrections are less important than for ggH since it is based on an electroweak interaction).

6.1.2.2 Backgrounds

The backgrounds can be grouped into three major categories:

- Events containing a true lepton and a true hadronic tau signature. This category is dominated by the Z/$\gamma^* \longrightarrow \tau\tau$ process with a small contribution from diboson VV$\longrightarrow$ l + τ_{had} + X (V= W or Z), $t\bar{t}$, single top processes. The Z/$\gamma^* \longrightarrow \tau\tau$ process is potentially the most dangerous background since it has the same final state as the signal and a mass peak at the Z mass, close to the Higgs mass.

- Events with a QCD jet faking the hadronic tau. This category is dominated by multijet QCD background, W+jets, diboson and top quark background, with a contribution from Z$\longrightarrow$ll + jets (where l = e or μ) background.

- Events with a lepton (mostly electrons) faking the hadronic tau. It is dominated by the Z$\longrightarrow$ll process.

6.1.3 Data and simulated samples

6.1.3.1 Data

The analyzed data correspond to the proton-proton collisons at the center-of-mass energy of 13 TeV collected in 2015 and 2016 with an integrated luminosities of 3.2 fb^{-1} and 10 fb^{-1} respectively (LHC Run II). The two datasets are analysed separately and only the final results correspond to the combination of the two samples. Events are kept if they belong to the so-called "Good Run List (GRL)" which specifies the set of data satisfying our data quality constraints.

6.1.3.2 Simulated samples

The ATLAS simulation infrastructure is used to produce the Monte Carlo samples needed for this analysis, as a part of the so-called ATLAS mc15 production campaign [6].

Signal samples

- The signal samples for the ggF and VBF production modes are modelled with POWHEG generator [7] interfaced with PYTHIA8 [8].
- The ttH mode is generated with McAtNlo [9] interfaced with HERWIG for the parton shower.
- The VH production mode is generated using PYTHIA8 for the parton shower.
- TAUOLA [10] is used to model the τ-lepton decays. All the decay modes of the τ lepton are considered in the event generators.

Background samples

- The V+jets (V= Z,W) background is simulated using MADGRAPH for the hard scattering, and PYTHIA8 for the parton shower. SHERPA 2.2 is used as alternative samples to estimate modeling uncertainties (see Section 6.5.1). The V +jets electroweak production is not included in our MADGRAPH V+jets samples. It is simulated using SHERPA 2.1.
- The $t\bar{t}$ and single top samples are generated with POWHEG and PYTHIA8 is used for the parton shower.
- The diboson samples are simulated with SHERPA 2.1 for both the hard scattering generation and the parton shower.

Each MC sample is passed through the full GEANT4 simulation [11] of the ATLAS detector and is reconstructed with the same software as used for data. For this analysis, the DAOD-HIGG4D2 derivation and the ntuple production xTau framework are used (See Sections 6.2.1 and 6.2.2).

6.2 Analysis chain

The H$\longrightarrow \tau\tau$ analysis in Run II [12] uses a completely new chain from the raw data to the final results extraction, as compared to Run I [5]. It includes various steps and frameworks dedicated to produce the final files (ntuples) used for the analysis. In this section, we will describe the different steps, starting from the xAOD input files (described in Section 5.4.1), then the "Derivation" step which produces the so-called Derived-xAOD (DxAOD). These files are then used as inputs by an another tool that produce plots validating the background model, and produce also the histograms input for the final step of the analysis which is the statistical model used to extract the final results. Figure 6.1 shows a workflow of these different steps.

6.2.1 Derivation

The principle of the analysis model in Run II is that most of the physics analysis need the ability to run frequently over the data and simulation samples in order to add new variables and cuts, fix bugs, apply new and/or revised recommendations from the combined performance group (the Tau combined performance group for example).
In Run I analysis, almost all physics analysis had to reduce the initial sample to smaller ones. These were not the final files used to produce plots and final statistical results, but were in the format from which these final samples were obtained. This was not centralized in Run I and done by the users themselves.
In Run II, this intermediate step is the so-called "Derivations" [13]. The derivation framework is made centrally and provides the offline software tools and structures for doing this step in a transparent way.
The input for this framework is the xAOD files and the outputs have the same format as the xAOD but containing less data and called "DxAOD".
There are four operations in the derivation step:

- Skimming: Removal of a whole event based on given criteria which depend on the analysis channel.
- Slimming: This involves the removal of specific variables from the samples, based on what is needed for each specific analysis.
- Thinning: Removing a whole object from an event (but keeping the rest of the event) based on given criteria.
- Augmentation: It is used to add data that are needed and are not in the input xAOD file.

In the H$\longrightarrow \tau\tau$ analysis, there are four branch of derivations, each one is dedicated to one sub-channel $\tau_{lep}\tau_{lep}$, $\tau_{had}\tau_{had}$ and $\tau_{lep}\tau_{had}$. An additional derivation is deticated to the H$\longrightarrow \tau\tau$ beyond Standard Model searches (BSM). Each type of derivation is designed to select a phase space of events that corresponds to the final

state topology of the given sub-channel.

6.2.2 Analysis files production

After producing centrally the DxAOD files as described in the previous paragraph, a framework produces files to be used to extract the results. It is called "xTauFramework" [14].
This is a general and common H$\longrightarrow \tau\tau$ (SM and BSM) framework developed for all sub-channels. It is designed in a way that every H$\longrightarrow \tau\tau$ sub-channel uses a branch of it and can develop tools related to the specifity of each of them.
Depending on the sub-channel final state topology, selections are applied in this framework in order to be as close as possible as the events phase space of the corresponding signature. For H$\longrightarrow \tau_{lep}\tau_{had}$ analysis, I have implemented the corresponding part in the xTauFramework.
There are two levels of selections:

- Selections on the physics objects that will be used in the analysis, such that leptons (electrons and muons), hadronic tau candidates, jets and missing transverse energy MET. For the H$\longrightarrow \tau_{lep}\tau_{had}$ analysis, the corresponding objects preselections will be discussed in details in Section 6.4.1.

- Very loose event preselections depending on the final state topology. In our case, it is:

  1. Reject bad events according to some primary criteria (detector cleaning, bad jet cleaning,...)
  2. Ask for at least one lepton in the event.
  3. Require at least one hadronic tau candidate.

  In addition to those selections, channel-specific variables are then added to the output file. For example, we have added the physics quantities needed to perform the signal events categories (see Section 6.4.3). Some examples of variables added to the files are:

  - The physical observables of the all the objects (lepton, tau, jets, MET): η, ϕ, p_T, ...
  - The trigger variables that will be used offline to select events.
  - The mass of the di-tau system calculated from the lepton, the hadronic tau and the MET (see Section 6.3 on the di-tau mass measurement methods).
  - All the variables needed for the events preselection and categorisation (see Section 6.4).

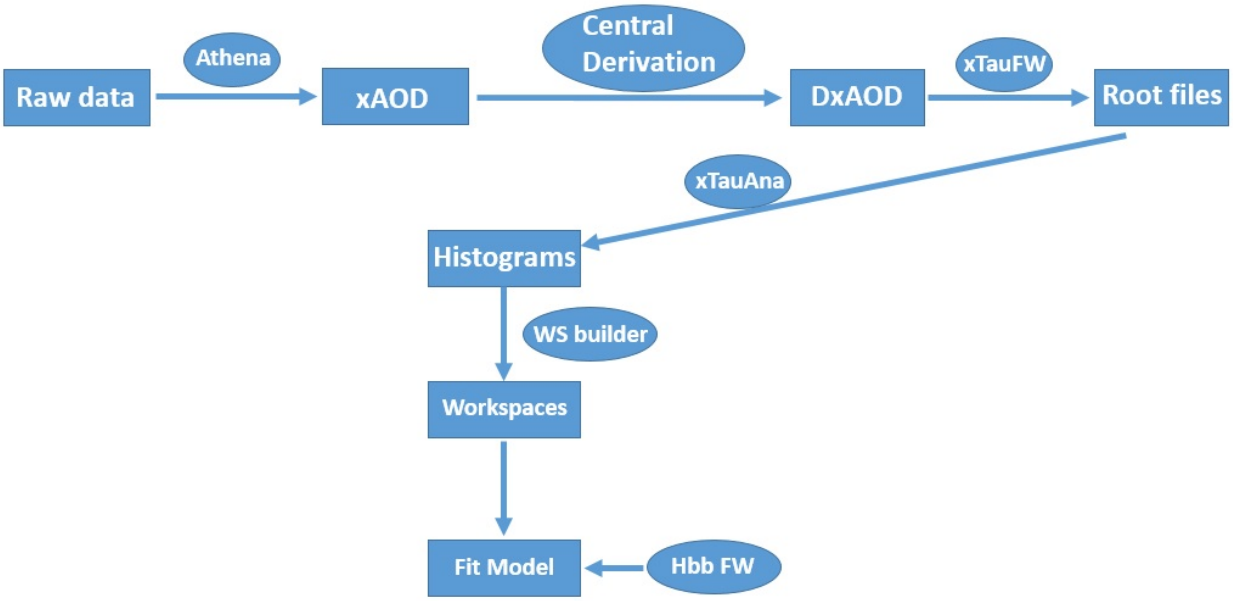

Figure 6.1: Work flow of the different steps of the analysis.

- All the correction factors coming from the combined performance groups and needed to be applied to the Monte Carlo simulation are also included.

This production step is done for all Monte Carlo simulation files that will be used so far in the analysis, in addition to the real data samples.

6.2.3 Analysis

Once the production files, described in the previous paragraph, are available, the next step of the analysis is performed in a standalone framework, called xTauAna [15].
The steps at this level can be summarized as follows:

- Start by the basic event selections, called "Preselection", in order to select H$\longrightarrow \tau_{lep}\tau_{had}$ signal events (described in Section 6.4.2). Then define the signal events (described 6.4.3).
- Develop the models used to estimate and predict the different type of backgrounds to the H$\longrightarrow \tau_{lep}\tau_{had}$ channel (see Section 6.5).
- Check the modeling and the agreement between the observed real data and the background prediction to validate the background estimation models. The so-called "control regions", described in Section 6.4.4, are also used at this level for the same purpose.

6.2.4 Signal extraction

The framework described in the previous paragraph is also used to produce root files containing all the histograms for the data, background predictions and expected Standard Model Higgs signal (including the histograms for all the systematic uncertainties that will be described in Section 6.6), and this will be used then to build the so-called "workspaces". These files are the final ones used in order to perform the statistical analysis. A framework developed by the H$\longrightarrow$ b$\bar{\text{b}}$ analysis team is used in order to produce these results. All these steps will be described in Sections 6.6 and 6.7.

6.3 Invariant mass reconstruction of the di-tau system

The invariant mass of the two lepton taus in the final state cannot be fully reconstructed due to the presence of three neutrinos in the $\tau_{lep}\tau_{had}$ final state, and since the contributions of these neutrinos to the four-momenta of the tau leptons are not directly measured.

6.3.1 Visible mass

The first basic mass estimation can be obtained using only the visible tau decay products, called $m_{\tau\tau}^{vis}$. It is obtained by neglecting the neutrinos in the final state [5].

$$m_{\tau\tau}^{vis} = \sqrt{(E_l + E_{\tau_{had-vis}})^2 - (\overrightarrow{P_l} + \overrightarrow{P}_{\tau_{had-vis}})^2} \tag{6.1}$$

Figure 6.2 shows that the $Z \longrightarrow \tau\tau$ and Higgs resulting mass distributions peaks are not well separated. In addition, since the neutrinos are omitted from the calculation, the entire mass distribution is shifted to lower values as seen clearly for the Z mass peak.

To estimate the full final state invariant mass of the di-tau system, including neutrinos, an approximation can be made due to the strong boost of the two τ leptons which are much lighter than the Higgs boson [16]. In this approximation, the neutrino and tau-jet are emitted in a narrow cone around the direction of the mother τ lepton in each τ decay. Two mass estimation techniques are presented below.

6.3.2 Collinear Mass Approximation

In this approximation, the decay products of the τ are assumed to be collinear with the τ in the laboratory frame. This approximation is made since the tau's are highly boosted ($m_H >> m_\tau$). Therefore, the direction of the emitted neutrinos can be assumed to be the same as the direction of the visible τ-decay products (electrons, muons or τ-jets).
In addition, the other assumption is that the neutrinos from the τ lepton decays are

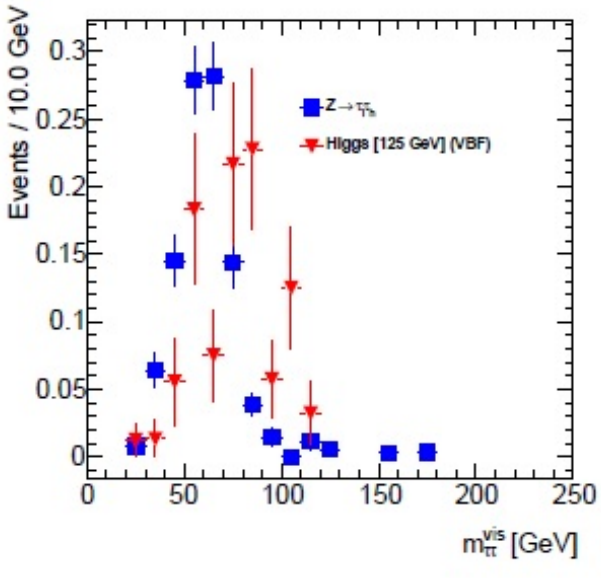

Figure 6.2: Normalized visible mass distributions of the MC VBF Higgs signal and Z$\longrightarrow \tau\tau$.

the only source of MET.
Figure 6.3 shows, for illustrative purpose, an example of a Z/H $\longrightarrow \tau_{lep}\tau_{lep}$ decays using the collinear mass approximation.

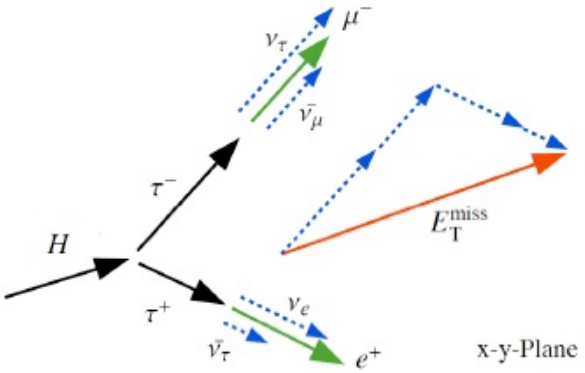

Figure 6.3: Figure showing an example of Z/H $\longrightarrow \tau_{lep}\tau_{lep}$ decays with collinear mass approximation. The emitted tau decay products are collinear to the tau direction. The MET vector, assuming neutrinos are the only source of MET in the event, is illustrated as well.

Given the assumptions described above, the collinear mass of the di-tau system can be expressed in terms of the visible mass as:

$$m_{coll} = \frac{m_{vis}}{\sqrt{x_l x_{had}}} \tag{6.2}$$

where x_l and x_{had} are the fractions of the tau transverse momentum carried by the visible decay products in leptonic and hadronic decays respectively [17].

This method has some limitation since it fails when the angular separation between the two taus is close to zero or π. It is also sensitive to the measured MET value and if this value is low, the neutrinos are back-to-back, which causes the method to fail. In addition, this method fails if the MET vector direction does not fall within the opening angle of the two tau leptons. The non-physical solution of the equations in this algorithm leads to the rejection of the events falling in the conditions described just above. For these reasons, a more sophisticated mass estimation method, called Missing Mass Calculator, has been developed.

6.3.3 Missing Mass Calculator MMC

The MMC invariant mass estimator is a likelihood based method which is valid for various event topologies. It provides an estimation of the di-tau invariant mass system with a good resolution without the limitations of the collinear mass approximation method.
Depending on the tau decay mode in the H$\longrightarrow \tau\tau$ channel, the event kinematics can be described by a system of 6 to 8 unknown variables [16]. In the $\tau_{lep}\tau_{had}$ channel, there are seven unknowns needed to describe the neutrino systems, $\nu_{\tau_{had}}$ and ν_{τ_l} ν_l systems: two 3-vector components for each neutrino(s) system in addition to the angular separation between $\nu_{\tau_{had}}$ and ν_{τ_l} ν_l describing the invariant mass of the neutrinos from the leptonic decay.
This leads to an underconstrained system of four equations in x and y components of the MET (E_x^{miss} and E_y^{miss}) and the invariant mass of each tau ($m_{\tau,1}$ and $m_{\tau,2}$).

To solve the system, a scan of various grid point in ($\Delta\phi_1$, ($\Delta\phi_2$) is performed, where $\Delta\phi_i$ is the azimuthal angular separation between the visible and invisible decay products of τ_i(i=1,2). Among the infinite set of solutions, not all of them are equally probable and the most likely one is determined based on the kinematic properties of the tau lepton decay products.
The kinematic variable used to do this choice is the three-dimensional angular separation $\Delta\eta_{3D}$ between the invisible neutrino(s) momentum vector and the visible tau decay products [18].
The distribution of this kinematic variable is parametrized for different p_T^τ. It is defined as a probability density function (PDF) that enters the MMC likelihood estimator by which the estimated mass candidate $m_{\tau\tau}$ will be weighted. These probability density functions P($\Delta\eta_{3D}$, p_T^τ), shown in Figure 6.4, are obtained from the simulated Z/γ^* $\longrightarrow \tau\tau$ process as a function of p_T^τ, separately for the 1-prong or 3-prong in hadronic τ decays, and for the leptonic tau decay.

The estimator for the $\tau\tau$ mass is defined as the most probable value of the scan points.

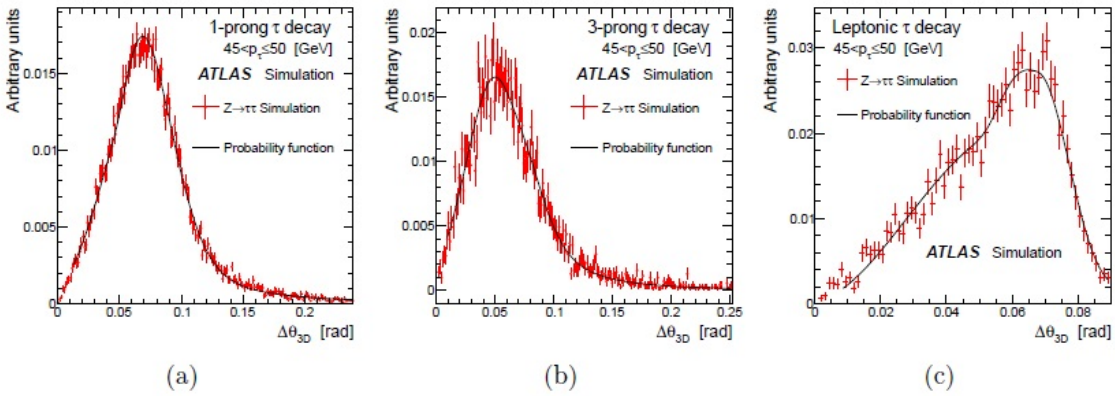

Figure 6.4: Plots showing the probability distribution function of the 3-dimensional angular separation $\Delta\eta_{3D}$ between the neutrino(s) and the visible tau decay products in simulated Z $\longrightarrow \tau\tau$ events for hadronic 1-prong(a) and 3-prong(b), in addition to leptonic(c) tau decays [18]. The results are shown for taus with a generated momentum $45 < p \leqslant 50$ GeV.

Concerning the MMC mass reconstruction efficiency, defined as the fraction of input events for which the MMC algorithm finds a solution, there are two sources of inefficiencies:

- The mis-measurement of visible tau decay product leading to a slight mass reconstruction efficiency degradation of 3 - 7 %. But this does not affect the mass peak and its resolution.
- The MET resolution can affect the mass reconstruction efficiency by about 30 - 40 % for 5 GeV E_T^{miss} resolution, if it is not taken into account in the mass estimation. It also causes a degradation of the reconstructed mass resolution resulting in longer tails. This is mainly due to assuming that neutrinos originating from tau decays are the only source of MET in the event.

Therefore, to improve the $m_{\tau\tau}$ measurement, the MET resolution needs to be taken into account in the MMC calculation.
The efficiency is more than 96% for Higgs mass hypothesis less than 250 GeV and for Z events. It is not exactly 100% for Z/H events, and is less than 96% for non-Z background events since the topology of those non-Z background events may not be consistent with the Z $\longrightarrow \tau\tau$ decay [18]. And the small loss rate for Z/H $\longrightarrow \tau\tau$ decay is due to the mis-reconstruction of the MET where the wrong MET value causes the MMC algorithm to fail (no convergence).
Figure 6.5 shows the MMC distribution (black) and the collinear approximation

distribution (red) for MC H$\longrightarrow \tau_{lep}\tau_{had}$ events. The difference in normalizations of the MMC and collinear approximation results reflects the higher efficiency of the MMC method. And a high mass tail can be observed in the collinear mass distribution [16].

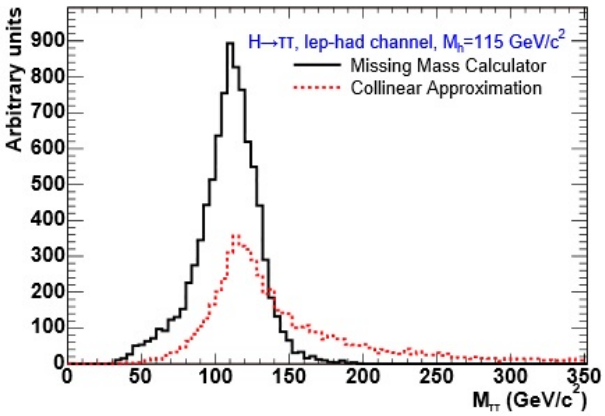

Figure 6.5: Reconstructed ditau mass distributions in MC H$\longrightarrow \tau_{lep}\tau_{had}$ events with M_h=115 GeV for the MMC method (black) and the collinear approximation method (red) [16].

6.4 Event selection and categorization

In this section, the objects and the events selections from the so-called "Preselection" to the signal categorization for the Higgs boson search in the H$\longrightarrow \tau_{lep}\tau_{had}$ decay channel are presented [12] [19].

6.4.1 Physics objects selection

The relevant objects to be considered include muons, electrons, hadronic taus, jets and Missing Transverse Energy (MET). A detailed description of the reconstruction algorithms and the identification criteria is given in Chapter 4.

Leptons Muons have to be of type "combined" or "ST" (see Section 4.4.1) and need to pass loose identification criteria (see Section 4.4.2), have a transverse momentum greater than 10 GeV and fall within the region $|\eta| < 2.5$. Electrons need to pass the medium identification criteria with a transverse momentum higher than 15 GeV and in the region $|\eta| < 2.47$. Electrons in the transition region $1.37 < |\eta| < 1.52$ are not considered.

Hadronic taus A medium BDT identification is applied (Section 5.1.3) to the candidates that should have a p_T greater than 20 GeV, falling in the region $|\eta| < 2.47$

with 1 or 3 prongs, and with a charge ± 1. An electron veto is also applied as described in Section 5.1.5.

Jets We use jets reconstructed with the anti-k_T algorithm and a distance parameter R = 0.4 and using the local hadronic calibration (LCW) scheme (Section 4.5.2). Jets should have a $p_T > 30$ GeV and fall within $|\eta| < 4.5$. To reduce the number of jets in the event due to pileup activity, JVF requirements are applied. The b-jets are identified using the MV1 b-tagging algorithm (see Section 4.5).

MET The signal signature is characterized by the presence of true E_T^{miss} from the tau decay. In this analysis, it is mainly a calorimeter based MET definition, with a track corrected soft term (see Section 4.7).

A so-called "object overlap removal (OLR)" is applied when different objects selected according to the above criteria overlap with each other geometrically (within $\Delta R < 0.2$). Only one of them is considered for further analysis. This is resolved by selecting objects in the following order of priority dictated by the object reconstruction efficiency, being the largest in case of muons: muon, electron, τ_{had} and jet. For this OLR, the leptons requirements are looser than the ones described earlier, in order to maximize the reduction of leptons mis-identified as τ_{had}.

6.4.2 Preselection

The basic event selection requirements applied to select signal-like events are listed in Table 6.1.

Primary vertex with at least four associated tracks
Pass Single-Lepton trigger SLT
Exactly one lepton and at least one hadronic tau (medium idenfication criteria, p_T requirement on each object, gradient isolation for leptons)
Opposite charged requirement between lepton and hadronic tau
B-jet veto
$m_T < 70$ GeV

Table 6.1: Table summarizing the preselection cuts used of the lep-had channel.

- A basic check is done for each event to ensure it is coming from a proton-proton collision in order to reduce the contamination from other sources like cosmic rays, etc. For this purpose, a primary vertex is required for each event with at least four associated tracks with $p_T > 400$ MeV, and the vertex position should be compatible with the beam spot.

- Each event has to pass the trigger requirement for the 2015 and 2016 data periods. It is a Single-Lepton Trigger (SLT), where events that don't pass this requirement are rejected. The offline transverse momentum thresholds for the trigger combination are as follows: For the 2015 dataset we apply a cut of 21 (25) GeV for the SLT for muons (electrons). For the 2016 dataset the lower cut for the SLT is 25.5 GeV (25 GeV) for muons (electrons). For both 2015 and 2016, a cut of 20 GeV is applied on the transverse momentum of the tau for the SLT.
  There is another type of trigger called "Tau+Lepton Trigger" (TLT) for the $\tau_{lep}\tau_{had}$ channel based on the presence of a hadronic tau and a lepton. This trigger is not used in the analysis presented in this thesis due to some mismodeling between the background prediction and data in the corresponding region, which needs further understanding.

- Exactly one lepton (muon or electron) and at least one hadronic tau are required. Leptons (e/μ) should pass medium criteria, gradient isolation (see Sections 4.3.2 and 4.4.3) and pass the following p_T thresholds: 16 GeV for muons and 19 GeV for electrons. The hadronic tau has to pass medium criteria and a p_T >20 GeV.

- The lepton and the tau are required to have opposite electric charges.

- B-jet veto is applied in order to remove events with b-tagged jets to reduce the $t\bar{t}$ background in the signal region. The minimum p_T for b-jet candidates for the "BTagging Selection Tool" is 20 GeV.

- A cut on the transverse mass (calculated from the lepton and the MET), m_T <40 GeV is applied in order to reduce the W+jets background.

The sample of events selected at this preselection stage is expected to contain a small fraction of Higgs boson signal events (< 1%) compared to the background contribution. Therefore, it can be used to test the validity of the background estimation which has to fit the observed data at this level.

Figures 6.6 shows a good agreement between data and background predictions after the preselection requirements for the muon and electron channels combined and for the 2015+2016 datasets combined. It illustrates the p_T of the leading lepton, p_T of the τ_{had} candidate and the MMC distribution. The data are the black points and the various colors represent the background compositions introduced in Section 6.1.2.2. The estimation methods for the various types of backgrounds will be detailed in the next Section.
The error band represent the statistical and systematic uncertainties combined. The various systematic uncertainties will be detailed in Section 6.6.

Table 6.2 shows the data and the various backgrounds yield for the combined 2015 and 2016 datasets after preselection. The error numbers combine statistical and systematic uncertainties. As can be seen in the table, the fake and Z$\longrightarrow \tau\tau$

processes are the dominant backgrounds.
Table 6.3 shows the total expected signal yield and the breakdown into the various signal production processes based on MC simulations. As expected, the dominant Higgs production modes for this channel are the ggH and VBF.

Dataset	Data	Fake	Diboson	Z$\longrightarrow$ll	Z$\longrightarrow \tau\tau$	Top
Yield	542822	321604.9 $\pm$ 278.2	2161.1 $\pm$ 19.0	79259.7 $\pm$ 1074.5	128322.8 $\pm$ 840.9	1844.1 $\pm$ 22.0

Table 6.2: $\tau_{lep}\tau_{had}$ preselection events yield for the data and the various backgrounds for the 2015 and 2016 datasets combined.

Dataset	total Signal	ggH	VBF	ttH	ZH	WH
Yield	771.3 $\pm$ 4.9	677.1 $\pm$ 3.7	61.1 $\pm$ 0.3	0.9 $\pm$ 0.06	14.0 $\pm$ 1.9	18.0 $\pm$ 2.6

Table 6.3: $\tau_{lep}\tau_{had}$ preselection events yield for the various signal processes for the 2015 and 2016 datasets combined.

6.4.3 Event categorisation

Events passing the preselection stage are then divided into categories defined by selection criteria. They are optimised to select signal events in which the Higgs boson is produced either via ggH or VBF production. Two inclusive signal categories are defined at this stage: VBF and Boosted. Further subdivisions into sub-categories with different background compositions and signal-to-background ratios are applied as shown in Figure 6.7.

6.4.3.1 VBF category

VBF-like events are selected based on the characteristic signature of the VBF Higgs boson production mode with two hard jets in the final state emitted in the forward detector regions.
The cuts used are:

- Leading and sub-leading jets should have a transverse momentum greater than 40 GeV and 30 GeV respectively (leading and sub-leading jets are jets having the highest and second highest p_T).
- The two jets must be well separated:
  1. The $\Delta\eta$ between the two jets should be greater than 3.
  2. The jets must be in opposite hemisphere.
- Di-jets visible mass m_{jj} should be greater than 300 GeV.

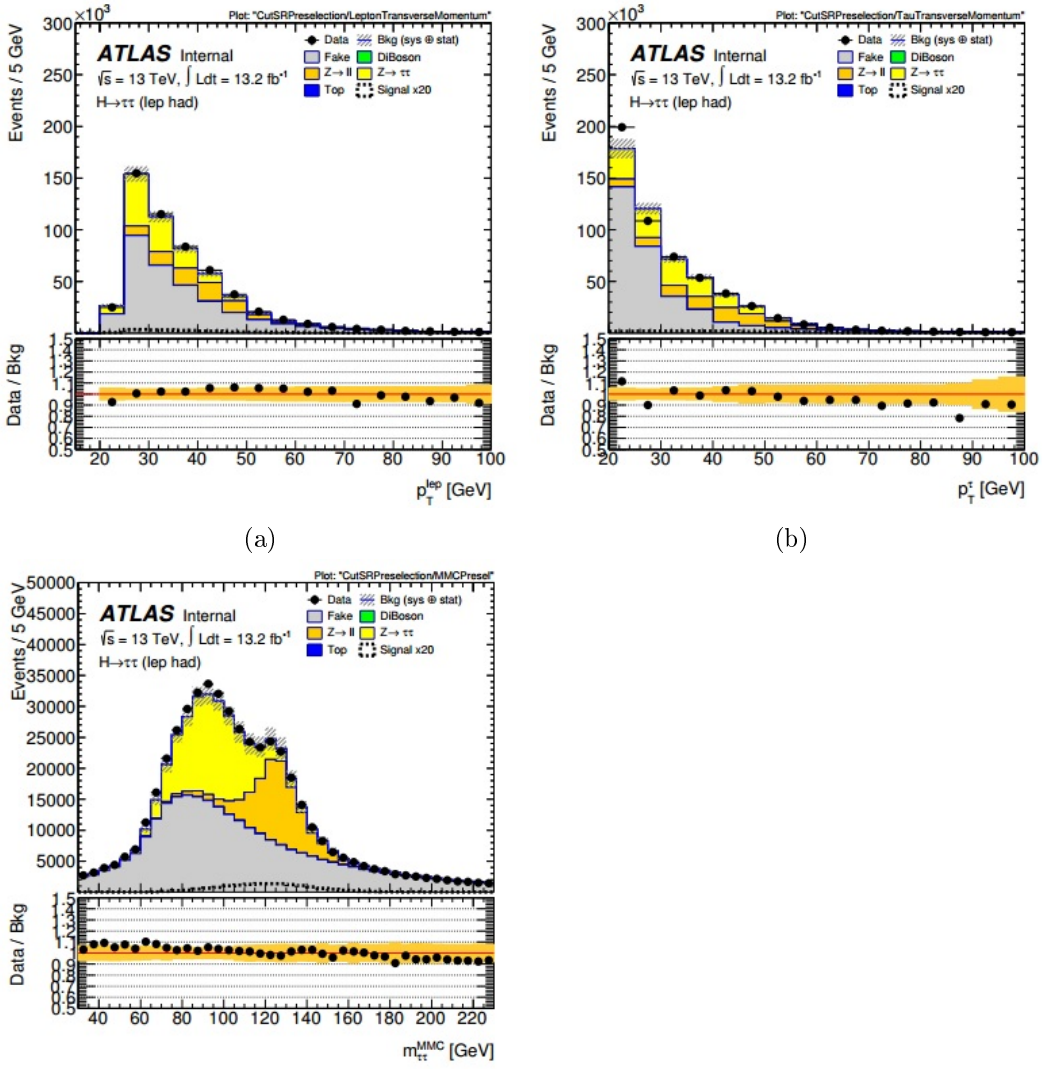

Figure 6.6: $\tau_{lep}\tau_{had}$ preselection distributions for muon and electron channels combined (data and background predictions). Data are points and colored regions represent the various background compositions. (a) p_T of the leading lepton, (b) p_T of the τ_{had} candidate and (c) the MMC distribution. The size of the statistical and systematic uncertainties is indicated by the hashed band. The ratios of the data to the model are shown in the lower panels where the yellow band represent the statistical and systematic uncertainties.

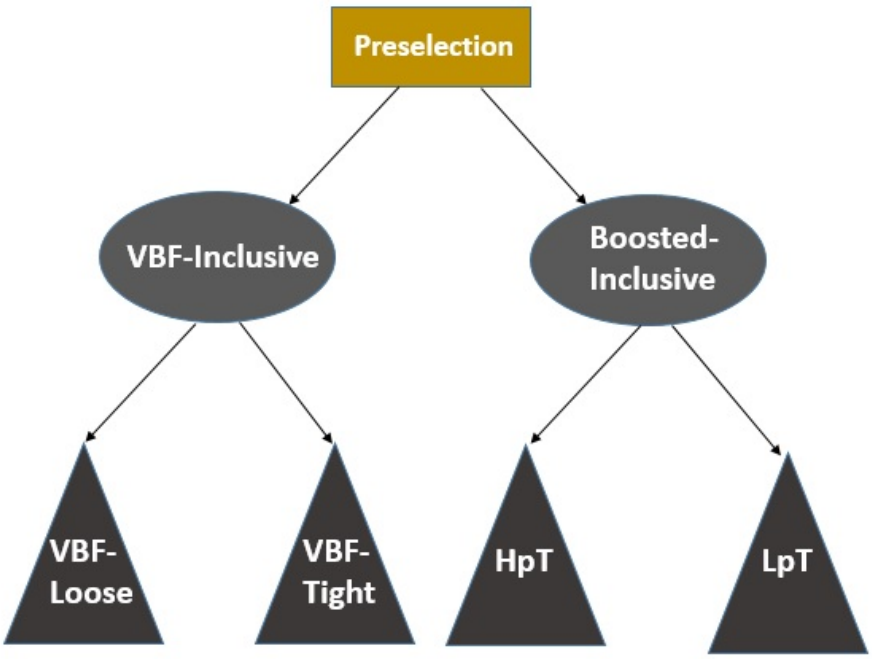

Figure 6.7: Flow-chart of the event categorisation for the Higgs boson search in $\tau_{lep}\tau_{had}$ channel for the cut based analysis.

- The η of the lepton and the hadronic tau should be greater than the minimum jet η and lower than the maximum jet η (jet centrality requirement).
- A cut on the missing transverse energy (MET) above 20 GeV is applied.
- The hadronic tau candidate should have a p_T >30 GeV.

This was the baseline selection for the cut-based analysis developed in Run I. A cut optimisation study has been performed for the Run II. It has shown that adding angular cuts similarly to what is done in the fully hadronic (H$\longrightarrow \tau_{had}\tau_{had}$) channel, do improve the final analysis significance. This includes a cut on $|\Delta\eta|$ and ΔR between the hadronic tau and the lepton ($|\Delta\eta(\tau_{had},\mathrm{l})|$<1.5 and $\Delta\mathrm{R}(\tau_{had},\mathrm{l})$ <3). The VBF inclusive category is further split into two sub-regions:

VBF-Tight Tighter selections are further applied, leading to a lower statistic but higher signal sensitivity:

1. The di-jets visible mass $\mathrm{m_{jj}}$ has to be greater than 500 GeV.
2. The transverse momentum of the Higgs candidates $\mathrm{p_T(H)}$ is required to be greater than 100 GeV.
   $\mathrm{p_T(H)}$ is the transverse momentum vector sum of $\overrightarrow{\tau_{lep}}$, $\overrightarrow{\tau_{had}}$ and $\overrightarrow{E_T^{miss}}$.

3. The visible mass of the di-tau system must be greater than 40 GeV.

4. The transverse momentum of the tau must be greater than 30 GeV.

VBF-Loose It includes events which have passed the inclusive VBF cuts and failed the VBF-Tight selection.

6.4.3.2 Boosted category

This category is designed to select mostly ggF signal events in which the Higgs boson has a high transverse momentum. Such events are selected by requiring the following cuts:

- Fails the VBF inclusive selection.
- p_T(H)>100 GeV.
- The missing transverse energy (MET) must be greater than 20 GeV.
- The tau candidate should have a p_T greater than 30 GeV.

As for the VBF category, this definition is following the categorization developed in Run I. A cut optimisation study has been performed and has lead to additional angular cuts ($|\Delta\eta(\tau_{had},l)|$<1.5 and $\Delta R(\tau_{had},l)$ <2.5).
A further sub-division into two Boosted sub-categories is applied. It is based on the p_T of the Higgs candidate:

Boosted High-p_T^H (HpT) It is the most sensitive Boosted category defined as follows:

1. p_T(H) should be greater than 140 GeV.
2. ΔR (τ_{had},l)<1.5.

Boosted Low-p_T^H (LpT) It selects events failing the Boosted HpT selection, with small Higgs p_T or high $\Delta R(\tau_{had},l)$:

1. p_T(H) <140 GeV or ΔR (τ_{had},l)>1.5.

Let's illustrate the events categorization with the following conditions:

- **Discriminant variable**: The MMC mass variable is the final discriminant for the statistical interpretation of the observed data in terms of the measured signal cross section in this cut-based analysis. In Run I, a BDT has been used (see Ref. [5]).

- **Blinding vs unblinding**: The "blinding" means that we do not look at the data in the signal window between 100 GeV and 150 GeV of the MMC, until all the various steps of the analysis are fully tested. The "unBlinding" of this regions will be done at the end of the analysis chain as it is described in Section 6.8.

Figure 6.8 and 6.9 show some variables distributions in the inclusive VBF and Boosted regions respectively. They illustrate the good modeling of background that are discussed in Section 6.5. The MMC distributions in the signal regions (VBF and Boosted inclusive and sub-categories) are blinded.

Table 6.4 shows the data and various backgrounds yield for the VBF and Boosted categories (inclusive and exclusive). We can see that in the VBF category, the fake is the dominant background and the $Z \longrightarrow \tau\tau$ is the second dominant one. While in the Boosted category, $Z \longrightarrow \tau\tau$ is the dominant background and the fake is the second dominant one.

Tables 6.5 shows the total expected signal yield and the breakdown into the various signal production processes, based on MC simulations. We can see that the VBF category is dominated by the VBF process, and the Boosted category is dominated by the ggH process, as expected.

Category	Data	Fake	Diboson	$Z \longrightarrow ll$	$Z \longrightarrow \tau\tau$	Top
VBF inclusive	1718	1008.5 ± 12.7	19.1 ± 1.6	99.2 ± 17.6	551.2 ± 24.4	53.0 ± 3.8
VBF Tight	280	73.0 ± 2.9	6.5 ± 1.0	14.6 ± 4.7	147.8 ± 11.5	15.5 ± 2.3
VBF Loose	1438	935.4 ± 12.4	12.6 ± 1.3	84.6 ± 16.9	403.4 ± 21.5	37.5 ± 3.0
Boosted inclusive	6834	2119.8 ± 19.0	143.9 ± 4.6	444.8 ± 29.8	4302.5 ± 72.8	216.7 ± 7.7
Boosted HpT	3009	507.5 ± 10.0	76.0 ± 3.4	203.5 ± 17.9	2500.0 ± 54.5	68.4 ± 4.7
Boosted LpT	3825	1612.3 ± 16.1	67.9 ± 3.1	241.3 ± 23.7	1802.4 ± 48.3	148.3 ± 6.1

Table 6.4: $\tau_{lep}\tau_{had}$ events yield for VBF and Boosted inclusive and exclusive categories for the data and the various backgrounds with the 2015 and 2016 datasets combined.

Category	Signal	ggH	VBFH	ttH	ZH	WH
VBF inclusive	27.7 ± 0.5	10.0 ± 0.4	17.6 ± 0.15	0.03 ± 0.01	0.03 ± 0.01	0
VBF Tight	12.9 ± 0.3	3.7 ± 0.3	9.2 ± 0.1	0.01 ± 0.01	0	0
VBF Loose	14.8 ± 0.4	6.3 ± 0.4	8.4 ± 0.1	0.02 ± 0.01	0.07 ± 0.07	0
Boosted inclusive	71.7 ± 2.0	54.0 ± 1.0	9.7 ± 0.1	0.4 ± 0.04	2.8 ± 0.8	4.6 ± 1.6
Boosted HpT	40.0 ± 1.8	29.0 ± 0.8	5.2 ± 0.08	0.3 ± 0.03	1.6 ± 0.6	3.9 ± 1.5
Boosted LpT	31.7 ± 0.9	25.1 ± 0.7	4.5 ± 0.1	0.1 ± 0.03	1.2 ± 0.5	0.8 ± 0.3

Table 6.5: $\tau_{lep}\tau_{had}$ signal events yield for VBF and Boosted inclusive and exclusive categories with the 2015 and 2016 datasets combined.

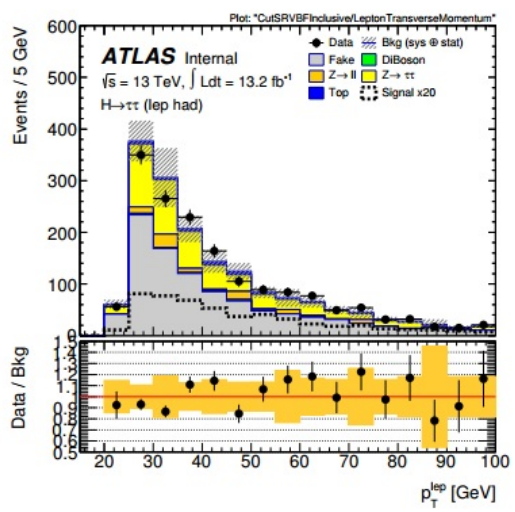

(a)

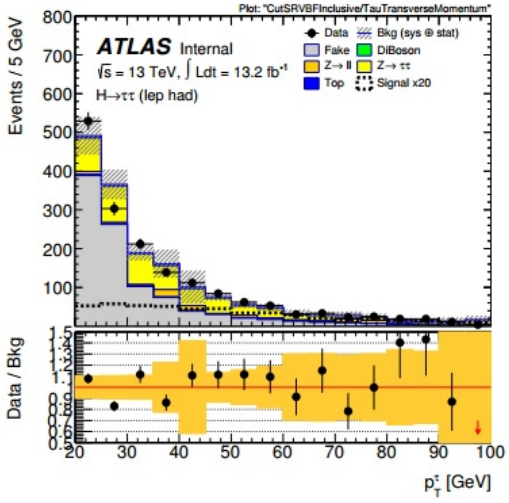

(b)

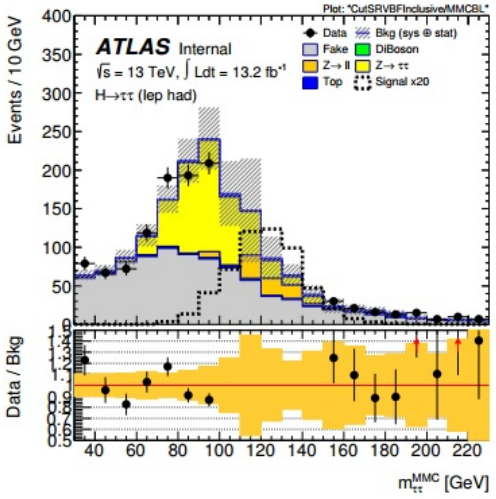

(c)

Figure 6.8: $\tau_{lep}\tau_{had}$ VBF inclusive category distributions for muon and electron channels combined. Data are points and colored regions represent the various background compositions. (a) p_T of the leading lepton, (b) p_T of the τ_{had} candidate and (c) the MMC distribution. The size of the statistical and systematic uncertainties is indicated by the hashed band. The ratios of the data to the model are shown in the lower panels where the yellow band represent the statistical and systematic uncertainties.

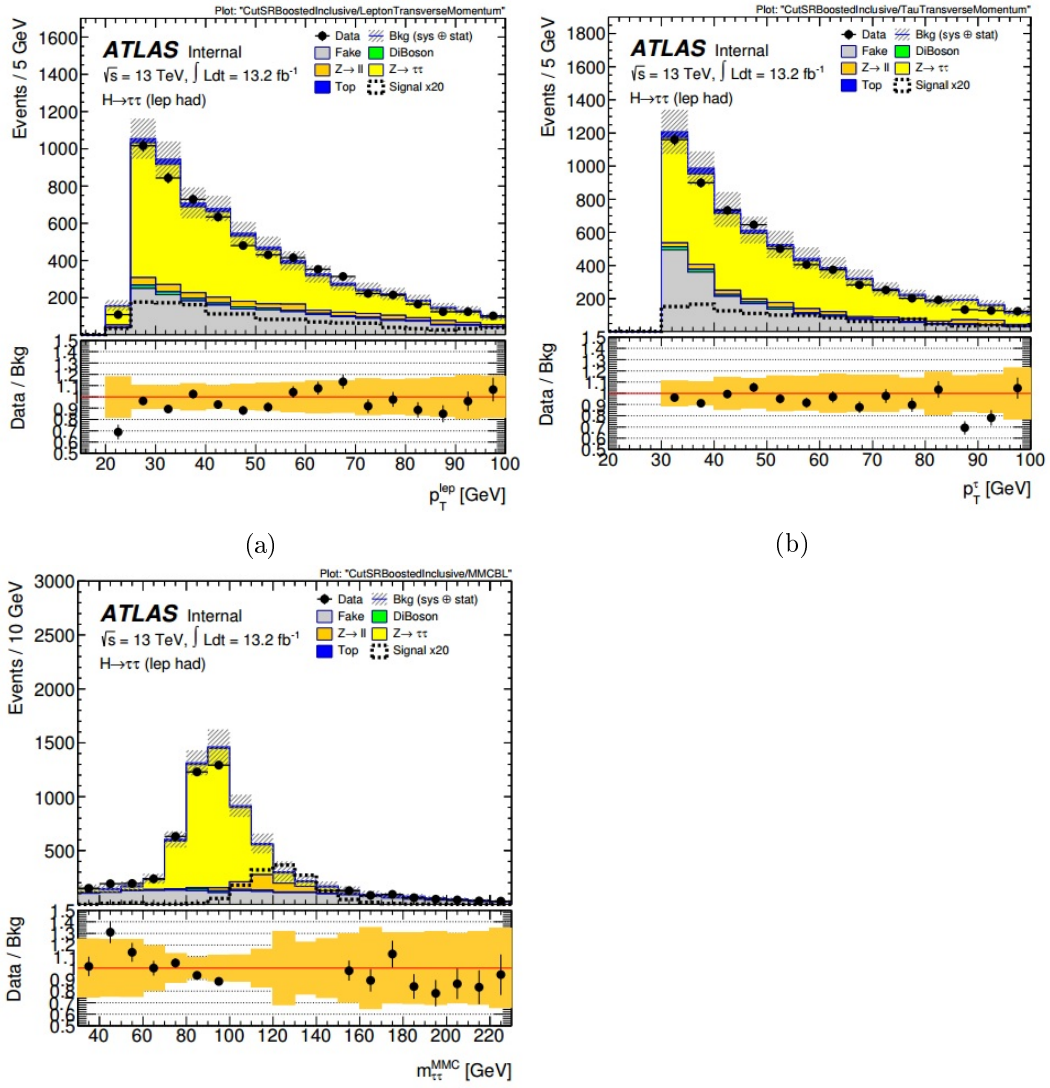

Figure 6.9: $\tau_{lep}\tau_{had}$ Boosted inclusive category distributions for muon and electron channels combined. Data are points and colored regions represent the various background compositions. (a) p_T of the leading lepton, (b) p_T of the τ_{had} candidate and (c) the MMC distribution. The size of the statistical and systematic uncertainties is indicated by the hashed band. The ratios of the data to the model are shown in the lower panels where the yellow band represent the statistical and systematic uncertainties.

6.4.4 Control regions

Control regions CRs (or validation regions) are phase space regions enriched for a given background process with a minimal amount of signal and other backgrounds. These regions are used to validate a background model and/or get the values of parameters related to that particular background type (see Section 6.7):

- **W+jets** CR: It is the same as the signal region but with inversion of the cut on the transverse mass m_T, i.e. $m_T > 70$ GeV, where most of the W+jets events at are located.
- **Top** CR: The same as the signal region but with inverting the b-veto cut, which means requiring the presence of a $\geq$1 b-jet(s). In addition, a cut on the transverse mass above 40 GeV is applied. It will be used to validate and extract the correct normalization for top events with real taus in the final state (no jet faking taus events).
- **Z** ($\longrightarrow ll$) CR: We require two same flavour leptons with opposite charge and mass between 61 and 121 GeV.
- **QCD** CR: The same as the signal region but with inverting the lepton isolation cut.

These control regions are used in order to validate the background estimation methods used in this analysis. They are also used to derive the normalization factor for each background process (by comparing the data to background prediction in the corresponding control region, as we will see in Section 6.5).
In Section 6.5.4.2, we will see how these CR are used in the derivation of the fake factors used to estimate the fake multijets background, one of the largest backgrounds for our study.

6.5 Background Model

The statistical interpretation of the observed data needs an accurate prediction of the backgrounds contribution.
The background model shapes are derived from a mixture of MC simulated samples and data. The normalization of these backgrounds generally relies on modeling individual backgrounds in signal-poor control regions by achieving good agreement with data in that region.

6.5.1 Z$\longrightarrow \tau\tau$

The Z $\longrightarrow \tau\tau$ and Drell-Yan processes are an irreducible source of backgrounds for the $\tau_{lep}\tau_{had}$ channel due to their similarity with the signal. This background can be distinguished from signal events only by the different $m_{\tau\tau}$ invariant mass, due to

the same final state topology.

In Run I analysis, the Z $\longrightarrow \tau\tau$ background has been estimated based on a data driven method, called "embedding" [20] [21]. It is a hybrid approach combining simulation with measurements in a control data sample. This sample contains Z $\longrightarrow \mu\mu$ events which are selected with high efficiency and purity. This approach is needed since it is not possible to select a pure control sample of Z $\longrightarrow \tau\tau$ events free of signal contributions.
In the control data sample, the two muons from the Z boson decay are replaced by two simulated hadronically decaying τ leptons while ensuring that the kinematic properties of the Z boson and its decay products remain preserved. In such a so-called "embedded" event the decays of the τ leptons from the Z boson are described by simulation while all other event properties, such as the Z boson transverse momentum, the jets produced in the hard-scattering process as well as the underlying event and pileup interactions are directly given by data.

In Run II analysis, the Z $\longrightarrow \tau\tau$ background is estimated using Monte-Carlo simulation. This is required to model very well the kinematic event properties which impacts the shape of the Z mass distribution (such as the transverse momentum of the Z boson and the number of jets in the event), since signal events are expected to contribute to the high tail of the $m_{\tau\tau}$ mass distribution above the Z boson mass peak. In fact, the H$\longrightarrow \tau\tau$ signal sits on the upper tail of the Z peak, and due to the presence of neutrinos in the tau decays, the two resonances are not very well separated. Furthermore, to reduce the Z+jets contribution to the Higgs signal regions either a high transverse momentum (possibly with additional jets) or at least two additional jets are required (Boosted and VBF phase spaces).

A data driven method method is developed to correct the normalization of the Z$\longrightarrow \tau\tau$ Monte Carlo prediction and validate the modeling of the properties of jets produced in association with Z bosons. A Z$\longrightarrow \tau\tau$ data control region dominated by Z$\longrightarrow$ll events (l=e or μ) is defined by requiring two isolated leptons with an invariant mass $|m_{ll} - M_Z| < 10$ GeV and missing transverse energy below 40 GeV. This is defined separately for the inclusive boosted and VBF signal regions.
The observed distributions of some of the relevant kinematic variables are compared to simulation in Figure 6.10. The MADGRAPH and SHERPA generators are used for the simulation of the Z/γ^* + jets process, as the nominal sample and for the estimation of systematic uncertainties, respectively (discussed later).

In this Z$\longrightarrow \tau\tau$ CR, the Z$\longrightarrow$ll transverse momentum spectra p_T(ll) is fitted in order to derive the data driven corrections to the normalization of the Z$\longrightarrow \tau\tau$ background in the exclusive regions which are defined mostly by cuts on the Higgs candidate transverse momentum.
The shape uncertainty on the Z transverse momentum is obtained from the difference between the Z p_T spectrum in MADGRAPH and SHERPA. The choice to use this difference as envelop for the systematic uncertainty on the Z p_T modeling is

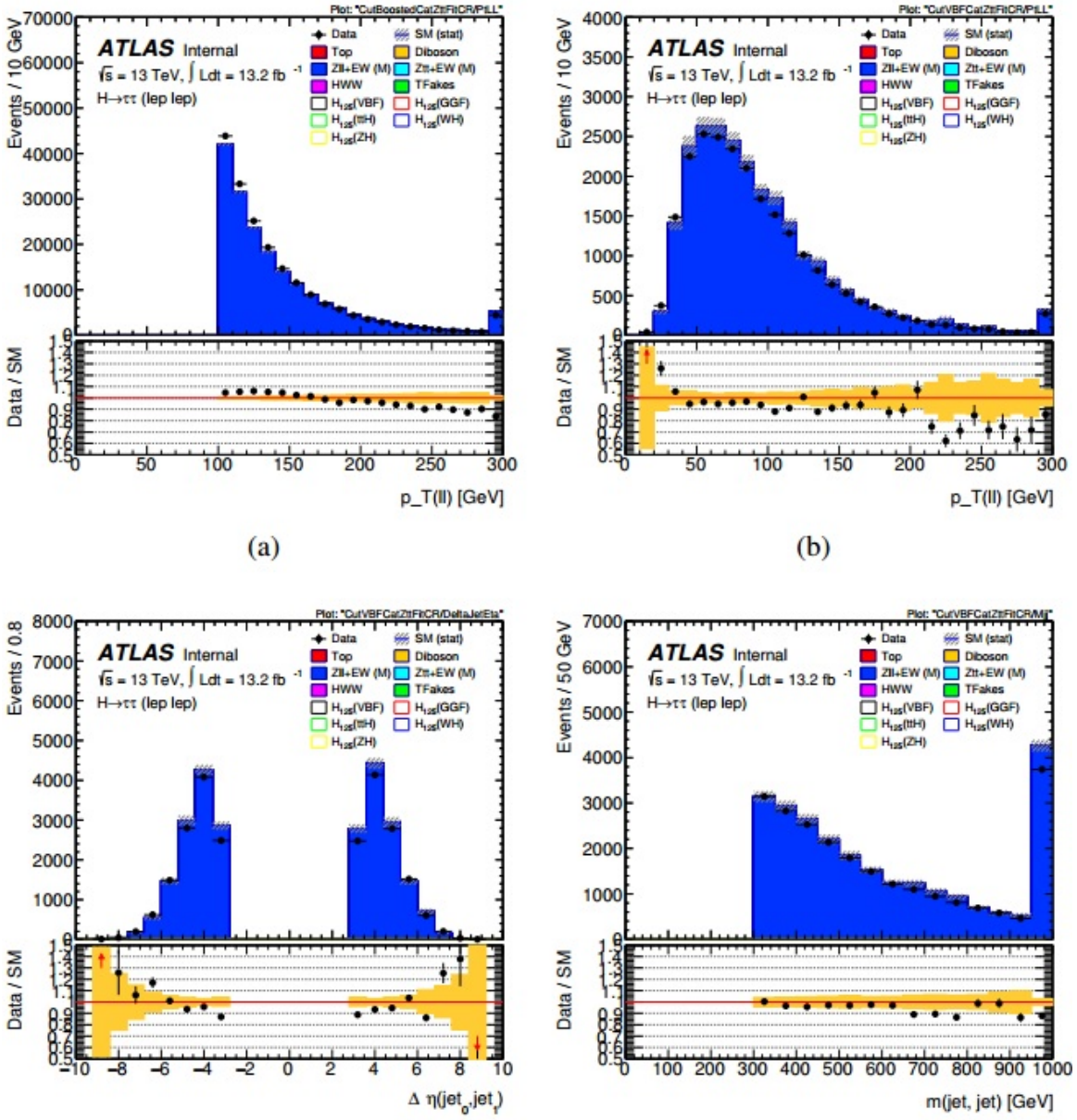

Figure 6.10: Distributions of selected kinematic variables in a selected Z⟶ll sample, after applying simplified selections for the boosted and VBF inclusive categories: (a) p_T of the lepton pair in the boosted category, (b) p_T of the lepton pair in the VBF category, (c) $\Delta\eta$ between the two leading jets in the VBF cateogry, and (d) invariant mass of the two leading jets in the VBF category.

based on the conservative choice to cover the theoretical systematic uncertainties taking the difference between generators that use different calculations at different QCD orders.

The strategy of normalizing the Z+jets and extract corrections to the Z p_T modeling from data are implemented in the fit as follows (see Section 6.7):

- One normalisation factor acting on Z $\longrightarrow \tau\tau$ events in VBF category; applied to all VBF exclusive signal regions in the three channels and the VBF Z $\longrightarrow \tau\tau$ control region.
- One normalisation factor acting on Z $\longrightarrow \tau\tau$ events in boost category; applied to all boost exclusive signal regions in the three channels and the boost Z $\longrightarrow \tau\tau$ control region.
- One systematic uncertainty on Z $\longrightarrow \tau\tau$ events based on the differences in predictions between MADGRAPH and SHERPA at reconstruction level applied to all signal regions in all channels and the two Z $\longrightarrow \tau\tau$ control regions (VBF and Boosted). This systematics includes also a normalization component in the exclusive signal regions corresponding to the acceptance difference of the generators.

The MADGRAPH sample does not include electroweak production diagrams (with tri-linear gauge boson production). The fraction of these events ending up in the signal region has been checked with SHERPA and found to be small and therefore is neglected.

6.5.2 Top background

This includes the background from $t\bar{t}$ and single top-quark productions, where leptons or hadronicaly decaying taus appear in the decay of top quark. The main contribution is from $t\bar{t}$, where events pass the analysis selections for two different reasons:

- A jet can be wrongly identified as a hadronic τ together with a real lepton coming from one of the two W decay.
  This component is noted Top(τ_{had}). The modeling of this component is based on a data-driven method as described in Section 6.5.4.2.
- A real hadronic tau τ_{had} from the W decay is reconstructed together with a real lepton from the other W decay. This component is noted Top(j$\longrightarrow \tau_{had}$). This component is modeled based on the POWHEG [7] simulation. This MC description is corrected by using data control regions enriched with top-quark production (see Section 6.4.4) by deriving normalization correction factors that are then applied to the top predictions in the signal region.

It is worth noting that these correction factors are free to float during the final fit and are measured with a proper propagation of all systematics. Indeed, for the extraction of the final analysis results, a Profile likelihood fit model is constructed as described in Section 6.7. In this model, separate top control regions for the boost and VBF categories are included.

To check the distributions of the Top CR, Figure 6.11 show the distributions of the Top CR for the VBF inclusive selections (left) and the Boosted inclusive selections (right).

6.5.3 Z$\longrightarrow$ll ($e^+e^-/\mu^+\mu^-$) and Diboson backgrounds

The Z($\longrightarrow$ll)+jets background where a jet is misidentified as a hadronic τ candidate is estimated by the method described in Section 6.5.4. The remaining component of the Z$\longrightarrow$ll (where an electron fakes a hadronic tau e$\longrightarrow \tau_{had}$) and background from Diboson events (small contribution) are taken from Monte Carlo, applying all relevant correction factors, including dedicated factors correcting the electron to τ candidate misidentification rate, which is particularly important for the Z $\longrightarrow$ ee background.

6.5.4 Fake Taus

Events with jet faking τ_{had} candidates constitute the dominant background for the VBF category and the second dominant one for the boosted category (the dominant being Z$\longrightarrow \tau\tau$, see Table 6.4). Therefore, an accurate method is needed to model it.
This background consists mostly of W+jets, QCD multijets, Top(j$\longrightarrow \tau_{had}$) and Z$\longrightarrow$ll+jets (jet faking tau).

Trying to evaluate the j$\longrightarrow \tau_{had}$ fraction by Monte Carlo presents various challenges such as the very large backgrounds cross section as well as the relatively poor modeling of the detector performance for QCD jets mis-identified as $\tau - jets$. Thus a data-driven method is needed. In the following, two methods will be presented.

6.5.4.1 OS-SS Method

This is a method that can be applied at the preselection level for the $\tau_{lep}\tau_{had}$ channel. It exploits the charge asymmetry between the opposite sign (OS) and same sign (SS) events for a given background type. It is based on the following important assumptions:

- The shape of the discriminant variable (MMC) for the QCD background in the signal region is the same for OS and SS events passing all kinematic selection cuts (except for charge requirements) for a given analysis category.

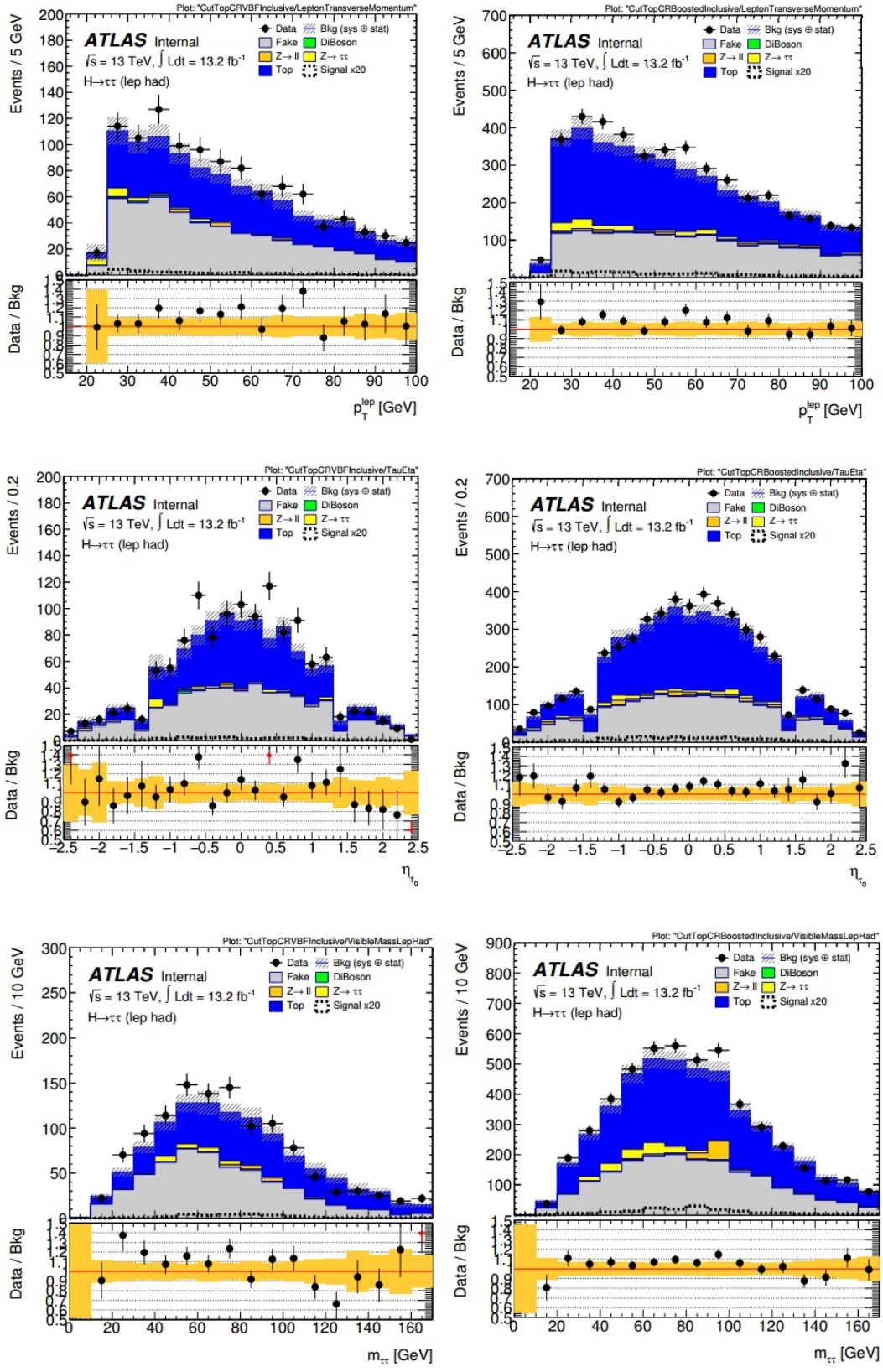

Figure 6.11: Left: Distributions for the Top control region for VBF inclusive selections for the lepton p_T (top), the hadronic tau η (middle) and the MMC distribution (bottom). Right: The same distributions for the Top control region for Boosted inclusive selections. Top background is in dark blue and the other dominant contribution is from fakes.

- The MC-to-data scale factor, k = N(data)/N(MC), for a given background is the same for events in the signal and corresponding control regions. However, scale factors k_{OS} and k_{SS} can have different values for some backgrounds and need to be obtained separately. The MC-based background predictions are multiplied by these k-factors in order to address possible mis-modeling of jet τ_{had} fake rates in MC simulation and to reduce systematic uncertainties on the normalization of backgrounds derived from the MC predictions.

Given this, the number of OS background events in each bin of the MMC, N_{OS}^{bkg} can be predicted as follows [5] [22] [23] [24]:

$$N_{OS}^{bkg} = r_{QCD}.N_{SS}^{data}+N_{add-on}^{Z\longrightarrow\tau\tau}+N_{add-on}^{Z\longrightarrow ll(l\longrightarrow\tau)}+N_{add-on}^{Z\longrightarrow ll+jet(\longrightarrow\tau)}+N_{add-on}^{W+jets}N_{add-on}^{top}+N_{add-on}^{VV} \quad (6.3)$$

where:

1. r_{QCD} is a factor accounting for the differences between QCD events present in the OS sample and the SS sample. It is derived in a QCD data control region as defined in Section 6.4.4.

2. N_{SS}^{data} is the number of SS data events. This is dominated by QCD events but also contain contributions from other backgrounds (mainly backgrounds with a jet faking a τ_{had}).

3. N_{add-on}^{X} is the number of background events of X process (Z$\longrightarrow \tau\tau$, Z$\longrightarrow ll(l\longrightarrow\tau)$, Z$\longrightarrow ll+jet(\longrightarrow\tau)$, W+jets, Top, VV) which is estimated using MC simulation. A part of the corresponding background is already included in the SS data sample.

N_{add-on}^{X} can be expressed as:

$$N_{add-on}^{X} = k_{OS}^{X} \times N_{OS}^{X} - r_{QCD} \times k_{SS}^{X} \times N_{SS} \quad (6.4)$$

where $k_{OS(SS)}^{X}$ is the background-to-data normalization factor, applied to the OS(SS) yield of background type X. They are derived from the corresponding control regions defined in Section 6.4.4.

The OS-SS is limited to the preselection level due to statistical limitations, in particular in SS data samples after applying selection cuts. As a result, a stronger, more robust method is needed such as the fake factor" method described in the next section.

6.5.4.2 Fake Factor

The Fake Factor method FF is a data-based technique used to estimate jet $\longrightarrow \tau_{had}$ background processes.

It uses a control data sample with only taus that fails the τ_{had} identification. These are called "anti-taus" and the control sample is referred to as the anti-tau sample. In order to minimize the differences between anti-τ and identified τ samples, the taus with very low BDT identification score are not included (see Section 5.3). A compromise between the statistics and difference between anti-τ and identified τ samples leads to define the anti-τ's as τ's failing the medium BDT identification and having a BDT score above 0.35.
To estimate the fake background in the signal regions, the anti-τ sample can be used thanks to a transfer factor, called fake factor (FF). The number of background events in the signal region (SR) can be expressed as:

$$N^{SR}_{fakebkg} = (N^{data,SR}_{anti-\tau} - N^{other,SR}_{anti-\tau}) \times \mathrm{FF}^{\mathrm{CR}} \tag{6.5}$$

$$\mathrm{FF}_{\mathrm{CR}} = \frac{N^{identified-\tau}_{CR}}{N^{anti-\tau}_{CR}} \tag{6.6}$$

where:

- $N^{data,SR}_{anti-\tau}$ is the number of anti-τ events in the data SR.
- $N^{others,SR}_{anti-\tau}$ is the number of events containing real τ failing the τ_{had} identification by accident from Z$\longrightarrow \tau\tau$, top. It also includes fake τ coming from dibosons and Z$\longrightarrow$ll(l$\longrightarrow \tau$). It is estimated using MC simulation.
- $\mathrm{FF}_{\mathrm{CR}}$ is the FF derived in data control regions where the signal does not contribute. $N^{identified-\tau}_{CR}$ is the number of events with one identified-τ and $N^{anti-\tau}_{CR}$ is the number of events having anti-τ candidates and zero identified τ.

The FF is calculated for different background processes with jet faking τ_{had} such as: QCD multijets, W+jets, Top (j$\longrightarrow \tau$) and Z($\longrightarrow$ll)+$\longrightarrow$jets. The definitions of the corresponding control regions are given in Section 6.4.4. Each control region is then further split into a "pass" and "fail" region, depending whether the τ-jet passed or failed the medium requirement. The individual fake-factor, for a given background process, is then obtained, in the corresponding control region, as the fraction of data events that pass the tau ID requirement.
The FF depends on some parameters of the τ_{had} candidate such as the number of tracks and the transverse momentum p_T. Therefore, it is measured for 1 and 3-prong separately and in bins on $\mathrm{p_T}$. In addition, it is measured separately in the different signal categories.
When we apply the FF in the anti-τ SR, one cannot know which data event is due to which process. Therefore, a combined FF which accounts for the relative fraction of each background process is needed. It can be expressed as:

$$\mathrm{FF}(\mathrm{p_T}, \mathrm{n_{prong}}, \mathrm{cat}) = \sum_{i=1} \mathrm{R_i FF_i}(\mathrm{p_T}, \mathrm{n_{prong}}, \mathrm{cat}) \tag{6.7}$$

where FF_i are the individual fake factors determined in dedicated control regions for each process, R_i is the expected fraction of background process i. They are determined from MC simulation, except for R_{QCD} which is obtained as R_{QCD} = 1 - $\sum R_i$. It is given by:

$$R_i = \frac{k_i . N^{anti-\tau,SR}_{i,MC,j\longrightarrow\tau}}{N^{anti-\tau,SR}_{Data} - N^{anti-\tau,SR}_{MC,notj\longrightarrow\tau}} \tag{6.8}$$

j$\longrightarrow \tau$ denotes MC events where a jet fakes a hadronic tau while notj$\longrightarrow \tau$ is for events where the hadronic tau is not faked by a jet.
k_i is a factor applied to correct for data/MC differences in anti-τ region. It is obtained from the corresponding control region CR_i and it is calculated simply as the ratio of data (with all other processes subtracted) to the MC prediction for the given process (excluding events where the τ is not faked by a jet). Mathematically, for background process i:

$$k_i = \frac{N^{anti-\tau,CR_i}_{Data} - N^{anti-\tau,CR_i}_{MC,noti} - N^{anti-\tau,CR_i}_{MC,i,notj\longrightarrow\tau}}{N^{anti-tau,CR_i}_{MC,i,j\longrightarrow\tau}} \tag{6.9}$$

Figure 6.12 shows the fake factors for 1-prong for boosted and VBF. The fake factors for 3-prong case for boosted and VBF are shown in Figure 6.13.

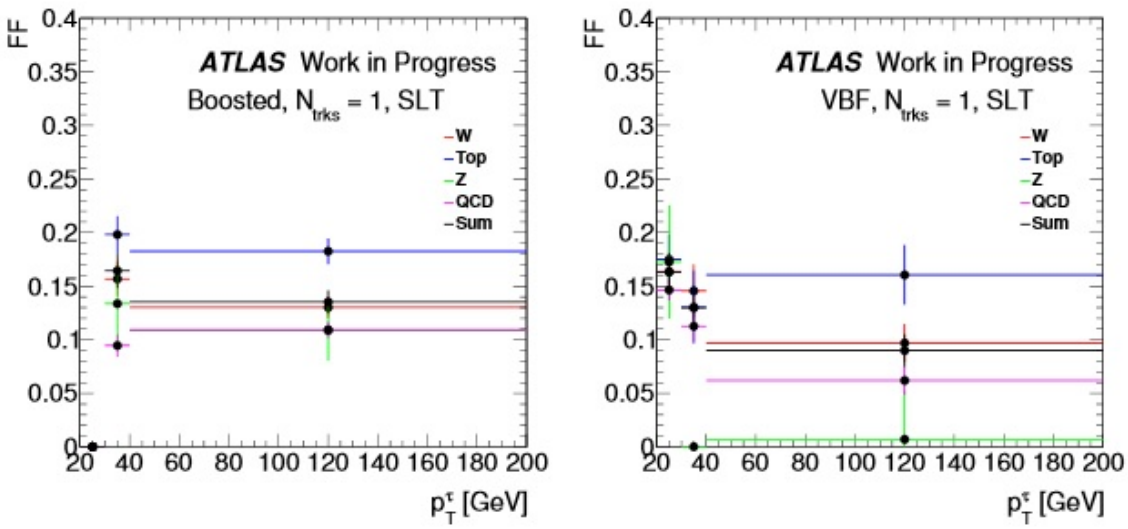

Figure 6.12: Fake factors for various processes in the boosted category (left) and VBF category (right) and for 1-prong.

There are two types of uncertainties assigned to the Fake Factor method:

Statistical uncertainty This uncertainty accounts for the statistical error when computing the Fake Factor FF itself. In each tau p_T bin, σ_{FF} represents the statis-

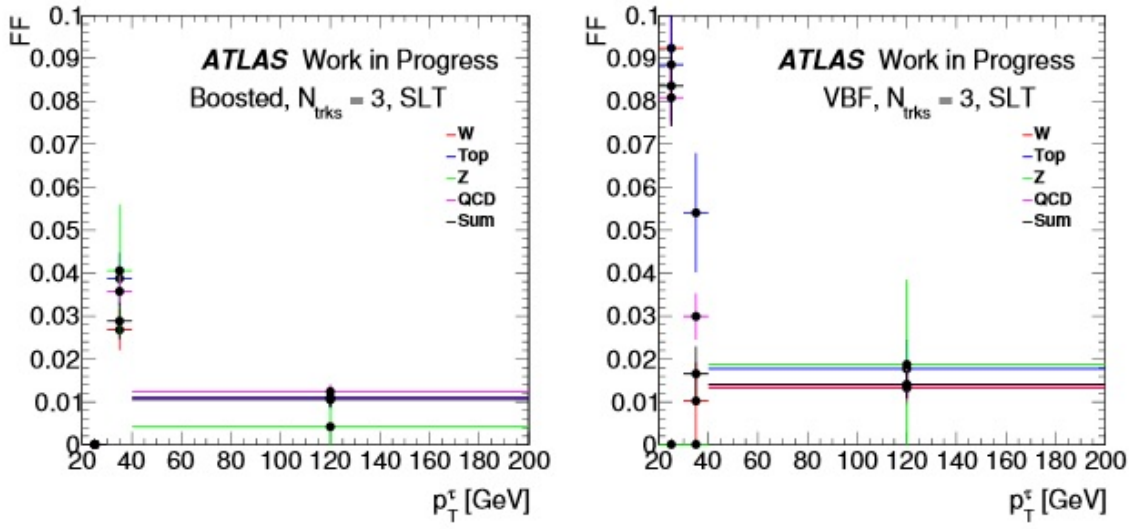

Figure 6.13: Fake factors for various processes in the boosted category (left) and VBF category (right) and for 3-prong.

tical uncertainty associated to the central FF value. To estimate this uncertainty, the fake yield is calculated using a fake factor varied up/down by the statistical associated error σ_{FF}.

Systematic uncertainty The major source of systematic uncertainties on the FF stems from the fake background composition estimation i.e. R_i calculation. This uncertainty is estimated by varying the R_i to be $\pm 50\%$ compared to the nominal value to compute the fake yield. In each tau p_T bin, the variation resulting in the largest fluctuation of FF central value, enveloping all others, is chosen for the systematic uncertainties evaluation. It is found to come from W+jets most of the time. Therefore, there are 2 values in each tau p_T bin: one for maximum upward variation and another for maximum downward variation.

6.6 Systematic uncertainties

Several sources of systematic uncertainties have to be taken into account in order to evaluate the compatibility of the observed data with the predicted signal and background contributions. There are three categories of systematic uncertainties: experimental, theoretical and background modeling. Experimental uncertainties are related to the simulation of the detector response and to the measurement of background contributions from control data. Theoretical uncertainties are related to the cross section predictions and the event modeling with Monte-Carlo event generators. Background modeling uncertainties are related to the background estimation techniques.

In order to take into account each source of systematic uncertainty, its impact is expressed in terms of relative changes of the expected event yields and in the shape of the MMC distributions in each event category. Each uncertainty is obtained by varying a given experimental or theoretical quantity by ± 1 standard deviation around the nominal value.
Below we give a list of the main systematic uncertainties included in this analysis.

6.6.1 Experimental uncertainties

Luminosity Measurement Uncertainty The measurement of the integrated luminosity has an uncertainty of 2.1% for the 2015 dataset and 3.7% for 2016. It is estimated from beam calibration scans [25].

Tau Energy Scale (TES) uncertainties To obtain the systematic uncertainty due to Tau Energy Scale, upwards and downwards variations are applied to the objects according to the recommendations of the corresponding working group. It is composed of several independent components affecting different ranges in τ_{had} transverse momentum. It takes also into account the modeling of τ_{had} properties with simulation, including uncertainties due to pileup contributions, underlying event description and detector geometry and response [26].
The TES uncertainties affect both the predicted event yields and the shape of the MMC distributions in each event category. They are determined primarily by fitting the reconstructed visible mass for Z$\longrightarrow \tau\tau$ events in data. The precision amounts to approximately $\pm 3\%$.

Figure 6.14 shows the impact of the in situ component of TES uncertainty on the MMC distribution in the Boosted (left) and VBF (right) combined categories.

Jet Energy Scale uncertainties The calibration of the energy scale of simulated jets (JES) is affected by several different systematic uncertainties [27] [28] [29]:

- Uncertainty of the JES measurement from the in-situ analyses (Z+jet, gamma+jet, and multi-jet).
- Eta-intercalibration and detector response uncertainties.
- Uncertainties to correct for high-p_T jets (pileup effects), and uncertainty for b-jets are taken into account.
- Uncertainty due to the difference in the calorimeter response to quark-initiated and gluon-initiated jets.

In addition to the systematic uncertainty on the jet energy scale, also the systematic uncertainty on the jet energy resolution (JER) data is taken into account [28] [30].

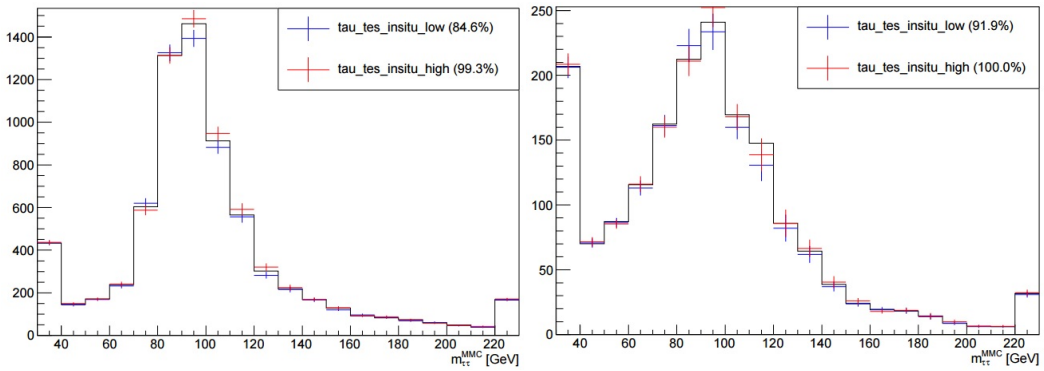

Figure 6.14: Impact of TES in situ component on the MMC distributions in the combined Boosted category (left) and combined VBF category (right) on all background plus signal components. The red(blue) line shows the MMC distribution resulting from the upward(downward) variation of the TES in situ by one standard deviation.

Figure 6.15 shows the impact of one in situ component of JES uncertainty on the MMC distribution in the Boosted (left) and VBF (right) combined categories. The signal yield in VBF event categories are the most affected by the JES due to the requirement of two tagging jets in the final state. Even though no jets are explicitly required in Boosted event categories, the requirement of a high pT(H) value indirectly selects events with a hard jet whose energy scale uncertainty can affect the E_T^{miss} calculation.

Efficiencies This includes the following uncertainties:

- Leptons reconstruction and identification uncertainties: They reflect the impact of the uncertainties on the efficiency correction factors provided by the corresponding combined performance groups for both electrons and muons and applied on Monte Carlo as described in Chapter 4 [31] [32] .

- Lepton isolation uncertainties: The efficiencies of the isolation cuts applied on the electron and muon candidates are measured through tag-and-probe studies, deriving correction factors for the Monte Carlo. These correction factors are then varied upwards and downwards within their uncertainties, to evaluate the impact on the analysis.

- Trigger efficiency uncertainties: The correction factors are derived for the Monte Carlo and applied in the analysis on trigger efficiencies, then varied upwards and downwards within their uncertainties.

- Efficiency uncertainties on the reconstruction, identification and trigger for the hadronic tau are also included [33]. The uncertainty on the τ_{had} identification

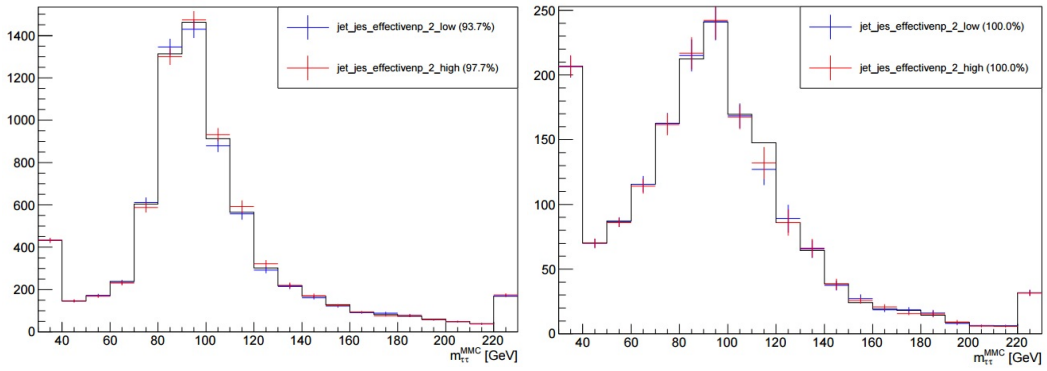

Figure 6.15: Impact of JES in situ component on the MMC distributions in the combined Boosted category (left) and combined VBF category (right) on all background plus signal components. The red(blue) line shows the MMC distribution resulting from the upward(downward) variation of the TES in situ by one standard deviation.

efficiency is ±3-5% for 1-prong and ±4-6% for 3-prong decays.
Furthermore, the correction factors on the rate of misidentification of electrons as hadronic τ candidates (applied on τ candidates matched with a true electron) are also varied within their uncertainties.

- The b-jet tagging efficiency has been measured from data using $t\bar{t}$ events.

Lepton energy resolution and scale Uncertainties on the muon energy scale and electron energy scale and resolution are also taken into account in the analysis.

E_T^{miss} **uncertainty** soft term scale and resolution uncertainties are also considered, as independent systematic uncertainties.

6.6.2 Theoretical uncertainties

Theoretical systematic uncertainties affect the prediction of the cross sections and the modeling of the simulated signal and background processes. They can be categorized as follows:

- Uncertainties on the parton distribution functions (PDF).
- Uncertainty on the branching ratio (BR) of the H $\longrightarrow \tau\tau$ decay.
- Uncertainties on the matrix elements calculations (QCD scale).
- Uncertainty on the modeling of the underlying event (UE).

- Theory systematics for Z production.

The uncertainty on the Higgs production cross-section is used as given by the Higgs cross section working group [34]. For a SM Higgs mass of 125.09 GeV the QCD scale uncertainties are ±4.0% for gluon fusion production and $^{+0.4\%}_{-0.3\%}$ for VBF production. The PDF uncertainties are ±3.2% for gluon fusion production and ±2.1% for VBF production.
The branching ratio for $H \longrightarrow \tau\tau$ is given as $0.06256^{+1.17\%}_{-1.16\%}$.
There are various sources of theory systematics for Z production, including PDF, Parton Shower Model, MC generator,... This can be applied as a cross section uncertainty and an acceptance and shape uncertainty (on Z p_T and jet activity).
With the normalization factors for VBF and Boosted included in the Fit Model as described in Section 6.5.1, one can absorb all theory uncertainties that affect the normalisation or the acceptance of the VBF and boosted selection.
The theory uncertainties can also affect the shape of the MMC distribution. This is added as one systematic uncertainty by comparing MADGRAPH and SHERPA generators as described in details in Section 6.5.1.

6.6.3 Background modeling uncertainty

An important systematic uncertainty on the background determination comes from the estimated fake background using the fake factor method. This includes the statistical uncertainty on the fake factor and systematic uncertainty on the methodology itself that arises from the composition of the combined fake background (W+jets, Z+jets, multijet, and $t\bar{t}$ fractions), which is largely estimated based on simulated event samples as explained in Section 6.5.4.2.

6.7 Fit model and signal extraction

The search for the Higgs boson signal in the analysis presented in this thesis is performed by testing the level of agreement between the observed data from ATLAS detector with either the "background-plus-signal" or the "background-only" hypothesis. For this, a proper model needs to be built for the selected data and all expected signal and background contributions, including data driven background measurements and systematic uncertainties.
The model depends on several input parameters. The "parameter of interest" (PoI) in our case is the Higgs boson production cross section times $H \longrightarrow \tau^+\tau^-$ decay branching ratio, expressed in units of the corresponding value predicted by the SM and referred to as the signal strength μ (for SM, μ=1).
The model includes also a number of nuisance parameters (NP) which correspond to the statistical and systematic uncertainties (as described in 6.6) and the normalisation of background contributions measured in data control regions.

6.7.1 Construction of the fit model

To build the fit model, starting from Root histograms, a RooFit workspace is created using the WorkspaceBuilder software package based on the histogram-based fitmodel machinery HistFactory in the RooStat package [35] (see Figure 6.1). It will create the probability density functions (pdf) of the binned discriminating variable distribution expected in each event category (MMC). It offers a good discrimination power between the signal and the background processes and also as it is sensitive to the Higgs boson mass.
The histograms of the expected MMC distributions are composed of the individual samples from VBF, ggH, VH and $t\bar{t}$ for signal processes and Fake tau, Z$\longrightarrow \tau\tau$ and the other background processes. The modeling of these contributions together with the corresponding relative uncertainties have been described previously.

The total event yield and thus, the normalization of the Z $\longrightarrow \tau\tau$ and Top background processes are obtained directly from the fit to the MMC distributions. The relative yield in each event category is given by the respective models. The fake tau background is determined by the Fake Factor method and the event yield of the signal and of the remaining background processes are obtained from the calculated cross sections and the measured integrated luminosity relying on simulation for the relative yield in each event category, together with their associated systematic uncertainties.
Let's now define α=$\{\mu, \alpha_p, \phi_p, \gamma_p\}$ as the set of parameters of the fit model, where μ is the parameter of interest and the other terms represent the different nuisance parameters classified as follows:

- The systematic uncertainties S = $\{\alpha_p\}$.
- The normalisation factors N = $\{\phi_p\}$ determined directly from the fit.
- The statistical uncertainties Γ = $\{\gamma_p\}$ of the expected number of events in each histogram bin.

The definition of the model can be defined as in Equation 6.10 [36] [38] :

$$P(\mathrm{n_{cb}}, \mathrm{a_p}|\mu, \phi_\mathrm{p}, \alpha_\mathrm{p}, \gamma_\mathrm{p}) = \prod_{c\in channels} \prod_{b\in bins} \mathrm{Pois}(\mathrm{n_{cb}}|\mathrm{v_{cb}}).\mathrm{G}(\mathrm{L_0}|\lambda, \Delta_\mathrm{L}).\prod \mathrm{f_p}(\mathrm{a_p}|\alpha_\mathrm{p}) \tag{6.10}$$

where c are the event categories, in the following referred to as channels, b are the bins of the MMC distribution in channel c, Pois($\mathrm{n_{cb}}|\mathrm{v_{cb}}$) is the Poisson probability of observing $\mathrm{n_{cb}}$ events in the bin b of channel c given the expected number of events $\mathrm{v_{cb}}$, G($\mathrm{L_0}|\lambda, \Delta_\mathrm{L}$) is the Gaussian probability for measuring integrated luminosity $\mathrm{L_0}$, given the true integrated luminosity λ and the measurement uncertainty Δ_L. $\mathrm{f_p}(\mathrm{a_p}|\alpha_\mathrm{p})$ is is the pdf that determines the constraint on the nuisance parameter α_p, based on auxiliary measurements or theoretical calculations $\mathrm{a_p}$.

The statistical description of the observed data is given by the maximum likelihood estimator (MLE), defined as the set of parameter values $\widehat{\alpha}$ that maximises the likelihood function 6.11 [38]:

$$\mathrm{L}(\alpha) = P(n_{cb}, a_p|\mu, \phi_p, \alpha_p, \gamma_p) \tag{6.11}$$

where $\mathrm{n_{cb}}$ is the observed number of events in the bin b of the channel c. The maximisation is performed with the Minuit programme [40] which minimises the value of -log L(α).
For the construction of the likelihood function, the following signal and background regions are included in the fit (see Section 6.4):

- Boosted:
  1. Boosted High-$\mathrm{p_T^H}$ signal region.
  2. Boosted Low-$\mathrm{p_T^H}$ signal region.
  3. Inclusive Boosted Top control region.
- VBF:
  1. VBF-Tight signal region.
  2. VBF-Loose signal region.
  3. Inclusive VBF Top control region.
- Z control regions (see Section 6.5.1):
  1. Boosted Z$\longrightarrow \tau\tau$ control region.
  2. VBF Z$\longrightarrow \tau\tau$ control region.

The $\tau_{lep}\tau_{had}$ fit model is illustrated in Figure 6.16 where the boxes represent the different signal and control regions and the arrows represent the different normalisation factors.

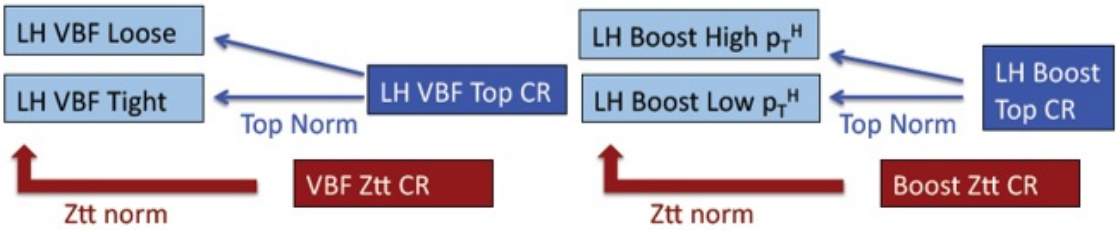

Figure 6.16: Schematic summary of the $\tau_{lep}\tau_{had}$ fit model employed. Boxes symbolise signal or control regions, while arrows and brackets represent normalisation factors.

While in signal regions the binned MMC distribution is used to infer information on the parameter of interest, control regions are employed to constrain the event

yield of specific background processes (i.e. top quark and Z $\longrightarrow$ll production) with a single-bin containing the number of events in this control region. Z control regions are also included in order to constrain the dominant Z $\longrightarrow \tau\tau$ background, as described in detail in Section 6.5.1.

As described previously, all systematic uncertainties enter the fit as Nuisance Parameters (NPs) on the normalization or/and on the MMC shape. An important issue in dealing with the shape NPs in the fit model is the fact that many of the samples are relatively low in statistics after all selections have been applied, meaning that in the case of small systematic variations, the corresponding upwards or downwards varied shapes may in fact be dominated by statistical noise which causes instabilities and allows for incorrect and unintentional variation of the NPs. In order to suppress this noisy effect, two methods, called "pruning" and "smoothing", have been used:

- Pruning: It is a χ^2 test between the upwards and the downwards fluctuated shape with respect to the nominal one, for each shape NP and each sample. It takes into account the statistical uncertainty and the systematic is retained if the result of the reduced χ^2 test is greater than 0.1, for either of the upwards or downwards fluctuated shape (i.e. prune the shape components which are very similar to the nominal).
  Another check is also performed which asks for at least one bin where the variation exceeds 50% of the samples statistical uncertainty to prune the systematic.

- Smoothing: it is the TH1::Smooth(1) method [37] on the up/down shape variations in order to minimize the effect of low statistics.

6.7.2 Test statistics

To quantify the agreement between the observed data and a given hypothesis, two situations may occur:

- If no signal is observed, we try to set a limit on its production cross-section. This is done by rejecting the S+B hypothesis (H_0) versus the B-only hypothesis (H_1).

- If an excess of events is observed, one needs to quantify the agreement compatibility of the data with the background-only hypothesis (H_0).
  H_0 is called the null hypothesis and is the one we want to validate. If the validation fails, we can claim we observe a signal (H_1 hypothesis).

At LHC, the choice made is to use a profile likelihood for the test statistics as explained in the previous section. This likelihood is defined as shown in equation 6.12 [38]:

$$q_\mu = -2ln(\frac{L(\mu, \widehat{\widehat{\theta}}_\mu)}{L(\widehat{\mu}, \widehat{\theta})}) = -2ln\lambda(\mu) \tag{6.12}$$

where μ is the value of the parameter of interest to be tested. $\widehat{\widehat{\theta}}_\mu$ is the value of the nuisance parameters that maximize the likelihood for a given value of μ. $\widehat{\mu}$ and $\widehat{\theta}$ are the values that maximize the likelihood $L(\mu, \theta)$.
The value of a test statistic q_μ can be estimated for the observed data. The next question is whether this value is consistent with the μ hypothesis. To quantify this agreement, the distributions of q_μ for the H_0 and H_1 hypotheses are needed.

Asymptotics formulae for discovery For a discovery analysis, we test the background-only hypothesis in order to reject the hypothesis according to which the excess could be due to a background fluctuation:

$$q_0 = \begin{cases} -2ln\lambda(0) & \text{if} \quad \widehat{\mu} \geq 0 \\ 0 & \text{if} \quad \widehat{\mu} < 0 \end{cases} \tag{6.13}$$

Let's now define the p-value (Equation 6.14) as the probability that the number of observed events in the background-only hypothesis is at least equal to the observed excess in data. If this probability is low, the data looks compatible with the presence of a signal. The p-value is translated into a significance Z, corresponding to the distance to the mean of a Gaussian of width 1, such that the integral of the tail is equal to the p-value (Figure 6.17). Discovery is claimed when the significance reaches 5σ, i.e. a p-value of the order of 10^{-7} [38] [39].

$$p_0 = \int_{q_0 obs}^{\infty} f(q_0|\mu = 0) \tag{6.14}$$

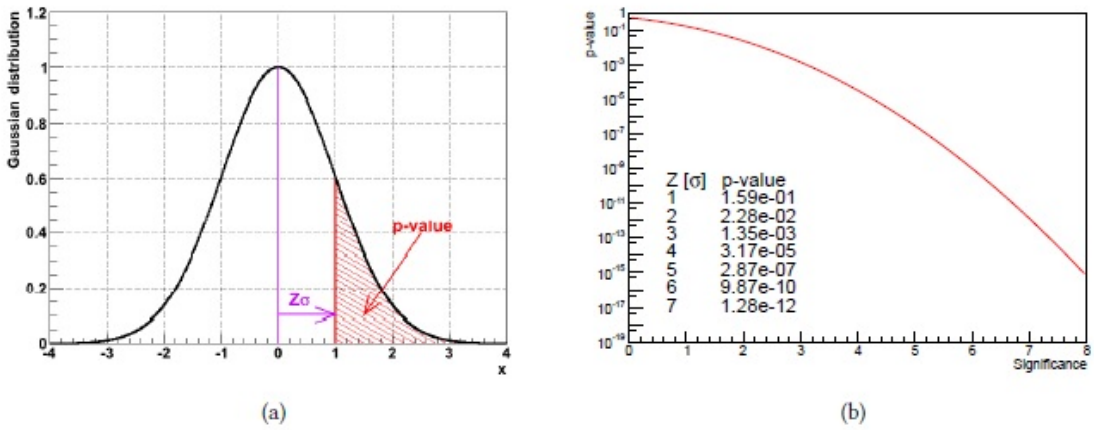

Figure 6.17: Relation between p-value and significance Z [38] [39].

Asimov dataset To estimate the expected values for the parameters, the so-called "Asimov" dataset is used [38]. It is a single representative dataset in which all the statistical fluctuations are suppressed. It is created such that the number of events in each bin is equal to the expected ones. The same statistical procedure can then be repeated for this dataset, using the test statistics of Equation 6.12.
The Asimov dataset has two great advantages:

- It allows to evaluate q_μ without using toy models.
- It allows to to extrapolate the sensitivity of the experiment (in terms of μ) for an expected luminosity.

Hybrid dataset In order to test the behavior of the fit model with the real data before unblinding the MMC distribution in the signal region between 100 GeV and 150 GeV, a "Hybrid" dataset is used. It is called hybrid because real data are used outside the signal region (called mass side-bands $0 <$ MMC < 100 GeV and MMC > 150 GeV) and an Asimov dataset in the signal region, thus it is an intermediate step between the Asimov dataset and the full unblinding. It takes thus into account statistical fluctuations, and by consequence also nuisance parameters.

Unblinded dataset The last step, after validating the model on the "Asimov" and the "Hybrid" datasets, is to unblind the full MMC mass range, perform the full fit machinery on the real data and produce the final sensitivity results.

Best fit value and profiling The best fit value $\widehat{\mu}$ is obtained by minimizing the likelihood (Equation 6.12). An iterative way of finding them is to scan the allowed range for the parameter of interest, fix it, and perform a fit of all the remaining parameters. The value of the likelihood one obtains is used to make profile plots as the one illustrated in Figure 6.18.

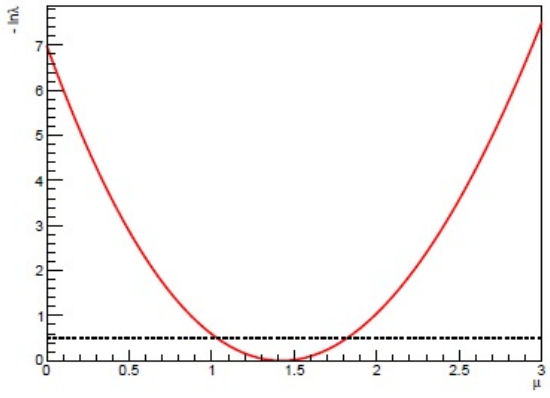

Figure 6.18: μ likelihood scan (profile) [38] [39].

6.8 Results for $\tau_{lep}\tau_{had}$ channel

6.8.1 Procedure

The fit procedure can be summarized by the following steps:

1. Make sure the MMC distributions entering the Maximum Likelihood Estimator (MLE), i.e. the prefit distributions, are reasonable and do not show a discrepancy between the dataset and the background plus signal predictions, especially for hybrid and unblinded datasets. For Asimov dataset, it is obvious by definition that the data fit exactly the background plus signal prediction as described before.

2. Run the fit machinery and check the behavior of the nuisance parameters (NP). As described in Section 6.7, a large number of systematic uncertainties, taken into account via nuisance parameters, affect the final results. It is important to investigate the behavior of the global fit and in particular to investigate how far the nuisance parameters are pulled away from their nominal values and how well their errors are understood. Furthermore, it is important to understand which systematic uncertainties have the most impact on the final result. For this purpose, a ranking of nuisance parameters is introduced. For each parameter, the fit is performed again with the parameter fixed to its fitted value shifted up or down by its fitted error, with all the other parameters are let free to vary. This allows to look at the contribution of each nuisance parameter to the total uncertainty on μ.

3. Once the previous steps are validated, the so-called "postfit" results should be checked. This includes the final distributions and the observed and expected events yield resulting from the MLE, i.e. the best fit of the statistical model to the data with background normalization, signal normalization, and nuisance parameters adjusted by the profile likelihood global fit.

4. The fitted signal strength and the expected and observed significance are shown as final results.

This is performed successively for the three datasets described previously: Asimov, hybrid and unblinded datasets.

6.8.2 Asimov dataset

Prefit The MMC prefit distributions for the four exclusive signal regions are shown in Figure 6.19. The data points are fitting perfectly the Background plus Signal predictions which is natural since it is an "Asimov" dataset.

As described previously, the likelihood fit includes information on event yield in selected control regions defined previously to constrain the normalization of background estimates for various processes, i.e. a top and $Z \longrightarrow \tau\tau$ control regions for the VBF and boosted categories.

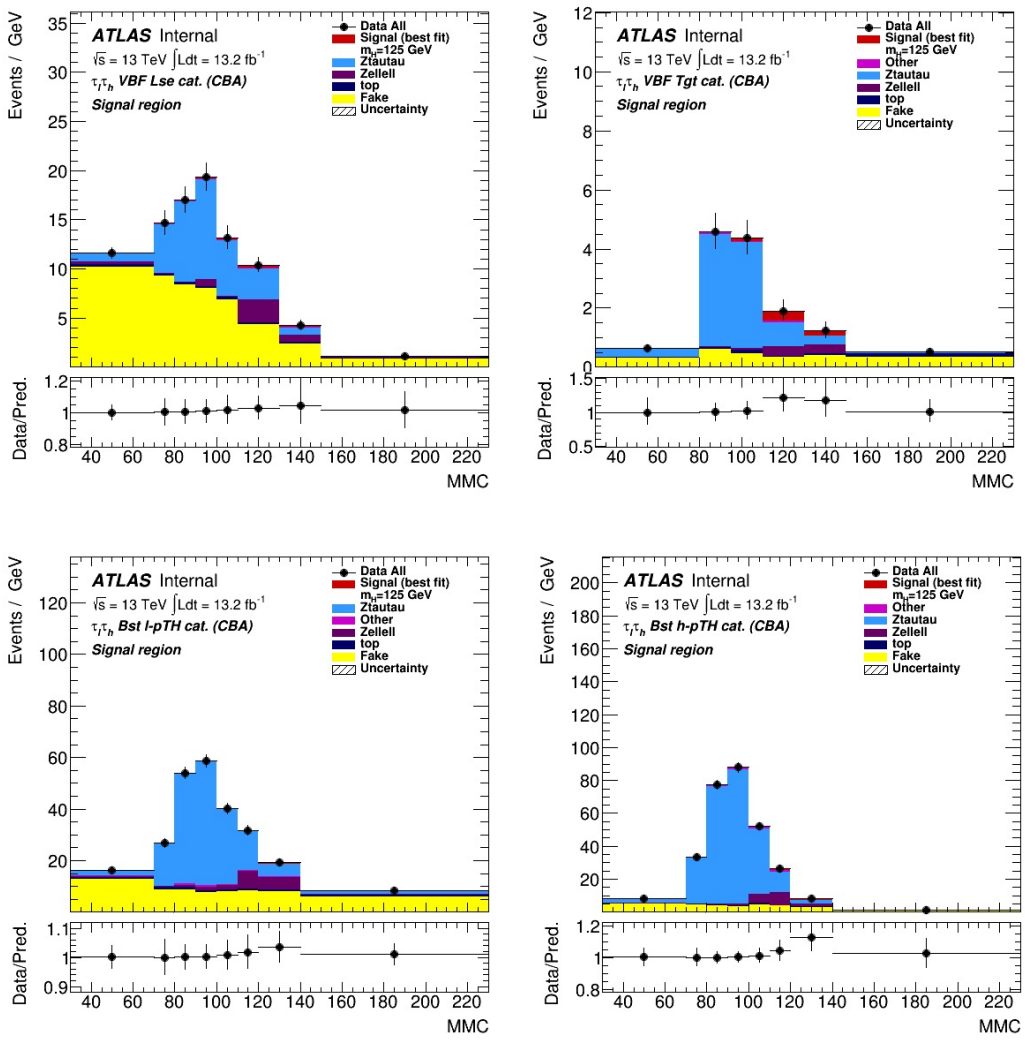

Figure 6.19: Prefit MMC distributions for the various signal regions used in the fit for the Asimov dataset(VBF loose in the top left, VBF tight in the top right, Boosted HpT in the bottom left and Boosted LpT in bottom right). Data points fit perfectly the background+signal predictions since it is an Asimov dataset. The ratio in the lower panels is not always one because it is between the data and Background prediction without including the signal MC contribution.

Nuisance parameters Figure 6.20 illustrate two informations concerning the NP behavior:

- **NP Ranking**: The systematic uncertainties are listed in decreasing order of their impact on the fitted signal-strength parameter $\widehat{\mu}$ on the y-axis (NP ranking), where the hatched blue and empty boxes show the variations of $\widehat{\mu}$ displayed on the top x-axis, when fixing the corresponding individual nuisance parameter θ to its post-fit value $\widehat{\theta}$ and modified upwards or downwards by its post-fit uncertainty, and repeating the fit. The yellow bands represent the prefit impact of each NP on μ.
- **Pulls**: The deviations of the fitted parameters $\widehat{\theta}$ from their nominal values θ_0, normalized to their nominal uncertainties $\Delta\theta$ are illustrated by the filled circles referring to the bottom x-axis. The black lines show the post-fit uncertainties of the nuisance parameters, relative to their nominal uncertainties.

Figure 6.20 shows the first 15 NP impacting most the signal-strength parameter $\widehat{\mu}$. One can see that the parameters contributing most are: the efficiency uncertainty on the correction of the misidentification rate of electrons as hadronic τ, the jet energy scale and energy resolution systematics, the MET soft term scale, in addition to other systematics like the jet energy resolution, the statistical component of the uncertainty on the Fake Factor method (VBF category), the tau energy scale.
On the other hand, we see that the pulls are all centered at zero and their errors are closed to one which is expected since it is a fit on the Asimov dataset, so no deviation of the fitted NP from their nominal values is expected.

Postfit The postfit MMC distributions are shown in Figure 6.21. The data (Asimov) fit always the background plus signal predictions. Table 6.6 shows the observed and expected events yield in each category. A good agreement between the fitted yield and the MC prediction is achieved.

Signal strength and significance All the previously described tests do not single out any problem and confirm that the fit is stable and without unexpected features. The fitted signal strength for a Higgs boson signal with mass of $m_H = 125$ GeV is $\mu = 0.997^{+0.818}_{-0.818}$, knowing that μ should be one in this case since it is an Asimov dataset. The p-value is found to be 0.11 which corresponds to an expected significance of 1.22.

6.8.3 Next steps

The hybrid and unblinded datasets results are not shown in this thesis since there is still an ongoing work to understand the fit issues, in particular the problematic nuisance parameters, especially the Jet Energy resolution (JER), the Jet Energy Scale (JES) and the pileup reweighting (PWR). These nuisance parameters have

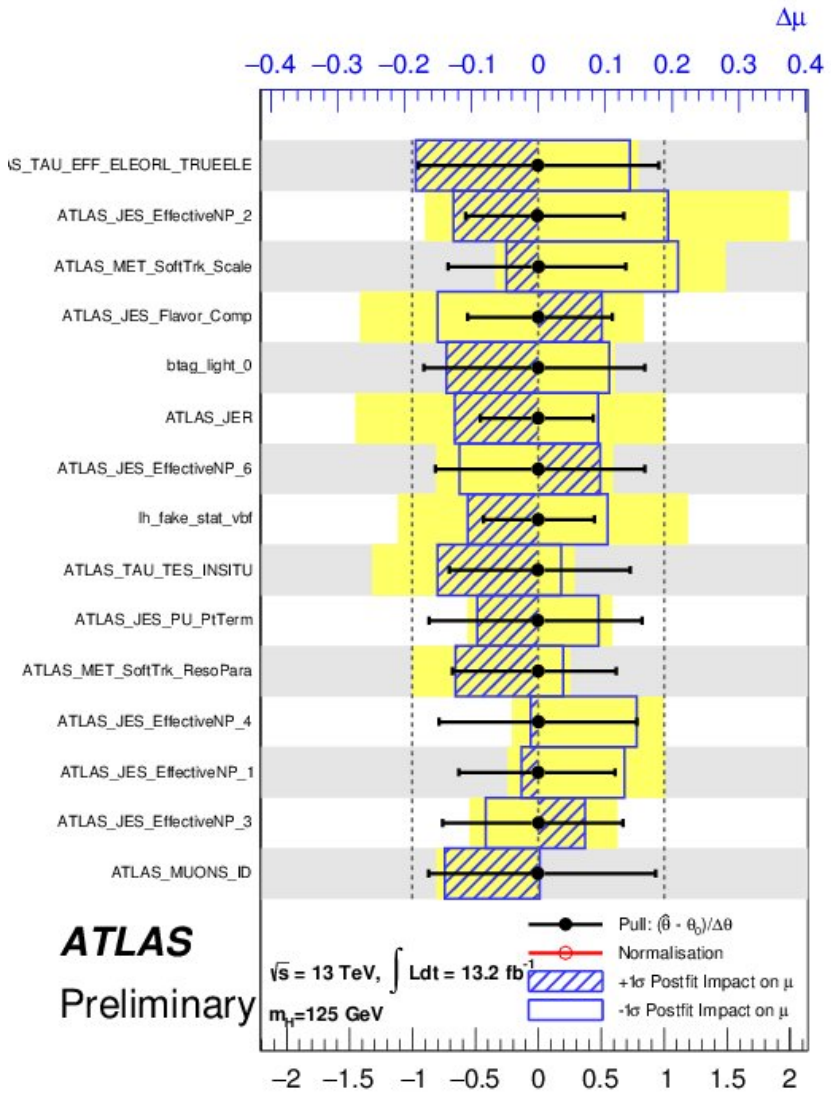

Figure 6.20: Ranking plot for the Asimov dataset. See the text for a detailed descripton of the different informations shown in this plot.

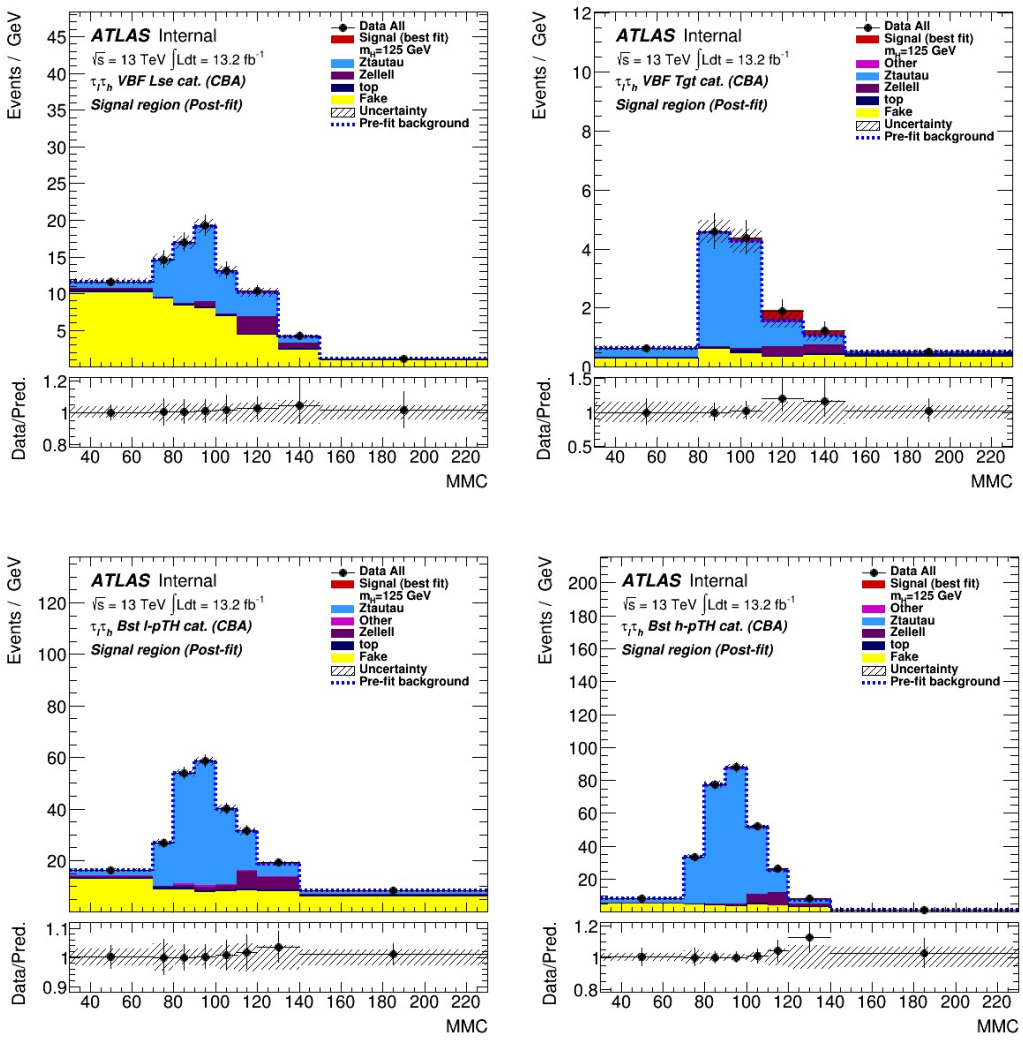

Figure 6.21: Postfit MMC distributions for the various signal regions used in the fit (VBF loose in the top left, VBF tight in the top right, Boosted HpT in the bottom left and Boosted LpT in bottom right). Data points fit perfectly the background+signal predictions since it is an Asimov dataset. The ratio in the lower panels is not always one because it is between the data and Background prediction without including the signal MC contribution.

Category	VBF Tight	VBF Loose	Boosted HpT	Boosted LpT
Fake	72.9 ± 5.4	934.6 ± 39.2	507.2 ± 21.9	1610.8 ± 66.2
Top	15.4 ± 2.6	37.4 ± 6.2	68.2 ± 10.5	148.3 ± 24.2
Diboson	6.4 ± 0.8	12.6 ± 1.0	75.7 ± 4.8	67.5 ± 4.0
Z$\longrightarrow$ll	14.9 ± 5.3	85.3 ± 14.5	202.8 ± 27.8	241.3 ± 37.4
Z$\longrightarrow \tau\tau$	148.5 ± 11.1	404.2 ± 21.4	2504.2 ± 58.7	1805.0 ± 58.0
Total bkg	258.2 ± 13.9	1474.1 ± 37.1	3358.2 ± 61.1	3873.0 ± 62.8
ttH	0.01 ± 0.01	0.02 ± 0.02	0.3 ± 0.2	0.1 ± 0.1
Zh	–	0.07 ± 0.06	1.6 ± 1.3	1.2 ± 1.0
WH	–	–	3.7 ± 3.0	0.8 ± 0.7
VBFH	9.1 ± 7.4	8.3 ± 6.8	5.2 ± 4.2	4.5 ± 3.6
ggH	3.7 ± 3.1	6.2 ± 5.3	28.7 ± 23.3	24.8 ± 20.2
Total Signal	12.8 ± 10.4	14.6 ± 12.0	39.5 ± 31.9	31.3 ± 25.6
data	270	1488	3396	3904

Table 6.6: The predicted postfit event yields for the four signal regions. The background normalizations, signal normalization, and their uncertainties represent the postfit values. The uncertainties on the total background and total signal represent the full statistical and systematic uncertainty.

shown an over-constraint from the fit and it needs to be understood. These issues are common to the three subchannels ($\tau_{lep}\tau_{lep}$, $\tau_{lep}\tau_{had}$ and $\tau_{had}\tau_{had}$). However, the $\tau_{lep}\tau_{lep}$ fit has shown the bigger over-constraint.
In the short term, there is no a plan to unblind the 13.2 fb^{-1} data presented in this document.

6.9 Prospects

In this thesis, the search for the Standard Model Higgs boson in the $\tau_{lep}\tau_{had}$ channel is presented. It is based on ATLAS data at 13 TeV with an integrated luminosity of 13.2 fb^{-1}.
In the first part, the work on the conversion tracks tagging study in order to improve the reconstruction of hadronic tau decay is presented. Two conversion tagging algorithms are available now in ATLAS tau software where their performance at 8 TeV and 13 TeV have been studied and presented.
The second part is focused on the H$\longrightarrow \tau_{lep}\tau_{had}$ search at 13 TeV where the analysis is presented from the first steps up to the fit results. Only expected results using Asimov dataset are shown since some aspects of the fit behavior still need to be understood.
The plan for the analysis now is to go for a publication in 2017 with the full 2015+2016 dataset (36 fb^{-1}) with H$\longrightarrow \tau\tau$ coupling results and possibly differential cross section measurements. The expected sensitivity with this luminosity for

the combined H$\longrightarrow \tau\tau$ cut-based analysis is a μ of 1 ± 0.38 and a significance of 2.7σ.
A MVA analysis will be performed with the full dataset. It is expected to give better sensitivity compared to the cut-based approach. In parallel, there is an ongoing work to make the embedding samples available for the Z$\longrightarrow \tau\tau$ background estimation.
A search for the Higgs CP is also ongoing using Run II data and the plan is to have a publication on the full 2015+2016 dataset in 2017.
Beyond the SM H$\longrightarrow \tau\tau$, preliminary H$\longrightarrow \mu\mu$ and Lepton Flavor Violation (LFV) analyses are finalized with the 13.2 fb^{-1} data to go for a publication on the full 2015+2016 data. In addition, a search for heavy $\tau\tau$ resonance interpreted as MSSM A/H is in progress.

Bibliography

[1] G. Aad et al., [ATLAS Collab.], Phys. Lett. B716, 1 (2012). (Cited on page 152.)

[2] S. Chatrchyan et al., [CMS Collab.], CMS Collab., Phys. Lett. B716, 30 (2012). (Cited on page 152.)

[3] LHC Higgs Cross Section Working Group, S. Heinemeyer, C. Mariotti, G. Passarino, and R. Tanaka (Eds.), *Handbook of LHC Higgs Cross Sections: 3. Higgs Properties*, CERN-2013-004 (CERN, Geneva, 2013), `arXiv:1307.1347 [hep-ph]`. (Cited on page 152.)

[4] Particle Data Group Collaboration, J. Beringer et al., Review of Particle Physics, Phys. Rev. D 86 (2012) 010001, http://link.aps.org/doi/10.1103/PhysRevD.86.010001. (Cited on page 152.)

[5] ATLAS Collaboration (Georges Aad et al.), Evidence for the Higgs-boson Yukawa coupling to tau leptons with the ATLAS detector, Jan 20, 2015 - 84 pages JHEP 1504 (2015) 117 (2015-04-21) DOI: 10.1007/JHEP04(2015)117 CERN-PH-EP-2014-262 (Cited on pages 153, 155, 158, 168 and 178.)

[6] ATLAS Collaboration, The ATLAS simulation infrastructure,Eur.Phys.J. C 70 (2010)823-874,arXiv: 1005.4568[physics.ins-det]. (Cited on page 154.)

[7] S. Alioli, P. Nason, C. Oleari and E. Re, A general framework for implementing NLO calculations in shower Monte Carlo programs : the POWHEG BOX, JHEP 1006, 043 (2010), arXiv:1002.2581 [hep-ph], DESY-10-018, SFB-CPP-10-22, IPPP-10-11, DCPT-10-22. (Cited on pages 154 and 175.)

[8] T. Sjostrand, S. Mrenna and P. Skands, PYTHIA 6.4 physics and manual, JHEP 05 (2006) 026, arXiv: hep-ph/0603175 [hep-ph]. (Cited on page 154.)

[9] J. Alwall et al., The automated computation of tree-level and next-to-leading order differential cross sections, and their matching to parton shower simulations, JHEP 1407 (2014) 079, arXiv: 1405.0301 [hep-ph] (Cited on page 154.)

[10] S. Jadach, J. H. Kuhn and Z. Was, TAUOLA - a library of Monte Carlo programs to simulate decays of polarized leptons, Comput. Phys. Commun. 64(1990) 275-299. (Cited on page 154.)

[11] GEANT4 Collaboration, S.Agostinelli et al., GEANT4 - A simulation toolkit, Nucl. Instrum. Meth. A 506 (2003) 250-303. (Cited on page 154.)

[12] ATLAS NOTE, "Measurement of the Higgs boson production cross section at 13 TeV in H $\longrightarrow$ $\tau\tau$ decays with the ATLAS detector", https://cds.cern.ch/record/2212838/files/ATLAS-COM-CONF-2016-112.pdf? (Cited on pages 155 and 162.)

[13] https://twiki.cern.ch/twiki/bin/viewauth/AtlasProtected/DerivationFramework (Cited on page 155.)

[14] https://twiki.cern.ch/twiki/bin/viewauth/AtlasProtected/XTauAnalysisFramework (Cited on page 156.)

[15] "Plotting Framework Tutorial", Christian Grefe, Bonn University, https://indico.cern.ch/event/460714/contributions/1131563/attachments/1184524/1716570/PlottingTutorial.pdf (Cited on page 157.)

[16] A. Elagin et al., A New Mass Reconstruction Technique for Resonances Decaying to $\tau\tau$, Nucl. Instrum. Meth. A654 (2011) 481-489, [arxiv:1012.4686] (Cited on pages 158, 160 and 162.)

[17] ATLAS Collaboration, Expected Performance of the ATLAS Experiment - Detector, Trigger and Physics, arXiv:0901.0512 (Cited on page 160.)

[18] ATLAS Collaboration,Search for the neutral MSSM Higgs bosons decaying to $\tau\tau$ pairs in proton-proton collisions at $\sqrt{s} = 7$ TeV with the ATLAS detector, ATLAS-CONF-2011-132 (2011) (Cited on pages 160 and 161.)

[19] ATLAS supporting note, "Measurement of the Higgs boson couplings to τ leptons in H$\longrightarrow \tau\tau$ decays produced in 13 TeV Collisions with the ATLAS Detector", https://cds.cern.ch/record/2151918/files/ATL-COM-PHYS-2016-489.pdf (Cited on page 162.)

[20] ATLAS Collaboration, G. Aad et al., Search for the Standard Model Higgs boson in the H $\longrightarrow \tau^+\tau^-$ decay mode with 4.7 fb^{-1} of ATLAS data at 7 TeV, ATLAS-CONF-2012-014, CERN, Geneva, March 2012. (Cited on page 173.)

[21] ATLAS Collaboration, Modeling Z $\longrightarrow \tau\tau$ processes in ATLAS with τ-embedded Z$\longrightarrow \mu\mu$ data, arXiv:1506.05623 [hep-ex], CERN-PH-EP-2015-130. (Cited on page 173.)

[22] ATLAS Collaboration, Search for the Standard Model Higgs boson in H $\longrightarrow \tau^+\tau^-$ decays in proton-proton collisions with the ATLAS detector, ATLAS-CONF-2012-160. (Cited on page 178.)

[23] ATLAS Collaboration, Evidence for Higgs Boson Decays to the $\tau^+\tau^-$ Final State with the ATLAS detector, ATLAS-CONF-2012-160. (Cited on page 178.)

[24] "Recherche de la désintgration du boson de Higgs en deux leptons taus dans l'expérience ATLAS" PhD thesis of Faten Hariri, Laboratoire de l'accélerateur linéaire (LAL). (Cited on page 178.)

[25] ATLAS Collaboration, Improved luminosity determination in pp collisions at $\sqrt{s} = 7$ TeV using the ATLAS detector at the LHC, Eur. Phys. J. C 73 (2013) 2518, arXiv: 1302.4393 [hep-ex]. (Cited on page 182.)

[26] Identification and energy calibration of hadronically decaying tau leptons with the ATLAS experiment in pp collisions at $\sqrt{s}$=8 TeV (Cited on page 182.)

[27] ATLAS Collaboration, In-situ determination of the ATLAS forward jet energy scale and uncertainty using dijet events at $\sqrt{s}$ = 13 TeV, ATLAS-COM-CONF-2015-023 (2015), url: https://cds.cern.ch/record/2015470. (Cited on page 182.)

[28] Jet Calibration and Systematic Uncertainties for Jets Reconstructed in the ATLAS Detector at $\sqrt{s}$ = 13 TeV, ATLAS-PHYS-PUB-2015-015 22nd July 2015 (Cited on page 182.)

[29] https://twiki.cern.ch/twiki/bin/viewauth/AtlasProtected/JetUncertainties2015ICHEP2016 (Cited on page 182.)

[30] https://twiki.cern.ch/twiki/bin/view/AtlasProtected/JetResolution2015Prerecom (Cited on page 182.)

[31] ATLAS Collaboration, G. Aad et al., Electron performance measurements with the ATLAS detector using the 2010 LHC proton-proton collision data, Eur.Phys.J. C72 (2012) 1909, arXiv:1110.3174 [hep-ex]. (Cited on page 183.)

[32] ATLAS Collaboration, Muon reconstruction performance of the ATLAS detector in proton-proton collision data at $\sqrt{s}$ = 13 TeV. arXiv:1603.05598v1 [hep-ex] 17 Mar 2016. (Cited on page 183.)

[33] ATLAS NOTE. ATL-PHYS-PUB-2015-045 2nd November 2015. Reconstruction, Energy Calibration, and Identification of Hadronically Decaying Tau Leptons in the ATLAS Experiment for Run-2 of the LHC. (Cited on page 183.)

[34] LHC Higgs Cross Section Working Group, S. Heinemeyer, C. Mariotti, G. Passarino, and R. Tanaka (Eds.), Handbook of LHC Higgs Cross Sections: 3. Higgs Properties, CERN-2013-004 (CERN, Geneva, 2013), arXiv:1307.1347 [hep-ph]. (Cited on page 185.)

[35] ROOT Collaboration, K. Cranmer, G. Lewis, L. Moneta, A. Shibata, W. Verkerke et al., HistFactory: A tool for creating statistical models for use with RooFit and RooStats, CERN-OPEN-2012-016, New York University, New York, Jan. 2012. (Cited on page 186.)

[36] "Search for the Standard Model Higgs Boson in Hadronic $\tau^+\tau^-$ Decays with the ATLAS Detector" CERN-THESIS-2014-085 20/05/2014 (Cited on page 186.)

[37] J. Friedman, 'Data analysis techniques for high energy particle physics', Proceedings of 3rd CERN School on Computing, 1974. (Cited on page 188.)

[38] G. Cowan et al. "Asymptotic formulae for likelihood-based tests of new physics". In: Eur. Phys. J. C71 (2011), p. 1554. DOI: 10.1140/epjc/s10052-011- 1554- 0. arXiv:1007.1727 [physics.data-an] (Cited on pages 186, 187, 188, 189 and 190.)

[39] These de Doctorat, Estelle Scifo, "Measurement of the Brout-Englert-Higgs boson couplings in its diphoton decay channel with the ATLAS detector at the LHC" (Cited on pages 189 and 190.)

[40] F. James and M. Roos, Minuit: A System for Function Minimization and Analysis of the Parameter Errors and Correlations, Comp.Phys.Comm. 10(1975) 343-367. (Cited on page 187.)

Résumé

1. Contexte théorique

Le Modèle Standard est une description unifiée des interactions électromagnétique, faible et forte. C'est une théorie de jauge qui a été formulée par Glashow, Salam et Ward, et Weinberg.

Les équations fondamentales de la théorie unifiée rendent parfaitement compte de la force électrofaible et des particules associées qui véhiculent la force, à savoir le photon et les bosons W et Z. Mais il y a un hic : selon ce modèle, ces particules seraient dépourvues de masse. Or, si le photon n'a bel et bien aucune masse ; nous savons que les particules W et Z en ont une, équivalent à près de 100 fois la masse du proton. Heureusement, les théoriciens Robert Brout, François Englert et Peter Higgs ont élaboré une théorie permettant de résoudre le problème. Ce que nous appelons aujourd'hui le mécanisme de Brout-Englert-Higgs donne une masse au W et au Z lorsqu'ils interagissent avec un champ invisible mais omniprésent dans l'Univers, récemment baptisé le champ de Higgs.

Comme pour le W et le Z, le mécanisme de Higgs est capable de donner une masse aux fermions, leptons et quarks, à travers le couplage de Yukawa. Ce couplage est proportionnel à la masse des fermions. Ce qui fait que dans le secteur leptonique, sachant que le tau est le lepton le plus massif (par rapport à l'électron et au muon), la désintégration du boson de Higgs en deux leptons taus est très importante pour l'étude du couplage de Yukawa aux fermions. La recherche de ce canal de désintégration dans l'expérience ATLAS au LHC constitue la partie principale de cette thèse. Ce couplage peut être également sondé par l'étude la désintégration du boson de Higgs en deux quarks b, lui aussi canal de recherche dans ATLAS, mais qui souffre d'un grand bruit de fond.

2. Phénoménologie du boson de Higgs

Le boson de Higgs peut être produit via différents modes dans les collisionneurs hadroniques proton-proton comme le LHC. Les principaux modes de production sont la fusion de gluons (ggH), la fusion de bosons vecteurs (VBF), la production associée avec un boson vecteur (WH et ZH) et la production associée avec une paire de quarks top (ttH). Les modes dominants au LHC sont ggH et VBF. La section efficace de production dépend de l'énergie dans le centre de masse $s^{1/2}$ de la collision des protons au LHC.

Concernant la désintégration du boson de Higgs, la Figure 1 montre les rapports d'embranchement des différents modes de désintégration en fonction de sa masse.

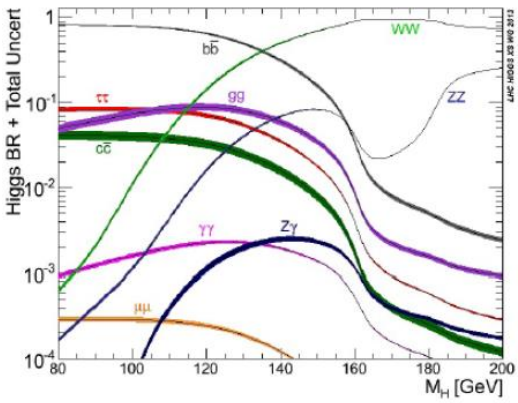

Figure 1 : Les rapports d'embranchement des différents modes de désintégration du Higgs en fonction de sa masse.

La découverte du boson de Higgs Après la combinaison des résultats des deux premières années de données du LHC (2011 et 2012 à $s^{1/2}$ = 7 TeV et 8 TeV respectivement) et en combinant tous les canaux, l'observation d'une résonance étroite autour d'une masse de 125 GeV a été annoncé en juillet 2012 (il existait un signal clair de la désintégration de cette nouvelle particule en $\gamma\gamma$ et ZZ, ainsi qu'une indication d'une désintégration possible en WW). Les collaborations ATLAS et CMS au LHC ont observé le plus grand excès avec une signifiance de 5.9σ (à m_H = 126.5 GeV) et 4.9σ (à m_H = 125.5 GeV) respectivement.

Concernant le couplage aux fermions, d'après l'analyse faite au Run I du LHC, une indication forte dans le mode leptonique Higgs en $\tau^+\tau^-$ a été observée. Avec les données du Run II, nous visons un signal sans ambiguïté (> 5σ) par expérience.

En ce qui concerne les paramètres du boson de Higgs (production, désintégration, masse, spin, paramètres CP), toutes les mesures montrent jusqu'à présent une compatibilité avec les prédictions du Modèle Standard.

3. Le LHC et le détecteur ATLAS

Le LHC est le collisionneur le plus puissant du monde, permettant d'étudier la physique des particules en collisionnant des protons à très haute énergie. Il y a quatre points d'interaction le long de l'anneau du LHC où les protons sont collisionnés. Les expériences à ces points sont ATLAS, CMS, LHCb et ALICE. ATLAS et CMS sont les plus grandes expériences dédiées à la compréhension de la physique du Modèle Standard et au-delà.

L'augmentation de l'énergie jusqu'à 13 TeV au Run II va permettre d'accroître le potentiel de découverte de particules lourdes. Le gain en luminosité permet d'étudier avec plus de précision les processus qui ont une section efficace faible.

Le détecteur ATLAS est le plus grand des détecteurs au LHC. C'est un détecteur 4π qui mesure environ 44 m en longueur et 25 m en hauteur. Il a une géométrie cylindrique avec des bouchons de chaque côté afin d'assurer une couverture quasi-complète en rapidité.

Il est divisé en trois parties principales :

- Le détecteur interne destiné à mesurer les trajectoires des particules chargées dans le volume central. Un champ magnétique solénoïdal courbe les trajectoires des chargées et permet de mesurer leur impulsion.
- Le système de calorimètres qui permet la mesure d'énergie des particules chargées et neutres. Il est composé de deux parties : électromagnétique pour mesurer l'énergie des électrons et des photons, et hadronique pour les jets et l'énergie transverse manquante.
- Le spectromètre à muons qui baigne dans un champ magnétique toroïdal et qui permet la mesure des muons à l'aide de chambres à fils.

En outre, un système de déclenchement est utilisé afin de réduire la quantité des données produites par les collisions de protons, sachant que dans les collisionneurs hadroniques, une grande quantité d'événements ne correspond pas à une collision dure.

4. Reconstruction des taus hadroniques

La reconstruction des objets physiques dans ATLAS, utilisés dans l'analyse Higgs en $\tau^+\tau^-$, est décrite dans cette thèse. Cette étape consiste à reconstruire les objets en partant des informations provenant du détecteur, c'est-à-dire identifier et mesurer les objets finaux (traces chargées, vertex, électrons, muons, jets, taus et énergie transverse manquante).

Les taus sont les leptons les plus lourds. Ils se désintègrent en deux modes : leptonique (35%) et hadronique (65%). Les taus leptoniques sont reconstruits via les produits de désintégration visibles, électrons et muons. La désintégration hadronique est divisée en deux catégories 1-prong avec un pion chargé et 3-prong avec trois pions chargés. Des pions neutres peuvent aussi exister dans les produits finaux.

La reconstruction des taus hadroniques est la partie la plus difficile étant donné le grand bruit de fond provenant des jets pouvant simuler un tau hadronique. Ils sont reconstruits en utilisant des algorithmes de jets anti-k_T avec des sélections appliquées sur les candidats. Une identification supplémentaire contre le bruit de fonds de jets et utilisant une méthode multivariée est appliquée.

Une nouvelle méthode de reconstruction est en développement, le « Tau Particle Flow ». Son but est d'améliorer la classification des modes de désintégration des candidats taus, et ainsi la reconstruction de leurs quadrivecteurs.

Conversions dans les désintégrations hadroniques de taus Dans 40% des cas environ, il y a un pion neutre dans l'état final qui se désintègre à son tour en deux photons. Ces derniers peuvent interagir avec des parties passives du détecteur et ainsi se convertir en une paire e^+e^-. Ces extra-traces chargées peuvent affecter la reconstruction des taus hadroniques, en y ajoutant des traces qui peuvent être identifiées à tort comme des traces provenant directement du tau.

Des algorithmes ont été développés afin d'étiqueter les traces provenant de la conversion des photons. L'algorithme « Single Track Tagger » est basé sur les

informations du détecteur interne et cherche à étiqueter les conversions trace par trace. Un autre algorithme cherche les conversions en évaluant toutes les combinaisons de paires de traces chargées d'un candidat tau, et effectue un ajustement basé sur plusieurs paramètres pour décider si l'on est en présence de conversions.

Les performances de ces algorithmes ont été étudiées dans ATLAS et comparées entre différentes version du code de reconstruction des taus. Une comparaison des performances entre les données à 8 TeV et 13 TeV a également été effectuée.

5. Analyse H —> ττ dans le canal de désintégration $\tau_{lep}\tau_{had}$

Le canal H → $\tau^+\tau^-$ est le seul canal accessible aujourd'hui pour l'observation directe du couplage du boson de Higgs aux fermions.

Comme indiqué dans la section précédente, compte tenu des deux modes de désintégration du tau, leptonique et hadronique, cela conduit à trois états finaux : $\tau_{lep}\tau_{lep}$, $\tau_{lep}\tau_{had}$, $\tau_{had}\tau_{had}$. L'analyse présentée dans cette thèse correspond au statut actuel de l'analyse du mode $\tau_{lep}\tau_{had}$.

Les modes d production dominants pour cette analyse sont ggH et VBF. Les bruits de fond dominants sont le processus Z → $\tau^+\tau^-$ qui ressemble à l'état final étudié, et le bruit de fond des jets simulant des taus hadroniques (fakes). D'autres sources de bruits de fond sont aussi prises en compte comme top-antitop, Z → ll, diboson.

Le fond Z → $\tau^+\tau^-$est estimé en utilisant la simulation Monte Carlo de ce processus. Les fakes sont estimés en utilisant la méthode du « Fake Factor ».

Pour sélectionner les événements de signal, une série de coupures est appliquée, en partant de ce que l'on appelle la « Présélection », puis les événements sont regroupés en différentes catégories afin d'optimiser la sensibilité.

Un modèle de fit est ainsi utilisé pour tester l'accord entre les données observées par ATLAS et les hypothèses « bruit de fond plus signal » ou « bruit de fond seulement ». Ce modèle est construit en tenant compte des erreurs statistiques et systématique, à partir des données observées et des bruits de fond prédits.

Le modèle dépend de plusieurs paramètres. Dans notre cas, le paramètre d'intérêt est la section efficace de production du Higgs multipliée par le rapport d'embranchement du Higgs en $\tau^+\tau^-$, exprimé en unités de la valeur prédite par le Modèle Standard.

A l'heure actuelle, le modèle a été validé sur des données spéciales, dites Asimov, et l'extraction des résultats à partir des vraies données est imminente.